



PhD-FSTC-2012-31
The Faculty of Science, Technology and Communication

DISSERTATION

Defense held on 28/11/2012 in Luxembourg

to obtain the degree of

DOCTEUR DE L'UNIVERSITÉ DU LUXEMBOURG

EN BIOLOGIE

by

Aliaksandr HALAVATYI

Born on 5 March 1985 in Minsk, (Republic of Belarus)

SIMULATION AND COMPUTER-ASSISTED ANALYSIS OF ACTIN CYTOSKELETON DYNAMICS IN LIVING CELLS USING FLUORESCENCE MICROSCOPY METHODS

Dissertation defense committee

Dr Evelyne Friederich, dissertation supervisor
Professor, Université du Luxembourg

Dr Albrecht Ott
Professor, Universität des Saarlandes, Saarbrücken, Germany

Dr Thomas Sauter, Chairman
Professor, Université du Luxembourg

Dr Clément Thomas
Senior researcher, CRP-Santé, Luxembourg

Dr Rainer Pepperkok, Vice Chairman
*Group leader and head of the advanced light microscopy core facility
European Molecular Biology Laboratory (EMBL), Heidelberg, Germany*



UNIVERSITÉ DU LUXEMBOURG
Life Sciences Research Unit (LSRU)

University of Luxembourg
Faculty of Science Technology and Communication
Life Sciences Research Unit
Cytoskeleton and Cell Plasticity Laboratory

Thesis submitted to fulfil the requirements for achievement of the degree of Doctor of
the University of Luxembourg

By **Aliaksandr HALAVATYI**

**Simulation and computer-assisted analysis of actin cytoskeleton
dynamics in living cells using fluorescence microscopy methods**

Public PhD defence November 28, 2012

Committee members:

| | | |
|-----------|--------------------------|---------------------------------------|
| Promoter: | Prof. Evelyne Friederich | (University of Luxembourg) |
| Chairman: | Prof. Thomas Sauter | (University of Luxembourg) |
| Members: | Dr. Rainer Pepperkok | (EMBL Heidelberg, Germany) |
| | Prof. Albrecht Ott | (Universität des Saarlandes, Germany) |
| | Dr. Clément Thomas | (CRP-Santé, Luxembourg) |

Contents

| | |
|---|-----------|
| Abbreviations..... | 5 |
| Summary | 7 |
| Structure of the thesis | 8 |
| Chapter 1 General introduction..... | 9 |
| <i>1.1 Actin cytoskeleton.....</i> | <i>9</i> |
| 1.1.1. Biological functions of the actin cytoskeleton..... | 9 |
| 1.1.2. Molecular mechanisms of actin assembly..... | 11 |
| 1.1.3. Regulation of actin dynamics by actin-binding proteins. | 14 |
| 1.1.4. Regulation of actin cytoskeleton in living cells..... | 21 |
| <i>1.2 Experimental techniques for studying actin dynamics</i> | <i>27</i> |
| 1.2.1. Biochemical assays | 27 |
| 1.2.2. Studying actin dynamics in living cells..... | 32 |
| <i>1.3 Mathematical models of actin polymerisation and associated phenomena</i> | <i>39</i> |
| 1.3.1. Methods for simulating biomolecular kinetics..... | 42 |
| <i>1.4 Scope of the thesis</i> | <i>46</i> |
| Chapter 2 Materials and methods..... | 49 |
| <i>2.1 Biomimetic motility assay for actin-based processes.....</i> | <i>49</i> |
| 2.1.1. Proteins..... | 49 |
| 2.1.2. Motility assay preparation..... | 49 |
| 2.1.3. Time-lapse microscopy and FRAP experiments | 50 |
| 2.1.4. Data processing | 50 |
| <i>2.2 Experiments with the living cells.....</i> | <i>51</i> |
| 2.2.1. DNA Constructs | 51 |
| 2.2.2. Cell culture and transfection | 51 |
| 2.2.3. FRAP experiments | 52 |
| 2.2.4. Data processing | 52 |
| <i>2.3 Development of the Integrated approach for analysing FRAP intensities.....</i> | <i>53</i> |
| 2.3.1. General scheme..... | 53 |
| 2.3.2. Software tools | 55 |
| Chapter 3 Development of models for actin dynamics | 57 |
| <i>3.1 Stochastic simulation algorithm for predicting actin dynamics.....</i> | <i>57</i> |
| 3.1.1. Introduction..... | 57 |
| 3.1.2. Model | 58 |
| 3.1.3. Results and discussion..... | 69 |
| 3.1.4. Software ActinSimChem..... | 78 |
| 3.1.5. Concluding remarks..... | 78 |
| <i>3.2 Model of actin turnover for analysing FRAP data.....</i> | <i>80</i> |
| 3.2.1. Introduction..... | 80 |
| 3.2.2. Kinetic model for fitting equation | 81 |

| | |
|--|------------|
| 3.2.3. Simulation results and discussion | 87 |
| 3.2.4. Conclusion | 93 |
| Chapter 4 Combining actin-based biomimetic assay with FRAP method to study spatially and temporarily controlled actin turnover..... | 95 |
| 4.1 Introduction..... | 95 |
| 4.2 Establishment of FRAP experiments with the biomimetic assay..... | 98 |
| 4.3 Development of tools for the analysis of spatio-temporal regulation of actin turnover..... | 100 |
| 4.4 Role of depolymerisation in the turnover of actin comets..... | 102 |
| 4.5 Effect of capping on actin turnover..... | 105 |
| 4.6 Concluding remarks | 108 |
| Chapter 5 Analysing the dynamics of the actin cytoskeleton at focal adhesions of living cells..... | 111 |
| 5.1 Zyxin and Tes - focal adhesion proteins regulating actin dynamics (introduction) | 111 |
| 5.2 Role of Tes in actin turnover at focal adhesions..... | 114 |
| 5.2.1. Overexpression of Tes stimulates actin polymerisation at focal adhesions | 114 |
| 5.2.2. Silencing of endogenous Tes slows down actin turnover | 115 |
| 5.3 Role of zyxin-Tes interactions in the regulation of the cytoskeleton at focal adhesions..... | 116 |
| 5.3.1. The binding kinetics of zyxin in focal adhesions accelerates upon loss of its interaction with Tes | 116 |
| 5.3.2. Loss of interaction between zyxin and Tes decreases the rate of actin turnover at focal adhesions | 119 |
| 5.4 Conclusions | 120 |
| Chapter 6 General discussion and perspectives | 121 |
| 6.1 Linking experiments and mathematical models for the quantitative analysis of the actin polymerisation cycle..... | 121 |
| 6.2 Measurements of actin turnover with the actin-based biomimetic assay..... | 122 |
| 6.3 Cytoskeleton turnover at focal adhesions: functions of zyxin and Tes | 125 |
| 6.4 General conclusions..... | 127 |
| References | 129 |
| Appendix | 145 |

Abbreviations

ADF – actin depolymerising factor;
ADP – adenosine-5'-diphosphate;
Aip1 – actin-interacting protein 1;
ATP – adenosine-5'-triphosphate;
BE – barbed end of actin filament;
CP – heterodimeric capping protein;
ECM – extracellular matrix;
EGTA – ethylene glycol tetraacetic acid;
Ena/VASP – enabled/vasodilator-stimulated phosphoprotein;
FA – focal adhesion;
F-actin – filamentous actin;
FC – focal complex;
FCS – fluorescence correlation spectroscopy;
FRAP – fluorescence recovery after photobleaching;
FSM – fluorescence speckle microscopy;
G-actin – globular (monomeric) actin;
G(C,Y,R)FP – green (cyan, yellow, red) fluorescent protein;
MD – molecular dynamics;
NPF – nucleation promotion factor;
ODE – ordinary differential equations;
PA – photoactivation;
PDE – partial differential equations;
PE – pointed end of actin filament;
PIP₂ – phosphatidylinositol 4,5-bisphosphate;
pyrene – N-(1-pyrenyl)iodoacetamide;
ROI – region of interest;
SD – standard deviation;
SEM – standard error of the mean;
SF – stress fiber;
SSA – stochastic simulation algorithm;
TIRF – total internal reflection fluorescence;
TRITC – tetramethyl rhodamine iso-thiocyanate;
VCA – verprolin/cofilin/acidic domain;
WASP – Wiskott–Aldrich-syndrome protein;

Summary

Controlled in time and space by a variety of actin-binding proteins, assembly and disassembly of the actin cytoskeleton is involved in many biological and biophysical phenomena. In order to understand the dynamics of such a complex intracellular system quantitative time-lapse imaging approaches are required.

This thesis presents the results of the interdisciplinary project aimed at the quantitative evaluation of the effects of actin-binding proteins on actin turnover under physiological conditions. It combines fluorescence microscopy experiments, development of mathematical models and data processing tools to understand how regulatory proteins control actin dynamics. Confocal-microscopy-based Fluorescence Recovery After Photobleaching (FRAP) technique is a major experimental tool to measure the exchange of actin and actin-binding proteins between polymerised and monomeric pools. The developed models and computational algorithms allow to predict actin dynamics depending on regulatory proteins and to connect the experimental data to parameters characterising polymerisation dynamics, length and structures of actin filaments and activities of tested regulatory proteins.

To test the models and to evaluate the activities of actin-binding proteins without cellular constraints I combined quantitative FRAP analysis with a biomimetic assay which allows to reproduce major features of actin motility. This combination of techniques was utilised to measure the influence of previously characterised actin-binding proteins working together on actin dynamics in a concentration-dependent manner. In particular we investigated how capping and severing of actin filaments influences actin exchange in a bulk meshwork generated from spatially restricted nucleation.

The experimental and analysis methods I developed were also used to investigate the dynamics of the actin cytoskeleton at focal adhesions of living cells. Taking as an example the focal adhesion protein zyxin and its binding partner Tes we addressed how the interactions of these proteins with actin regulate cytoskeleton dynamics.

Taken together, the developed approaches and collected data help to better understand how regulatory proteins control actin dynamics in living cells.

Structure of the thesis

This thesis includes different interdisciplinary aspects, which are highlighted in the corresponding chapters of this manuscript.

Chapter 1 provides a general introduction to the actin cytoskeleton. Properties of the actin system and major historical steps in understanding actin structure and dynamics at different levels are described. Experimental techniques and modelling methods currently applied for the understanding of actin dynamics are discussed together with major open questions and upcoming challenges.

Experimental protocols and computational algorithms developed for analysing the collected experimental data are introduced in **Chapter 2**. They include procedures for quantification of FRAP intensities from time-lapse images, normalisation, modelling, fitting of the collected FRAP recoveries and statistical analysis of the estimated parameters. All these algorithms were implemented as computational tools, which are available as supplementary files on the web-page actinsim.uni.lu.

Chapter 3 describes mathematical models developed during the initial phase of the thesis project. First, a stochastic simulation algorithm (SSA) for the prediction of actin polymerisation dynamics and effects of various actin-binding proteins is presented. Second, a specific mathematical model for the analysis of actin polymerisation by FRAP is described.

Chapter 4 is dedicated to the quantitative study of actin turnover without cellular constraints. It takes advantage of an actin-based biomimetic assay combined with FRAP to evaluate the dynamic properties of bulk of actin filaments under controlled biochemical conditions. Using this approach we measured how capping and severing proteins regulate turnover of actin filaments in time and in space.

Finally in **Chapter 5** applications of the developed algorithms and tools to study actin polymerisation in living cells are presented. To investigate the regulation of actin cycle by selected proteins, FRAP data with fluorescently-labelled actin, Tes and zyxin, actin-associated focal adhesion proteins presently studied in the host laboratory, were collected and analysed.

Chapter 1 General introduction

1.1 Actin cytoskeleton

1.1.1. Biological functions of the actin cytoskeleton

Actin is a cytoplasmic protein which exists in the cell as monomeric or globular (G-) actin and filamentous (F-) actin. G-actin has a molecular weight of 43 kDa and a structure which is highly conserved among all known living species (Ng and Abelson, 1980; Vandekerckhove and Weber, 1978). Actin is a highly abundant protein in cells and is the major component of one of the three cell cytoskeleton types: actin filaments (microfilaments), intermediate filaments and microtubules. Actin cytoskeleton is responsible for providing mechanical structure and motility to the cells (Stossel, 1993). The ability of actin to polymerise under physiological conditions is involved in many cellular processes like endocytosis, cytokinesis, adhesion and signalling (Pollard and Borisy, 2003). In eukaryotic cells, actin filaments serve as tracks for myosins in the transport of organelles and vesicles (Sellers and Veigel, 2006). Importantly, during these processes actin polymers are not static but undergo continuous cycles of assembly/disassembly controlled by numerous regulatory proteins.

All actin-associated intracellular phenomena are associated to physiological functions such as morphogenesis, cell migration, division or cell communication. Perturbation in actin assembly and disassembly processes affect these functions and often lead to pathological situations including cancer and neurodegenerative disorders (Dos Remedios and Chhabra, 2008; Lambrechts et al., 2004). Uncontrolled migration of cancer cells leading to metastasis significantly depends on perturbed actin polymerisation (Golsteyn et al., 1997; Janji et al., 2010). Also, spreading of several pathogens, such as *Listeria monocytogenes*, is driven by mechanical forces generated by actin assembly (Theriot et al., 1992). Therefore, actin polymerisation and its regulation at a molecular level have to be studied to understand the functions of individual cells, tissues and multicellular organisms.

To ensure various biological functions, actin filaments are organised in living cells into structurally distinct assemblies (Fig. 1.1a). The structures that are responsible for cell spreading, motility and attachment to the extracellular

environment are schematically shown in Fig. 1.1b (Le Clainche and Carlier, 2008). The lamellipodium is a dendritic network of short actin filaments formed at the leading edge of migrating cells (Small, 1994; Svitkina and Borisy, 1999). Rapid polymerisation of actin in the lamellipodium provides forces sufficient for pushing the plasma membrane forward. The lamella is a network of longer and more stable filaments, which is situated behind the lamellipodium and has a supplementary or redundant role for the protrusion of the leading edge (Gupton et al., 2005). Distinct actin cytoskeleton structures are assembled in cells to sense the extracellular environment. Filopodia are plasma membrane extensions containing long aligned filaments, which are initiated at the leading edge (Mattila and Lappalainen, 2008). The attachment of the cell to the extracellular environment is achieved via the formation of adhesion structures including very dynamic focal complexes (FC) and more stable focal adhesions (FA) (Webb et al., 2002; Wolfenson et al., 2009). FAs are associated with stress fibers (SF) – long cables of antiparallel actin filaments that define cell shape and apply mechanical stress for the retraction of the trailing edge (Hotulainen and Lappalainen, 2006). The formation and dynamics of all these distinct structures is coordinated in time and space to support cell motility as well as other actin-dependent processes (Huber and Kas, 2011).

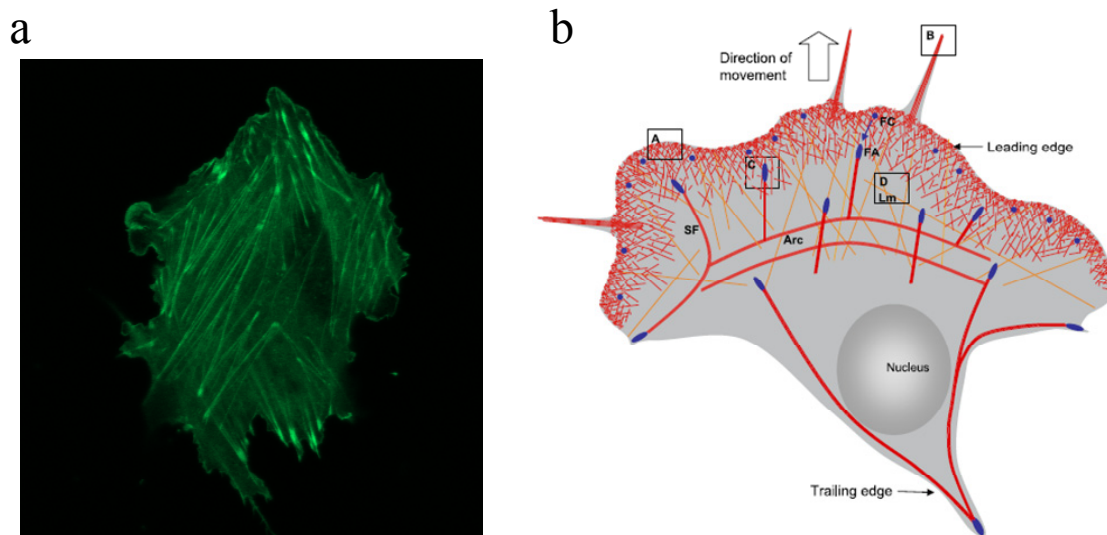


Figure 1.1: Roles of the actin cytoskeleton in cell motility

a) GFP-actin in a Vero cell. Various actin structures contribute to distinct intracellular processes; b) scheme of actin structures in migrating cells (adapted from (Le Clainche and Carlier, 2008); actin shown in red). Boxes outline lamellipodium (A), filopodium (B), focal adhesion (C) and lamella (D).

To ensure its biological functions and to react rapidly to extracellular and intracellular changes, actin is highly regulated in the cytoplasm by numerous molecules that are interconnected via various regulatory pathways into the actin system. The actin system comprises: i) actin and actin-binding proteins that interact directly with actin monomers or filaments and change their organisation and dynamics; ii) signalling molecules (Rho GTPases, transmembrane receptors, etc.) that regulate the activities of actin-binding proteins in time and space through phosphorylation or through other mechanisms including second messengers (e.g. Ca^{2+} , phosphoinositides) in response to intracellular or extracellular stimuli. Since this thesis aims at studying the dynamics of the actin cytoskeleton, I will primarily focus on the roles of actin-binding proteins in the regulation of actin polymerisation kinetics.

1.1.2. Molecular mechanisms of actin assembly

To understand how actin forms various structures in cells in response to different regulatory factors, it is crucial to characterise the self-assembly process of cytoskeleton-associated protein complexes at biochemical and cellular levels.

Under physiological ionic conditions, actin is able to self-assemble into long linear filaments with a double helix structure (Fig. 1.2) (Holmes et al., 1990). The filaments are ~7 nm thick and can vary in length from hundreds of nanometers to dozens of micrometres depending on the involved regulatory factors. The actin monomer is an asymmetric molecule and, when assembled into filaments, all protomers (actin subunits in the filaments) are oriented in the same direction. Therefore the ends of actin filaments are structurally and biochemically different. At the plus end also termed barbed end (BE), filament assembly and disassembly reactions occur much faster than at the minus end called pointed end (PE). The polymerisation process is reversible: under steady-state conditions G- and F- actin coexist in a rapid equilibrium.

Besides the association and disassociation of G-actin at the ends of filaments, fragmentation and annealing of the filaments lead to the changes in their lengths (Fass et al., 2008). Fragmentation of filaments is supported in cells by pools of the dedicated proteins. Annealing requires the collision of free BE and PE of neighbouring filaments and becomes less favourable upon growth of filaments (Andrianantoandro et al., 2001).

G-actin does not necessarily require preformed filaments to polymerise. Actin monomers can form oligomers (dimers and trimers) that serve as nuclei for polymerisation. Actin dimers are highly unstable and rapidly disassociate, but when a more stable trimer is formed, filaments polymerise rapidly by the assembly of monomers at their ends (Sept and McCammon, 2001). The nucleation of new filaments is often the rate-limiting factor for the polymerisation process and is promoted in cells by different actin-binding proteins, which form new or stabilise existing actin nuclei (see section 1.1.3).

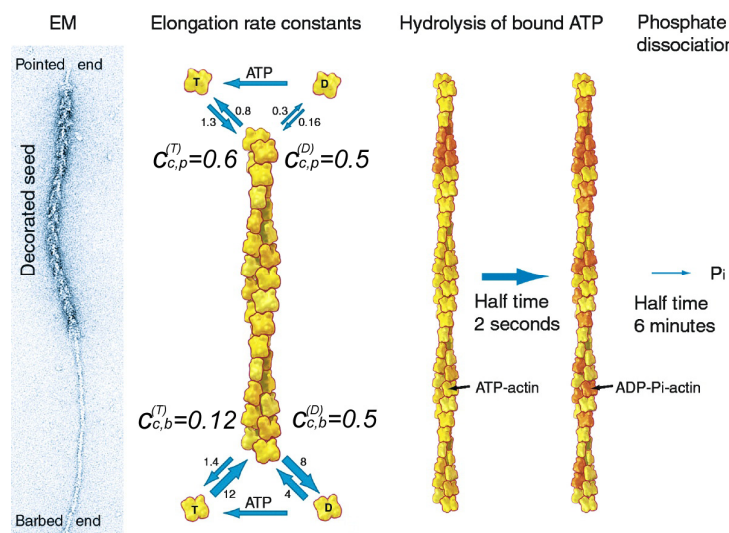


Figure 1.2: Structure of actin filament and reactions of actin assembly/disassembly (Pollard and Borisy, 2003)

Measured *in vitro* parameters of subunit association and disassociation for actin monomers bound with ATP (T) or ADP (D) are provided. Association rates are in $\mu\text{M}^{-1}\text{s}^{-1}$, disassociation rates are in s^{-1} , the equilibrium dissociation constants c_c are in μM .

The extent and rate of polymerisation depend on several structural properties of monomers and filaments. First, each actin monomer or protomer in filaments binds one adenine nucleotide molecule (ATP, ADP-Pi or ADP). Binding of ATP is not required for actin to assemble with filaments, but prevents denaturation of actin monomers and affects filament stability (De La Cruz et al., 2000). ATP-G-actin has a higher affinity for filaments in comparison to ADP-G-actin and only ATP-G-actin can nucleate new filaments. Therefore, the major part of newly polymerised F-actin is ATP-bound. ATP molecules associated to actin protomer in filaments are converted into ADP in a two step process (Fig. 1.2) (Carlier and Pantaloni, 1986). First, hydrolysis occurs during several seconds. Second, ADP-Pi undergoes a γ -phosphate

release at a much slower rate. Because ADP-F-actin is more favourable for depolymerisation than ATP-F-actin, the time delay required for hydrolysis/Pi-release contributes to the stability of filaments. Rapidly occurring nucleotide exchange (ADP to ATP) on disassembled ADP-actin promotes recycling of these monomers for new polymerisation events (Neidl and Engel, 1979).

For a long time the nucleotide state was considered as a major determinant of actin filament turnover. The monomer assembly and disassembly at the ends of filaments are considered to be the second and the first order reactions respectively. The corresponding rate constants k_+ and k_- and critical actin concentrations c_c , which in this case can be evaluated as k_-/k_+ , depend on the nucleotide state of the involved actin subunit and the type of filament end (Kuhn and Pollard, 2005; Pollard, 1986). Although the critical concentrations for ADP-actin are equal at the BE and PE ($c_{c,BE}^{(P)} = c_{c,PE}^{(P)}$), ATP-actin has a much higher affinity for the BE ($c_{c,BE}^{(T)} < c_{c,PE}^{(T)}$). Because the elongation rate is proportional to the difference between the actual (c) and the critical actin concentrations ($v_+ = k_+(c - c_c)$), in the case of excess of ATP-G-actin filaments grow faster at the BE and slower at the PE. When the actual actin concentration is above $c_{c,b}$ and below $c_{c,p}$, filaments undergo treadmilling – elongation at BE and simultaneous shortening at PE. As a result, all actin protomers will migrate through the filaments towards the PE. When the assembly at the BE is balanced by the depolymerisation at PE, filaments treadmill while maintaining the constant average length (Carlier and Pantaloni, 1997; Korn et al., 1987; Wegner, 1976).

However, recent experimental evidence suggested that turnover of actin protomers in filaments could not be considered as a treadmilling with a constant rate. The measured diffusivities of the ends of filaments (Fujiwara et al., 2002), e.g. fluctuations of the lengths of filaments over time, were much higher than one would expect from association/disassociation of monomers with the estimated kinetic rates. Depolymerisation in *Listeria* comet tails was shown to occur in bursts, e.g. the relatively stable filaments may rapidly disassemble their large terminal parts (Kueh et al., 2010). Visualisation of the depolymerisation of single newly polymerised filaments in G-actin-deficient conditions revealed their fast shrinkage from the BEs, which terminated after several minutes, and slow shrinkage from the PEs, which was

observed for a long time (Kueh et al., 2008a). These findings are consistent with the structural studies of actin filaments using electron microscopy (Orlova et al., 2004), which found multiple twisted conformations in the helical structure of young filaments. Upon maturation, filaments convert to unique and more rigid structures with more stable interactions between adjacent filament subunits. Thus, ATP hydrolysis/P-release and structural stabilisation of filaments have opposite effects on actin disassembly. Although most kinetic models of actin turnover currently rely on the treadmilling mechanism (Bugyi and Carlier, 2010), they might need to be revised when more quantitative data revealing the role of structural fluctuations of filaments on their assembly and disassembly become available.

1.1.3. Regulation of actin dynamics by actin-binding proteins.

The actin-binding proteins can stimulate or inhibit actin polymerisation by nucleating new filaments, changing (dis-)association rates at BE and PE, severing filaments into pieces or stabilising them. Some proteins also interact with actin monomers and change their ability to polymerise via elongation or nucleation reactions (Paavilainen et al., 2004). The list of currently known actin-binding proteins consists of many hundreds of items and continues to grow. Despite a vast variety of proteins, they can be classified into families based on structural similarities (dos Remedios et al., 2003) or based on their functions in changing actin dynamics (Carlier et al., 2007). It has been shown that proteins which belong to different structural protein families might have similar roles in regulating actin turnover. At the same time proteins having a high degree of structural similarity and sharing similar actin-interacting domains often exhibit different functions (Poukkula et al., 2011) and even the same protein might have multiple functions depending on its quantity or the presence of regulatory molecules (Husson et al., 2011; Van Troys et al., 2008). Here, I first describe the basic regulation mechanisms of actin dynamics linked to well characterised actin-binding proteins. The structural properties of these proteins are only considered when they are essential for explaining protein functions.

1.1.3.1. Actin-monomer interacting proteins

The sequestering of G-actin, e.g. preventing its spontaneous polymerisation or association at the ends of preformed filaments, is essential for maintaining a high pool of polymerisable actin. Profilin binds barbed sides of actin monomers and

prevents them from spontaneous nucleation or from binding to the PE of filaments. However profilin-actin complexes associate with BEs (Witke, 2004), and therefore facilitate the treadmilling of filaments (Didry et al., 1998). Shortly after the elongation event, profilin disassembles from the terminal subunit to allow new assembly cycles. Because it has a low affinity to BEs, profilin can slow down their elongation at high concentrations. Additionally binding of profilin stimulates ATP recharge on actin monomers. Furthermore, different ADF/cofilins might play a role of actin sequesters, but unlike profilin, they bind preferentially to ADP-G-actin, inhibit ATP recharge and prevent binding to either end of the filament (Yeoh et al., 2002).

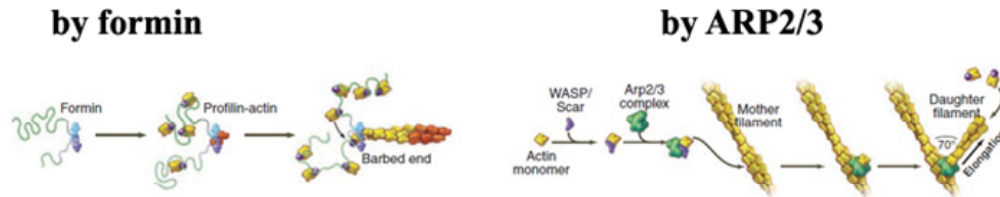
1.1.3.2. Actin nucleating proteins

The creation of new filaments from the pool of actin monomers is quite unfavourable without additional stimulus. To form specific actin filament structures, actin nucleation is stimulated considerably in appropriate locations by dedicated actin-binding proteins. Among those, the Arp2/3 protein complex and formins are the best characterised (Pollard, 2007).

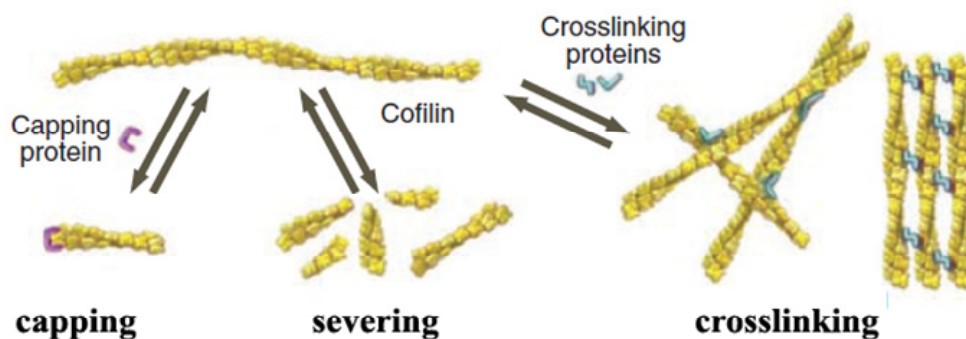
Arp2/3 is a seven subunit protein complex which consists of two actin-related proteins (Arp2 and Arp3) and five additional subunits. Globular Arp2/3 complex has to be first activated by one of the nucleation promotion factors (NPFs) such as Wiskott–Aldrich-syndrome protein (WASp), neuronal WASP (n-WASP) or WASP and verprolin homologs (WAVEs) (Marchand et al., 2001). WASp binds one actin monomer and , following this, the Arp2/3 complex. The formed ternary complex associates with the sides or barbed ends of a pre-existing filament and serves as a starting point for the growth of new actin filaments (Pollard and Beltzner, 2002) at an angle of ~70 degrees between old and new filaments. During the subsequent filament elongation, the BE of the filament is always distal to the branching point and its properties are not further affected by the Arp2/3 complex. PE remains bound to the Arp2/3 complex for a certain time period (Mullins et al., 1998) . Therefore, Arp2/3 has an additional role as PE capping protein and might be a rate-limiting factor for the disassembly of branched filaments. The debranching of filaments and disassembly of Arp2/3 complex is promoted by ATP hydrolysis on its Arp2 subunit and direct binding of coronin and glia maturation factor (GMF) proteins. Binding of ADF/cofilin to filaments, that will be considered further in detail, decreases affinity of

Arp2/3 complex to the filaments by competing for available binding sites or by changing the filament structure (Chan et al., 2009).

a Nucleation and elongation



b Reactions with filaments



c Sequestering

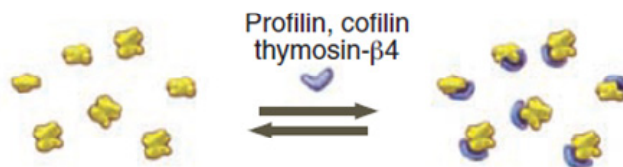


Figure 1.3: Regulation of the turnover of actin filaments by actin-binding proteins. Adapted from (Pollard and Cooper, 2009)

a) Actin-nucleating proteins stimulate the formation of linear (by formin) or branched (by Arp2/3) filament structures; b) Various proteins can cap filament ends, sever filaments into pieces or cross-link them to form stable cytoskeleton structures; c) sequestering proteins bind G-actin and prevent it from association to filaments.

Proteins of the formin family do not require any polymerised actin to initiate nucleation of new filaments. They bind and stabilise self-assembling actin dimer and remain associated with the growing BEs (Pring et al., 2003). Most formins contain highly conserved formin homology domains 1 and 2 (FH1 and FH2), which have distinct roles in actin assembly (Higgs, 2005; Kovar, 2006). In the cytoplasm formin exists in an auto-inhibited conformation which is released into an active form upon binding to Rho GTPases (Li and Higgs, 2005). The activation permits FH2 domains

of two formin molecules to form a dimer, which then associates with the actin nucleus (Zigmond, 2004). The FH1 domain is not required for the nucleating activity, but, as discussed in section 1.1.3.4, it changes the kinetic properties of the BEs during their subsequent growth (Paul and Pollard, 2008).

More recently, a new group of actin nucleators including Spire (Quinlan et al., 2005) and Cordon-bleu (Cobl) (Ahuja et al., 2007) was discovered. These proteins bind several actin monomers via their repeated WASp homology 2 (WH2) domains and bring them together to form the nuclei. The mechanistic details of their activity are presently under investigation. Currently it has been shown that different members of this group lead to a different alignment of actin subunits (Renault et al., 2008). These proteins also exhibit cross-talk with formins and Arp2/3 NPFs to further stimulate actin nucleation. Alternatively, they can play competitive roles in polymerisation (Bosch et al., 2007). Besides nucleation, these proteins might interact with the BEs and initiate filament severing (Husson et al., 2011).

The existence of multiple actin nucleators accounts for the different actin cytoskeleton structures. However, the stimulation of polymerisation dynamics in certain cell regions such as focal adhesions is not completely understood (see discussion below), therefore new actin nucleators are likely to be identified in future.

1.1.3.3. Capping proteins

Proteins of several other families can interact with individual filaments and change their kinetic properties. Capping proteins bind to the ends of the actin filament and completely prevent assembly and disassembly reactions on them. One example for capping shown above is the interaction of Arp2/3 complex with the PEs of filaments. Other proteins having capping properties typically bind to the BEs of filaments and prevent them from further growth (Schafer et al., 1996). Under such conditions critical monomer concentration will increase and filaments can either slowly elongate or depolymerise at the PEs. Capping properties are not exclusive to one structural protein family. Members of the gelsolin family including gelsolin, villin, CapG and others require Ca^{2+} ions to interact with actin (McGough et al., 1998), while other capping proteins such as heterodimeric capping protein $\alpha\beta$ (CP) or CapZ are Ca^{2+} -independent. The activity of all capping proteins is highly regulated in cells. In particular, phosphoinositides (e.g. PIP_2) inhibit the activity and initiate the

unbinding of several capping proteins from the BEs (Janmey and Stossel, 1987). CP, but not gelsolin or CapG, can also be inhibited by the protein CARMIL (Kim et al., 2012; Yang et al., 2005). CARMIL was identified as a molecular scaffold linking CP with Arp2/3 complex and myosin I (Jung et al., 2001). Besides preventing capping of filaments and triggering rapid CP disassembly from the BEs (Urano et al., 2006), CARMIL is able to activate filament nucleation by the Arp2/3 complex (Jung et al., 2001). CARMIL is therefore an essential potent regulator of synergetic activities of CP and Arp2/3 complex in the lamellipodia of living cells.

1.1.3.4. Proteins accelerating the elongation of filaments

Multiple actin intracellular structures, such as filopodia and the cytokinetic ring, are composed of linear actin filaments which have to grow rapidly to produce the required mechanical forces. Formins and enabled/vasodilator-stimulated phosphoprotein (Ena/VASP) catalyse the elongation of filaments, remain processively associated with the growing BEs and protect them from the binding of capping proteins (Chesarone and Goode, 2009).

Formin increases the elongation rate of filaments by recruiting profilin-actin complexes (Kovar et al., 2006; Neidt et al., 2009; Paul and Pollard, 2009). The interaction of the FH2 domains of a formin dimer, which are involved in the filament nucleation, with the terminal subunits of the filament can be in two states (Vavylonis et al., 2006). In the “closed” state, the BE is tightly capped. Switching to the “open” state allows the assembly of actin monomers to the filament. This is followed by a shift of the FH2 dimer towards the BE. The adjacent FH1 domains contain multiple profilin binding sites, which are able to recruit profilin-actin complexes from the environment. The resulting accumulation of G-actin increases probability of the collisions between actin monomers and the BE when the latter is in the “open” state (Paul and Pollard, 2008).

Because of the time that the filament is in the “closed” state, the average elongation rate of formin-bound BE is lower than that of free BE in the absence of profilin. However, when profilin is present, formin stimulates BE growth beyond the diffusion limit. Remarkably, high profilin concentrations might slow down the formin-mediated elongation of filaments, because monomeric profilin could compete with profilin-actin complexes for the binding to the FH1 domain (Kovar et al., 2006).

Unlike formins, Ena/VASP proteins do not nucleate new filaments (Barzik et al., 2005) and do not necessarily require profilin for promoting the elongation of BE (Hansen and Mullins, 2010). VASP forms tetramers in which every subunit can bind actin monomers and filaments with a higher affinity for the BE terminal actin protomers. While one VASP subunit is associated to the side of filament near the BE, others capture free actin or profilin-actin complexes in the medium and deliver it to the BE (Breitsprecher et al., 2011). Clustering of VASP on the surfaces of beads in *in vitro* experiments further accelerates the filament elongation and effectively protects them from the CP (Breitsprecher et al., 2008).

1.1.3.5. Depolymerising proteins

Members of this class of actin-binding proteins increase the disassembly rate of filaments either by facilitating actin disassociation at the PE of filaments or by severing them into fragments. Two structural protein families are considered to be directly involved in the disassembly of filaments: ADF/cofilins and gelsolins.

Proteins of the ADF/cofilin family have the most prominent actin depolymerising activity (Carrier et al., 1997). Similarly to capping proteins, ADF/cofilins are regulated in the cytoplasm by multiple factors including PIP₂, Ca²⁺, ATP, pH and others (Bernstein and Bamburg, 2010). Despite a high level of structural similarity between different members of this family, they vary considerably in their affinity to F-actin and in their ability to depolymerise and sever actin filaments (Yeoh et al., 2002). Usually ADF/cofilins have a higher affinity for ADP-F-actin and therefore stimulate treadmilling by depolymerising preferentially older filament parts near the PEs. When bound to filaments, cofilin stimulates nucleotide exchange on the neighbouring protomers, thereby further promoting actin depolymerisation. In cells the disassembly activity of cofilin is stimulated by other actin-binding proteins such as coronin and Aip1 (actin-interacting protein 1) (Brieher et al., 2006), which do not exhibit actin depolymerisation activity without cofilin, but reduce the amount of cofilin required for efficient depolymerisation of filaments. It has been proposed that when cofilin, coronin and Aip1 are present, depolymerisation may occur in bursts at the BE of filaments (Kueh et al., 2008b).

Gelsolin and its homologs also sever filaments. Unlike cofilin, gelsolin remains associated with the BEs after breaking the filaments. The severing activity of gelsolin

family members is differently regulated by Ca^{2+} levels. Micromolar concentrations of ions are already sufficient to reach the maximum severing activity of gelsolin. In contrast, the severing activity of villin requires higher Ca^{2+} concentrations in the range of millimolar (Janmey and Matsudaira, 1988).

1.1.3.6. Cross-linking proteins

The mechanical forces generated due to the assembly of individual filaments cannot account for actin-based biophysical phenomena, such as dynamics of filopodial protrusions or movement of bacteria. In the cytoplasm cross-linking/bundling proteins interact with several filaments to form resilient networks or bundles of filaments. Whether filaments in networks are positioned at different angles, bundles contain parallel filaments with either all BEs oriented in the same (like in filopodia) or in opposite (like in stress fibers) directions. Currently known cross-linking proteins co-localise to different actin structures and have sometimes overlapping functions (Tseng et al., 2002). In addition to changing mechanical properties of these networks, cross-linking proteins affect the rates of filament assembly and disassembly (Al Tanoury et al., 2010; Giganti et al., 2005) by competing with other actin-binding proteins or by changing the accessibility of monomers to densely packed filaments. It has to be noted that filament bundling could also be due to their steric interactions.

1.1.3.7. Modulation of activities of actin-binding proteins

There is large evidence that proteins known for certain actin regulatory activities might have additional functions. Surprisingly, high concentrations of cofilin were shown to stabilise actin filaments or even initiate nucleation of new filaments (Andrianantoandro and Pollard, 2006). In addition, *Arabidopsis* ADF9 was shown to form actin bundles (Tholl et al., 2011). Therefore, different concentrations of ADF/cofilins might have antagonistic effects on actin turnover. High concentrations of gelsolin or other capping proteins might also nucleate filaments (Ditsch and Wegner, 1994). Some formins do not remain attached to the BE during the polymerisation process but create filament bundles, sever filaments and promote their depolymerisation (Goode and Eck, 2007; Harris et al., 2006).

Actin-binding proteins frequently interact and cooperate to regulate actin turnover. As discussed above, ADF/cofilin binds Arp2/3 complex to stimulate filament

debranching (Chan et al., 2009) and interaction of formin with profilin drastically increases the rate of BE elongation (Paul and Pollard, 2008). In addition, gelsolin stimulates disassembly of formin from growing BE (Romero et al., 2004). The multidomain scaffolding proteins, such as IQGAP1 and IRSp53, can bind multiple actin assembly factors to spatially organise them (Chesarone and Goode, 2009).

Thus, the cooperative activity of several actin-binding proteins working together may often not be anticipated from their individual activities. Consequently, cellular functions of actin-binding proteins can not be identified by just determining their biochemical properties and measuring the corresponding kinetic rates in solutions of purified proteins. The next chapter shows that the regulation of the actin cytoskeleton in living cells has an even higher level of complexity.

1.1.4. Regulation of actin cytoskeleton in living cells

Each distinct actin network in a cell is regulated by a set of actin-binding proteins working in concert to maintain the required turnover rate of filaments, orientation of filaments and mechanical stiffness of the networks. Some proteins such as ADF/cofilin and formin contribute to the regulation of the cytoskeleton in different intracellular actin structures. Here I consider how different combinations control actin cycle in compartments responsible for cell motility, spreading and adherence (Fig. 1.1).

1.1.4.1. Lamellipodium and lamella

To supply the mechanical force needed for the protrusion of the leading edge, actin rapidly polymerises in the lamellipodia into dendritic networks of short filaments (Fig. 1.4a) (Svitkina and Borisy, 1999). Assembly of new filaments starts from the activation of WASp (or alternatively Scar) proteins by small GTPases or other molecules located at the plasma membrane. This interaction changes the conformation of auto-inhibited WASp and makes its VCA domain available, which then acts as a nucleation promotion factor (Marchand et al., 2001). VCA binds Arp2/3 and one actin monomer, and this ternary complex associates with BE or sides of pre-existing filaments. When bound to the filament, the WASP-Arp2/3-actin complex gives rise to a new filament with the BE directed outward of the branching point and PE remaining associated to the Arp2/3 complex (Mahaffy and Pollard, 2006). The elongation of the BEs is terminated after some time by one of the capping proteins.

Upon disassembly from Arp2/3 complex, the PEs of filaments start to depolymerise due to the activity of ADF/cofilins. Disassociated actin monomers bind profilin, undergo nucleotide exchange and participate in filament assembly in the vicinity of the plasma membrane.

The combination of all involved proteins is critical for motility. Activation of NPF at the plasma membrane and capping of the new BEs narrow the area of actin polymerisation to the leading edge, limit the length of filaments in the network and guarantee preferential orientation of BEs towards the membrane. Debranching of filaments and ATP-hydrolysis ensure a time delay between filament assembly and disassembly contributing to the elastic properties of lamellipodia. The pool of ATP-G-actin, which is required for the polymerisation, is maintained through the activities of cofilin and profilin. Taken together, this protein system guarantees the fast turnover of filaments with a half-time in the range of seconds and provides the forces required for cell protrusion.

The lamella is the second actin filament network responsible for generating the protrusive force in cell motility (Huber et al., 2008). It is situated behind the lamellipodium and consists of longer, more stable and unbranched filaments decorated by tropomyosin (Fig. 1.1b). Tropomyosin inhibits binding of cofilin to filaments and prevents their depolymerisation, which leads to a much slower turnover in comparison with the lamellipodium (Bugyi et al., 2010). There are two hypotheses about the origin of filaments in lamella: i) filaments are initially formed in the lamellipodium and are retained due to the interaction with tropomyosin when the leading edge moves forward; ii) they are nucleated in the lamellipodium region at the focal complexes by mDia2 formin (Gupton et al., 2007). The molecular regulation of lamella is not completely understood. It has been shown however that in cells which overexpress tropomyosin, no lamellipodium is formed and protrusive movement is initiated only by lamella (Gupton et al., 2005).

1.1.4.2. Filopodia

Filopodia are actin-rich thin linear protrusions of cellular membranes (Fig. 1.4b), whose primary role is sensing the extracellular environment in various motility processes. Thus, they play a role in the determination of the movement direction of migrating cells by testing adhesive surfaces and soluble chemical

attractants, finding a proper partner, making primary contacts in cellular interactions and participating in the proper alignment of epithelial sheets (Mattila and Lappalainen, 2008). Depending on their function and the cell type, filopodia can considerably vary in structure and length. In contrast to lamellipodia and lamella, filopodia consist of a bundle of long parallel filaments with all BEs directed to its tip. Because of their diverse functions, different proteins might be involved in the regulation of actin polymerisation dynamics in filopodia, but the basic set of actin-binding proteins and the key interactions regulating its formation have been identified.

The filopodium is initiated by filaments which are nucleated by the Arp2/3 complex in the lamellipodium (Fig. 1.4b) and regulated by small GTPases and plasma membrane phospholipids (Svitkina et al., 2003; Yang and Svitkina, 2011). Uncapped BEs near the plasma membrane could bind formins or Ena/VASP proteins that stimulate the filament elongation and protect them from capping. These growing BEs then converge near the membrane, because of the myosin motor activity or the ability of VASP and formins to oligomerise. The converged filaments start to elongate synchronously and deform the plasma membrane to form finger-like protrusions. I-BAR domain proteins such as IRSp53 contribute to the initial membrane deformation. In the meantime, filaments are cross-linked by fascin and other bundling proteins. Interestingly, the characteristic time of the interaction between fascin and the filaments is relatively short (several seconds). It guarantees that filopodia remain stiff when the rapid mechanical tensions are applied, but that they can undergo slow changes in length and shape under continuous tension. The transient interaction between fascin and actin might also be required for myosin-dependent transport of cytoskeleton components to the tip of the filopodium. After some time, PE of filaments detach from the Arp2/3 complex and filopodial filaments undergo treadmilling. The difference between the rate of filament polymerisation and the speed of membrane protrusion is compensated by the retrograde flow (sliding) of the actin bundle towards the cell body.

An alternative but still disputed hypothesis assumes that the Arp2/3 complex together with its activators is not required for the formation of filopodia (Steffen et al., 2006). According to this hypothesis, the filaments are nucleated by formins, which are clustered at the plasma membrane, and constantly undergo treadmilling. The two

models are not mutually exclusive and could account for filopodia formation in distinct cell types.

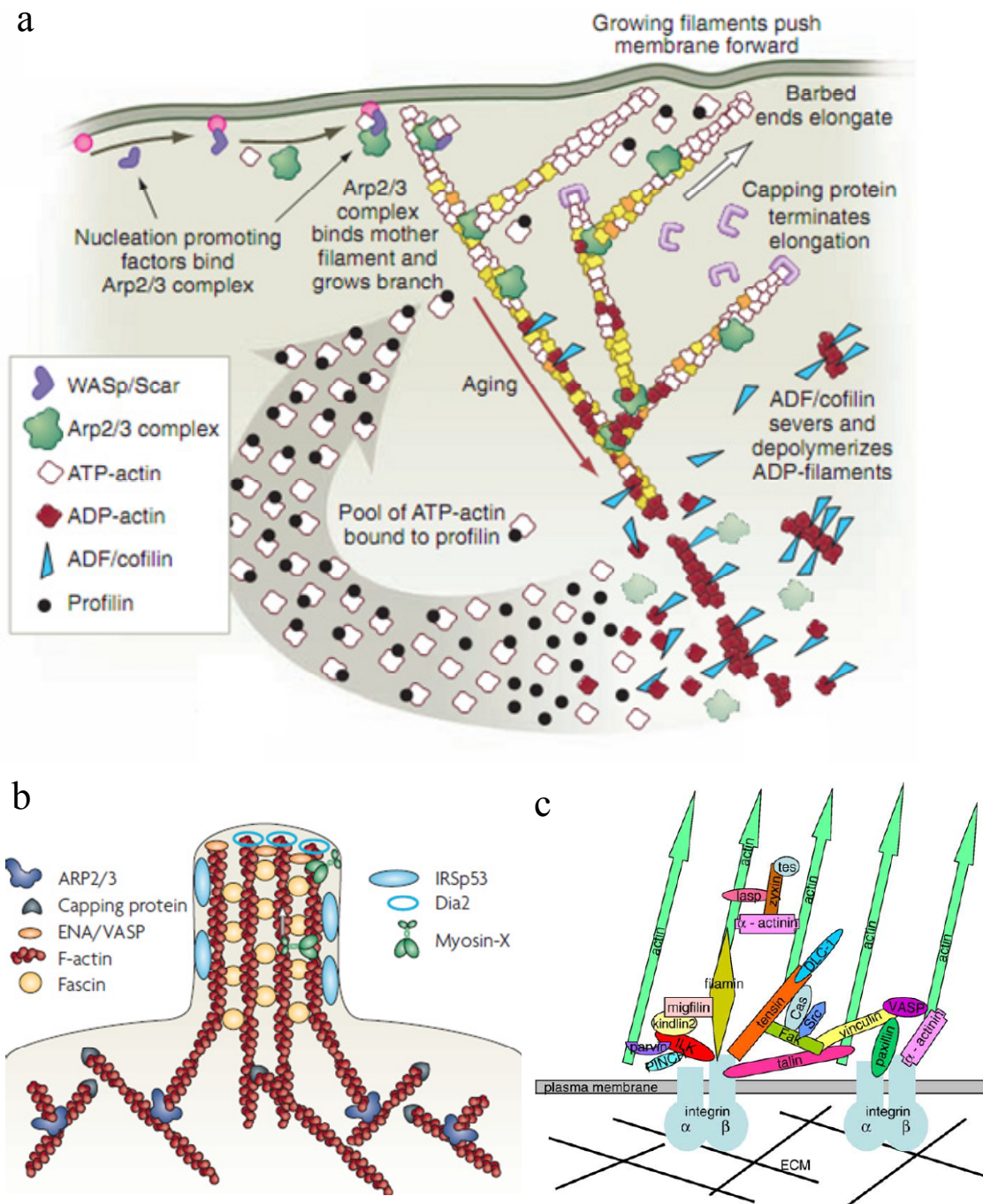


Figure 1.4: Schematic representation of various actin cytoskeleton structures in the living cells

a) Lamellipodium at the leading edge of the cells (Pollard and Cooper, 2009); b) filopodium formation (Mattila and Lappalainen, 2008); c) focal adhesion structure (Lo, 2006).

1.1.4.1. Cell adhesions and their link to the actin cytoskeleton

Cell adhesions are multiprotein complexes responsible for the linkage of the cell with the external environment by connecting the actin cytoskeleton to the extracellular matrix (ECM). All adhesions are classified in three major types: focal complexes (FC), focal adhesions (FA) and fibrillar adhesions (Fig. 1.4c) (Webb et al., 2002). FCs are formed at the leading edge during cell protrusion and either disassemble rapidly or mature into FAs.

In comparison with other actin intracellular structures such as lamellipodia, FAs are less studied (Lo, 2006). Many proteins were identified in FAs and characterised using biochemical methods, but their organisation and orchestrated activities are not yet understood. Transmembrane integrins bind to ECM and recruit other FA proteins to their cytoplasmic domains. Talin and filamin provide the linkage between integrins and actin filaments. α -actinin and VASP cross-link filaments and increase the stiffness of the formed actin cables. Other proteins regulate the assembly of filaments by playing a role of complete (tensin) or leaky (vinculin) BE cappers.

Many FA proteins are regulated by intramolecular interactions and need to bind one or several other FA components to become activated. Therefore, proteins enter and leave focal adhesions in an appropriate order. Nascent FCs contain only integrin, talin and paxillin. Vinculin, filamin, talin, tensin and α -actinin enter adhesions during their maturation (Zaidel-Bar et al., 2003). Fibrillar adhesions are substantially composed by integrins and tensin (Zamir et al., 2000). Importantly, mechanosensitivity of FA proteins is needed to change the structure of adhesions in response to applied tensions (Bershadsky et al., 2006).

All kinds of cell adhesions are linked with different types of actin structures. Coupling of the nascent FCs to lamellipodia converts the force generated by actin assembly at the leading edge into protrusions. FAs are structurally and functionally associated with stress fibers (SF) – bundles of antiparallel actin filaments containing myosin. A myosin dimer is normally bound to two filaments with inverse polarity. The contractile force generated by the movement of myosin towards the BEs of each filament is involved in the retraction of the cell membrane. Contractility of SFs also controls the structure of mechanosensitive FAs.

Molecular mechanisms that control *de novo* actin assembly and turnover of filaments at FAs are not completely understood. Formin, which nucleates new filaments and stays processively attached with them *in vitro*, is activated by RhoA at focal adhesions and controls the elongation of filaments. However, recent experimental data showed that formin is not essential for polymerisation of actin at FA and other nucleation machineries are likely to be involved. According to one hypothesis, filaments growing out of all adhesions are nucleated by Arp2/3 in nascent FCs and no nucleation events occur in the mature FAs (Hotulainen and Lappalainen, 2006).

1.2 *Experimental techniques for studying actin dynamics*

Advances in the understanding of the actin cytoskeleton structure and functions are strongly linked to available experimental techniques. Many empirical tools for studying actin dynamics *in vitro* and in living cells are currently available. However, it is still challenging to gain information about protein interactions at a molecular scale in the context of the cell. In addition, experimental results depend on the applied technique, which can yield rather different conclusions about molecular mechanisms. A short discussion of the methods dedicated to the analysis of actin dynamics is presented with a focus on fluorescence microscopy methods which I used in my work and which are widely applied to study molecular dynamics in living cells.

1.2.1. *Biochemical assays*

Actin polymerisation kinetics is rather difficult to study quantitatively in living cells. Several biochemical assays have been developed to reduce the complexity of the system and to allow the investigation of structures and dynamics of actin filaments (Bugyi et al., 2008) without cellular constraints. They are used to quantitatively assess how proteins, which are able to affect intracellular dynamics, govern actin turnover. Production of pure, functionally active actin-binding proteins is essential for precise measurements of actin kinetics in these assays. For some proteins of high molecular weight, such as formins, only protein domains harbouring specific activities could be obtained and studied in these assays (Moseley et al., 2006).

1.2.1.1. Bulk assay

Many actin-binding proteins have been primarily characterised by their ability to change the rate of actin polymerisation or shift the equilibrium between G- and F-actin pools. Among the methods suitable to estimate the changes in F-actin concentration over time in *in vitro* bulk solutions, the pyrene-actin assay is the most ubiquitously used nowadays (Cooper et al., 1983). Measurements with other techniques, such as light scattering, intrinsic fluorescence and NBD-fluorescence, are less sensitive or affected by the structural properties of filaments (Brooks and Carlsson, 2008).

At specific excitation and emission wavelengths ($\lambda_{\text{ex}} \approx 365 \text{ nm}$, $\lambda_{\text{em}} \approx 407 \text{ nm}$) polymerised N-(1-pyrenyl)iodoacetamide-labelled actin (further called pyrene-actin) emits a seven-fold higher fluorescence signal in comparison with non-polymerised pyrene-actin (Kouyama and Mihashi, 1981). To test the activity of proteins which stimulate actin polymerisation, a mix of non-labelled G-actin and pyrene-G-actin is used. The increase of fluorescence intensity over time is recorded with a spectrofluorimeter or plate reader (Fig. 1.5a). Alternatively, a small quantity of pre-formed filaments can be used to measure the rate of filament elongation under conditions preventing spontaneous nucleation. When studying proteins that promote or inhibit filament disassembly, actin is polymerised before the start of the experiment and the rate of depolymerisation is measured under different experimental conditions. Steady-state fluorescence levels provide an estimate of the critical actin concentration and the increase or decrease of the signal over time determines the assembly/disassembly kinetics. If the experiment is designed appropriately and polymerisation curves are measured for several concentrations of the studied actin-binding protein, absolute values of some of the rate constants can be derived using specially developed fitting equations or simulation algorithms (Carlsson et al., 2004; Matzavinos and Othmer, 2007).

Despite its relative simplicity, the bulk assay is powerful to assess the global effects of proteins on polymerisation kinetics of actin, but it is rather unsuitable to analyse molecular mechanisms of the underlying reactions. The major disadvantage of this approach is that it does not provide any direct information about the lengths and structures of the filaments. Because all proteins in the sample are randomly distributed, it is impossible to study the effect of spatially localised nucleation and consequently, of polarised polymerisation of dense actin networks like it is observed in living cells. Furthermore, the fluorescence signal from polymerised pyrene-actin depends on the actin nucleotide state giving a higher signal for ADP-loaded subunits (Carlier et al., 1984; Grazi, 1985). Similar, profilin has lower affinity for pyrene-actin than for non-labelled actin, thus the obtained fluorescence plateau may yield a biased estimation of equilibrium F-actin concentration (Romero et al., 2004). While this assay may allow to estimate the influence of one or two actin-binding partners on actin polymerisation dynamics, it is not appropriate for the analysis of the combined effects of many proteins on actin turnover.

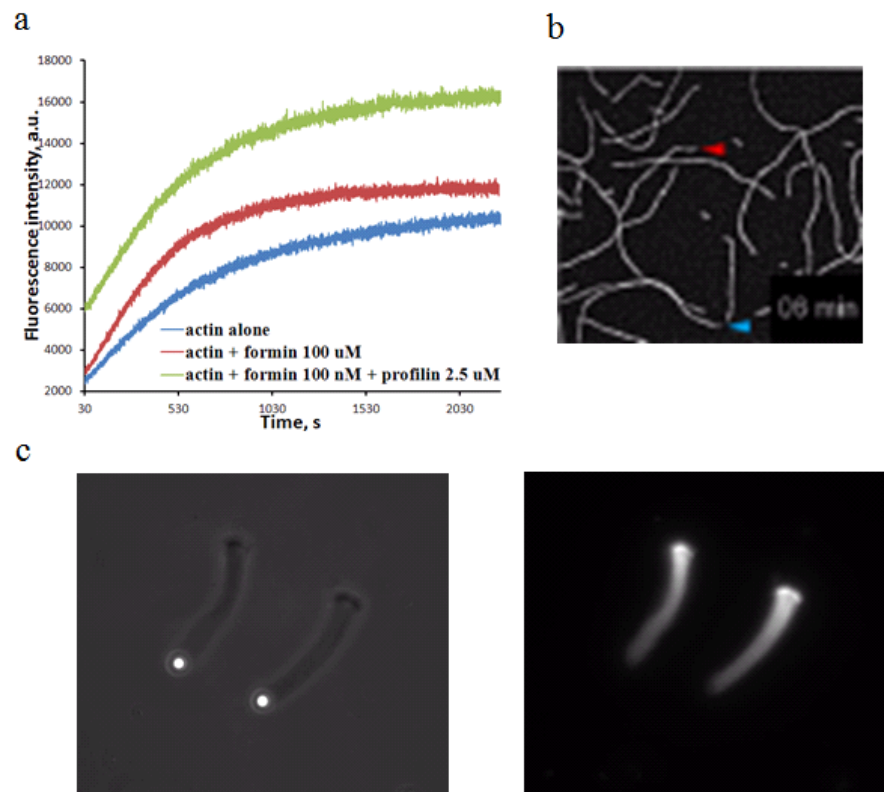


Figure 1.5: Biochemical assays to study actin dynamics.

a) Actin-pyrene (bulk) assay. Fluorescence intensity is proportional to the concentration of F-actin; b) TIRF with individual actin filaments (adapted from (Gould et al., 2011)). Blue and red arrows indicate respectively BE and PE of the same filament; c) Actin-based biomimetic motility assay. Phase contrast (left) and fluorescent (right) images. Bright circles on the left image represent beads.

1.2.1.1. Fluorescence microscopy of individual filaments

To understand the regulation of dynamics and function of the actin cytoskeleton, the structure of filaments has to be taken into account. *In vitro* actin polymerisation assays with relatively low concentrations of actin molecules labelled with fluorescent dyes, such as TRITC-rhodamine or Alexa-488, allow to visualise single actin filaments using light microscopy (Fig. 1.5b) (Fujiwara et al., 2002; Kuhn and Pollard, 2005). Either wide-field or Total Internal Reflection Fluorescence (TIRF) microscopy can be applied to study the structure and dynamics of single filaments. The latter will result in imaging with higher signal-to-noise ratio when filaments are anchored to the coverslip surface by myosin molecules. The evolution of individual filament lengths and distribution of filament lengths in the sample can be measured over time under steady-state or non-steady-state conditions. Single fragmentation

and annealing events can be registered and the number of filament branches nucleated by Arp2/3 complex can be determined (Amann and Pollard, 2001).

BEs and PEs of filaments can be identified in several ways. Proteins, which stay associated with BE during polymerisation process such as formins can be grafted to the surface of microscopy coverslips or polystyrene beads placed in the medium (Romero et al., 2004). Acquisition photobleaching can give an estimate of the time when a particular part of the filament was polymerised with a dimmer intensity corresponding to PEs (Michelot et al., 2007).

Although this assay provides information about the polymerisation process it has many limitations for quantitative studies. The used actin concentrations are $\approx 1 \mu M$, which is far below cytoplasmic quantities. The bulk properties of dense filament meshworks involved in force generation cannot be studied and activities of cross-linking proteins cannot be addressed quantitatively.

1.2.1.2. Actin-based biomimetic motility assay

Actin assembly and turnover are involved in various biophysical phenomena. Reconstruction of these processes *in vitro* allows to identify the minimal set of actin-binding proteins required for a given cellular activity and to measure the influence of these proteins on actin-based processes in a concentration-dependent manner (Le Clainche and Carlier, 2004; Upadhyaya and van Oudenaarden, 2003).

The movement of bacteria *Listeria monocytogenes* was reconstructed in an acellular assay using a set of purified proteins (Loisel et al., 1999). The same NPFs and filament regulating proteins participate in the formation of lamellipodia, leading to the progression of the leading edge of motile cells. To mimic the movement of bacteria or the leading edge of the cell, the protein WASP, its VCA domain or ActA of *Listeria* (all of them bind and activate Arp2/3 complex) can be grafted to the surface of polystyrene beads (Noireaux et al., 2000), oil droplets or lipid vesicles (Delatour et al., 2008). The minimum medium required for bead motility contains the Arp2/3 complex to nucleate new filaments, a capping protein to block barbed ends and ADF/cofilin to depolymerise filaments and to recycle monomers for polymerisation (Loisel et al., 1999).

The application of this assay was extended to other actin nucleating machineries. Motility was generated with formin-coated beads in a medium

containing profilin and cofilin (Romero et al., 2004). The ActA proline-rich domain grafted to the bead surface is able to initiate the formation of actin shells in an Arp2/3 independent manner (Fradelizi et al., 2001).

This assay was utilised intensively for the quantitative evaluation of the relative contributions of cytoskeletal components to the initiation (van der Gucht et al., 2005) and to the rate of actin-based movement. Each component of the minimal motility medium was characterised to determine the optimal concentration supporting the fastest movement of the bead or bacteria (Paluch and Heisenberg, 2009). If the concentration of Arp2/3, capping protein or ADF/cofilin is far above or far below its optimal concentration, particle movement does not occur. It was further shown that ADF/cofilin is not a critical component for the initiation of bead motility but is needed to enhance filament turnover and stimulate processive movement of beads for a longer time (van der Gucht et al., 2005). The effects of other proteins such as VASP (Breitsprecher et al., 2008; Samarin et al., 2003), tropomyosin (Bugyi et al., 2010) and cross-linking proteins (Giganti et al., 2005; van der Gucht et al., 2005) on spatially-localised actin assembly or actin-based motility were analysed by adding these proteins to the motility medium. Synergetic effects of several proteins in promoting motility were also studied. For example, by changing the concentrations of the Arp2/3 complex and capping protein at the same time, it was found that capping protein promotes nucleation of filaments by the Arp2/3 complex (Akin and Mullins, 2008).

The assay could also be used to measure the biophysical parameters characterising particle protrusion. The relation between the force generated by actin assembly and the speed of the vesicle movement could be estimated by varying the viscosity of the motility medium with methylcellulose (McGrath et al., 2003; Wiesner et al., 2003). Changing the size of the beads, replacing them by cylindrical glass rods or modifying density of NPFs on their surface allows to evaluate the role of the surface geometry, and in particular its curvature, on the shapes of the created clouds speed of particle movement and conditions of movement initiation (Bernheim-Groswasser et al., 2002). When soft lipid vesicles coated with the NPFs are placed in the medium, changes of their shape is a direct indicator of pushing and pulling forces created by the actin cloud (DelaTour et al., 2008).

The biomimetic assay was used in this thesis to study actin turnover quantitatively without cellular constraints (see section 2.1 for experimental procedures Chapter 4 for further details).

1.2.2. *Studying actin dynamics in living cells*

Measurement of the kinetics of the actin cytoskeleton and other protein systems in living cells is usually achieved with time-lapse fluorescence microscopy. The fluorescently-labelled proteins can be microinjected into the cells or expressed by the cells when the encoding cDNA is transfected into them. Individual actin filaments in the cells cannot be visualised, the diffraction-limited spatial resolution of conventional epifluorescence and confocal microscopes is at least several hundreds nanometers, which is far above the thickness of the filaments and the distances between them.

The mobility of proteins in cells is affected by their biochemical interactions and, therefore, is used as an indicator of underlying reaction kinetics. Monomeric actin and many actin-binding proteins diffuse rapidly in the cytoplasm and become completely or partially immobilised when associated to cytoskeleton structures. The dedicated microscopy-based methods, reviewed in the following sections, either measure the exchange of labelled proteins between a selected cell region and its surroundings (FRAP and FCS) or track the movement of fluorescent particles through the cell (FSM).

The remodelling of the actin network in living cells is governed by polymerisation, turnover and spatial rearrangement of filaments. In the latter case, forces, which are generated by motor proteins or due to the actin assembly itself, initiate the structural modification of actin bundles or dendritic networks (Hotulainen and Lappalainen, 2006; Wang, 1984). The appearance and evolution of actin stress fibers, FAs and other cytoskeleton structures can be addressed when applying morphological analysis to the collected data (Berginski et al., 2011). The local changes in the quantity of polymerised actin, which occur due to directed flow, have to be taken into account when measuring the biochemical rates of actin assembly and disassembly. Therefore, widely accepted protocols for the measurement of intracellular protein kinetics need to be customised appropriately when they are applied to study the actin cytoskeleton.

1.2.2.1. FRAP and other photomanipulation methods

Laser-assisted confocal microscopy approaches, such as fluorescence recovery after photobleaching (FRAP) (Carrero et al., 2003), fluorescence loss in photobleaching (FLIP) (Phair and Misteli, 2000) and fluorescence localisation after photobleaching (FLAP) (Dunn et al., 2002), make use of the instant bleaching of fluorescent probes under a high intensity laser pulse. The spatial fluorescence inhomogeneity generated by bleaching decreases due to the diffusion of non-fluorescent molecules out of the bleached area and of fluorescent molecules into the bleached area. The rate of diffusion can be influenced by molecular interactions in and out of the bleached region. Measuring exchange rates of bleached molecules by fluorescent ones provides quantitative information about molecular reactions and mobility of proteins in living cells.

Because FRAP is a major experimental technique used in this work, its general properties and application for the studies of actin cytoskeleton are discussed in more detail. FRAP was developed as a tool for the analysis of protein mobility more than 30 years ago (Axelrod et al., 1976), but has become more popular in biological applications since the development of robust confocal microscopes (Lippincott-Schwartz et al., 2003), which allow instant bleaching of regions of arbitrary shape. Nowadays FRAP is a widely applied technique to analyse protein kinetics in various intracellular molecular systems, such as nuclear receptors (Beaudouin et al., 2006; Mueller et al., 2008) and proteins involved in membrane trafficking (Forster et al., 2006). FRAP is also combined with *in vitro* assays to measure mobility of proteins and other fluorescently labelled molecules (Seiffert and Oppermann, 2005) or their interaction kinetics in solutions with immobilised binding partners (Vink et al., 2006).

In FRAP experiments, relatively small regions of the cell are bleached at once, while molecules in other cellular areas remain fluorescently active (Fig. 1.6). Due to diffusion and transport processes, unbleached proteins enter the bleached spot, participating in biochemical reactions with bleached molecules. In most cases the time evolution of the average fluorescence intensity in the bleached spot, which is proportional to the number of fluorescent molecules in case of a relatively low concentration of labelled particles, is analysed. Alternatively, the set of collected

images is analysed to study spatial effects of molecular mobility in a non-homogeneous environment.

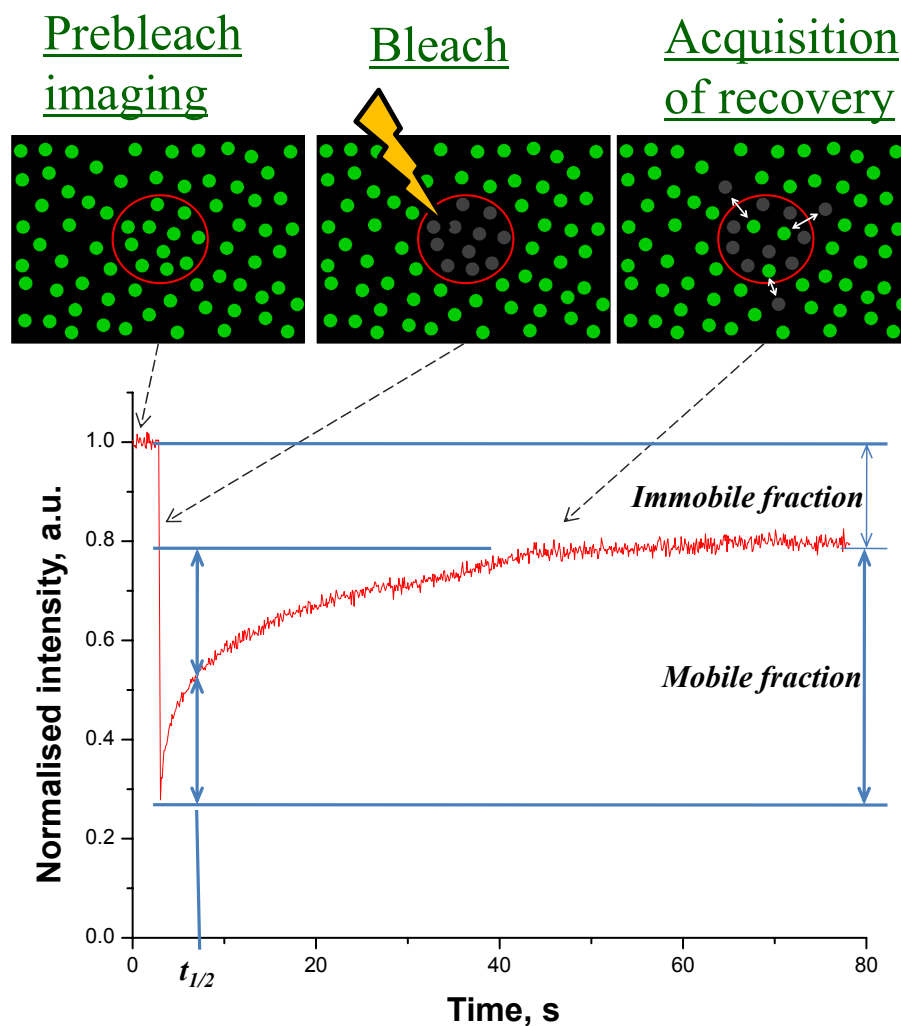


Figure 1.6: Principal scheme of a conventional FRAP experiment.

Dark and light circles correspond to photobleached and non-photobleached fluorochromes. After acquisition of several prebleach images, fluorochromes in the selected region of the cell are bleached instantly with high laser power. A set of postbleach images is acquired and average fluorescent intensity is measured over time.

There are several modifications of FRAP method that provide complementary information about protein mobility and facilitate the interpretation of the collected data. In FLIP (Phair and Misteli, 2000), all fluorescence in the selected compartment is continuously bleached during the observation time. Loss of fluorescence in the adjacent compartment gives an estimate of the efficiency of directional transport of fluorescent particles from the non-bleached to the bleached zone. FLAP (Dunn et al.,

2002) is similar to FRAP except that the same protein is labelled with two fluorescent dyes and imaged simultaneously in both fluorescent channels. The signal in the second channel is not bleached but shows redistribution of the fluorochrome in the cell. Calculating the difference between images in the non-bleached and bleached channels gives spatial mobility information for non-steady-state processes. Photoactivation (PA) (Garbett and Bretscher, 2012) takes advantage of dyes that, in contrast to FRAP, switch from invisible to visible state when irradiated with an intense laser pulse (Lippincott-Schwartz and Patterson, 2008). In some applications, replacement of FRAP by PA increases signal-to-noise ratio and allows to directly visualise movement of particles out of the irradiated spot. Recently developed photoconvertible fluorescent proteins, that can change their excitation and emission spectral properties, allow to conduct PA and FLAP measurements in combination without need to transfect two plasmids simultaneously (Shaner et al., 2007).

Results of FRAP and other photomanipulation experiments are subjected to either qualitative or quantitative analysis. In case of qualitative FRAP analysis, fluorescence recoveries are visually compared for multiple experimental conditions or for bleached spots at different intracellular locations. The tested conditions often imply overexpression or downregulation of the intracellular factor, that is hypothesized to change the mobility and/or biochemical properties of the imaged protein.

Quantitative FRAP is aimed at estimating numerical parameters of processes, such as diffusion and biomolecular reactions, which determine the rate of recovery (Mueller et al., 2010). After the calculation of the average fluorescence intensity recovery in the bleached region has been performed, it can be fitted with appropriate mathematical equation to determine static and dynamic parameters of the underlying process. Without knowledge about interactions of molecules in this underlying molecular process, the only dynamic parameter which can be extracted is the half-time of the recovery. The difference between prebleach fluorescent signal and steady state recovery level provides an estimation of the immobile fraction of the bleached protein, which was not replaced by non-bleached particles during the observation period.

When the mechanistic details of protein interactions and mobility are known or at least hypothesised, a mathematical model may be applied to fit relevant

parameters such as diffusion coefficients and binding/unbinding rate constants (Ellenberg et al., 1997; Soumpasis, 1983; Sprague et al., 2006; Tardy et al., 1995). The model equations or simulation algorithms describe the increase of the fluorescent signal as a function of its rate limiting factors. These models may differ by accounting for spatial inhomogeneities in the sample, structures of biomolecular complexes or specific features of experimental set-ups, such as bleaching time or spatial inhomogeneity of the bleaching efficiency. It has been shown that transport and diffusion processes lead to distinct recovery shapes (Axelrod et al., 1976). The binding/unbinding kinetics can also be separated from diffusion in a limited parameter space (Sprague et al., 2004). When image analysis is applied to interpret the results of FRAP experiments, characteristics of protein diffusion and transport may be extracted by measuring the changes in shape and position of the bleached spot (Hotulainen and Lappalainen, 2006) or by fitting intensity profiles along the lines crossing the bleached spot (Beaudouin et al., 2006).

Over the last three decades, photobleaching techniques were intensively applied to study the dynamic properties of the actin cytoskeleton in cells. Most quantitative analyses were performed with actin-binding proteins, for which the rates of binding/unbinding kinetics were measured (Lele et al., 2008; Weisswange et al., 2009). In particular, FRAP experiments with proteins localised in FAs showed, that different FA components have very different dynamic properties with the corresponding half-times ranging from several seconds to several minutes (Lele et al., 2006). The measured kinetic parameters are also sensitive to the applied mechanical stress. While some proteins start to turnover faster in focal adhesions under mechanical stress, the recovery half-time for others increases showing stabilisation effect (Wolfenson et al., 2011).

In several studies FRAP experiments with fluorescently labelled actin were performed to measure its turnover in lamellipodia, filopodia, FAs and stress fibers (Campbell and Knight, 2007; Hotulainen and Lappalainen, 2006; Lai et al., 2008) (see Fig. 1.7). Although the actin incorporation and exchange in these structures was successfully characterised, the numerical analysis of the data was limited by the restricted knowledge about underlying actin regulatory mechanisms. Some of these studies have used binding approximation (Carrero et al., 2004; McDonald et al., 2006) to measure actin turnover in the nucleus or in the cytoplasm (Campbell and

Knight, 2007; Gupton et al., 2007). The model of Tardy and coworkers (Tardy et al., 1995) was established specifically for FRAP experiments with actin filaments and was applied for fitting the corresponding datasets. The model accounts for several important factors, such as diffusion of actin monomers, but operates with a rate of exchange between pools of G- and F-actin to describe the polymerisation reactions. In the work of Lai and coworkers (Lai et al., 2008), probabilities of conversion between filamentous and monomeric forms of actin were assumed to be functions of the distance from the leading edge. This assumption allowed to obtain an accurate fit for measured recoveries, but the mentioned dependences were not quantitatively linked to the spatial properties of filaments. The photobleaching of the fragments of stress fibers near focal adhesions (Hotulainen and Lappalainen, 2006) allowed to measure the rates of stress fiber elongation, but the kinetic rates of actin (dis-)assembly linked to the structural features of actin bundles were not identified. Overall there is a need to provide a quantitative link between modelling of actin dynamics and advanced fluorescence microscopy techniques to understand the regulation of the actin cytoskeleton on a molecular level under physiological conditions.

1.2.2.2. Fluorescence Speckle Microscopy (FSM)

In FSM, movement of the virtual fluorescent particles is tracked to characterise the protein flow (Danuser and Waterman-Storer, 2006; Watanabe and Mitchison, 2002). Provided that the ratio of labelled to non-labelled actin molecules is very low, the filament network is represented by spatially separated speckles. Each speckle represents fluorophores which stay relatively immobile during the image acquisition time within the diffraction-limited area. Because rapidly diffusing actin monomers do not contribute to the speckle formation, one can assume that the increase or decrease of the speckle intensity is caused by the actin assembly or disassembly, while the movement of the speckles corresponds to the directed flow of polymerised actin.

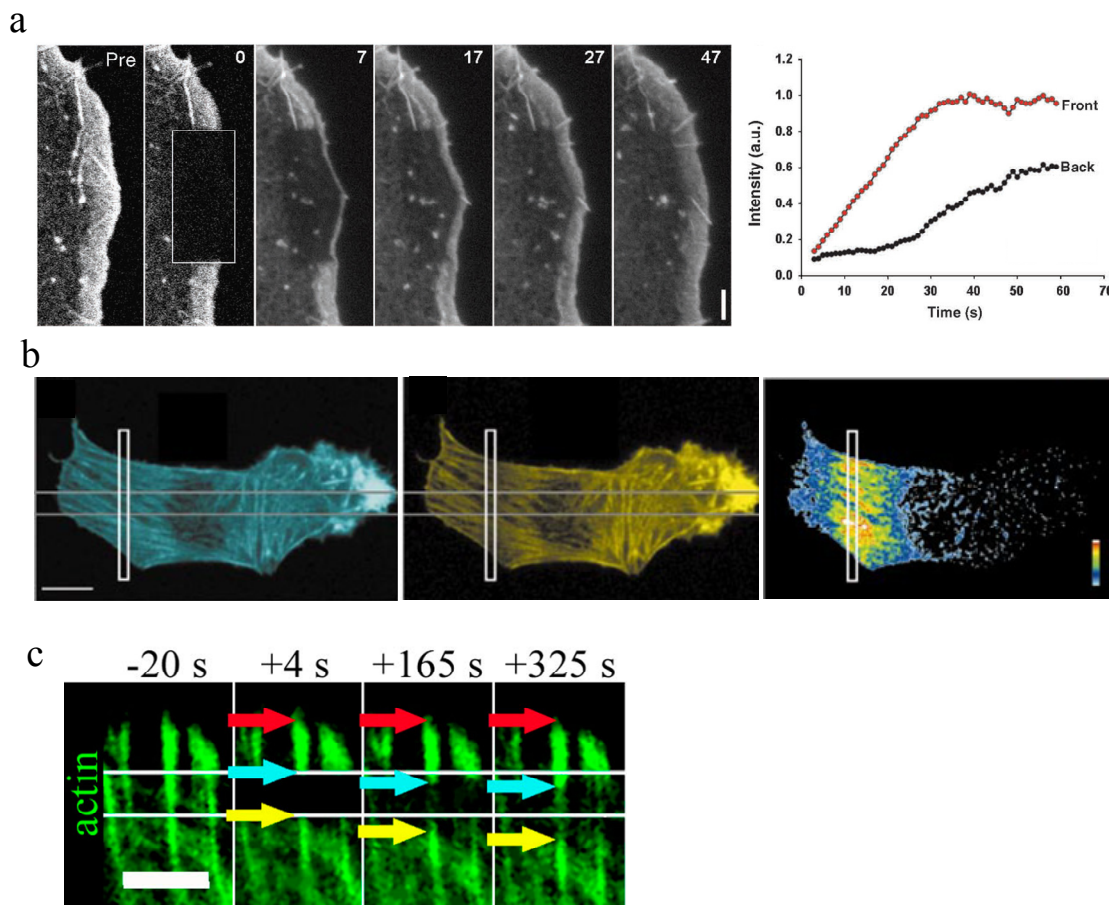


Figure 1.7: Applications of photobleaching methods for the analysis of actin dynamics
a) FRAP experiment with EGFP-actin in a lamellipodium (Lai et al., 2008). The plot on the right shows fluorescence recoveries in the front and rear parts of the lamellipodium. b) FLAP experiment with CFP and YFP labelled actin shows the time-course of actin redistribution (adopted from (Dunn et al., 2002)). YFP was bleached in the shown rectangle. Images are (from left to right) CFP, YFP and difference “CFP”-“YFP” in pseudocolour immediately after bleach. c) Photobleaching of GFP-actin in stress fibers near focal adhesions to measure elongation of stress fibers (Hotulainen and Lappalainen, 2006)

Thus, FSM measurements provide information about polymerisation dynamics and the flow of polymerised networks. Therefore, this method was applied to investigate spatio-temporal actin turnover close to the leading edge of the cells and allowed to identify zones of preferential actin assembly and disassembly and link the contraction of the actin network to its depolymerisation (Vallotton et al., 2004). This method was also used to study actin flow in FAs and analyse its correlation with mobility of other FA proteins (Hu et al., 2007). Despite its advantages, this method requires specialised equipment for the fast acquisition of low level fluorescent signals. In addition, the simultaneous tracking of many identical particles requires the

development of special image analysis algorithms and considerable computational resources (Ponti et al., 2003). Since actin bundles and meshworks are not visible on the FSM images, actin must be labelled with a second fluorescent marker in order to associate measured kinetic parameters with particular cytoskeleton structures.

1.2.2.3. Fluorescence (cross-)correlation spectroscopy (F(C)CS)

F(C)CS is based on the measurements of the fluctuations of the fluorophore quantity in the diffraction-limited spot. The calculation of the parameters of the (auto-)correlation function provides an estimation of the mobility parameters of the labelled proteins in the studied area. This method is more suitable for the measurements of fast processes such as free protein diffusion or interaction of the diffusing proteins. FCS has been applied to study the fast dynamics of cortical actin near the plasma membrane (Gowrishankar et al., 2012) and kinetics of FA proteins (Digman et al., 2008; Digman et al., 2009). Interestingly, they found that these proteins disassemble from FAs in large complexes, which rapidly disassociate afterwards.

FCS requires specialised equipment for the data acquisition. Until recently, experimental set-ups allowed acquisition of FCS signal only at one spatial position, therefore characterisation of bigger cellular areas was time consuming. Newly developed techniques, which allow instantaneous acquisition of FCS data in 2D regions with high spatial and temporal resolution (Capoulade et al., 2011), will, most likely, contribute to the understanding of the kinetics of different cytoskeleton components.

1.3 *Mathematical models of actin polymerisation and associated phenomena*

As shown above, the actin cytoskeleton is a complex system, whose dynamics depends on multiple factors: i) nucleotide state of actin monomers and filament protomers; ii) age and structural properties of filaments; iii) activities of actin-binding proteins; iv) properties of the environment, including its viscosity and ion concentration; v) spatial distribution of filaments affecting steric interactions between them; vi) force applied to individual filaments or their assemblies. The influence of individual factors on structural properties of the cytoskeleton and on actin polymerisation dynamics can be measured either *in vitro* or in living cells, but their combined effects on actin assembly cannot be understood without application of

proper mathematical techniques. Therefore, numerous mathematical models have been developed either to predict structural and dynamical properties of the cytoskeleton or to derive unknown parameters from experimental data. Based on the amount of details and the accounted properties of actin cytoskeleton structure and dynamics, these models could be divided into several subgroups:

1. Atom-scale molecular dynamics (MD) simulations are based on the experimental data produced by x-ray crystallography or electron microscopy, and focus on the structural properties of actin molecules and actin-binding proteins (Splettstoesser et al., 2011). These simulations identified modifications in secondary and tertiary structures of actin molecules associated with change of the bound nucleotide (ATP/ADP-Pi/ADP) (Dalhaimer et al., 2008; Zheng et al., 2007) and with switches between G- and F- forms (Oda et al., 2009). The MD models of actin interacting with one of the actin-binding proteins, for example profilin, revealed modifications of the actin molecular structure, caused by these interactions (Minehardt et al., 2006). Less precise coarse-grained models assembled information derived from MD simulations and addressed packaging of actin protomers in the filaments to explain multiple possible twists in filament helix structure (Chu and Voth, 2006).

2. Thermodynamic models and Brownian dynamics simulations study energy requirements for different steps of actin polymerisation and associated force production. The early thermodynamic models addressed assembly/disassembly of actin molecules at the ends of filaments (Hill, 1981). These models were particularly useful to understand the spontaneous filament nucleation and to derive the size and configuration of the smallest stable actin nuclei, which can give rise to filaments (Sept and McCammon, 2001).

3. Biochemical kinetic models intend to predict the time-course of actin polymerisation or to calculate the corresponding steady states (Bindschadler, 2010). The assembly/disassembly of actin monomers at the ends of filaments, nucleotide exchange and interactions of G- and F-actin with actin-binding proteins are represented as biochemical reactions characterised by the kinetic rate constants. Predictions generated by these models are often compared to the results of *in vitro* experiments to validate the models and/or to estimate the unknown rate constants. Examples of addressed biological questions include: i) evaluation of the mechanistic

functions of actin nucleators, capping and depolymerising proteins (Carlsson, 2006; Cooper and Pollard, 1985; Vavylonis et al., 2006); ii) calculation of distributions and fluctuations of the lengths of filaments due to the different affinities of ATP-, ADP-Pi-, and ADP-bound actin monomers to their ends and due to activities of actin-binding proteins (Edelstein-Keshet and Ermentrout, 2001; Fass et al., 2008; Stukalin and Kolomeisky, 2006). Because one of the goals of this thesis is the development of advanced biochemical kinetics models of the actin system, the mathematical aspects of model formulation and generation of predictions are considered in section 1.3.1.

4. Spatially resolved biochemical models include information about changes of F-actin concentration in space and/or orientation of filaments in addition to the description of their biochemical kinetics. Because the spatially localised nucleation and spatially dependent regulation of actin turnover by other actin-binding proteins was shown to be important for actin physiological functions, these models aimed to predict the formation of actin intracellular structures, such as lamellipodia and filopodia (Atilgan et al., 2006; Ditlev et al., 2009; Haviv et al., 2006; Schaub et al., 2007). The diffusion of monomeric actin and actin-binding proteins was shown to be a rate-limiting factor for polymerisation in some conditions. Another subclass of spatially resolved models is dedicated to the analysis of the results of fluorescence microscopy experiments, including FRAP, on actin kinetics in biochemical assays and in living cells (Michelot et al., 2007; Reymann et al., 2011; Tardy et al., 1995).

5. Mechanical biophysical models are developed to predict the force generated due to actin polymerisation as well as associated cell motility. The examples of the simulated phenomena include propulsion of the cell leading edge by lamellipodia, formation of filopodia and kinetics of stress fibers (Sabass and Schwarz, 2010; Schreiber et al., 2010; Stachowiak and O'Shaughnessy, 2008). Most of the generated predictions share the view, that the assembly of cross-linked filament structures is essential for cellular motility, as individual filaments do not produce enough force.

The analysis of Bacteria movement in cytoplasm and the establishment of biomimetic assays gave much impetus to the development of mechanical models. Multiple hypotheses on the mechanisms, which initiate and maintain the movement of functionalised particles, were developed. Macroscopic models considered the polymerised actin cloud as a continuous gel, whose elastic properties are determined

by the interacting actin-binding proteins (Bernheim-Groswasser et al., 2005; Gerbal et al., 2000). The mechanical stress, which accumulated due to the difference of the actin assembly/disassembly rates in different parts of the actin cloud and due to the curvature of the polymerising surface, is released by pushing the particle forward. Alternative microscopic models consider interactions of individual filaments with the obstacle and between themselves. The different models of this type hypothesized different mechanisms of force generation, specifically “Brownian ratchet” (Peskin et al., 1993), “elastic Brownian ratchet” (Mogilner and Oster, 1996) and “tethered ratchet” (Mogilner and Oster, 2003). The models were able to explain numerous observed phenomena, including the switch between continuous and pulsative movement of particles (Alberts and Odell, 2004) and the dependence of the particle speed on the environmental resistance (Lee and Liu, 2009). Most of the mechanical models, however, neglected the peculiarities of the molecular regulation of actin polymersation kinetics, thus limiting its description to a simplified treadmilling cycle. Recent experimental data highlighted the importance of the regulation of actin networks on a molecular level (Achard et al., 2010) and stimulated the development of novel multiscale models, considering the regulation of actin assembly by actin-binding proteins and associated force generation at the same time (Kawska et al., 2012).

1.3.1. *Methods for simulating biomolecular kinetics*

Multiple techniques are available to simulate the dynamics of biomolecular systems. In the simplest case a system can be described as a limited set of N biomolecular compounds, represented by their mass or molar concentrations (C_1, C_2, \dots, C_N) that interact through M reaction channels. In well-mixed solutions of rapidly-diffusing molecules the concentration changes of each reagent depends only on the biochemical reaction rates k_j ($j=1, \dots, M$) which is represented by the mass action law (van Kampen, 2007):

$$\frac{dC_i}{dt} = \sum_{j=1}^M k_j C_k^{n_{jk}} \quad i=1, \dots, N. \quad (1.1)$$

The left part of this equation represents the change of the concentration of the i -th reagent in time, each term in the right part represents one of the reactions which

affects this concentration. n_{jk} are stoichiometric coefficients, e.g. number of molecules of the k -th reagent that are involved in j -th reaction.

When the “well-mixed” assumption is not satisfied, the spatial distribution and migration of the reacting compounds has to be considered. If the reacting species undergo free diffusion, the evolution of the reactant concentrations in time and space is represented by the system of partial differential equations (PDE):

$$\frac{\partial C_i(\vec{r}, t)}{\partial t} = \sum_{j=1}^M k_j C_k^{n_{jk}} + D_i \nabla^2 C_i(\vec{r}, t) \quad i=1, \dots, N, \quad (1.2)$$

where D_i – diffusion coefficient for the i -th reactant, which will become a function of coordinates for an inhomogeneous environment and a tensor for an anisotropic environment.

Solutions of the equations (1.1) and (1.2) predict the time evolution of the entire molecular system when the initial system configuration (the concentrations of all species at $t=0$) and the limiting conditions, such as the properties of the borders of the simulated volume or the total number of interacting molecules, are specified. When the right parts of these equations equal to 0, e.g. concentrations remain unchanged over time, the obtained non-linear equations describe the molecular system in its steady state. Therefore these equations can be used to analyse steady states of the systems. Equations corresponding to steady-state or non-steady-state conditions often cannot be solved analytically because reactions of second or higher orders are often involved. In such situations, the computational algorithms are applied to solve these equations numerically. Nonlinear equations corresponding to steady-state systems are solved by making the initial guesses about the desired solution and refining them through the iterative algorithms. To predict time course of concentrations starting from arbitrary non-steady-state conditions, the continuous time interval $[0, T]$, on which systems dynamics needs to be simulated, is represented by discrete time moments $f \times \Delta t$, where Δt is the selected small time step and $f=0, 1, 2, \dots, T/\Delta t$. The derivatives in the Eqs. (1.1) and (1.2) are approximated by finite differences and for each time step adjustments of reagent concentrations are calculated.

Despite the methodologies and large variety of tools that were established for solving these ODE and PDE, this approach has fundamental limitations for the applications to real systems, and in particular, for the modelling of actin polymerisation kinetics. First, the limited set of reagents has to be directly defined, which is complicated or even impossible for actin polymers that can have different structural properties due to the stochasticity of the occurring reactions. Second, the deterministic models operate with average concentrations of reactants, which does not allow to properly analyse the role of rare events (e.g. nucleation or annealing of actin filaments), that may trigger important physiological processes, and to evaluate the stochastic variations for the calculated mean values. These limitations are overcome by using stochastic approaches, that use probability functions to describe possible states of any system. The behaviour of such an arbitrary stochastic system is described by the master (or Kolmogorov-Smirnov) equation (Gardiner, 2004):

$$\frac{dP(\xi, t)}{dt} = \sum_{\eta \in \Omega} (\mathfrak{R}(\eta, \xi) \cdot P(\eta, t) - \mathfrak{R}(\xi, \eta) \cdot P(\xi, t)), \quad (1.3)$$

where $P(\xi, t)$ - probability to find the system in the state ξ at time t ; $\mathfrak{R}(\eta, \xi) \cdot dt$ - probability of the system to switch from the state η to state ξ during time interval dt , Ω - set of all possible system states. When this approach is applied to analyse chemical reactions in a well-mixed solution, the system state is defined by vector $\vec{x} = (x_1, x_2, \dots, x_N)$, where x_i - number of molecules for the i -th substance. Transition probabilities correspond to the propensity density functions $a_j(\vec{x})$, which are equal to the probability of one j -th reaction to occur during the short time interval dt . The Eq. (1.3) would then transform to the chemical master equation (Gadgil et al., 2005):

$$\frac{dP(\vec{x}, t)}{dt} = \sum_{j=1}^M \left[-P(\vec{x}, t) a_j(\vec{x}) + \sum_{j=1}^M P(\vec{x} - \Delta \vec{x}, t) a_j(\vec{x} - \Delta \vec{x}) \right] \quad (1.4)$$

Coefficients $a_j(\vec{x})$ depend on the reaction rate constants k_j and can be calculated by using the Eqs. (3.1) and (3.2). The Eq. (1.4) is the analogue of Eq. (1.1) in deterministic case. The stochastic approach could be used for analysing spatially resolved molecular systems represented by Eq. (1.2) if the probabilities of system states are considered to be functions of coordinates.

If the analytical or numerical solution for the chemical master equation can be derived, e.g. probabilities $P(\bar{x}, t)$ can be calculated on the considered time interval, the evolution of the modelled system including its stochastic fluctuations can be predicted. For complex biomolecular systems, which are often characterised by a huge number of possible states, the exact solutions often cannot be obtained. In these cases a Monte Carlo methodology (Binder and Heermann, 2010) is applied to predict chemical kinetics, described by Eq. (1.4). These calculation procedures are often referred to as Gillespie algorithms named after the researcher who developed them in 1970s (Gillespie, 1976; Gillespie, 1977). In these algorithms numbers of molecules for each substance are stored and used to calculate coefficients $a_j(\bar{x})$. On each simulation step the random number generator is used to determine the type of the next reaction and time τ , after which it will occur. The numbers of molecules for all substances are adjusted according to the determined reaction and the current simulated time t is increased by τ . If the stochastic movement of molecules has to be taken into account, their shifts are also determined as random numbers. The simulation continues until the simulated time would reach the predetermined value T . Figure 3.2 represents an example of block diagram for such a stochastic simulation algorithm (SSA).

The SSAs are capable to predict the evolution of any biomolecular system, for which initial system configuration (numbers of molecules for all substances and their positions for spatially resolved models) could be determined and probability densities for all possible reactions could be calculated. However for complex systems, which consist of many reactants interacting via numerous reaction channels, such simulations require large computational costs. Simulations of the same system often have to be repeated several times, because different runs would lead to different results due to the stochasticity of the occurring reactions. Several modifications of the Gillespie algorithms were reported, that allow to speed up calculations (Cao et al., 2004; E et al., 2005; Gibson and Bruck, 2000; Gillespie, 2001). However, simulations of spatially resolved models are often computationally arduous. Hence, combination of deterministic and stochastic approaches might be used to predict behaviour of such systems.

1.4 *Scope of the thesis*

Investigation of the regulation of actin polymerisation at a molecular level in physiological conditions is still limited by presently available experimental and analytical techniques and protocols. Although imaging of individual filaments in low-concentrated actin solutions provides quantitative information about the polymerisation process, it does not allow studying the bulk properties of dense meshworks of filaments such as those present in the cell. In contrast, the quantitative, real-time analysis of actin dynamics in living cells often operates with over-simplified models, which do not account for structural properties of the actin cytoskeleton.

The major aim of this study is the development of theoretical and experimental tools for the investigation of the actin cytoskeleton dynamics in living cells. The distinctive feature of the actin cytoskeleton over many other intracellular systems is the structure of filaments and their assemblies. The ability of these structures to change rapidly in response to intracellular or extracellular stimuli is needed for the associated biomolecular processes and has to be studied quantitatively to understand underlying phenomena.

The quantitative understanding of actin polymerisation dynamics implies, that it can be reconstructed *in silico* to link key features of this system to experimentally measured parameters. Because assembly and disassembly of actin monomers primarily occur at the ends of filaments, the dynamic properties of filaments depend on their structures with short filaments being generally less stable than long filaments. The structure and stability of filaments are determined by the simultaneous activities of actin-binding proteins. The same set of regulatory proteins might lead to the various filament structures depending on their quantities and regulatory factors. Therefore two questions need to be answered: i) is it possible to predict the dynamics of actin structures in response to actin-binding proteins working in concert?; and ii) which kinetic parameters of actin assembly can be measured in physiological conditions and how are they linked to the association and disassociation reaction rates and the structures of filaments? These questions were addressed in Chapter 3 by formulating and validating the dedicated mathematical models.

The predictions generated by these models could not simply be compared to the experimental data. As individual filaments in tight bundles and bulk meshworks cannot be visualised, indirect methods to measure actin exchange in the assemblies of filaments are required. We selected the confocal-microscopy-based Fluorescence Recovery After Photobleaching (FRAP) technique as a major experimental method for several reasons. First, it allows to quantify the local exchange of actin between polymerised and monomeric pools in the steady-state and non-steady-state conditions in each actin structure. Second, it does not require specialised equipment and can be performed on any confocal microscope with the bleaching option. Third, collected sets of the confocal images allow studying spatial effects of actin incorporation and disassembly of the structures such as lamellipodia and focal adhesions. Despite these advantages, special computational routines are needed for the estimation of the relevant parameters of the actin cytoskeleton dynamics from the collected FRAP data. We aimed at developing tools to accurately conduct all steps of data analysis and to estimate the parameters characterising turnover of the actin cytoskeleton. The experimental procedures and the created tools are described in the Chapter 2.

One of the major differences of actin polymerisation in physiological conditions and as compared to simplified biochemical experiments is that the actin-binding proteins affect the dynamics of filaments simultaneously. Localisation of some regulatory proteins, particularly nucleators and/or NPFs, in specific regions at cell membranes and free diffusion of other actin regulators, such as cappers and severing proteins, govern both the spatial organisation of filaments and their turnover properties. We decided to take advantage of the actin-based biomimetic motility assay that enables to reconstruct these important features of actin motility in order i) to validate the algorithms and tools we developed for the analysis of actin turnover data and ii) to quantitatively address the effect of well-characterised actin-binding proteins on the network turnover. The installation of the FRAP experiments with this assay, their results and analysis are discussed in Chapter 4.

Among other actin structures, focal adhesions retain the interest of researchers in the field because of their importance in many essential biological processes such as adhesion, migration and signalling. The identification and biochemical characterisation of actin regulators at focal adhesions is necessary but

not sufficient for the understanding of actin polymerisation dynamics in these structures. Measurement and accurate interpretation of actin turnover in focal adhesions are required to characterise their regulation by associated proteins and upstream signalling pathways. The actin-associated protein zyxin and its binding partner Tes, which represent the long-term interest of the lab, were shown to be important for adherence and migration of the cells and to change dynamic properties of actin filaments *in vitro* and in living cells. Therefore, the interaction of these proteins with actin at focal adhesions was selected as to apply the created tools in a biological study. In Chapter 5 we show, how the quantitative analysis of FRAP experiments performed with actin and zyxin in conditions where Tes or zyxin are overexpressed or inhibited by siRNA, provide an insight into mechanisms that control cytoskeleton turnover at focal adhesions.

Chapter 2 Materials and methods

2.1 Biomimetic motility assay for actin-based processes

2.1.1. Proteins

Purified proteins were used to reconstruct actin turnover cycle similar to that occurring in the different regions of living cells. Actin, rhodamine-labelled actin, Arp2/3, gelsolin, cofilin, profilin, GST-VCA were purchased from Cytoskeleton (Denver). Alexa Fluor 488-labelled actin was obtained from Molecular Probes. *Arabidopsis* ADF1 was a kind gift from Monika Dieterle (CRP-Sante, Luxembourg). Concentrations of all proteins were determined by scanning densitometry of protein bands on SDS-PAGE gels stained with Commassie Blue or Oriole fluorescent stain (Bio-Rad Laboratories), using BSA as a standard. Gels were scanned with ChemiDocTMXRS fluorescent scanner and quantified with ImageLab software (Bio-Rad Laboratories).

2.1.2. Motility assay preparation

GST-tagged VCA was grafted on the surface of polystyrene beads (Polysciences) having a diameter of 3 μ M. F-actin was prepared by resuspending G-actin in G-buffer (5 mM Tris pH 7.8, 0.1 mM CaCl_2 , 0.2 mM ATP, 1mM DTT) supplemented with 0.1 M KCl, 1 mM MgCl_2 and 0.2 mM EGTA (Le Clainche and Carlier, 2004). The motility medium was prepared by mixing F-actin with actin-binding proteins in the assay buffer (10 mM HEPES pH7.8, 0.1 M KCl, 1 mM MgCl_2 , 1 mM ATP, 0.1 mM CaCl_2), supplemented with 1.8 mM Mg-ATP, 6 mM DTT and 0.13 mM DABCO. Motility medium was mixed with the coated beads. Methylcellulose (final concentration 0.2% w/v) was added when indicated in the text to increase the viscosity in the sample and to minimise convective flux. To avoid photodamage effect which is critical for time-lapse fluorescence microscopy experiments, the motility medium was supplemented with 1.5 mg/ml ascorbic acid (vitamin C) - a scavenger of free oxygen radicals. Several microliters of the final mix were mounted between a microscopy glass slide and a coverslip (18×18 mm). The preparation was sealed with VALAP (Vaseline/lanolin/paraffin 1:1:1) to avoid the evaporation of the medium. A detailed protocol of bead coating and preparation of the motility mix is presented in Appendix B.

To avoid non-specific interactions with surfaces of the motility chamber, slides and coverslips were prepared in advance as follows. First, they were washed with NaOH 3M and ethanol 100%. Then, they were incubated with APTES (Sigma-Aldrich) for 10 min and washed 3 times with isopropanol. Slides and coverslips were then racked and backed for at least 8 h at 90°C. Finally, they were washed 2 times with ethanol, rinsed with water, dried and stored at room temperature.

2.1.3. Time-lapse microscopy and FRAP experiments

FRAP experiments were conducted on Zeiss LSM 510 Meta and Zeiss LSM 710 confocal microscopes using 63x/1.4 NA oil immersion objective. To track polymerisation dynamics with time-lapse microscopy, the motility medium contained actin molecules labelled with two fluorescent dyes (10% of actin labelled with Alexa Fluor 488 and 10% labelled with TRITC-rhodamine). Rhodamine was detected and bleached with DPSS-561 laser. For the analysis of non-steady-state actin polymerisation, the total amount of polymerised actin was measured as a function of time using Alexa Fluor 488 detected with the 488 spectral line of an Argon laser. For every time point, images in two fluorescent channels were scanned sequentially to avoid an emission cross-talk. Simultaneously with imaging in the non-bleached channel, a bright field image with the detector of transmitted light was acquired to track the bead position. Depending on the composition of the motility mix, a total of 60-120 images was collected with time intervals of 5-60 s between images to track actin exchange in the bleached cloud.

2.1.4. Data processing

Quantification of fluorescent signals and building of kymographs for the analysis of spatial actin incorporation in the clouds was performed using ImageJ as specified in section 4.3. To measure the total exchange of fluorescence in the clouds, fluorescent images first were subjected to background subtraction and filtering with a low-pass filter for the reduction of noise levels. Then, images collected in the non-bleached channel were used for the segmentation of actin clouds. Total fluorescence intensities in both channels were quantified in the segmented regions. The recovery curves characterising actin exchange in the clouds were calculated according to the Eq. (2.1):

$$F(t) = \frac{I_{rhod}(t)}{I_{Alexa}(t)} \cdot \frac{I_{Alexa_pre}}{I_{rhod_pre}} \quad (2.1)$$

where $I_{rhod}(t)$, $I_{Alexa}(t)$ - quantified intensities in the bleached and non-bleached channels, subscript *_pre* means the averaging of intensities for the prebleach time points. All collected fluorescence recoveries were fitted with FRAPAnalyser software to estimate the half-times of actin exchange in the clouds.

To quantify the intensity profiles and to build the kymographs, the position of the bead was automatically tracked using the collected bright field images. At each time point, regions of interest for the quantification of intensities were formed at the intersection of rings of different radii concentric with the bead and the segmented cloud shape. The ratio of intensities in the two channels was calculated for each zone and normalised to the maximal value found over all time points. The obtained numbers were visualised as pixel intensities on the final image.

2.2 *Experiments with the living cells*

2.2.1. *DNA Constructs*

cDNA corresponding to β -actin was cloned into a pCDNA3 GFP vector. cDNA corresponding to wild type zyxin (WT) and VGEI zyxin mutant (MT) were cloned into a pEGFP-N1 vector (Clontech). The zyxin MT construct, which was generated by the DNA2.0 Company, corresponds to a mutant of zyxin in which the four amino acids [60VGEI63] were substituted by alanins. The zyxin sequence targeted by siRNA was changed. In zyxin WT, the sequence 5'GTGTTACAAGTGTGAGGAC3', chosen for zyxin silencing, was replaced by the silent mutant sequence Mut HP (Mutation of HairPin site) 5'GTGCTATAAATGCGAAGAT3' (synthesized by DNA2.0 Company). The transcripts of GFP-zyxin WT HP and GFP-zyxin MT Mut HP are not recognized by zyxin siRNA, and encode the same proteins as GFP-zyxin WT and GFP-zyxin MT respectively. All constructs were sequenced by LGC Genomics.

2.2.2. *Cell culture and transfection*

Vero green monkey kidney cells [ATCC CCL-81] and zyxin knock-down human cancer HeLa B9 cells (generated in our lab) were grown at 37°C 5% CO₂ in Dulbecco's modified Eagle's medium (DMEM) supplemented with 10% fetal bovine

serum, 2 mM L-glutamine, 100 u/ml pencillin and 100 u/ml streptomycin. For HeLa B9 cells 2 µg puromycin was added to the medium to keep the selection pressure. Vero cells were transiently transfected by electroporation (Toneguzzo et al., 1986) and used for FRAP 48 h after transfection. HeLa cells were transfected with calcium-phosphate-DNA coprecipitation (Graham and van der Eb, 1973; Jordan et al., 1996) and used for FRAP 24 h after transfection.

2.2.3. FRAP experiments

FRAP experiments with GFP-actin and GFP-zyxin variants were performed with a Zeiss LSM 510 Meta laser scanning confocal microscope (Carl Zeiss, Jena, Germany) with a Plan-Apochromat 63x/1.4NA oil-immersion objective and a confocal pinhole set to 300 µm. Cells were maintained at 37°C using an air-stream incubator and a heating frame (Pecon GmbH). DMEM imaging medium lacking phenol-red and supplemented with 15 mM HEPES pH 7.4 was put on the cells just before the experiment. Twenty images before bleach and 400 images after bleach were acquired. In experiments with GFP-actin we used 1s time interval between scans. For the analysis of GFP-zyxin the time interval was set to 0.25 s because the turnover of zyxin at FAs is faster in comparison with actin. FRAP acquisitions were performed in the rectangular regions of 512×128 pixels (0.14 µm/pixel) with 488-nm Argon laser line at 2% power and 505 to 550 nm band-pass emission filter. Three bleaching iterations were performed in less than 0.2 sec within a circular spot with a diameter of 2.7 µm using the same laser line at 100% power.

2.2.4. Data processing

The fluorescence recoveries and reference signals were quantified as time courses of average intensities inside the respective regions with the microscope running software (LSM 510, Carl Zeiss). When focal adhesions significantly changed in size and shape during the acquisition time, the corresponding datasets were excluded from the analysis. Subsequently, data processing was performed using the FRAPAnalyser tool described in section 2.3. Normalised FRAP curves were generated from raw data using the double normalisation method (Phair et al., 2004). Each experimental curve was fitted separately to determine optimal parameters of the selected fitting equation. The statistical analysis was then performed on the fitted

parameters to calculate their average values and test for statistical significance between compared conditions.

2.3 Development of the Integrated approach for analysing FRAP intensities

2.3.1. General scheme

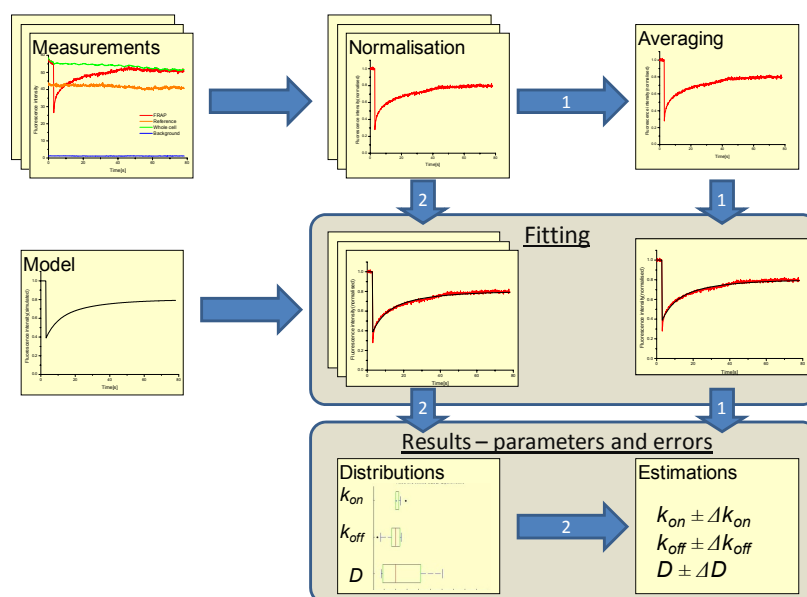


Figure 2.1. Flow-scheme for the analysis of FRAP intensities.

We aimed at implementing an approach for the analysis of FRAP intensities to estimate mobility parameters of fluorescently-labelled bio-molecules or kinetic parameters of biochemical interactions, changing this mobility. The general scheme for the developed approach is illustrated in Fig. 2.1. We decided to have a modular structure of the implemented analysis scheme to easily update for new models and normalisation algorithms. The properties of each block as well as the interactions between them are described below.

Measurements are saved in a tabular format. This table has to contain time points of the scans and the corresponding FRAP intensities (often average intensities inside a bleached spot) and all intensities required for normalisation (reference signal, background signal, etc.).

Normalisation is performed to correct the experimental data for autofluorescence, acquisition photobleaching, potential laser fluctuations and other technical artefacts using the signals from the one or several reference regions. Because absolute values of fluorescence intensities do not often contain biological information but represent, for example, variation in expression levels for transfected fluorescent proteins, all measured intensities can be scaled relative to prebleach levels.

Model represents a mathematical formulation of the biological process under study which can be compared to normalised experimental data in a quantitative manner. Models differ by underlying phenomena and number of parameters N , but each model in our scheme contains: i) fitting equation $F(t; a_1, \dots, a_N)$ that allows to simulate time course of FRAP recovery for a given set of parameters a_1, \dots, a_N ; ii) minimal and maximal parameter values $(a_1^{\min}, a_1^{\max}), \dots, (a_N^{\min}, a_N^{\max})$ that would limit the search space when fitting for the optimal parameter values.

Averaging. In many earlier published FRAP analysis protocols individual FRAP curves are averaged "point by point" before optimisation of model parameters. This allows to reduce the noise levels and compare qualitatively experiments performed at different conditions. Since recent studies suggest to fit every single curve separately for the accurate quantitative analysis, we included both approaches to our analysis scheme (compare track 1 and track 2 in Fig. 2.1).

Fitting makes use of one of the non-linear iterative regression methods to find optimum parameters a_1^*, \dots, a_N^* that lead to the approximation of experimental data by the model. The fitting algorithm optimizes the goodness-of-fit criterion – a numerical measure that characterises the difference between experimental and theoretical curves.

Final parameter estimations are represented depending if single or averaged curves were fitted. When fitting average curves, the best parameter values from fitting algorithm are considered to represent sample means. The errors are calculated from the remaining difference between model and experiment. Fitting of single curves allows to calculate means and variations of parameters accounting for biological differences between samples. At the same time, the whole analysis approach is verified by looking for example on the skewness of parameter distributions

2.3.2. Software tools

Stand-alone program FRAPAnalyser. The methodology described in 2.3.1 was implemented as a stand-alone computational tool called *FRAPAnalyser*. The program is an object-oriented software package in C++ with a user-friendly interface. The executable program version runs under Microsoft Windows operating system. C++ Builder 2007 (CodeGear) was used for the development of user interface and program compilation. Modules for the models, data storage and manipulation algorithms and fitting are created as C++ classes and do not depend on any particular compiling environment. Potentially they can be recompiled using any C++ compiler to run on other platforms.

Here, major properties of the *FRAPAnalyser* software are listed (the full technical specification, executable program and its user manual can be found in the supplementary files):

- The program uses quantified time course intensities stored as text files. It allows to upload many datasets simultaneously and group them according to the used experimental conditions for further analysis;
- The fitted values of parameters for the selected model are generated by the program as a result of analysis. The table with parameters for all uploaded datasets can be exported in tabular format to a text file;
- The graphical support to plot experimentally measured, normalised and simulated (fitted) FRAP curves.
- Currently integrated models allow fitting of FRAP intensities for several intracellular processes in steady-state conditions: one- and two-exponentials, binding models for one- or two binding sites in a reaction dominant regime (fast diffusion), diffusion for circular (Soumpasis, 1983) and rectangular (Ellenberg et al., 1997) bleached regions, diffusion-limited binding (Sprague et al., 2004). The list of models is easily extendable on request;
- Fitting with Levenberg-Marquardt and Nelder-Mead algorithms to minimise χ^2 goodness of fit criterion (Nelder and Mead, 1965; Press et al., 2007).

Procedures for visualisation of fitted parameters. Having the parameters estimated for each dataset for multiple conditions, one might need to provide

statistical analysis of these parameters and their proper graphical representation. Therefore we developed a special script for *R* package (*frap_parameters_plots.r*) that uses a table with fitted parameters to calculate mean values, standard errors of the mean (SEM), and other statistical measures for each experimental condition. Thus, the data are visualised as:

- Histograms representing mean values of parameters \pm SEM;
- Boxplots showing mean, median, range, percentiles for parameter distributions;
- Scatterplots for pairs of model parameters to analyse correlations between them.

Chapter 3 Development of models for actin dynamics

3.1 Stochastic simulation algorithm for predicting actin dynamics

This section represents work published in the Biophysical Chemistry journal (Halavatyi et al., 2009).

3.1.1. Introduction

Many biophysical models have been proposed for the mechanisms by which actin filament assembly generates force that is translated into movement (see (Mogilner, 2009) for review). In addition, specific biochemical models were established to evaluate the effects of regulatory proteins on the actin polymerization reaction such as nucleation and filament elongation in the presence of formins (Kovar, 2006; Pring et al., 2003; Romero et al., 2004) or the Arp2/3 complex (Carlsson et al., 2004; Mahaffy and Pollard, 2006; Pollard and Beltzner, 2002), effects of capping (Carlsson et al., 2004; Cooper and Pollard, 1985; Matzavinos and Othmer, 2007), or of severing proteins (Carlsson, 2006; DesMarais et al., 2005; McGrath et al., 2000). These deterministic models rely on solving differential equations. One of the efficient non-analytical approaches which in principle can describe the actin polymerization processes is the Monte Carlo simulation (Binder and Heermann, 2010). Obviously, stochastic Monte Carlo models have a considerable potential because: i) they can describe adequately many actin-polymerization processes simultaneously, such as spontaneous or stimulated actin nucleation, (un)branching, fragmentation, annealing, complete depolymerisation, (un)capping, two-step ATP-hydrolysis (Brooks and Carlsson, 2008; Matzavinos and Othmer, 2007); ii) in addition stochastic models have the advantage that they can be applied to complex situations involving structural information and distribution of actin filament lengths (Fass et al., 2008; Roland et al., 2008). Moreover, Monte Carlo models are easy to understand, since the simulation algorithms are made from so-called first principles known on the studied systems, and not requiring a strong mathematical background (Nazarov et al., 2004; Yatskou et al., 2001). However, so far, no comprehensive universal Monte Carlo model and software of actin-polymerization reactions with a broad application panel for various actin polymerization processes are available.

In this work, we developed a systematic Monte Carlo simulation formalism and an computational tool for modelling and analysing the main actin polymerization reactions, uniquely including the nucleotide compositions of monomers and filaments, and the distribution of actin filament lengths. This tool was evaluated using well-characterized reactions such as actin association to and dissociation from filaments, assembly of actin nuclei (spontaneous and stimulated by capping proteins or formin), filament capping-related reactions, ATP-hydrolysis and ATP recharge of actin monomers, filament branching, fragmentation and annealing. The simulation models and computational algorithms were integrated in the stand-alone executable software package *ActinSimChem*.

3.1.2. Model

3.1.2.1. The model formalism

Actin polymerization is used by cells as a source of mechanical forces, which can be translated into cell propulsion. The process of actin assembly is influenced by the concentration of monomeric actin charged with ATP or ADP nucleotide, physical and biochemical conditions and, importantly, by different actin-regulatory proteins: actin nucleators such as the Arp2/3 complex and formin, different end cappers and severing proteins like cofilins. In this work, we considered the reactions between ATP- and ADP-actin monomers (ATM, ADM, *cf.* the Table 3.1), formin (FOM, a protein stimulating actin monomer assembly), actin nucleator Arp2/3 complex (ARM), and end cappers (CBM, CPM, regulating actin filament dynamics at barbed (B) or pointed (P) ends). Kinetic actin polymerization experiments have shown that capping proteins also nucleate actin polymerization in the presence of excess actin ATP-monomers (Maree et al., 2006).

Diagrams, showing the formalization of actin polymerization processes, are given in Fig. 3.1. Actin monomers self-assemble to form trimers with the rate constant k_{SNUC} . Actin filaments grow from these “nuclei” by addition of monomers. The structural asymmetry of the filament ends is correlated with dissimilar assembly and disassembly rates. An actin filament grows under appropriate conditions approximately ten times faster at the barbed end than at its pointed end. The growing process is reversible and it is controlled by a polymerization-depolymerisation equilibrium. The aging of F-actins occurs when ATP hydrolyses with the rate

constants k_{TTOP} and k_{PTOD} via the ADP-Pi “intermediate” state, consisting in ADP with a weakly associated phosphate. ATP hydrolysis results in weakening of actin subunit interaction and destabilization of the actin filament. Free ADP-actin monomers exchange their nucleotide for ATP because of the higher affinity of monomeric actin for ATP (Neidl and Engel, 1979); we introduced here the rate constant k_{DTOT} to describe this process.

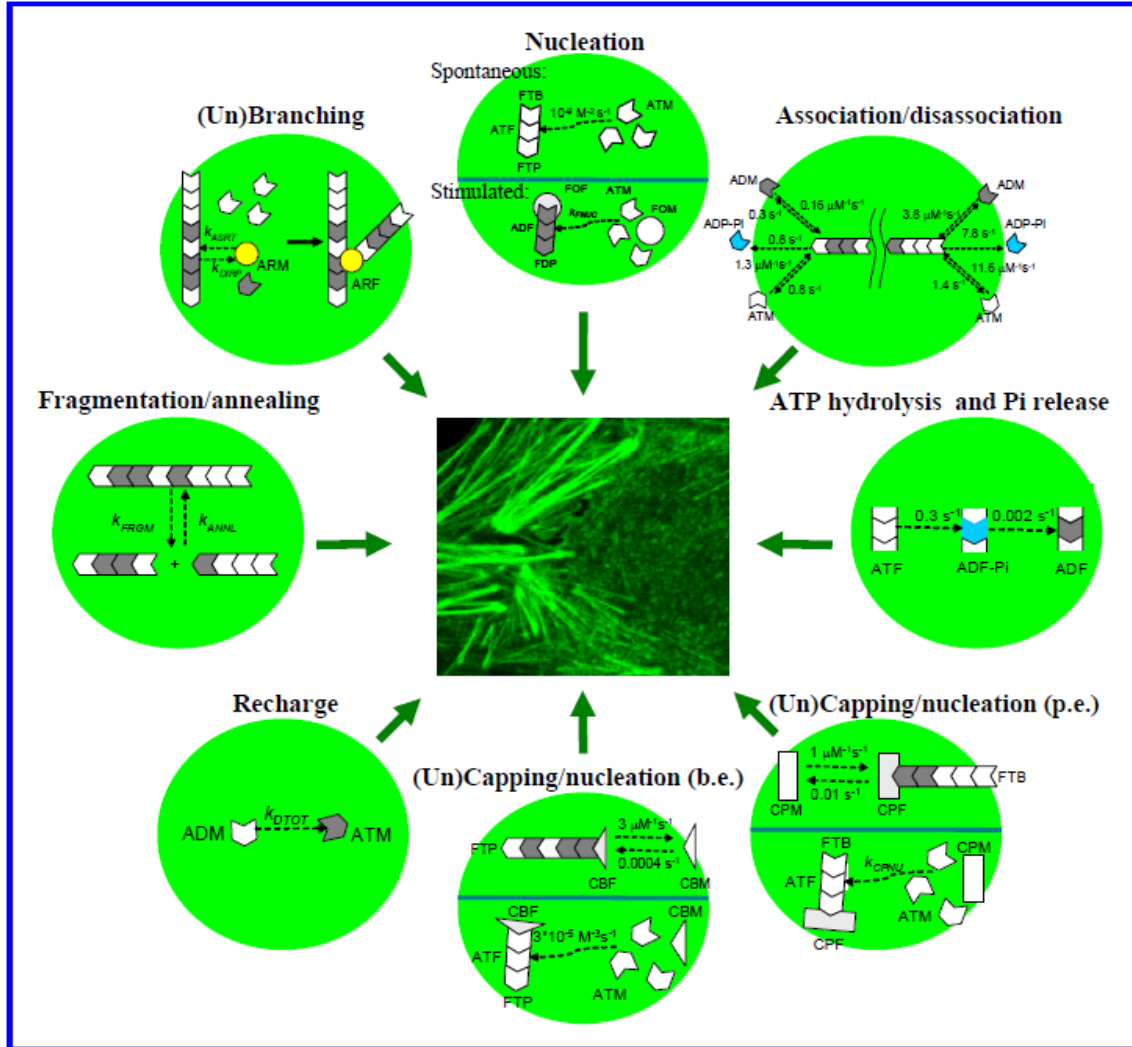


Figure 3.1: Diagrams of simulated actin-polymerization processes

For the non-mentioned rate constants see Table 3.2, for abbreviations of reagents see Table 3.1.

Free ends of a filament can be reversibly capped by either barbed or pointed end cappers. Capping proteins or formin promote actin nucleation, mostly by stabilizing actin trimers, at much higher rates (k_{CBNU} , k_{CPNU} and k_{FNUC}) when

compared to the rate of spontaneous actin nucleation (k_{SNUC}). In addition, formin being attached to the barbed end of nucleated actin oligomers, can significantly speed up barbed end elongation of the filament (Romero et al., 2004). Branching reactions of Arp2/3 complex with F-actins are realized according to the mechanism of side branching (Carlsson et al., 2004). The reactions of filament fragmentation and annealing were integrated as reported in (Fass et al., 2008). We assume spontaneous fragmentation occurs in a manner invariant to position and nucleotide state of the actin-protomer (the rate constant k_{FRGM}). Annealing reaction consists in adhesion of free barbed ends and pointed ends of filaments with the rate constant k_{ANNL} . Other hypotheses on mechanisms of filament branching, fragmentation, annealing, nucleation, capping, can accordingly also be integrated within the frame of our simulation scheme.

Table 3.1. Model abbreviations

| | |
|------------|--|
| nSRF model | non-structurally-resolved filament model |
| SRF model | structurally-resolved filament model |
| ATM | Globular actin (monomeric form) with incorporated ATP |
| ADM | Globular actin (monomeric form) with incorporated ADP |
| ATF | Filamentous actin protomer (F-actin) with incorporated ATP |
| APF | Filamentous actin protomer (F-actin) with incorporated ADP-Pi |
| ADf | Filamentous actin protomer (F-actin) with incorporated ADP |
| FTB | Barbed ends of filaments, terminating by ATP-actin |
| FPB | Barbed ends of filaments, terminating by ADP-Pi-actin |
| FDB | Barbed ends of filaments, terminating by ADP-actin |
| FTP | Pointed ends of filaments, terminating by ATP-actin |
| FPP | Pointed ends of filaments, terminating by ADP-Pi-actin |
| FDP | Pointed ends of filaments, terminating by ADP-actin |
| CBM | Barbed-end capping protein (capper) in monomer (free) form |
| CBF | Barbed-end capper bound to filament |
| CPM | Pointed-end capper in monomer (free) form |
| CPF | Pointed-end capper bound to filament |
| FOM | Formin in monomer (free) form |
| FOF | Formin, bound to filament barbed ends |
| ARM | Arp2/3 complex in monomer (free) form |
| ARF | Arp2/3 complex associated with filament |
| FRP | Arp2/3 complex associated with filament pointed end (pointed ends of filaments, terminating by Arp2/3 complexes) |
| FRB | Arp2/3 complex associated with filament with no bound actins (barbed ends of filaments, terminating by Arp2/3 complexes) |

Table 3.2. Simulated reactions and corresponding rate constants

| Reaction and equation | Symbol | Values |
|---|------------|---|
| Spontaneous nucleation of the filament $3 \text{ ATM} \rightarrow 3 \text{ ATF} + \text{FTB} + \text{FTP}$ | k_{SNUC} | $2.3 \times 10^{-11} \mu\text{M}^{-2}\text{s}^{-1}$ (Samarin et al., 2003); $1.1 \times 10^{-9} \mu\text{M}^{-2}\text{s}^{-1}$ (Carlsson et al., 2004); $\sim 2 \times 10^{-8} \mu\text{M}^{-2}\text{s}^{-1}$ (Sept and McCammon, 2001) |
| Formin-initiated nucleation $\text{FOM} + 3 \text{ ATM} \rightarrow 3 \text{ ADf} + \text{FOF} + \text{FDP}$ | k_{FNUC} | $7 \times 10^{-5} \mu\text{M}^{-3}\text{s}^{-1}$ (Pring et al., 2003) |
| Nucleation by barbed-end capping protein $\text{CBM} + 3 \text{ ATM} \rightarrow 3 \text{ ATF} + \text{CBF} + \text{FTP}$ | k_{CBNU} | Used in simulations – $3 \times 10^{-5} \mu\text{M}^{-3}\text{s}^{-1}$; for six ATM – $2.94 \times 10^{-5} \mu\text{M}^{-6}\text{s}^{-1}$ (Carlsson et al., 2004) |
| Nucleation by pointed-end capping protein $\text{CPM} + 3 \text{ ATM} \rightarrow 3 \text{ ATF} + \text{CPF} + \text{FTB}$ | k_{CPNU} | no data |
| ATP-actin association at barbed end $\text{FxB}^* + \text{ATM} \rightarrow \text{FTB} + \text{ATF}$ | k_{ASTB} | $11.5 \mu\text{M}^{-1}\text{s}^{-1}$ (Pollard, 1986) |
| ADP-actin association at barbed end $\text{FxB} + \text{ADM} \rightarrow \text{FDB} + \text{ADf}$ | k_{ASDB} | $3.8 \mu\text{M}^{-1}\text{s}^{-1}$ (Pollard, 1986) |
| ATP-actin association at pointed end $\text{FxP} + \text{ATM} \rightarrow \text{FTP} + \text{ATF}$ | k_{ASTP} | $1.3 \mu\text{M}^{-1}\text{s}^{-1}$ (Pollard, 1986) |
| ADP-actin association at pointed end $\text{FxP} + \text{ADM} \rightarrow \text{FDP} + \text{ADf}$ | k_{ASDP} | $0.16 \mu\text{M}^{-1}\text{s}^{-1}$ (Pollard, 1986) |
| Dissociation of ATP-actin from barbed end $\text{FTB} \rightarrow \text{FxB} + \text{ATM}(+\text{FRP})$ | k_{DIPB} | 1.4 s^{-1} (Pollard, 1986) |
| Dissociation of ADP-Pi-actin from barbed end $\text{FPB} \rightarrow \text{FxB} + \text{ADM}(+\text{FRP})$ | k_{DIPB} | 7.2 s^{-1} (Fass et al., 2008; Pollard, 1986) |
| Dissociation of ADP-actin from barbed end $\text{FDB} \rightarrow \text{FxB} + \text{ADM}(+\text{FRP})$ | k_{DIDB} | 7.2 s^{-1} (Pollard, 1986) |
| Dissociation of ATP-actin from pointed end $\text{FDB} \rightarrow \text{FxB} + \text{ATM}(+\text{FRP})$ | k_{DIPP} | 0.8 s^{-1} (Pollard, 1986) |
| Dissociation of ADP-Pi-actin from pointed end $\text{FPP} \rightarrow \text{FxP} + \text{ADM}(+\text{FRP})$ | k_{DITP} | 0.8 s^{-1} (Fass et al., 2008; Pollard, 1986) |
| Dissociation of ADP-actin from pointed end $\text{FDB} \rightarrow \text{FxB} + \text{ADM}(+\text{FRP})$ | k_{DIDP} | 0.27 s^{-1} (Pollard, 1986) |
| Capping of the barbed end $\text{CBM} + \text{FxB} \rightarrow \text{CBF}$ | k_{ASCB} | $3.0 \mu\text{M}^{-1}\text{s}^{-1}$ (Schafer et al., 1996) $8.0 \mu\text{M}^{-1}\text{s}^{-1}$ (Carlsson et al., 2004) |
| Capping of the pointed end $\text{CPM} + \text{FxP} \rightarrow \text{CPF}$ | k_{ASCP} | $\sim 0.25 - 1.0 \mu\text{M}^{-1}\text{s}^{-1}$ (Carlsson et al., 2004) |
| Uncapping of the barbed end $\text{CBF} \rightarrow \text{CBM} + \text{FxB}$ | k_{DICB} | $4.0 \times 10^{-4} \text{ s}^{-1}$ (Schafer et al., 1996) 4.2 s^{-1} (Carlsson et al., 2004) |
| Uncapping of the pointed end $\text{CPF} \rightarrow \text{CPM} + \text{FxP}$ | k_{DICP} | no data |
| Association of formin to barbed end $\text{FOM} + \text{FxB} \rightarrow \text{FOF}$ | k_{ASFB} | no data |
| Detachment of formin from barbed end $\text{FOF} \rightarrow \text{FOM} + \text{FDB}$ | k_{DIFB} | $7.5 \times 10^{-4} \text{ s}^{-1}$ (Romero et al., 2004) |

| | | |
|--|------------|--|
| Formin-initiated association at barbed end $\text{FOF} + \text{ATM} \rightarrow \text{FOF} + \text{ADf}$ | k_{FASB} | for mDia formin in the presence of profilin $45\text{-}110 \mu\text{M}^{-1}\text{s}^{-1}$ (Kovar, 2006; Romero et al., 2004) without profilin – $9 \mu\text{M}^{-1}\text{s}^{-1}$ (Kovar, 2006) |
| Arp2/3 association to the F-actin $\text{AxF} + \text{ARM} \rightarrow \text{AxF} + \text{ARF} + \text{FRB}$ | k_{ASRT} | $5.4 \times 10^{-4} \mu\text{M}^{-3}\text{s}^{-1}$ (Carlsson et al., 2004) |
| Dissociation of the Arp2/3 from the pointed end $\text{FRP} + [\text{ARF}] \rightarrow \text{ARM} + \text{FxP}$ | k_{DIRP} | 0.0018 s^{-1} (Carlsson et al., 2004) |
| Fragmentation: $\wedge \rightarrow \text{FyB} + \text{FxP}$ | k_{FRGM} | no data |
| Annealing: $\text{FyB} + \text{FxP} \rightarrow \wedge$ | k_{ANNL} | no data |
| ATP-hydrolysis: $\text{ATF} \rightarrow \text{APF}$ | k_{TTOP} | 0.3 s^{-1} (Blanchoin and Pollard, 2002; Kuhn and Pollard, 2005) |
| Phosphate release: $\text{APF} \rightarrow \text{ADf}$ | k_{PTOD} | 0.0026 s^{-1} (Bindschadler et al., 2004; Kuhn and Pollard, 2005) |
| Recharge of monomeric actins in the pool $\text{ADM} \rightarrow \text{ATM}$ | k_{DTOT} | $\sim 20 \text{ (pro) s}^{-1}$ (Mogilner and Edelstein-Keshet, 2002) |

To build the simulation model for actin polymerization we made the following assumptions:

- Actin-polymerization is simulated in a cubic volume of the size V with periodic boundary conditions.
- Since free actin monomers and free actin-associated proteins (cappers, Arp2/3, formins) diffuse rapidly (Braeckmans et al., 2007; Lippincott-Schwartz et al., 2001; McGrath et al., 1998; Sprague et al., 2004), we assumed their spatial distribution is homogeneous.
- Quantities of monomeric proteins, i.e. the numbers of molecules N_{ATM} , N_{CBM} , etc. in the volume V , are calculated from the initial molecular concentrations $[ATM]_{t=0}$, $[CBM]_{t=0}$, etc.
- Filaments are simulated as independent objects.
- The total concentrations of the monomeric proteins are constant over the volume V .

The flow diagram of the developed integrative stochastic simulation model of actin polymerization processes is shown in Fig. 3.2a. The core of this model is the ability to reproduce any complex actin polymerization system in a unique and universal way, whatever particular actin-based system is used. It combines various molecular reagents, chemical reactions and structures of actin filaments within a unique stochastic simulation scheme (Fig. 3.2b). The integrity of this modelling approach is based on an open-architecture principle, allowing easy incorporation of new reagents, additional actin-polymerization reactions, filament structures or even new stochastic simulation algorithms.

Presently, to simulate actin polymerization processes, we used $n_R=21$ molecular reagents participating in $M=28$ chemical actin-related reactions (*cf.* Table 3.2). Reagents are globular and filamentous actins (with incorporated ATP/ADP-Pi/ADP nucleotide), barbed and pointed ends of filaments (terminated by ATP-/ADP-Pi-/ADP-actins), barbed and pointed end capping proteins, formin and the Arp2/3 complex (either as free forms or associated with filaments). The filaments are represented as consequences of protomer associations characterised by the number of protomers, the nucleotide states of these protomers, the number and types of

pointed and barbed ends, pointers to filamentous ends and actin related proteins, branching units, i.e. the sites for growth of 'daughter' branches. Any 'daughter' branches to a 'mother' filament are similarly organised.

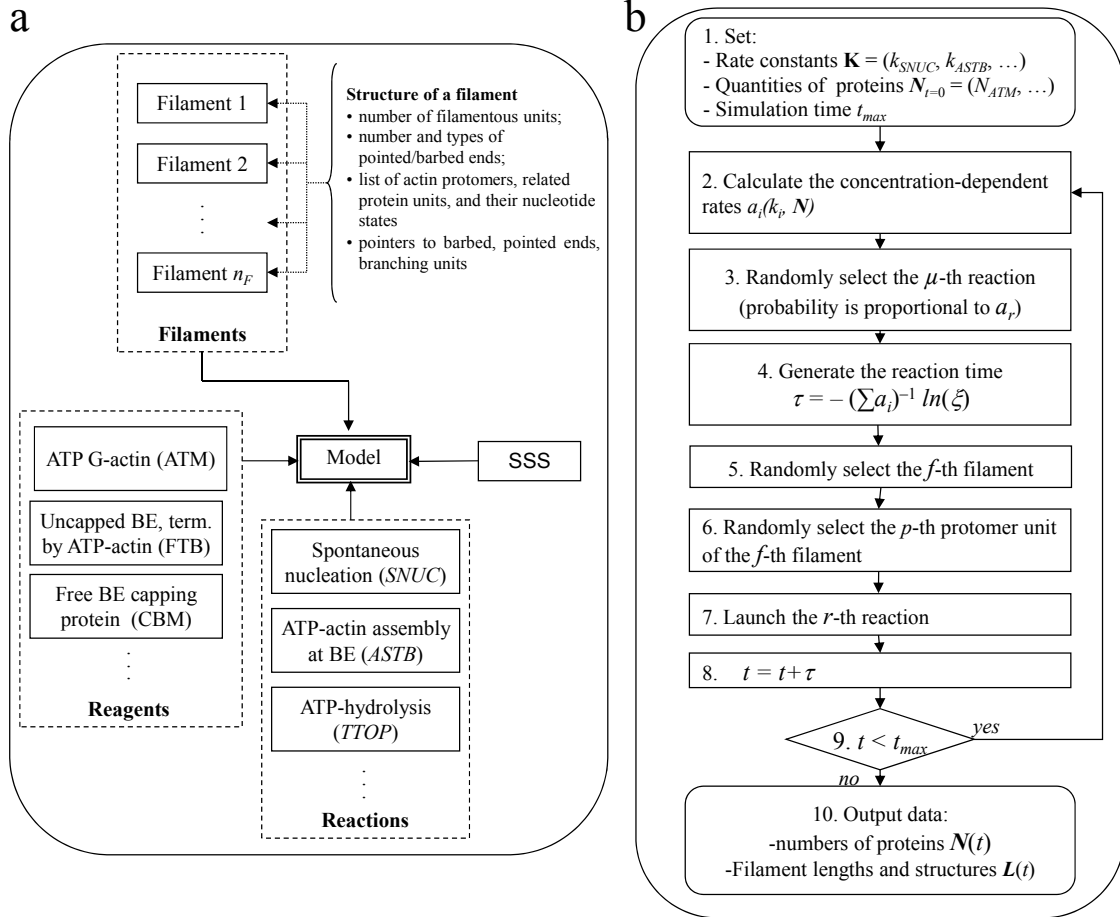


Figure 3.2: Integrative stochastic simulation model of actin polymerization processes.

a) Schematic diagram of the developed simulation model. Presently, we incorporated $n_R=21$ molecular reagents participating in $M=28$ chemical actin-related reactions (cf. Table 3.2). SSS — stochastic simulation scheme. b) Flow diagram for the SSS. Vector $\mathbf{N}=\{N_k\}=(N_{ATM}, N_{ADM}, \dots, N_{FRB})$ contains the number of molecules of each reagent. The evolution vector \mathbf{N} in time is denoted as $\mathbf{N}(t)$.

3.1.2.2. The simulation of reactions

To simulate the chemical interactions between molecular reagents in the actin filaments a proper discrete-event Monte Carlo simulation methodology is needed. Several stochastic simulation strategies have been implemented and compared. More specifically, we developed new simulation schemes based on the updates of the Gillespie's "direct" method and its modifications: the "first reaction" method

(Gillespie, 1976), the “next reaction” method of Gibson-Bruck (Gibson and Bruck, 2000) and the τ -leap algorithm (Gillespie, 2001). The best results were obtained for the one generated on the base of the Gillespie's “direct” algorithm (see Appendix B). A flow diagram of the stochastic simulation scheme implemented in our model is shown in Fig. 3.2b.

The simulation starts in **block 1** by setting the volume V , the initial numbers of molecules $N=(N_{ATM}, N_{ADM}, \dots, N_{FRB})$, and the rate constants $K=(k_{SNUC}, k_{CBNU}, \dots, k_{DTOT})$. In **block 2** the concentration-dependent reaction rates a_i , where i is the index running for 28 reactions $\{SNUC, CBNU, \dots, DTOT\}$ (*cf.* Table 3.2), are calculated using Eq. (3.1) or Eq. (3.2).

$$a_i = k_i (10^{-6} N_A V)^{1-n_i} \prod_{j=1}^{n_i} N_j, \quad (3.1)$$

where n_i is the number of reagents participating in the i -th reaction; k_i is the experimental concentration-independent rate constant, given in the same units as in Table 3.2 (s^{-1} , $\mu M^{-1} s^{-1}$, $\mu M^{-2} s^{-1}$, and $\mu M^{-3} s^{-1}$ for $n = 1, 2, 3$, and 4 correspondingly); N_A is the Avogadro number; N_j is the number of molecules of j -th type, contained in volume V . This number is linked with the concentration of the j -th reagent as $C_j = N_j/V$.

Eq. (3.1) is applied if only one molecule of each reacting reagent is simulated in the i -th reaction. If more than one molecule of at least one reagent participates in the reaction, as, for instance, in the formin-initiated nucleation, then Eq. (3.2) can be calculated based on an analogy with (Gillespie, 1977).

$$a_i = k_i (10^{-6} N_A V)^{1-\eta_i} \prod_{j=1}^{n_i} \left(\prod_{l=1}^{m_i^j} (N_j - l + 1) \right), \quad (3.2)$$

where m_i^j is the number of molecules of j -th reagent, required for occurrence of i -th reaction; $\eta_i = \sum_{j=1}^{n_i} m_i^j$ is the total number of molecules, participating in the i -th reaction.

For instance for the formin-initiated nucleation $n_{FNUC} = 2$ (ATM and FOM are the reagents for this reaction), $m_{FNUC}^{ATM} = 3$, $m_{FNUC}^{FOM} = 1$, $\eta_{FNUC} = 4$.

The selection of the type of the next reaction is performed in **block 3** using a random number generator so that the probability to select r -th reaction is proportional to the value of a_r , where r is the index running for 28 reactions $\{SNUC, CBNU, \dots, DTOT\}$.

The time towards the reaction τ is calculated in **block 4**, using an assumption that the flow of reaction-events is a Poisson flow (Gillespie, 1976), and, therefore, the times between events are exponentially distributed. Using the method of inverse functions, the time τ can be calculated as

$$\tau = -\left(\sum_i a_i\right)^{-1} \ln(\xi), \quad (3.3)$$

where ξ is the uniformly distributed random number from the interval (0,1).

The f -th filament, to which the reaction will be applied, is randomly selected among the total number n_F of filaments in **block 5** using a new realization of a random number generator. The filament selection procedure is a numeric routine governed by a complex density probability function of the numbers of branches, pointed and barbed ends for the current state of filaments distribution. If the annealing reaction is gambled then two new random numbers are generated. This step is not needed in case of the nucleation reactions.

In **block 6** the p -th filamentous unit in the f -th filament is generated, using a new realization of a random number generator, on which a reaction either of hydrolysis, branching, or fragmentation occurs. This step is ignored in case of nucleation, association, dissociation, capping, uncapping, annealing reactions.

The reaction is performed in **block 7** in accordance with a formal scheme listed in Table 3.2. Each reaction results in a modification of the number of molecules and structure of one of the filaments. Exceptions to this are the hydrolysis and recharging reactions, which affect only structure of proteins. Nucleation and fragmentation reactions result in appearance of new filaments. Annealing reaction leads to the disappearance of one of the filaments. Branching reaction yields a new filament branch. When one type of the actin-monomer dissociation reactions occurs, the length of the filament is checked. If it contains less than 3 actin protomers — the filament dissociates, releasing all attached proteins (i.e. formin, capping proteins).

The ATP-related type of F-actin ends (FTB, FDB, FTP, FDP) can be changed after association and dissociation reactions.

Finally, the systems time t is increased by τ (**block 8**), and if the simulation time is less than the predefined maximal simulation time t_{max} (**block 9**), the algorithm returns to **block 2**. Otherwise simulation stops in **block 10**, providing a list of output characteristics, i.e. evolution of concentrations in time, the distribution of filament lengths, and actin nucleotide states in filaments.

3.1.2.3. Non-structurally-resolved filament (nSRF) and structurally-resolved filament (SRF) models

We developed two variants of structural representations of actin filaments: the non-structurally-resolved filament (nSRF) model and the structurally-resolved filament (SRF) model.

In the nSRF model a filament is represented by the number of ATP-containing actins (ATF), the number of ADP-Pi-containing actins (APF), the number of ADP-containing actins (ADF) and by type and state of the barbed and pointed ends. Selection of the state of actins (ATF/APF/ADF) bound to filament ends is performed as follows. The state of a last attached protein is stored in a model parameter called as “state of barbed/pointed end”. It thus defines the states of the corresponding ends of the filament, i.e. FTB/FTP, FPB/FPP, FDB/FDP, FRB/FRP, CBF/CPF, or FOF. After dissociation of a monomer from the filament, the state of the next filament-bound actin monomer, that will define a new type of end, is selected preferably from ATF actins. If no ATF actins are left, the filament end switches into ADP-Pi- (preferably) or ADP-related form. The SRF model is similar to the nSRF model but is additionally represented by the bidirectional list of actin types (ATF/APF/ADF) and actinaccessory proteins (CBF/CPF/FOF/ARF), which defines mutual positions of protomers in the filament. During filament growth, a marker is stored in the bidirectional list to define ATP/ADP-Pi/ADP-state of each actin or subunit and/or actin-associated protein in filament. The list has two access points — pointers to the barbed and pointed ends. This organization permits swift addition/removal of monomers at the ends and splitting/merging of lists for fragmentation/ annealing reactions. When Arp2/3 induced-branching is included, the pointers to ‘mother’ and

‘daughter’ filament branches are stored in the SRF and nSRF models. The SRF model also stores positions of attachment points on the ‘mother’ filament or branch regarding the pointed end.

Using the SRF model is more time-consuming due to processing the bidirectional list. The nSRF model is aimed to speed up the simulation by simplifying the representation of filaments. The SRF model is more accurate than the nSRF model and, by accounting for mutual positions of ATP- and ADP-actins in filaments as described above, it gives a powerful opportunity for the evaluation of nucleotide compositions without any restrictions and conditions imposed on the distribution of filament lengths. By using the SRF model one is additionally able to check: (i) depolymerization of preformed actin filaments networks, (ii) filament severing, for example, by cofilins, which have a higher affinity for ADP-actin (Maciver and Weeds, 1994), (iii) other polymerization processes taking in account the nature of the nucleotide such as the Arp2/3 association and side branch initiation which is preferable occurring at an ATP-charged protomer.

3.1.2.4. Error analysis

Stochastic deviations in the simulated results, yielding asymptotic solutions of the investigated processes, are inherent to the Monte Carlo simulation technique. In addition, powerful computational facilities are required. Increasing a volume V and averaging the results of n_A independent simulations help to reduce the stochastic deviation. Therefore, we developed a verification rule for an optimal selection of the simulation volume V and the number of averaging n_A (see Appendix B). An increase of n_A is preferable over an increase of V . The latter has a bottom cut-off to avoid any discontinuity at low concentrations and rare reactions. We estimated a possibly minimal volume needed for analysis of actin polymerization processes. Assume that the minimal number of reacting molecules is equal 20. If the minimal initial concentration of a reagent is 1 nM then the minimal volume becomes $V_{min} \approx 33 \mu\text{m}^3$. If the polymerization starts from a low-rate nucleation with the rate constant of $\sim 10^{-9}$ – $10^{-8} \mu\text{M}^{-2}\text{s}^{-1}$, the selection of a larger volume of $V > 125 \mu\text{m}^3$ may, however, be required.

3.1.3. Results and discussion

We performed several tests to validate our model and analyse its applicability for experimental studies. First, the source code was verified (see Appendix B). Second, we tested and validated the Monte Carlo model by comparison with synthetic theoretical data. A system of corresponding differential equations was used for a number of pre-selected sets of biochemical parameters published elsewhere. Third, we compared the computational efficiency and agreement of various actin filament models: nonstructurally-resolved (nSRF) and structurally-resolved filament (SRF) models. Finally, we applied our model for the analysis of pyrene-actin based fluorescence actin-polymerization experiments: i) actin polymerization, ii) actin polymerization in the presence of actin-capping protein, or iii) formin using data reported in literature (Carlsson et al., 2004) or kindly provided by the lab members.

3.1.3.1. Strategy for model evaluation and analysis

We evaluated the performance of the developed models on well-characterized theoretical and published data. We considered fundamental reactions including monomer assembly into filaments, filament end capping and assembly of actin oligomer nuclei by capping protein or formin. The complete list of the reactions events simulated is shown in Fig. 3.1. Our simulations are performed for $V=125 \mu\text{m}^3$ and $n_A=50$. For computational reasons and taking into account its minor effect on the systems considered in our tests we do not include in the simulations the reactions associated with the ADP-Pi “intermediate” nucleotide state. Instead, we approximated the filament aging reaction (hydrolysis of ATP in filaments) with the overall rate constant 0.0007 s^{-1} , which is assumed to be a lowest limit for an approximative two-step hydrolysis rate constant (including phosphate release), and is a product of rate constants for hydrolysis 0.3 s^{-1} (Blanchoin and Pollard, 2002) and phosphate release $0.0026\text{--}0.004 \text{ s}^{-1}$ (Bindschadler et al., 2004; Vavylonis et al., 2005).

We compared the nSRF model with a deterministic kinetic model for the simplest situation, in which the behaviour of the actin system can be described by a system of differential equations. Such deterministic models have been used to describe actin polymerization kinetics (see e.g. (Carlsson et al., 2004; Pring et al., 2003; Sept et al., 1999; Tobacman and Korn, 1983)). Subsequently, we compared

and evaluated simulations obtained with the SRF and nSRF models, a key step towards the model validation. First, agreement between two independently implemented models gives a good confidence that no technical or logical errors were made during programming of the modelling algorithms. Second, this comparison helps to investigate the application range of the nSRF model, i.e. to determine when the simplifications of the nSRF model are acceptable and do not lead to significant changes in simulation results. Finally, to further evaluate the robustness of the developed models, we applied the simulation models to some selected experimental data and evaluated how reagents affect the reactions.

3.1.3.2. Evaluation of the developed models by analytical solutions

Assembly of actin without any regulatory proteins is the simplest model system. The concentration of F-actin only slowly increases in the early phase (the so-called *lag phase*) due to slow spontaneous nucleation. Then a period of fast elongation follows, during which the concentration of F-actin increases more rapidly. Consequently globular actin decreases and asymptotically approaches to the so-called critical concentration C_c . The critical concentration, which is independent from the initial actin concentration, can be calculated via association/dissociation rates, Eq. (3.4)

$$C_c = (k_{DITB} + k_{DITP}) / (k_{ASTB} + k_{ASTP}) \quad (3.4)$$

We initially assume that no ATP-hydrolysis occurs in a system, i.e. no aging of F-actins, and, thus, only ATM and ATF actins exist in this system. This assumption is needed to build the system of the analytical equations (see Appendix B) and not a limitation linked to the presented simulation (see Section 3.1.3.3). The rate constants (for references see Table 3.2) used in modelling are listed in the figure legend. The nSRF model was launched and tested at three initial actin concentrations $[ATM]_{t=0} = 3, 6$ and $12 \mu\text{M}$. Predicted F-actin concentrations obtained either by the nSRF model or by the analytical model (Eq. (C1), Appendix B) for the actin systems with different actin concentrations are plotted in Fig. 3.3a and indicate a good agreement between simulated and analytical data.

Addition of barbed-end capping protein in the system above introduced two effects: i) increase of the nucleation rate and ii) inhibition of further elongation from the barbed end by capping. The analytical model for actin polymerization in the

presence of a barbed-end capping protein was reported in (Carlsson et al., 2004) and briefly given in Appendix B (Eq. (C2)). Again, no aging of F-actins is assumed (this is necessary to avoid tracking the ATP/ADP state of the ends for each separate filament). Predicted concentrations of F-actin by the nSRF (circles, diamonds) and analytical model (lines) for the initial protein concentrations $[ATM]_{t=0}=2 \mu\text{M}$, and $[CBM]_{t=0}=0.1, 0.01 \mu\text{M}$ are plotted in Fig. 3.3b. The fact that the results of simulated and analytical models of actin polymerization, with or without capping protein, are in good agreement validates the developed simulation model. A broader range of examples and tests of the models is shown in Appendix B (Fig. S1–S2). Fig. S1 demonstrates that simulations that predict the average filament length and the filament length distribution at steady-state changed drastically in presence of fragmentation and annealing, in line with (Fass et al., 2008). Fig. S2 shows a simulation of overshoot occurrence under various conditions of polymerization kinetics.

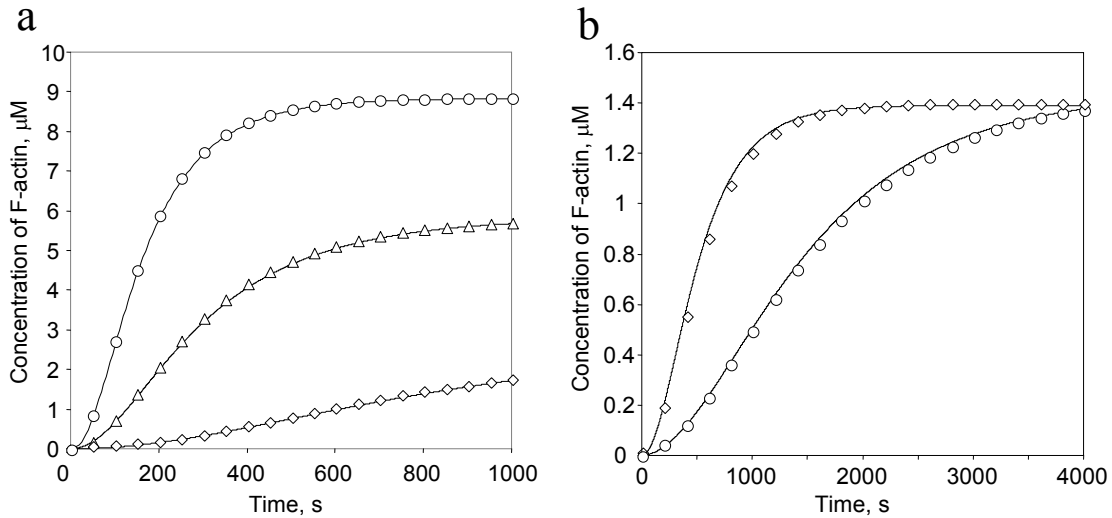


Figure 3.3: Predicted concentrations of F-actin by the nSRF (symbols) and analytical models (lines) for (a) actin polymerisation and (b) actin polymerisation in presence of a filament barbed end capping protein

a) $[ATM]_{t=0}=3, 6$ and $12 \mu\text{M}$ (bottom, middle and top curves), $k_{SNUC}=10^{-8} \mu\text{M}^{-2}\text{s}^{-1}$,
b) $[ATM]_{t=0}=2 \mu\text{M}$, $[CBM]_{t=0}=0.1 \mu\text{M}$ (top curve) and $0.01 \mu\text{M}$ (bottom curve),
 $k_{CBNU}=10^{-5} \mu\text{M}^{-3}\text{s}^{-1}$. If a parameter is not mentioned specifically, the value from Table 3.2 is used.

3.1.3.3. Comparison of the nSRF and SRF models

Polymerisation of actin in the absence of other proteins. A major difference between SRF and the nSRF model (and, *a fortiori*, previous analytical models) is that

the former inherently incorporates the possibility of aging of F-actin. This is now taken into account and simulated as a stochastic reaction with the rate constant 0.0007 s^{-1} . The SRF model combines information about type and position of each monomer in the filament, whereas in the nSRF model it is assumed that ATP-containing F-actins (ATF) are allocated near the filament ends, and ADP-actins (ADF) in the middle. The latter, rather rough approximation of the F-actin aging mechanism may result in biased models solutions, in particular for a time period longer than 1000 s, assuming a slow rate constant $\sim 10^{-3} \text{ s}^{-1}$ for the hydrolysis reaction.

Fig. 3.4a plots the predicted concentrations of F-actin resulting from the SRF (symbols) and nSRF (lines) models for three initial concentrations of actin $[ATM]_{t=0}=3, 6$ and $9 \text{ } \mu\text{M}$. The concentration of F-actin slowly increases in early phase, consistent with the experimentally observed *lag phase* (see e.g. Fig. 3.5b), due to slow spontaneous nucleation ($k_{SNUC}=10^{-8} \text{ } \mu\text{M}^{-2}\text{s}^{-1}$). During fast elongation the concentration of F-actin increases, consequently globular actin decreases and asymptotically approaches the critical concentration C_c which here is $0.17 \text{ } \mu\text{M}$. Therefore, the concentration of F-actin asymptotically approaches values of 2.83, 5.83 and $8.83 \text{ } \mu\text{M}$ (Fig. 3.4a).

During nucleation and elongation the rates of ADP-actin association and dissociation do not play an important role, because of fast ATP-actin recharge in the monomer pool and significant prevailing of the ATP-actin association reactions. At this stage no deviation can be detected when comparing both models, therefore the nSRF model can be used instead of SRF to predict systems behaviour in the nonequilibrium elongation phase of the filament. The simulation time required by the nSRF model for an actin system is about 30 times lower than that of the SRF model.

To evaluate the effect of ATP hydrolysis and filament aging, we varied the model parameters. We assumed that no actin recharge occurred and, to make the effect of aging more pronounced, we increased the aging rate up to one hundred times, and increased the rate of spontaneous nucleation up to $k_{SNUC}=10^{-6} \text{ } \mu\text{M}^{-2}\text{s}^{-1}$. Since the effect may appear only when association no longer prevails over dissociation, a long time period of $t_{max}=8000 \text{ s}$ was considered. The simulation results of the system for $[ATM]_{t=0}=2 \text{ } \mu\text{M}$ are shown in Fig. 3.4b. No deviation was observed

for the period of filament elongation, however, the subsequent late dissociation phase significantly differed for the two models. This deviation occurred even if actin ATP-recharge was switched on, however to a much lesser degree (data not shown). This result indicates that when ATP-actin recharge exists in the system, the simplified nSRF model can be used during the periods of lag-phase and fast filament elongation.

Formin-mediated effects on actin polymerization system. There are two main functions of formin in actin polymerization: it assembles actin and acts as a processive motor of filament elongation. In the presence of profilin, formin effectively generates long ADP-rich filaments, as was reported in (Romero et al., 2004). The elongation rate in this situation may reach values of $110 \mu\text{M}^{-1}\text{s}^{-1}$. In the absence of profilin, the elongation is less efficient, with a rate constant of $9 \mu\text{M}^{-1}\text{s}^{-1}$ (Kovar, 2006).

In our simulations we used the information from (Romero et al., 2004) and (Pring et al., 2003) to estimate formin-associated rate constants (see Table 3.2, reactions with rate constants k_{FNUC} , k_{FASB} , k_{DIFB}). The rate of spontaneous association of formin to a free barbed-end was put arbitrary, $k_{ASFB}=3 \mu\text{M}^{-1}\text{s}^{-1}$, however, this reaction does not demonstrate a high influence on the polymerization, because usually all free formins tend to nucleate new filaments. The result of the comparison of SRF and nSRF models for a $2 \mu\text{M}$ actin assay is given in Fig. 3.4c. Note, that the time window of the simulation $[0; 200 \text{ s}]$ is very different from the previous situations and that the speed of filament growth has increased significantly. For both formin concentrations tested, the final F-actin concentration is equal to $1.997 \mu\text{M}$, calculated as extrapolation to longer times, with almost all actin molecules in the F-form.

Similarly we tested an effect of capping proteins (Cooper and Pollard, 1985; Schafer et al., 1996) that can also nucleate actin polymerisation at high concentrations. The simulations were in good agreement between nSRF and SRF models (data not shown). The results revealed an increase of polymerisation rate and slight decrease of steady-state F-actin concentration upon increase of capping protein concentration.

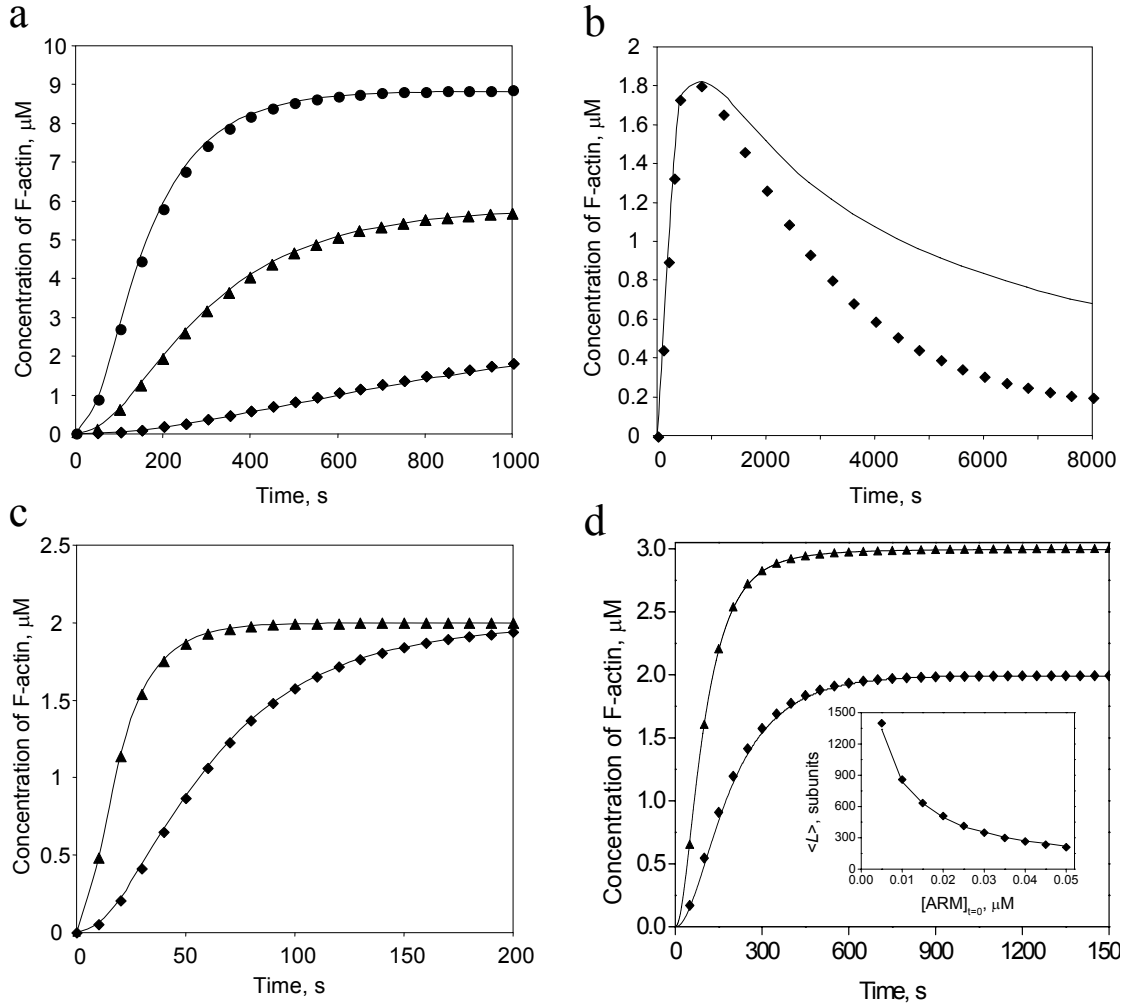


Figure 3.4: Predicted concentrations of F-actin by the SRF (symbols) and nSRF (lines) models in function of time.

a) Actin polymerisation, $[ATM]_{t=0} = 3, 6$ and $9 \mu M$ (bottom, middle and top curves in the plot), $k_{SNUC} = 10^{-8} \mu M^{-2} s^{-1}$. b) Actin polymerisation without monomer recharge ($k_{DTOT} = 0 s^{-1}$), simulated for a long time period, $[ATM]_{t=0} = 2 \mu M$, $k_{SNUC} = 10^{-6} \mu M^{-2} s^{-1}$ and $k_{TTOD} = 10^{-2} s^{-1}$. c) Formin-initiated actin polymerization, the top curve corresponds to $0.1 \mu M$ of formin, the bottom curve to $0.01 \mu M$; $k_{FNUC} = 7 \times 10^{-5} \mu M^{-3} s^{-1}$, $k_{FASB} = 110 \mu M^{-1} s^{-1}$. d) Actin polymerisation in the presence of all reagents (ATM, CBM, CPM, FOM, ARM) included and branching to either ATF/APF/ADF. The top curve corresponds to $3 \mu M$ of actin, the bottom curve to $2 \mu M$. (Inset) Decrease of the average filament length $\langle L \rangle$ in the steady-state phase with the concentration of the Arp2/3 complex ($2 \mu M$ of actin). $[CBM]_{t=0} = [CPM]_{t=0} = 0.01 \mu M$, $[FOM]_{t=0} = 0.001 \mu M$, $[ARM]_{t=0} = 0.01 \mu M$, $k_{SNUC} = 10^{-8} \mu M^{-2} s^{-1}$, $k_{CBNU} = k_{CPNU} = 10^{-5} \mu M^{-3} s^{-1}$, $k_{FNUC} = 7 \times 10^{-5} \mu M^{-3} s^{-1}$, $k_{FASB} = 110 \mu M^{-1} s^{-1}$, $k_{FRGM} = 1.8 \times 10^{-8} s^{-1}$, $k_{ANNL} = 10^{-8} \mu M^{-1} s^{-1}$, $k_{ASRT} = 10^{-5} \mu M^{-1} s^{-1}$, $k_{DIRP} = 10^{-3} s^{-1}$. If a parameter is not mentioned specifically, the value from Table 3.2 is used.

Effect of the full reaction set on actin polymerization system. We theoretically compared the simulation results for the condition in which all reagents and reactions are present (Table 3.2, Fig. 3.1). Selected initial concentrations are: $[ATM]_{t=0} = 2$ and

3 μM ; $[\text{CBM}]_{t=0}=0.01 \mu\text{M}$, $[\text{CPM}]_{t=0}=0.01 \mu\text{M}$, $[\text{FOM}]_{t=0}=0.001 \mu\text{M}$, $[\text{ARM}]_{t=0}=0.01 \mu\text{M}$. This is a very complex situation since barbed end capping protein interferes with formin and formin lowers the binding of capping protein to barbed ends by 100 fold without, however, competing for barbed end binding ((Romero et al., 2004), supplement data on gelsolin). In addition, several reactions including the Arp2/3 dependent branching reaction, change the number of (barbed) filament ends. Despite this complexity, the comparison of F-actin behaviour for two tested actin concentrations shown in Fig. 3.4d, demonstrates that the results for SRF and nSRF models were in a good agreement. Using our model, we can in addition investigate an effect of the branching reaction, in terms of the relevant rate constant and the concentration of the Arp2/3 complex, on the average filament length at steady state. We developed two mechanisms of the side branching: the Arp2/3 complex random nucleation to only ATF or to either ATF/APF/ADF. The latter case, despite not yielding a difference between nSRF and SRF models even at steady state, is needed to validate the simulation algorithms (Fig. 3.4d, inset). The average filament length in the steady-state phase decreases with the concentration of the Arp2/3 complex by both nSRF and SRF models – as is indeed expected from previous analytical calculations (Carlsson, 2005). In Appendix B we show an additional simulation example demonstrating that the outcome of Arp2/3 complex association and side branch initiation, which preferably occurs at an ATP-charged protomer, may differ for SRF and nSRF models (see Fig. S3 of Appendix B).

Based on the synthetic data we obtained for systems with increasing complexity and from comparing the two models where one model ignores the positional information of actin monomers in the filament, one is lead to conclude that unless the system is deprived of ATP-actin, both models yield the same result. This surprisingly suggests that the relative positions of ATP-actin and ADP-actin protomers within a filament are not important. One possible explanation is that the ATP hydrolysis rate does not influence the early time kinetics because it is very slow (0.0007 s^{-1}). This interpretation explains why kinetic models without ATP hydrolysis are also successful. Once the system reaches the steady-state phase, however, the nucleotide status may play a significant role for actin polymerisation (as demonstrated in Fig. 3.4b) for severing of filaments by cofilin (at ADP-actin protomers) or branching by Arp2/3 complex (at ATP-actin protomers as shown in

Fig. S3, Appendix B). In this case the developed SRF will yield more accurate results.

Additional numerical tests on validation of the developed models, in particular, effects of capping protein concentration and of various rate constants on actin polymerization, are reported in Appendix B. Collectively, this leads to the following conclusions. Increasing the concentration of capping proteins leads to increase of the overall polymerization rate due to faster nucleation. Second, we detected that already a moderate, twofold increase/decrease in monomer association/dissociation rates at the barbed ends strongly affects actin polymerization kinetics and almost no effect can be seen for the pointed ends. The simulation shows that increasing the nucleation rate results in a considerable rise in polymerized actin. Finally, variation in the aging rate does not modify the actin polymerization kinetics until steady-state is reached.

3.1.3.4. Evaluation on experimental data

To further evaluate the robustness of the developed models, we applied them to fitting of experimental data.

Actin polymerization. The simulation for 2 and 3 μM of actin concentrations has been performed with the same nucleation rate $k_{SNUC}=4.1\times 10^{-9} \mu\text{M}^{-2}\text{s}^{-1}$. The results of the comparison are given in Fig. 3.5a. Possible inconsistency between simulated and experimental data would result in curvature difference. Simulated and experimental data were however in good agreement, although small non-significant differences could be observed (3 μM of actin, top curve).

Actin polymerization in the presence of capping proteins. We next evaluated the effect of barbed end capping protein. We tested our models on data published previously in (Carlsson et al., 2004). Keeping the actin concentration constant (2 μM), the concentration of CBM was increased between 0 and 25 nM. The resulting change in pyrene fluorescence in time is given by solid lines in Fig. 3.5b. These experimental data and the simulation results, presented by symbols, highly correlated. The best fitting was obtained with the nucleation rate $k_{CBNU}=1.2\times 10^{-5} \mu\text{M}^{-3}\text{s}^{-1}$.

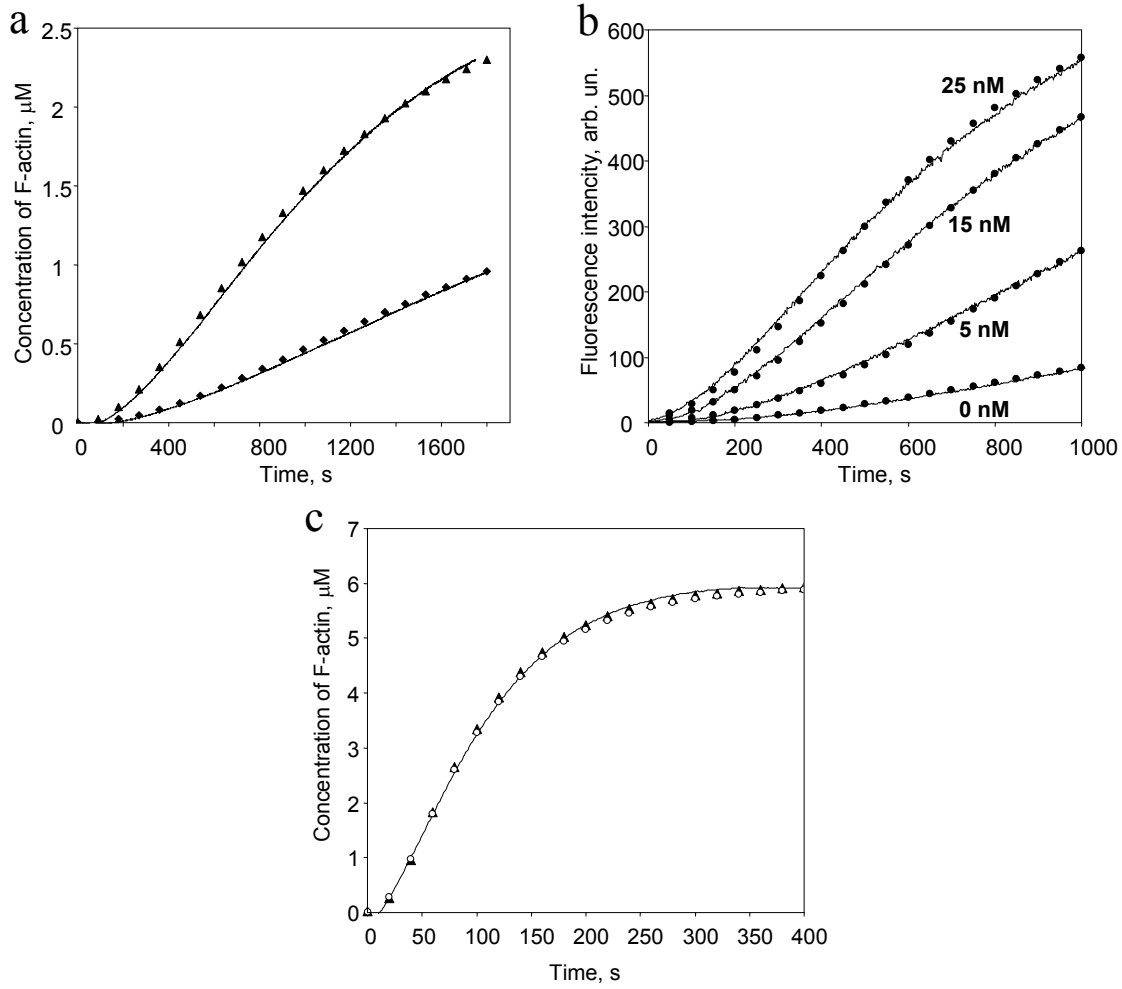


Figure 3.5: Comparison of the simulation results (symbols) with experimentally obtained data (solid lines).

a) Actin assay with $[\text{ATM}]_{t=0} = 2 \mu\text{M}$ (bottom curve) and $3 \mu\text{M}$ (top curve). Experimental fluorescence data were corrected for background and normalized by amplitude to fit simulated concentrations. During simulation $k_{\text{SNUC}} = 4.1 \times 10^{-9} \mu\text{M}^{-2}\text{s}^{-1}$, the other rates are the same as listed in Table 3.2. b) Experimental data showing the effect of capping-protein nucleation from (Carlsson et al., 2004) (solid lines). Experimental assays contain $2 \mu\text{M}$ of actin and various concentrations of barbed-end capping protein: $[\text{CBM}]_{t=0} = 0, 5, 15$ and 25 nM . c) Formin-initiated actinpolymerization. Here the comparison of the experimental fluorescence data (solid line), normalized by amplitude, and simulation results for two models of formin-actin polymerization (symbols) are given. The experimental sample contains $[\text{ATM}]_{t=0} = 6 \mu\text{M}$ and $[\text{FOM}]_{t=0} = 0.2 \mu\text{M}$. Triangles corresponds to the model with $k_{\text{FASB}} = 9 \mu\text{M}^{-1}\text{s}^{-1}$ and $k_{\text{FNUC}} = 4.7 \times 10^{-7} \mu\text{M}^{-3}\text{s}^{-1}$. Circles corresponds to the model with $k_{\text{FASB}} = 90 \mu\text{M}^{-1}\text{s}^{-1}$ and $k_{\text{FNUC}} = 4.7 \times 10^{-8} \mu\text{M}^{-3}\text{s}^{-1}$.

Formin-actin polymerization. The experimental assay included $6 \mu\text{M}$ actin and $0.2 \mu\text{M}$ formin (in the absence of profilin). First, we fixed the formin-enhanced elongation rate of actin filament, taking the value of $k_{\text{FASB}} = 9 \mu\text{M}^{-1}\text{s}^{-1}$ (Kovar, 2006). Then the nucleation rate was fitted. The best fit (Fig. 3.5c) was obtained for a nucleation rate constant of $k_{\text{FNUC}} = 4.7 \times 10^{-7} \mu\text{M}^{-3}\text{s}^{-1}$, which is ~ 10 times higher than

the value for spontaneous actin nucleation. We could get acceptable fittings with other combinations of values for k_{FASB} and k_{FNUC} , for example, with $k_{FASB}=90 \mu\text{M}^{-1}\text{s}^{-1}$ and $k_{FNUC}=4.7\times 10^{-8} \mu\text{M}^{-3}\text{s}^{-1}$, indicating that the elongation rate and nucleation rate are highly correlated.

3.1.4. *Software ActinSimChem*

Although numerous software packages are available for biochemical kinetic modelling, no dedicated, Windows-based software which meets all the needs arising from analysis of any specific actin polymerization system is currently available. Therefore a new stand-alone software package, *ActinSimChem*, for the here presented Monte Carlo simulation of actin polymerization processes has been developed (for details see Appendix B). *ActinSimChem* provides the possibility for: i) switching between the nSRF and SRF models; ii) input/variation of the model parameters; iii) a compact set of the stochastic modelling algorithms (including the developed modifications of the Gillespie's "direct", the "first reaction", the "next reaction" methods); iv) simulation of actin polymerization (currently up to 21 molecular and 28 chemical actin-related reactions); v) graphical representation of simulation results; vi) storage of the results. The program and its manual are available as supplementary files.

3.1.5. *Concluding remarks*

We have developed and compared two stochastic simulation models of actin polymerization processes connecting multiple main actin polymerization-related biochemical reactions including spontaneous and enhanced actin nucleation, association/dissociation at filaments barbed and pointed ends, filament branching, fragmentation and annealing. Additionally the action of different actin-accessory protein that regulate filament dynamics, the structural composition of filaments and the distribution of filament lengths can be simulated. We evaluated the computational efficiency and simulation accuracy of the nSRF and SRF models, that differ in presentation of structural, i.e. ATP-hydrolysis-related, properties of actin filaments. In the majority of numerical tests, the nSRF model considerably saved computational time and still gave outcome characteristics at the same confidence level as the complete SRF model. This result realistically enables the nSRF model to be applied for experimental data fitting and for deriving reaction rate constants on the same

manner as reported in (Marushchak et al., 2007; Nazarov et al., 2006; Yatskou et al., 2003). For situations where ATP-actin monomers are limiting the SRF model needs, however, to be used.

The presented stochastic methodology forms a considerable improvement upon recently reported models (Brooks and Carlsson, 2008; Roland et al., 2008) in at least four ways. First, the number of already incorporated actin-polymerization reactions is very high. This allows evaluating outcome of complex biosystems closer to physiological situations, thus adding predictive power. Second, the Monte Carlo-based simulation algorithms are efficient and robust. Third, the open-architecture principle in the integrated modelling of actin-associated reactions events and filaments structures ensures flexibility in combination with a broad applicability. This architecture allows upgrading the utilised stochastic simulation algorithm for any newly-developed advanced modelling technique on the one hand, and permits further extension of the simulated system for additional actin-interacting proteins and polymerization mechanisms on the other hand. Fourth, we provide a free and user-friendly software package *ActinSimChem*, that contains the developed simulation algorithms. The package can be used to simulate *in silico* the numerical time-resolved outcome under form of the actin filament concentration and distribution of filament lengths for a complex set of actin-polymerization processes. This unique tool for simulation or fitting experimental data, will allow biologists comparing existing actin-polymerization systems and more easily design and interpret complex experiments in which more than “reaction” on actin is taking place.

As demonstrated potential of our model, we performed several numerical experiments on simulations of known and well-established actin polymerization systems. The results of these computer tests underscored important aspects of actin dynamics, namely that: i) under the conditions used, the reactions at pointed ends and by pointed-end capping proteins do not exhibit a significant effect on actin polymerization, unless pointed-end capping proteins work as nucleators; ii) the aging reaction has a minor effect on early state actin polymerization kinetics and only has an effect when equilibrium is reached; iii) nucleation and elongation are correlated when considering time evolution of actin in the filamentous form.

3.2 *Model of actin turnover for analysing FRAP data*

This section is based on the work published in the European Biophysical Journal (Halavatyi et al., 2010).

3.2.1. *Introduction*

The existing FRAP fitting models can be used for the analysis of protein diffusion (Ellenberg et al., 1997; Soumpasis, 1983) and binding reactions for one and several binding states, including cases where diffusion is a limiting factor for binding processes (Carrero et al., 2004; Mueller et al., 2008; Sprague et al., 2004). This methodology provides important quantitative information on molecular dynamics *in vivo*, such as diffusion constants, rate constants of protein (un)binding, (im)mobile fraction(s) of proteins, spatial localisation of the fluorescent protein analogues. Only a few studies at present used FRAP, associated with mathematical modelling, to gain quantitative information about actin polymerisation in living cells. Some of these studies have used binding approximation (Carrero et al., 2004; McDonald et al., 2006) to measure actin turnover in the nucleus or in cytoplasm (Campbell and Knight, 2007). The model of (Tardy et al., 1995) was established specifically for FRAP experiments with actin filaments and was applied for the fitting of corresponding datasets. The model accounts for several important factors, such as diffusion of actin monomers, but operates with a rate of exchange between two pools of actins to describe polymerisation reactions. In the work of (Lai et al., 2008), probabilities of conversion between filamentous and monomeric forms of actin were assumed to be functions of the distance from the leading edge. This assumption allowed obtaining an accurate fit for measured recoveries, but the mentioned dependences were not quantitatively linked to the spatial properties of filaments. Indeed, in all these models, the polarity and length of actin filaments as well as the dynamics of their pointed and barbed ends are neglected. Thus, they do not allow using values of fitted parameters as measures of actin gain/loss on the filament ends.

Direct visualisation of filaments and total internal reflection fluorescence microscopy (Fujiwara et al., 2002) together with stochastic simulation (Matzavinos and Othmer, 2007; Roland et al., 2008) have shown that both experimental procedures and models for data analysis should account for the length of filaments to estimate polymerisation rates. In addition, the filament length is an important

biophysical parameter of actin cytoskeleton mechanics. Results of FRAP experiments are potentially able to reflect the structure and turnover dynamics of actin filaments, but no dedicated mathematical treatment of FRAP data obtained with fluorescent actin analogues is available at the present date in the context of dynamic and structural properties of actin filaments. Thus, the formulation of new mathematical issues, which can be used to estimate the kinetic rate constants and filament length, are needed for FRAP studies of actin polymerisation.

In this chapter we present a novel mathematical model that can be used to fit the FRAP data obtained with GFP-actin and to calculate the FRAP response on actin polymerisation system with the parameters accounting for the average filament length ($\langle L \rangle$) and association/dissociation at the barbed and pointed ends of actin filaments (k_b^+ , k_b^- , k_p^+ , k_p^-). Unlike the previously published models, we show that FRAP curves may exhibit both non-linear and linear behaviours under some specific parametric configurations governed by the coefficients of elongation (v) and diffusivity (D), the parameters that are defined by the kinetic rate constants.

3.2.2. Kinetic model for fitting equation

Actin polymerisation leads to formation of long linear double helix filaments, 1-10 μm , with actin subunits spiral-bound around the axis of the filament (Pollard and Borisy, 2003). Both strands of the helix have the same polarity, so the two ends of the filament are structurally different, termed barbed (BE) and pointed ends (PE). Often a mathematical model of a filament is approximated by a linear chain of actin subunits (Fass et al., 2008). Under steady-state conditions, the average length $\langle L \rangle$ of filaments does not change in time and the actin dynamics of individual actin filaments is governed by treadmilling process, defining the actin turnover time (Matzavinos and Othmer, 2007). We would like to deduce a mathematical kinetic model to describe such an assay to be applied to FRAP experiments.

The scheme of the system formalization is shown in Fig. 3.6. A pool of free globular (G-) and filamentous (F-) actins with the constant concentrations c_m and c_f in time and volume is considered. An exchange between F-actin and G-actin is controlled by the turnover process, which is determined by the rates of actin association/dissociation at the BE and PE: k_b^+ , k_b^- , k_p^+ , k_p^- . We assume the following:

1. Since G-actins diffuse rapidly (McGrath et al., 1998), their spatial distribution is homogeneous.
2. Actin filaments do not diffuse. This is appropriate for many cell compartments because filaments are cross-linked into networks and linked by protein complexes to the plasma membrane.
3. Contribution of actin spontaneous nucleation in steady state is insignificant (Roland et al., 2008).
4. A spatial concentration of actin filaments is homogeneous.
5. The bleached area could be approximated by a cylinder with an axis perpendicular to the sample surface. Fluorescence intensity is measured in the thin layer inside this cylinder perpendicular to its axis by confocal microscope.
6. Disassembled actins leave a bleach spot instantly and irreversibly. This assumption is typically acceptable for modelling of the FRAP recovery in the reaction dominant regime, when a bleached spot has a rather small size and diffusion is fast compared to association/dissociation kinetics and the time scale of the FRAP experiment (Sprague et al., 2004).

At steady state, the full fluorescence recovery of the modelled system is merely due to the gain and loss of actin subunits. After laser illumination of a cell area, actin filaments may be composed of bleached and unbleached actin subunits whose distribution along the average filament length $\langle L \rangle$ is defined by the size of the bleached region. The resulting FRAP curve is calculated as a superposition of the probability events that any bleached actin disassembles before the time t at either end.

We applied a theory of stochastic processes to simulate the turnover of bleached/unbleached actins in the bleached area. The balance equation for the probability $p_i(t)$ of the chemical system state i in a closed volume can be given by the following master equation (van Kampen, 2007)

$$\frac{dp_i(t)}{dt} = \sum_{j=1}^J (-W_{ij}p_i(t) + W_{ji}p_j(t)), \quad (3.5)$$

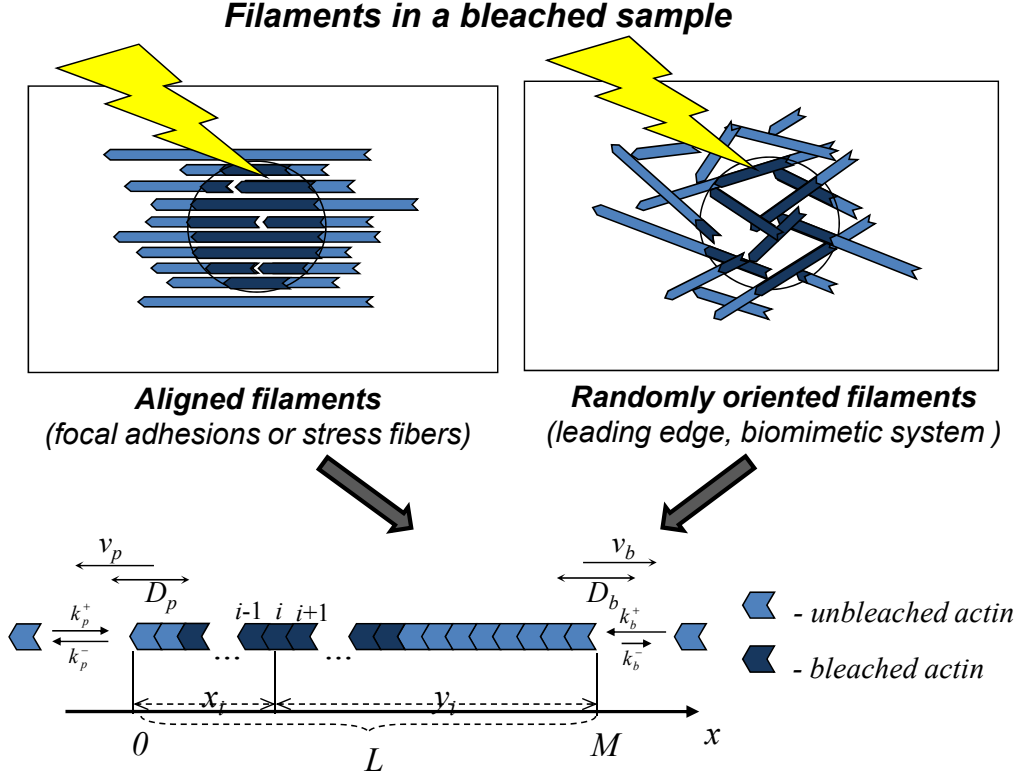


Figure 3.6: Schematic representation of a FRAP experiment with actin filaments.

Actin filaments are partially or completely bleached depending on the size of the bleached spot. Parameters are the association and dissociation rate constants at the BE and PE k_b^+ , k_b^- , k_p^+ , k_p^- , the average length of filaments $\langle L \rangle$, and the concentration of F-actin c_f .

where J is the total number of possible states; W_{ij} , W_{ji} are the transition probability per time unit from the states i to j and vice versa.

Without loss of generality, we start from consideration of a single bleached subunit in filament. Then, in Eq. 3.5 the state i is the position of the bleached subunit in relative to the PE. In the absence of the reactions at the BE, the state i can exchange with the neighbouring states $(i - 1)$ and $(i + 1)$ via association and dissociation reactions at the PE (Fig. 3.6a). The corresponding transition probabilities are $W_{i(i+1)} = W_{(i-1)i} = k_p^+ c_m$ and $W_{i(i-1)} = W_{(i+1)i} = k_p^-$ (Gadgil et al., 2005), and Eq. 3.5 becomes

$$\frac{dp_i(t)}{dt} = -(k_p^+ c_m + k_p^-) p_i(t) + k_p^+ c_m p_{i-1}(t) + k_p^- p_{i+1}(t), \quad i = 1, 2, \dots, M, \quad (3.6)$$

where M is the maximum number of actin subunits in filament and $p_0 = 0$. Equation 3.6 represents a set of M coupled differential equations. Assuming rather long filaments of 1 μm or more ($M > 400$), we can replace the probabilities $p_i(t)$ with a probability density function $\rho(x, t)$ of bleached actin subunit positions along filament. Applying a number of proper transformations, $p_i(t) = \rho(x_i, t)\delta$, $\rho(x_i, t) + \rho(x_{i+1}, t) \approx 2\rho(x_i, t)$, $\rho(x_{i+1}, t) - \rho(x_i, t) \approx \frac{\partial \rho(x_i + 0.5\delta, t)}{\partial x} \delta$, where δ is a distance between two neighbouring subunits in the filament and $x_i = i \times \delta$ is a position of the i -th bleached subunit in the filament, the system of Eq. 3.6 is approximated by a single continuous differential equation at the limit $M \rightarrow \infty$ as

$$\frac{\partial \rho(x, t)}{\partial t} \approx \frac{k_p^- + k_p^+ c_m}{2} \frac{\partial^2 \rho(x, t)}{\partial x^2} \delta^2 - (k_p^+ c_m - k_p^-) \delta \frac{\partial \rho(x, t)}{\partial x}, \quad (3.7)$$

where $\rho(0, t) = 0$ is an absorbing boundary condition (van Kampen, 2007). By introducing the parameter-dependent coefficients $v_p = (k_p^+ c_m - k_p^-) \delta$ and

$$D_p = \frac{k_p^- + k_p^+ c_m}{2} \delta^2 \text{ we obtain}$$

$$\frac{\partial \rho(x, t)}{\partial t} = D_p \frac{\partial^2 \rho(x, t)}{\partial x^2} - v_p \frac{\partial \rho(x, t)}{\partial x}. \quad (3.8)$$

Equation 3.8 is a Fokker-Plank equation used elsewhere to describe a diffusion type process (Gardiner, 2004). The term $v_p \frac{\partial \rho(x, t)}{\partial x}$ of Eq. 3.8 evaluates the average growth of the PE, and its coefficient v_p is the elongation rate of the PE. The value of v_p is positive when assembly reactions dominate over disassembly reactions leading to an elongation of the PE. It is negative in the opposite case. The term $D_p \frac{\partial^2 \rho(x, t)}{\partial x^2}$ describes a stochastic fluctuation of the filament length in time; its coefficient D_p has a meaning of the diffusion coefficient when Eq. 3.8 is treated as a one-dimensional diffusion. The variance σ_p^2 of the filament PE length is time-dependent

$$\sigma_p^2 = 2D_p t. \quad (3.9)$$

The solution of Eq. 3.8 satisfying the boundary condition (assumption 6) for a bleached actin subunit situated in the position x_0 at time $t = 0$ is given by Eq. 3.10:

$$\rho_{x_0}(x, t) = \frac{1}{2\sqrt{\pi D_p t}} \left(e^{-\frac{(x-x_0-v_p t)^2}{4D_p t}} - e^{-\frac{(x+x_0-v_p t)^2}{4D_p t}} \frac{v_p x_0}{D_p} \right). \quad (3.10)$$

The first term in Eq. 3.10 represents the equation of diffusion with a drift in the unlimited area. The second term accounts for the irreversible loss of the bleached particles when they dissociate at the filament ends.

Then, we calculate the probability function $P_p(x_0, t)$ of the random event that a bleached actin subunit at a fixed initial position x_0 is still associated with filament (or would not disassemble from the PE) by the time t after the bleach. This leads to integration of the probability density function $\rho_{x_0}(x, t)$ over the infinite range of the variable x :

$$P_p(x_0, t) = \int_0^\infty \rho_{x_0}(x, t) dx = \Phi\left(\frac{x_0 + v_p t}{\sqrt{2D_p t}}\right) - e^{-\frac{v_p x_0}{D_p}} \Phi\left(\frac{v_p t - x_0}{\sqrt{2D_p t}}\right), \quad (3.11)$$

where $\Phi(u) = \frac{1}{\sqrt{2\pi}} \int_{-\infty}^u e^{-t^2/2} dt$ is the cumulative distribution function for the standard normal distribution. If D_p is close to 0, the probability defined by Eq. 3.11 converges to unity.

Using a similar approach, we can calculate the probability function $P_b(y_0, t)$ for the BE in the absence of the reactions at the PE

$$P_b(y_0, t) = \Phi\left(\frac{y_0 + v_b t}{\sqrt{2D_b t}}\right) - e^{-\frac{v_b y_0}{D_b}} \Phi\left(\frac{v_b t - y_0}{\sqrt{2D_b t}}\right), \quad (3.12)$$

where $v_b = (k_b^+ c_m - k_b^-) \delta$ is the elongation rate at the BE, $D_b = \frac{k_b^+ c_m + k_b^-}{2} \delta^2$ is the diffusivity coefficient at the BE and y_0 is the position of a bleached actin subunit relative to the BE.

Assuming independent reactions at the BE and PE and replacing y_0 by $(\langle L \rangle - x_0)$, the total probability function for the bleached actin subunit to reside in the filament at time t is a product of the probability functions

$$P(x_0, t) = P_p(x_0, t)P_b(\langle L \rangle - x_0, t). \quad (3.13)$$

Integrating over all initial states, x_0 , of the bleached actin subunits in filament, we obtain

$$P(t) = \int_0^{\langle L \rangle} P(x_0, t) \varphi(x_0) dx_0, \quad (3.14)$$

where $\varphi(x_0)$ is a normalised distribution of the bleached states x_0 for all parts of the filaments inside the bleached region at the bleach moment ($t = 0$) and $\int_0^{\langle L \rangle} \varphi(\xi) d\xi = 1$.

When the ends of filaments are not bunched in the specific cell region, their various parts are situated randomly inside the bleached spot and $\varphi(x_0) = \langle L \rangle^{-1}$.

Finally, accounting for the steady-state concentrations of free actin proteins c_m and F-actins c_f we obtain the normalised FRAP recovery of the G- and F-actin

$$FRAP(t) = \frac{c_m}{c_m + c_f} + \frac{c_f}{c_m + c_f} (1 - P(t)) = 1 - \frac{c_f}{c_m + c_f} P(t). \quad (3.15)$$

The FRAP model was programmed in Mathematica 6.0 (Wolfram Research), and the corresponding routine *actinfrap.nb* is available at the website <http://actinsim.uni.lu/>.

To test the derived kinetic model, we applied a stochastic simulation algorithm (SSA), similar to that reported in (Fass et al., 2008) and (Roland et al., 2008). This stochastic approach provides precise information on the dynamics of G- and F-actin, including the structural compositions of actin filaments (Halavatyi et al., 2009). We adapted the SSA for the simulation of a FRAP experiment, considering bleached and unbleached actin subunits as independent molecular species. Synthetic datasets were generated to test and validate the deduced fitting equation. In particular, we estimated the time-resolved evolution of the F-actin concentration and the growth of the average filament length for the non-equilibrium initial system states and the

standard sets of reaction parameters. All FRAP curves were simulated for the steady-state phase and covered a broad range of the model parameters ($\langle L \rangle$, c_f , k_b^+ , k_b^- , k_p^+ , k_p^-).

3.2.3. Simulation results and discussion

Laser-assisted confocal microscopy is frequently used to visualise and analyse the dynamics of the actin cytoskeleton in living cells. Actin filaments of specific sub-regions of cells are grouped and cross-linked into bundles or networks. Such a bulk of filaments does not allow tracking individual filaments and changes in their structures. However, both filament lengths and their turnover properties are important characteristics of overall actin dynamics in cells. As shown above, FRAP curves depend on these quantities, which allow measuring cytoskeleton behaviour in different regions of the cell without changing cell properties.

Filaments may be oriented either in parallel to each other in bundles, for example at focal adhesion sites, or organised into branched networks in a lamellipodium. For a single filament only a part that is situated inside the bleached cylinder at the bleach moment may be bleached then. Because the resulting recovery is influenced by the spatial organisation of all the filaments in the region rather than the positions of individual filaments, we could account for the filament orientation relative to the bleached spot by the distribution function $\varphi(x_0)$ of bleached actin protomers along the filament (see Eq. 3.14). For most cases of bulk cytoskeleton in the cell regions where the ends of the filaments are not gathered, numbers of protomers corresponding to the different x_0 values inside the bleached spot are approximately equal, and this function can be represented by a uniform distribution.

Before the bleach, the system is in equilibrium, i.e. the probabilities for assembly and disassembly reactions at both ends of the filament are equal ($k_b^+ c_m + k_p^+ c_m = k_b^- + k_p^-$), the critical monomer concentration of actin or the steady-state monomer concentration showing the total equilibrium between association and dissociation processes is calculated as

$$c_m = \frac{k_b^- + k_p^-}{k_b^+ + k_p^+}. \quad (3.16)$$

Then the elongation rates v_b , v_p and diffusivity coefficients D_b , D_p defined by the rate constants are

$$\begin{aligned} v_b &= -v_p = \frac{k_b^+ k_p^- - k_p^+ k_b^-}{k_b^+ + k_p^+} \delta, \\ D_b &= \frac{2k_b^+ k_b^- + k_b^+ k_p^- + k_p^+ k_b^-}{2(k_b^+ + k_p^+)} \delta^2, \\ D_p &= \frac{2k_p^+ k_p^- + k_b^+ k_p^- + k_p^+ k_b^-}{2(k_b^+ + k_p^+)} \delta^2. \end{aligned} \quad (3.17)$$

Assuming independent reactions at the BE and PE and Eq. 3.9, we can estimate the variance σ^2 of the filament length as

$$\sigma^2 = \sigma_b^2 + \sigma_p^2 = 2(D_b + D_p)t = 2(k_b^- + k_p^-)\delta^2 t \quad (3.18)$$

Coefficients v_p and v_b are of opposite sign and equal absolute value, henceforth denoted as v , indicating that shortening from the PE will necessarily be compensated by growth of the BE. In the presence of any capped end, e.g. by a BE capper, the elongation rate v and the diffusivity coefficient D_b are 0. However, $D_p \neq 0$, and therefore the fluorescence recovery is not abolished. In the absence of capped ends, the elongation coefficient v is 0 only if (G-)actin critical concentrations at both filament ends, which are the local equilibrium conditions for BE and PE, are equal ($c_{c,b} \approx c_{c,p}$); then the following relation for the rate constants is relevant:

$$\left| \frac{k_b^-}{k_b^+} - \frac{k_p^-}{k_p^+} \right| = |c_{m,b} - c_{m,p}| \approx 0. \quad (3.19)$$

The fluorescence recovery relies on stochastic fluctuations of the filament length, characterised by the coefficients D_b and D_p , and exhibits an exponential-like curve.

If the value of v increases, the recovery is in the regime of intensive dissociation via the PE, and the FRAP exhibits a linear-like curve. Shortening of the PE is observed during the treadmilling process, and the number of disassembled actins may be estimated as the product of $v \times t$. This effect dominates over

disassembly due to diffusivity, characterised by standard deviation σ , increasing as a square root of the time ($\sigma \sim \sqrt{t}$; see Eq. 3.18). The slope of the normalised recovery in the linear regime is proportional to the ratio of the elongation rate v and the mean filament length $\langle L \rangle$. For such a treadmilling regime, bleached actins will dissociate mostly at the PE of filaments. The corresponding equation for linear FRAP recovery can be easily derived if the D_b value in Eq. 3.8 is set to 0 and the equations are solved with the same boundary conditions.

The following actin polymerisation reactions were implemented in the SSA to generate the synthetic data: (1) spontaneous and/or stimulated nucleation of actin filaments, (2) actin association at filament ends, (3) actin dissociation at filament ends. The reaction rates may vary depending on the actin-accessory proteins in the cells and cell environment (Lan and Papoian, 2008). For example, the actin nucleation mechanism may be accelerated by formin, capping protein, or by filament branching from a 'mother' filament by the Arp2/3 complex (Pollard and Borisy, 2003). The protein cofilin enhances filament depolymerisation by increasing the dissociation rate of ADP-actin from the PE (Van Troys et al., 2008). The actin turnover is governed by actin subunit gain and loss at the BE and PE, respectively. We took the values of the corresponding reaction rate constants close to those *in vitro* to generate the synthetic data (Kuhn and Pollard, 2005). The rate of actin dissociation at the PE was increased intentionally to simulate the effect of cofilin.

Taking a physiological range for parameters describing polymerisation mechanisms, we simulated the time evolution of the filament network from the pool of actin monomers. Our simulations were repeated for several nucleation rate constants to estimate further the effect of nucleating proteins on fluorescence recovery. We modelled three systems characterised by the nucleation rate constants $k_{nuc} = 1 \times 10^{-7}$, 1×10^{-6} , and $5 \times 10^{-6} \mu\text{M}^{-2}\text{s}^{-1}$, corresponding to spontaneous, capping-protein-stimulated or formin-stimulated actin nucleation respectively (newly created filaments are assumed to contain three actin protomers (Sept and McCammon, 2001)). Rate constants for the simulation of the stimulated nucleation are pseudo parameters and calculated as a product of the actual rate constant (Carlsson et al., 2004; Pring et al., 2003; Sept and McCammon, 2001) and the corresponding concentration of capping

protein or formin ($\sim 0.1 \mu\text{M}$). Results of the actin turnover simulations are shown in Fig. 3.7 and represent the average filament length as a function of time.

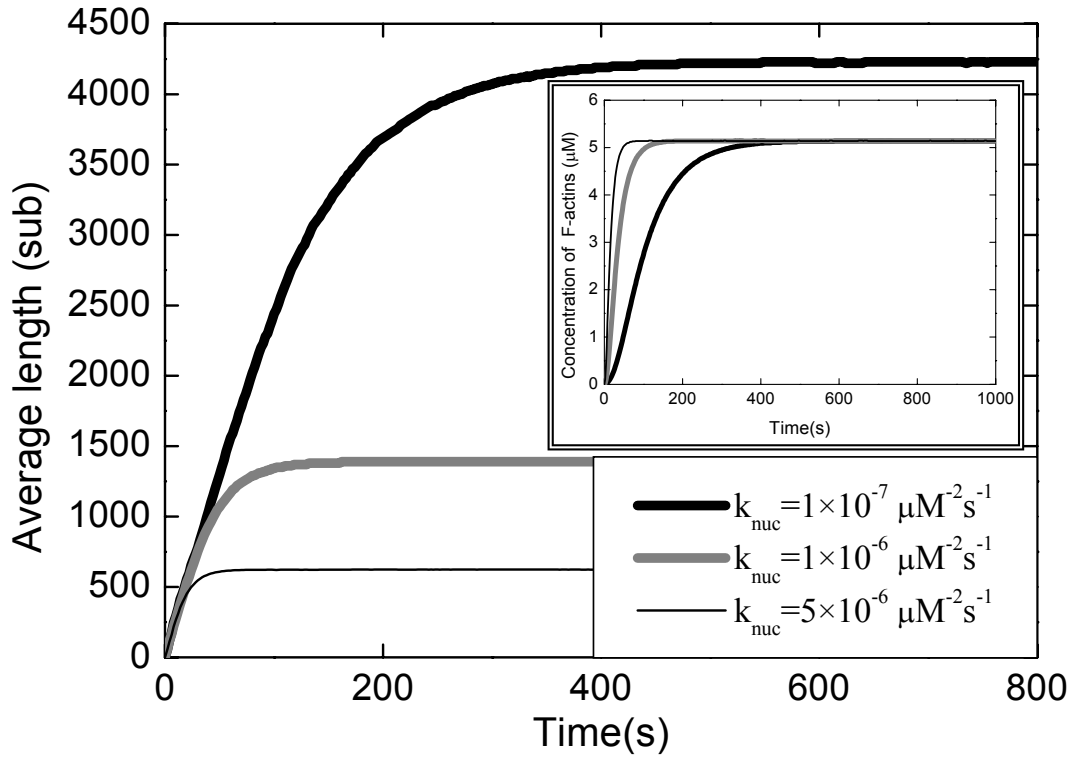


Figure 3.7: Results of stochastic simulation of artificial actin polymerisation systems at different nucleation rates.

The inset represents the increase in F-actin concentration as a function of time. Parameters are $k_b^+ = 10.0 \mu\text{M}^{-1} \text{s}^{-1}$, $k_b^- = 1.0 \text{s}^{-1}$, $k_p^+ = 0.5 \mu\text{M}^{-1} \text{s}^{-1}$, $k_p^- = 8.0 \text{s}^{-1}$, and the initial concentration of actin monomers is 6 μM .

The average length increased during the first phase and reached steady-state levels of 4200, 1400, and 600 subunits in accordance with the parameters $k_{nuc} = 1 \times 10^{-7}$, 1×10^{-6} , and $5 \times 10^{-6} \mu\text{M}^{-2} \text{s}^{-1}$. Decrease of the steady-state average length by increasing the nucleation rate is caused by the growing number of the nucleated filaments during earlier polymerisation phase. When the G-actin concentration is below 1.0 μM , the probability of actin nucleation becomes nearly negligible and turnover is due to the gain/loss of actin subunits at filament ends. In our simulations, the steady-state G-actin concentration was 0.86 μM (the initial G-actin concentration for all simulations was 6.0 μM), which is invariant by the nucleation rates (Fig. 3.7 ; inset). On the other hand, the value 0.86 μM appeared to be equal to the calculated critical concentration using Eq. 3.16 and the parameters of association/dissociation

reactions used for simulations: $k_b^+ = 10.0 \mu\text{M}^{-1}\text{s}^{-1}$, $k_b^- = 1.0 \text{s}^{-1}$, $k_p^+ = 0.5 \mu\text{M}^{-1}\text{s}^{-1}$, $k_p^- = 8.0 \text{s}^{-1}$. The obtained steady-state data and corresponding parametric configurations were further used to simulate the corresponding FRAP curves.

The FRAP curves were modelled for three average lengths of filaments at steady state, corresponding to various nucleation rates. The corresponding fits by the kinetic model are shown in Fig. 3.8a. Good fits were obtained indicating that our developed kinetic model could reproduce the results of stochastic simulations within an acceptable statistical error range (<5%). Being in excellent agreement as proved by the two modelling methods, our synthetic data showed an interesting and new effect of an actin turnover studied by fluorescence recovery: the FRAP curves were found to behave as a function of filament length, exhibiting faster recovery rates for systems with a short average filament length and slower recovery rates for systems with relatively long filaments. Importantly, we theoretically confirm experimental findings on accelerating the actin turnover in the presence of actin nucleating proteins (Lai et al., 2008). Additionally, the simulated fluorescence recovery shown in Fig. 3.8a exhibited a linear curve. Linearity is caused by the relatively high elongation rate $\nu = 7.6 \text{ sub s}^{-1}$ and the diffusivity coefficients 4.8 and 4.2 $\text{sub}^2 \text{s}^{-1}$ for BE and PE respectively (see Eq. 3.17). The FRAP curve is nonlinear when the absolute value of the elongation rate $\nu < 0.5 \text{ sub s}^{-1}$ (e.g. Fig. 3.8c).

To examine the effect of actin association and/or dissociation at either filament end on the FRAP response, we computed fluorescence recovery using the developed kinetic model for a range of the elongation coefficient ν , from 0.1 up to 10 sub s^{-1} , keeping constant values for other systems parameters: $D_b = 30.0 \text{ sub}^2 \cdot \text{s}^{-1}$, $D_p = 5.0 \text{ sub}^2 \cdot \text{s}^{-1}$, $c_m = 1.0 \mu\text{M}$, $c_f = 1.0 \mu\text{M}$, $L = 1000 \text{ sub}$. The results of the kinetic modelling are presented in Fig. 3.8b. The predicted FRAP curves differed noticeably, indicating strong dependence on the fitting parameter ν . As noted above, values of the elongation rate ν below 0.5 sub s^{-1} led to the non-linear curve and slow recovery. An increase in the parameter ν , indicating an acceleration of treadmilling, resulted in the nearly linear increase of the FRAP intensity. Fluctuations of the filament length, controlled by the diffusivity coefficients D_b and D_p for low ν values, had a weaker effect on the FRAP curves, as shown in Fig. 3.8c, and yielded a non-linear recovery.

We conclude that the FRAP curves may exhibit both a linear and non-linear behaviour, depending substantially on the elongation rate v .

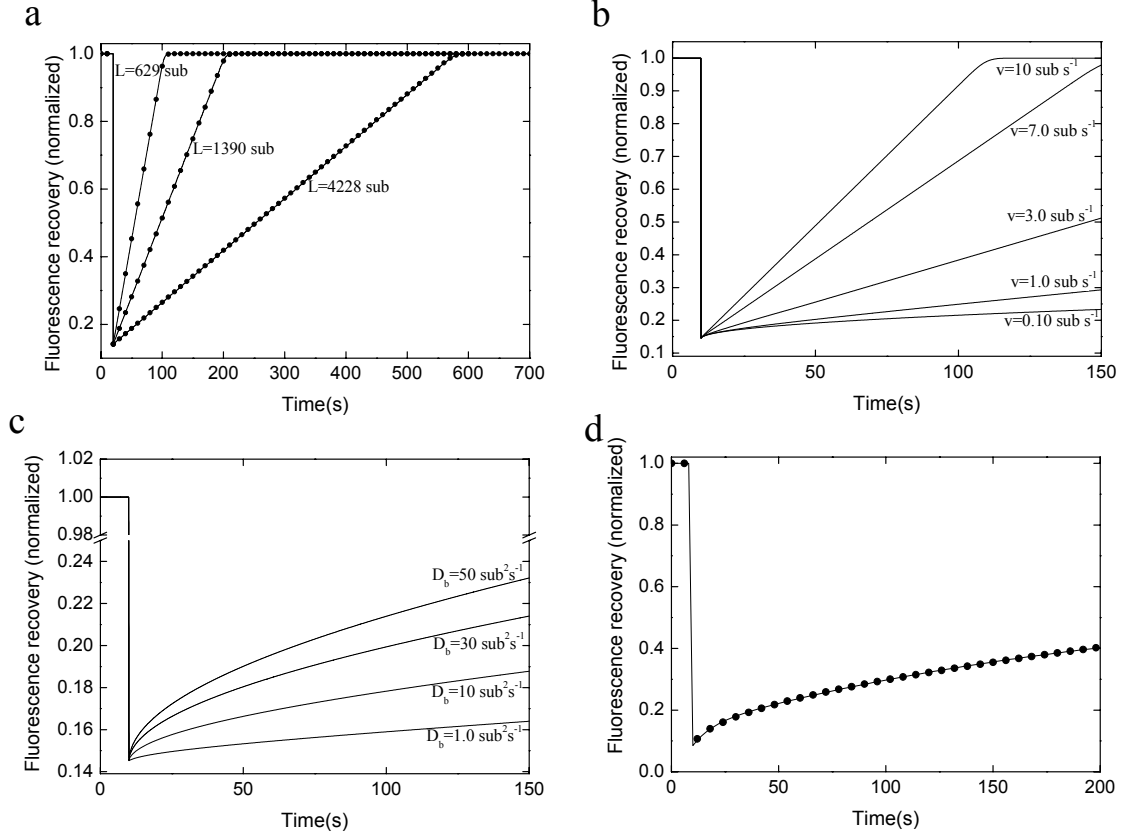


Figure 3.8: Model calculations of the FRAP curves for actin filaments under steady-state conditions.

a) Predicted FRAP using analytic (line) and stochastic simulation (dot) methods for different values of the average filament length $\langle L \rangle$, corresponding to the steady state mean lengths in Fig. 3.7 (slower recovery at the smaller nucleation rate), with parameters $k_b^+ = 10.0 \mu\text{M}^{-1}\text{s}^{-1}$, $k_b^- = 1.0 \text{s}^{-1}$, $k_p^+ = 0.5 \mu\text{M}^{-1}\text{s}^{-1}$, $k_p^- = 8.0 \text{s}^{-1}$, $c_f = 5.14 \mu\text{M}$. Dimensionality of $\langle L \rangle$ is 1 sub (subunit, $\sim 2.7 \text{ nm}$). b) Predicted FRAP for a range of the elongation rate v . Other kinetic parameters are $D_b = 30.0 \text{ sub}^2\cdot\text{s}^{-1}$, $D_p = 5.0 \text{ sub}^2\cdot\text{s}^{-1}$, $c_m = 0.17 \mu\text{M}$, $c_f = 1.0 \mu\text{M}$, $L = 1000 \text{ sub}$. c) Predicted FRAP for a range of diffusivity coefficients D_b . Other kinetic parameters are $D_p = 0.1 \text{ sub}^2\cdot\text{s}^{-1}$, $v = 0.1 \text{ sub}\cdot\text{s}^{-1}$, $c_m = 0.17 \mu\text{M}$, $c_f = 1.0 \mu\text{M}$, $L = 1000 \text{ sub}$. d) Predicted FRAP using the two-binding state (line) (Sprague et al., 2004) and the polymerization (dot) models. Parameters of the polymerization model are $D_b = 5.0 \text{ sub}^2\cdot\text{s}^{-1}$, $D_p = 5.0 \text{ sub}^2\cdot\text{s}^{-1}$, $c_m = 0.1 \mu\text{M}$, $c_f = 2.0 \mu\text{M}$, $L = 200 \text{ sub}$, $v = 0.1 \text{ sub}\cdot\text{s}^{-1}$. Parameters of the two-binding model are $c_1 = 0.74 \mu\text{M}$, $c_2 = 0.11 \mu\text{M}$, $k_{off1} = 0.0049 \text{s}^{-1}$, $k_{off2} = 0.11 \text{s}^{-1}$.

Finally, we investigated crossover of the developed kinetic model and the existing FRAP fitting models. The only match resulting in acceptable fits (an error $< 5\%$) was obtained when compared with a two-binding state model interpreted as the

outcome of the dynamically active PE and BE of filament and when our model was launched in the “non-linear” regime of the kinetic parameters ν , D_b and D_p (Fig. 3.8d). As follows from Eq. 3.18 the sum of diffusivity coefficients D_b and D_p is numerically equal to the sum of dissociation rate constants k_b^- and k_p^- multiplied by the distance between neighbouring subunits in filament $\delta = 1$ sub. This fitting parameter characterises the total effective depolymerisation of filaments and is used herein as a measure for comparison of two models. As an example for the comparison test, we generated a synthetic dataset with parameters $D_b=5.0 \text{ sub}^2\cdot\text{s}^{-1}$, $D_p=5.0 \text{ sub}^2\cdot\text{s}^{-1}$, $c_m=0.1 \text{ }\mu\text{M}$, $c_f=2.0 \text{ }\mu\text{M}$, $L=200 \text{ sub}$, $\nu=0.1 \text{ sub}\cdot\text{s}^{-1}$. Then we fitted the synthetic data by the two-binding state equation (Sprague et al., 2004). A sum of the unbinding rate constants obtained by fitting the two-binding state model is 0.12 s^{-1} , which is inconsistent with the value set in simulations. Therefore, the unbinding coefficients obtained by the two-binding state model can not be accepted generally as accurate estimations of the dissociation rates of F-actin unless being used as a rough approximation in some comparative studies.

Our model perfectly agreed with stochastic simulations and resulted in more confident data fitting and accurate estimation of the kinetic parameters than those done by previously reported models (Sprague et al., 2004; Tardy et al., 1995).

The presented model provides a relation between actin filament dynamics and the shape of FRAP curves. The application of our mathematical formalism for specific biological systems may require, however, an adaptation of the equations. For example, non-steady-state monomer concentration at the cell leading edge will cause various polymerisation rates at filament ends. In addition, special spatial ordering of filaments may require some modification of the function $\phi(x_0)$, where higher values of $\phi(x_0)$ should correspond to the parts of filaments situated inside the bleached spot. Our present results pave the way for future verifications of extensions of our approach by fitting experimental data and by modelling FRAP curves obtained in different areas in cells.

3.2.4. Conclusion

We have developed a mathematical model that will considerably improve analysis and interpretation of FRAP experiments carried out on actin-polymerisation

assays. As proved by the Monte Carlo simulations, this model provides unbiased reaction rate constants at the pointed and barbed ends of filaments and the average length of filaments. Our findings demonstrate that: (1) FRAP is a function of the average filament length, (2) FRAP is faster at higher actin nucleation rates, (3) the transition from the nonlinear to linear FRAP curves is mainly caused by the increase of the elongation rate v , (4) in contrast to existing FRAP models, our fitting equation correctly estimates parameters of polymerisation processes in different regimes of actin polymerisation dynamics. In the future, the model will allow for studying parameters regulating actin polymerisation *in vivo* and help establish predictive or fitting models for actin polymerisation mechanisms in living cells.

Chapter 4 Combining actin-based biomimetic assay with FRAP method to study spatially and temporarily controlled actin turnover

4.1 Introduction

The biochemical kinetics of the actin cytoskeleton is responsible for generating pushing and pulling forces directed to the inner surface of the plasma membrane or the outer surface of intracellular vesicles. There are two distinct mechanisms for force generation: i) walking of motor proteins, such as myosins, along the filaments create contractile forces in actin bundles (Gillo et al., 2009); and ii) polymerisation of cross-linked actin meshworks, such as those in lamellipodia, initiate membrane protrusions and pathogen motion (Mogilner and Oster, 2003). In both cases, simultaneous activities of several actin-binding proteins are required to initiate and maintain the sustainable movement of the membranes (Huber and Kas, 2011). Biochemical studies allowed to categorise these proteins as actin nucleators, leaky or permanent cappers, bundling proteins, depolymerising and severing agents and others (Carlier et al., 1997; Mullins et al., 1998; Schafer et al., 1996). Later, the actin-binding proteins, which control the generation of actin structures and regulate the associated biophysical phenomena, were identified and characterised by knock-out and knock-down approaches (Brieher et al., 2004; Gupton et al., 2005). However, the activities of these proteins in intracellular actin networks might significantly vary from those identified *in vitro* because actin-binding proteins interact between themselves and with upstream regulatory molecules (Blanchoin et al., 2000; Lai et al., 2008). The mechanical tensions in actin meshworks and bundles were shown to change the polymerisation/depolymerisation rates and the affinities of regulatory proteins for the cytoskeleton structures (Yoshigi et al., 2005). Therefore, the rates of biochemical reactions involved in actin turnover, which were identified with actin bulk assays or by observation of individual filaments, could not always be applied to quantitatively predict dynamics of the actin system in cells.

The development of biomimetic assays opened a great perspective to understand the coupling between the molecular regulation of actin networks and actin-based motility phenomena (Bernheim-Groswasser et al., 2002; Carlier et al., 2003). First, the minimal set of actin-binding proteins needed to initiate movement of

membranes and organelles were identified. Second, other proteins, that were assumed to regulate the mimicked actin structure, were added to the assay and characterised in a concentration-dependent manner (Giganti et al., 2005; Samarin et al., 2003). Third, relationships between actin biochemical regulation, speed of the protrusion and generated forces could be empirically studied (McGrath et al., 2003).

Having as an ultimate goal the development of methods for analysing the turnover of actin networks in living cells, we combined FRAP technique with a biomimetic motility assay. This assay allows to reconstruct the motility of intracellular pathogens, such as *Listeria monocytogenes*, through the use of artificial functionalised particles and a set of purified proteins (Le Clainche and Carlier, 2004). *Listeria* expresses ActA protein on one side of its outer surface, which stimulates Arp2/3-dependent polymerisation of a localised on this side elastic actin network (Loisel et al., 1999; Theriot et al., 1992). The tensile stress accumulates due to actin polymerisation at the surface of the bacteria and then releases by pushing forward the bacterial body. In contrast, when the spherical beads or lipid vesicles coated with ActA or the functional domain of WASP homogeneously, polymerisation of actin clouds is initiated all around the beads. These actin clouds are structurally similar to those on bacterial surface (Fradelizi et al., 2001; Noireaux et al., 2000). Notably, homogeneous coating of the beads with NPFs still leads to the protrusion of the bead in cell extracts or in an appropriate mix of actin and the regulatory proteins (Fig. 4.1c). The disruption of the initially formed spherical actin cloud and its further concentration to one side of the bead occurs because elastic stress is accumulated in the outer actin layers when they are pushed away from the bead center by newly polymerised parts of the network (van der Gucht et al., 2005). Further actin polymerisation on one side of the bead promotes its protrusion.

The minimal set of proteins for initiating and maintaining movement of bacteria or functionalised beads consists of the Arp2/3 complex, one of the capping proteins and an actin depolymerising protein of the ADF/cofilin family. The capping protein is needed to limit the length of filaments and promote the elongation of newly formed filaments in the vicinity of the beads. ADF/cofilin depolymerises older parts of the actin network and maintains high concentration of G-actin required for the assembly at the bead surface (Fig. 4.1a). The increase or decrease of the concentrations of

these proteins changes the speed of bacteria propulsion and the shape of the formed actin comets (Loisel et al., 1999; Wiesner et al., 2003).

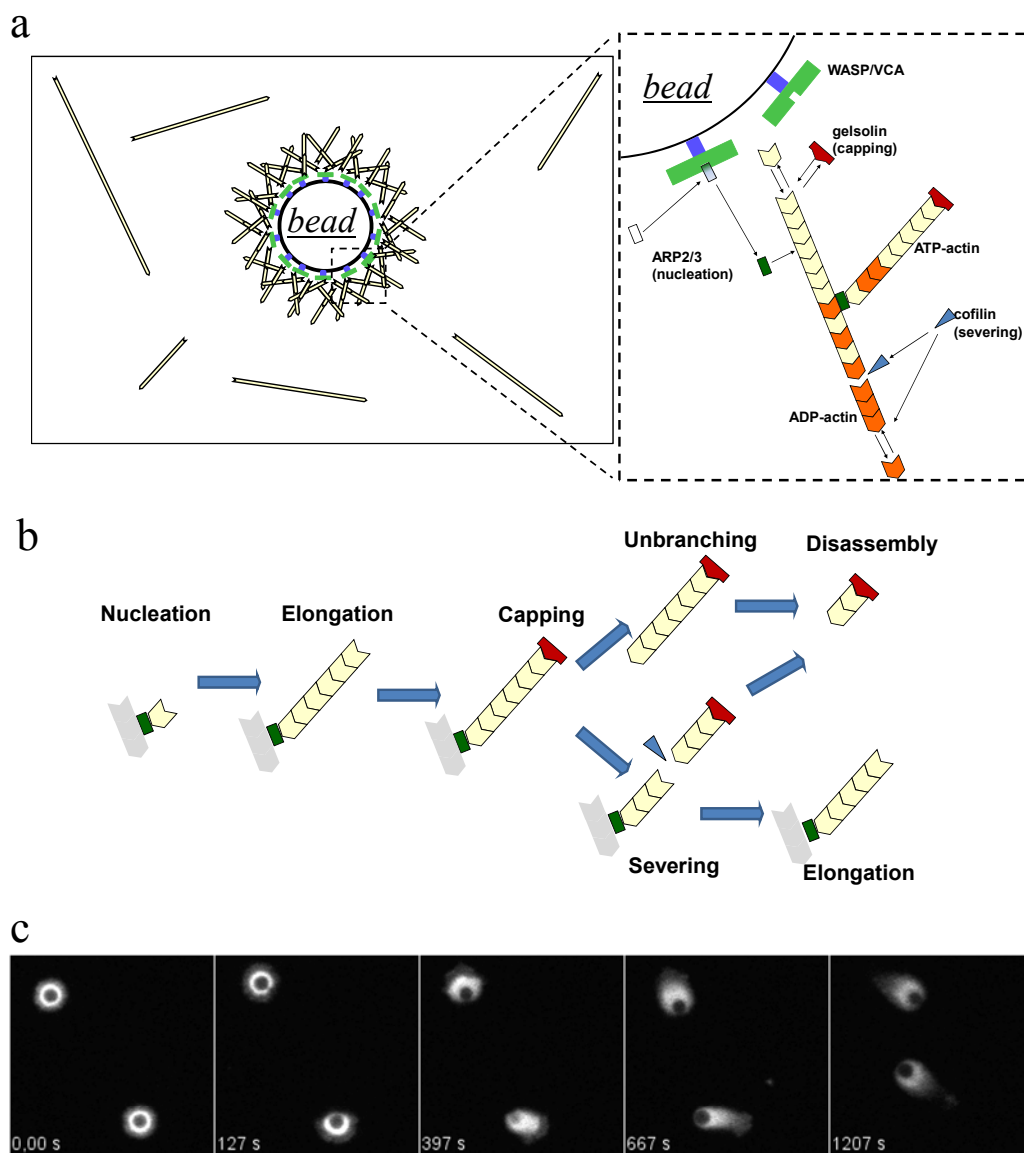


Figure 4.1: Actin-based biomimetic motility assay

a) Diagram representing core proteins and reactions in the assay; b) Scheme representing the filament cycle in the actin comet. The filaments are nucleated by Arp2/3 complex and elongate at the BEs until they are capped. The disassembly of filaments at PE is triggered by the disassembly of the Arp2/3 complex from daughter filaments (unbranching) or by severing of filaments; c) Time-course experiment with Alexa-488-labelled actin. The symmetrical shell breaks after some time leading to the development of the actin comet on one side of the bead.

The biophysical and biochemical properties of actin networks in this assay were extensively studied (Akin and Mullins, 2008; Paluch et al., 2006). Measurement

of the rates of particle motility showed that the concentration of each component of the motility mix needs to be optimised for the fastest propulsion. Too much or too little of Arp2/3, capping protein or ADF/cofilin would impair the formation of actin tails and bead movement. Studies of the comet structures (Plastino et al., 2004) and colocalisation analysis of actin with other proteins in the comets (Wiesner et al., 2003) provided indirect information about the filament structures in the clouds. Long comet tails were generated to measure their curvature and to analyse the intrinsic stresses and structures of filaments in the tail (Kang et al., 2010). Several experiments were designed to measure parameters of actin turnover in the comet tails. Some of them relied on the assumption, that the residence time of actin protomers is equal to the time needed by comet parts to propagate from their origin of polymerisation, the surface of the bead, to the far end of the tail (Kueh et al., 2010). However this assumption did not account for the possible remodelling of filaments in the middle of the comet, especially if free barbed ends might be created by severing events. The sequential incubation of functionalised beads in two motility mixes containing actin monomers, labelled with two fluorescent dyes, allowed to analyse the incorporation of actin monomers into preformed clouds (Akin and Mullins, 2008). However, such measurements are technically complicated and limited to particular system configurations.

Here we combined FRAP with quantitative image analysis to directly measure actin turnover in the actin clouds polymerised at the bead surface and to study spatial effects of actin monomer incorporation into the filament network. Using the approach we developed we analysed how capping and severing of filaments, working separately or in concert, control the turnover parameters of the dendritic actin network.

4.2 *Establishment of FRAP experiments with the biomimetic assay*

To install the protocol for FRAP experiments in the biomimetic system we used a well-established configuration of the actin-based motility assay that consists of polystyrene beads coated with the VCA subdomain of WASP and motility medium containing actin, Arp2/3 complex, gelsolin, cofilin and profilin (Fig. 4.1a) (Bernheim-Groswasser et al., 2002). Although profilin is not an essential protein for initiating the actin cloud on the bead surface and bead protrusion, it stimulates actin treadmilling in

the network by facilitating nucleotide exchange on the disassembled monomers and by preserving profilin-bound monomers from binding to the PEs of filaments (Didry et al., 1998).

The major challenge of my work was to setup the experimental procedures to measure actin turnover with FRAP in the formed actin clouds. In the classical assay, actin labelled with only one fluorescent dye is used to track the movement of the bead as well as morphological changes of the actin comets (Fig. 4.1c) (Paluch et al., 2006; Plastino et al., 2004). Depending on the composition of the motility mix, the actin comets on the surface of the beads can either rapidly reach the dynamic steady state with the assembly reactions completely compensated by disassembly, or polymerise into continuously growing comet tails until the motility medium is sufficiently depleted of G-actin (Bugyi et al., 2010). To distinguish between these possibilities and account for potential non-equilibrium actin turnover in further analysis, actin molecules labelled with two fluorescent dyes (Alexa-488 and TRITC-rhodamine) were added to the medium. While rhodamine was used for bleaching, the fluorescent signal in the second channel (Alexa-488) provided information about the total amount of polymerised actin (Fig. 4.2). The simultaneous observation of actin clouds in the bleached and non-bleached channels allowed us to distinguish between actin polymerised before and after the bleaching moment.

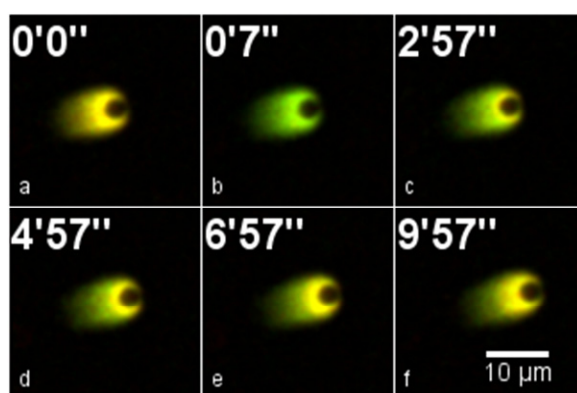


Figure 4.2: Time-course of a FRAP experiment with the actin-based biomimetic assay. Alexa-488 signal is shown in green and TRITC-rhodamine is shown in red. a) Prebleach image; b) Image acquired immediately after bleach; c-f) Observation of system dynamics. Actin polymerised before bleach is green. For actin polymerised after bleach green and red signals are merged (yellow).

The experimental system was tested extensively to determine conditions for time-lapse imaging which would not affect the investigated molecular processes. To

avoid photodamage observed in the first experiments, the motility medium was supplemented with ascorbic acid (vitamin C) - a scavenger of free oxygen radicals (Gerlich et al., 2001; Wagner et al., 2008). At the same time, the acquisition and photobleaching settings of the microscope were adjusted to minimize the amount of light to which the sample was exposed, while at the same time keeping the appropriate signal-to-noise ratio for further quantitative analysis (see section 2.1 and Appendix B for details of the experimental protocol).

4.3 *Development of tools for the analysis of spatio-temporal regulation of actin turnover*

To estimate kinetic parameters of actin turnover from the collected set of confocal images, we needed to quantify changes of fluorescent intensities in the bleached actin network. The bead and associated actin cloud are not immobile and can move out of the region, where bleaching has been applied, because of the protrusive force generated by actin assembly or diffusional movement. Therefore, calculation of FRAP recovery as the change of average intensity over time in the constant region could not be used.

To overcome this problem, a special procedure for quantifying FRAP recoveries from a set of confocal images was developed, implemented as ImageJ macro and tested on collected experimental data (Fig. 4.3a). According to this procedure, all images were first subjected to background subtraction and noise reduction with the low-pass filter. Then the position and the shape of the actin cloud were identified at every time-step by segmentation with a fixed threshold using images of the non-bleached channel. The identified regions of interest (ROIs) were used to quantify the evolution of total fluorescence intensity as a function of time for both channels. The turnover of actin, i.e. its exchange between polymerised and non-polymerised pools, was measured as normalised recovery of fluorescence intensity in the actin cloud. The calculated FRAP curves were then fitted using FRAPAnalyser software to estimate the recovery half-times and to characterise the total exchange of actin in the cloud.

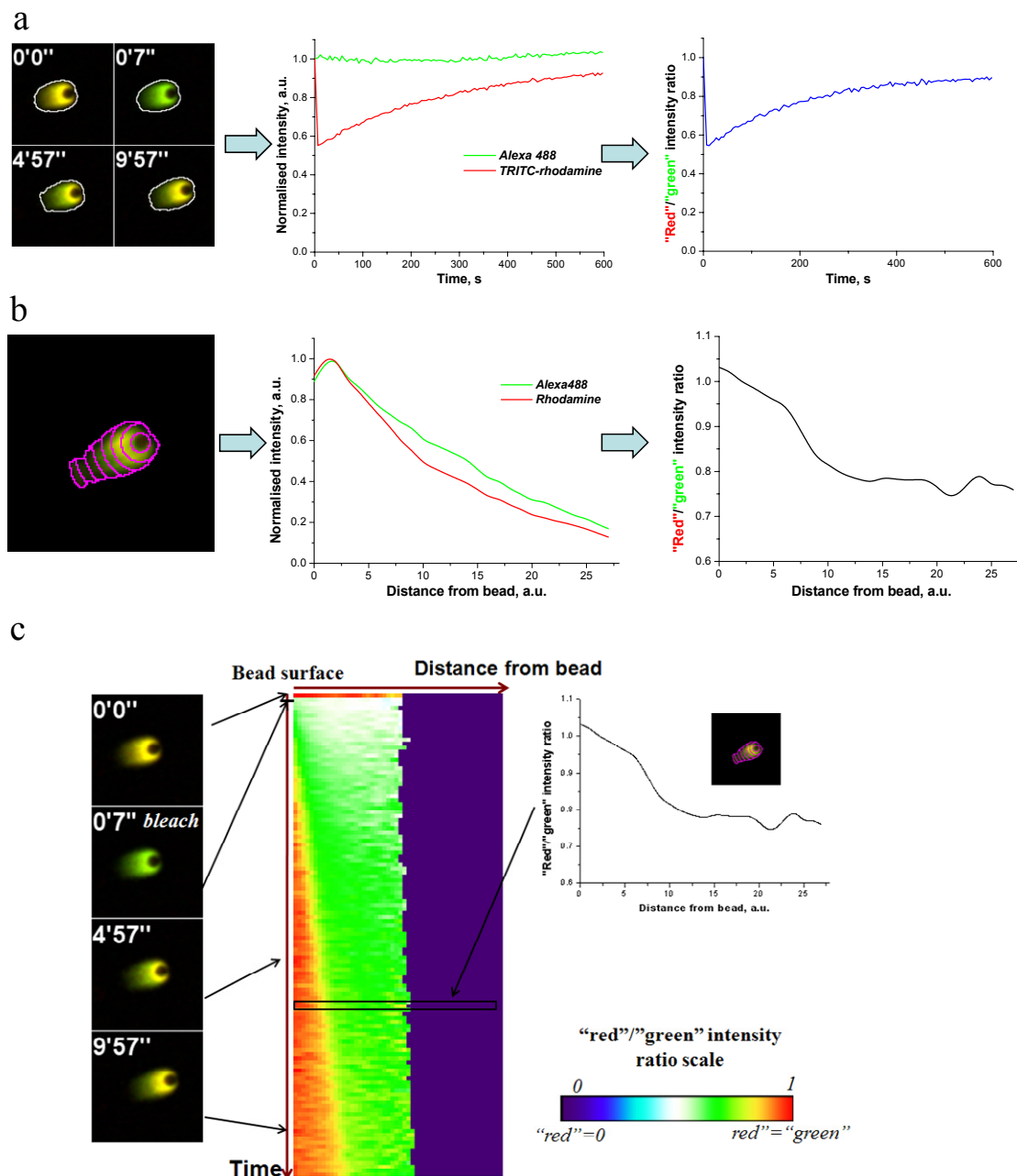


Figure 4.3: Quantification of actin exchange in time and space

a) Quantification of the total actin exchange in the cloud; b) Quantification of intensity profiles in actin comets depending on the distance from the bead surface; c) Kymograph representing the actin exchange in the clouds over time. For visualisation purposes ratios of fluorescence intensities are shown in pseudocolor.

Assembly and disassembly processes vary as a function of distance from the bead surface leading to inhomogeneous distribution of actin in the cloud. The analysis of the spatial inhomogeneity of actin exchange could provide more information about the structure of underlying filaments and the effects of actin-binding

proteins on filaments at different ages. We therefore developed another computational procedure for the analysis of the turnover at different distances from the bead surface using the collected FRAP data (Fig. 4.3 b,c). The bright field images, which were collected simultaneously with the fluorescent images, were used to automatically track the bead center over time. On each fluorescent image we created a special overlay that consisted of the overlaps of concentric rings surrounding the bead and the segmented shape of the cloud (Fig. 4.3b). The total fluorescence intensities were quantified for each obtained ROI to build intensity profiles along the tail for both acquisition channels. For each ROI, the ratio of the quantified intensities in bleached and non-bleached channels was calculated to estimate the fraction of bleached molecules, that were replaced by non-bleached molecules at a given distance from the bead surface.

To understand how actin exchange occurs in different parts of the cloud, all calculated profiles were put together in a kymograph (Fig. 4.3c), where horizontal coordinates correspond to the distances from the bead surface and vertical coordinates represent time points. Pixel intensities correspond to the ratio of intensities in bleached and non-bleached channels.

4.4 *Role of depolymerisation in the turnover of actin comets*

To test the developed experimental and analysis protocols, we varied the concentrations of the above mentioned proteins in the motility medium to quantify their influence on actin turnover rates.

In the first set of experiments, we analysed how cofilin influences the turnover of filaments in actin comet tails (Fig. 4.4). Initially, members of the ADF/cofilin family were reported to stimulate turnover of filaments by enhancing the rate of actin depolymerisation (Theriot, 1997). Thus, we expected that the presence of cofilin would lead to a faster exchange of actin in the clouds. Surprisingly, very slow actin turnover was observed for the cofilin concentrations below 5 μM . The dense actin shells that formed before symmetry breaking did not disassociate when actin comet tails elongated (Fig. 4.4a, upper left panel). The corresponding kymograph shows that no actin exchange occurred in the tail. However, the increase of cofilin concentration to 8 μM led to the depolymerisation of the older parts of the comet tails and significantly facilitated actin turnover. Actin monomers were incorporated in the

vicinity of the bead surface and the older parts of the tails were pushed away from the bead where they depolymerised. Further increase of cofilin concentration only slightly increased the turnover rate and facilitated propagation of the bleached zone throughout the comet tail.

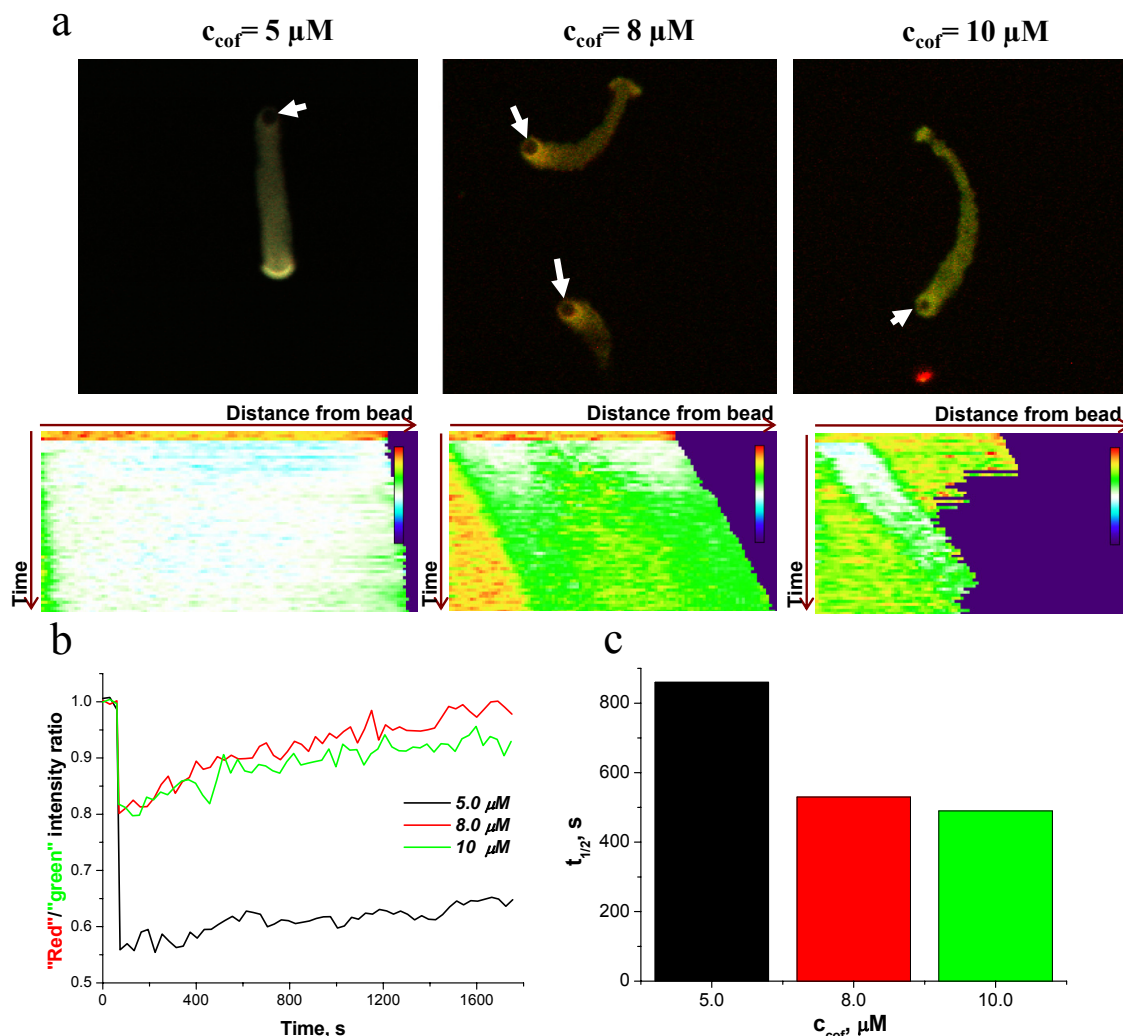


Figure 4.4: Effect of cofilin on actin turnover in the comet tail

Motility mixes contained 7.5 μM actin, 1 μM profilin, 0.1 μM gelsolin, 0.05 μM Arp2/3, 0.2% methylcellulose, and human cofilin as indicated. a) Representative pictures of the actin tails (upper panels) and corresponding kymographs (lower panels) for three cofilin concentrations. Positions of the beads are marked with white arrows; b) Quantified fluorescence recoveries; c) Estimated half-times of the recoveries in b.

To address whether the low depolymerising activity of cofilin observed in our first experiments depends on structural and functional differences between members of the ADF/cofilin family (Chen et al., 2004), we replaced human cofilin by *Arabidopsis* ADF1 in our assay and measured the corresponding rates of actin

turnover. Using the same concentration of ADF1 resulted in a 10 times decrease of the measured recovery half-time and much smaller steady-state clouds on the surfaces of the beads (Fig 4.5). The decrease of ADF1 concentration to 3.3 μM led to the growth of the clouds and an increase of the recovery half-time, which nevertheless was much smaller than in the presence of 10 μM cofilin.

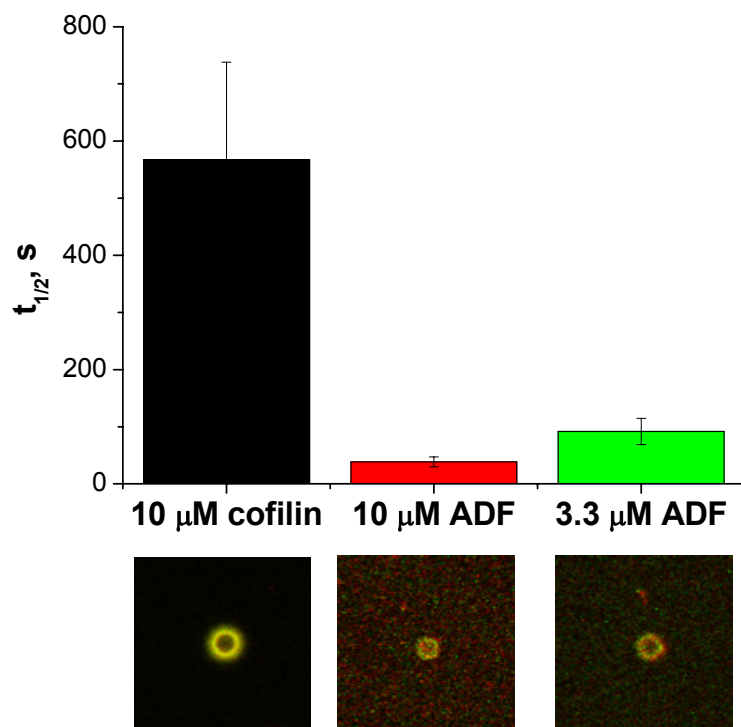


Figure 4.5: Comparison of depolymerising activities of human cofilin and *Arabidopsis* ADF1.

Motility mixes contained 7.5 μM actin, 2.5 μM profilin, 0.1 μM gelsolin, 0.05 μM Arp2/3 and human cofilin or *Arabidopsis* ADF1 as indicated. The histogram represents the half-times of fluorescence recoveries (mean \pm SD). The pictures below are representative images of the formed spherical clouds. The symmetrical cloud around the bead does not break (see Fig. 4.6).

The different effects of these two structurally similar proteins on actin dynamics most likely correspond to their distinctive capabilities to sever filaments or stimulate the disassembly of subunits from the filament ends (Chen et al., 2004). ADF was previously shown to depolymerise actin 4 times more efficiently in comparison to cofilin (Yeoh et al., 2002). Furthermore, ADF/cofilins might have other functions in actin cycle such as sequestering G-actin by staying associated with the disassembled monomers or stabilising filaments at high concentrations (Bamburg and Bernstein, 2010). ADF has a higher sequestering activity in comparison with

cofilin and could contribute to maintaining the pool of monomers required for the fast treadmilling on the bead surface. Cofilin is more capable to stabilise filaments than ADF, however we did not observe any stabilisation effect of cofilin even when the cofilin:actin stoichiometric ratio was higher than 1:1 (10 μM of cofilin and 7.5 μM of actin), which should have led to the stabilisation of filaments. The concentrations of ADF/cofilins required for depolymerising and stabilising activities were previously measured using actin-pyrene assay or single filament microscopy (Andrianantoandro and Pollard, 2006). In such an experiment the cofilin molecules have much better access to the filaments in comparison with the dense actin clouds in the biomimetic system. In agreement with our findings, Paluch *et. al.* observed protrusion of the beads without any significant depolymerisation of the comet tails for cofilin concentrations below 5 μM (Paluch *et al.*, 2006). We also do not exclude the possibility that cofilin stabilises actin filaments, which spontaneously polymerise in the motility medium, and therefore reduces the concentration of G-actin. That would explain why the increase of cofilin concentration above 8 μM (Fig. 4.4c) did not further stimulate the actin treadmilling process.

4.5 *Effect of capping on actin turnover*

Next we analysed how capping of the BEs influences actin kinetics in the assay and how it can interfere with depolymerisation by ADF/cofilin in the regulation of the structures and the kinetic properties of filaments. According to the funnelling model of actin treadmilling, the capping of filaments shortly after nucleation would limit the lengths of filaments and direct all G-actin towards a few uncapped BEs, stimulating their fast elongation and the nucleation of new filaments (Pantaloni *et al.*, 2001). The shorter filaments will disassemble faster, therefore capping should increase actin treadmilling by facilitating both polymerisation at BEs and depolymerisation at PE of filaments.

In our experiments we used gelsolin to modulate the capping of filaments. Gelsolin was first identified as a protein, which severs filaments *in vitro* and *in vivo* and remains associated with the newly created BEs (Janmey *et al.*, 1985). When these capped filaments disassemble from the PEs, gelsolin remains stably associated with one of the actin monomers (the disassociation of gelsolin from monomers or filaments in the cells is triggered by interaction with PIP_2) (Janmey and

Stossel, 1987). These gelsolin-actin complexes are not able to sever filaments but can cap free BEs. We incubated the motility medium for a short time before adding coated beads to ensure that the protein mix is at the dynamic equilibrium when the experiment is started. The gelsolin-to-actin stoichiometric ratios were relatively low (between 0.007 and 0.034) and no depolymerisation of actin comets was observed at low concentrations of cofilin regardless of the gelsolin quantities. This observation suggests that gelsolin affects the dynamics of filaments in our assay primarily by capping their BEs.

The increase of gelsolin concentrations in the assay resulted in a gradual increase of the measured actin turnover rate (Fig. 4.6), which is in agreement with the funnelling hypothesis. For low gelsolin concentrations, spherical actin clouds around the beads were formed and no symmetry breaking was observed. As shown on the kymograph, the incorporation of unbleached subunits in these clouds occurred not only in the vicinity of the bead, but also at the outer surface of the cloud. Fast symmetry breaking of the actin cloud, protrusive movement of the beads and the formation of elongated actin tails was observed for higher gelsolin concentrations. In these cases monomers incorporated primarily near the bead surface (see kymographs in Fig. 4.6a).

Collectively these observations support the hypothesis, that at low gelsolin concentrations the elongation of uncapped filaments leads to the formation of a dense network. The disruption of the symmetrical cloud is not accomplished in this case, because the network of long filaments requires a greater force to get broken. The sufficient stress for symmetry breaking is not accumulated because the available actin monomers are used for the elongation of filaments at the periphery of the actin cloud. On the other hand, efficient capping with higher concentrations of gelsolin led to a network of short filaments that rapidly broke under self-accumulated stress. The shortening of comet tails and very fast actin turnover for the highest gelsolin concentration emerge from the fast disassociation of the short filaments.

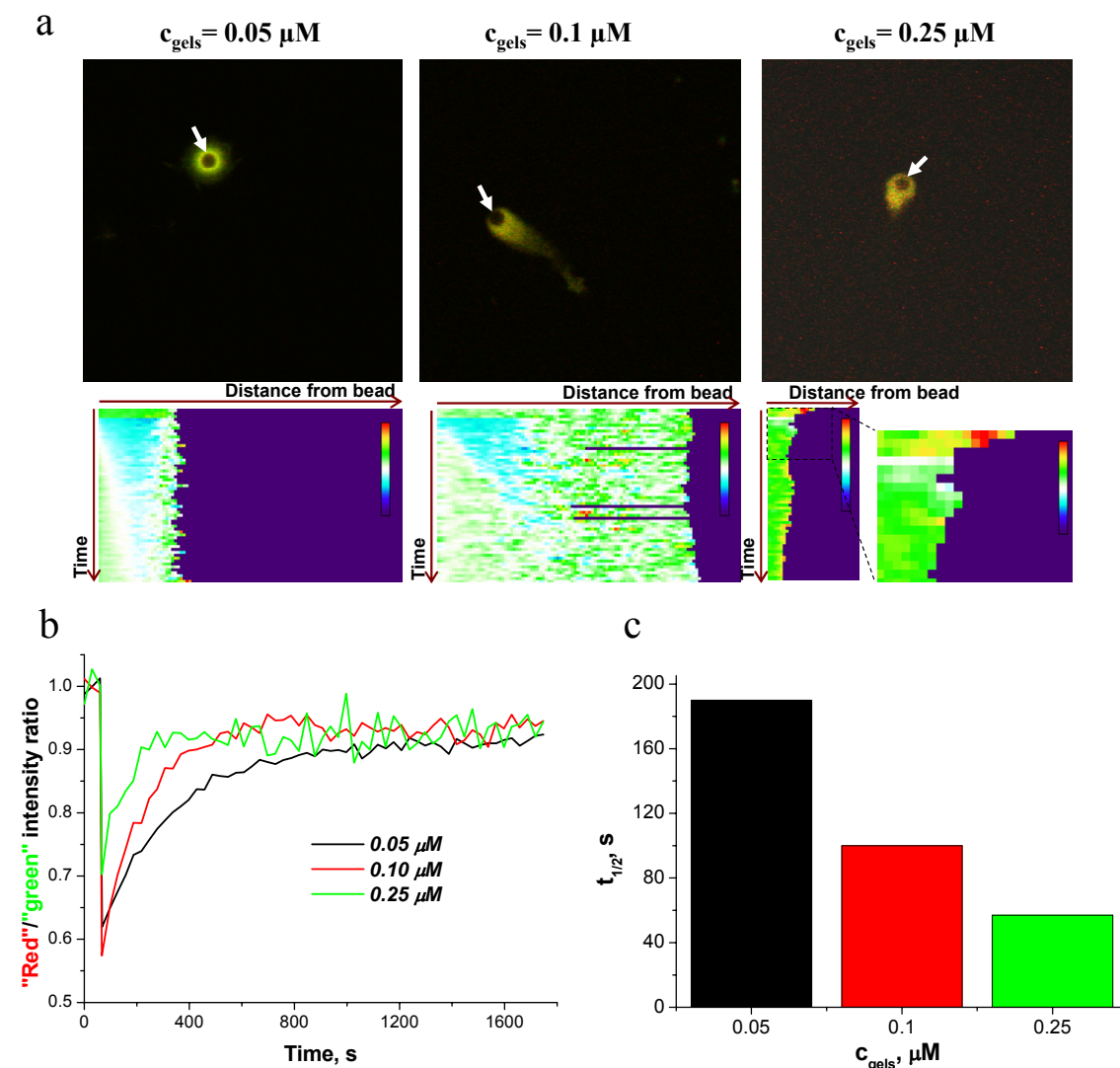


Figure 4.6: : Effect of gelsolin on actin turnover in the presence of human cofilin
Motility mixes contained $7.5 \mu\text{M}$ actin, $1 \mu\text{M}$ profilin, $10 \mu\text{M}$ human cofilin, $0.1 \mu\text{M}$ Arp2/3, 0.2% methylcellulose, and gelsolin as indicated. a) Representative pictures of the formed actin tails (upper panels) and corresponding kymographs (lower panels) for three different gelsolin concentrations. Positions of the beads are marked with white arrows; b) Quantified fluorescence recoveries; c) Estimated half-times of the recoveries shown in b.

Funnelling of actin polymerisation by capping depends on the disassembly of filaments (Carlier and Pantaloni, 1997). Since we have shown, that ADF and cofilin differ from each other in their capabilities to depolymerise actin in our assay, we decided to test how the turnover of actin comets is affected by these two proteins in the presence of different gelsolin concentrations. As shown in Fig. 4.7, variation of capping activity had almost no effect on the recovery half-time in the presence of ADF1. However in the presence of cofilin, the actin turnover in the clouds was faster

for high gelsolin concentrations (Fig. 4.6c and 4.7). These results indicate, that in case of slow depolymerisation of actin shells by cofilin the capping of filaments is the rate limiting factor for treadmilling. The disassembly of filaments by ADF1 was most likely fast enough to meet the needs of actin monomers for nucleation or elongation of filaments. Alternatively, the sequestering activity of ADF might be responsible for impairing the binding of actin subunits to the BEs in the clouds and therefore preventing acceleration of treadmilling when the capping activity is increased (Yeoh et al., 2002). Further tests are required to identify which of these two hypotheses is correct. In particular, simultaneous variations of the quantities of Arp2/3 and ADF/cofilin will help to clarify how and to what extent the change in the nucleation activity affects actin turnover under different depolymerising conditions.

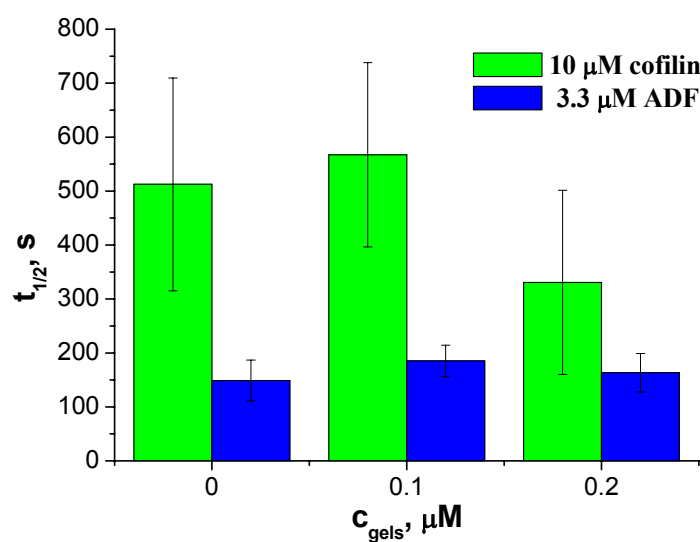


Figure 4.7 : Differential effect of gelsolin on actin turnover in the presence of ADF or cofilin.

Motility mixes contained 7.5 μM actin, 2.5 μM profilin, 0.05 μM Arp2/3, gelsolin and human cofilin or *Arabidopsis* ADF1 as indicated. The half-times of fluorescence recoveries in the presence of cofilin or ADF1 as a function of gelsolin concentration are represented (mean \pm SD).

4.6 Concluding remarks

In this work package we combined an actin-based biomimetic motility assay with FRAP methodology to study quantitatively the effect of actin-binding proteins on the turnover of dendritic actin meshworks. The computational tools that we have developed do not only allow to measure actin exchange between polymerised and non-polymerised pools, but they also enable us to characterise spatial properties of

actin polymerisation dynamics. Our approach can be used to test the activities of other actin-binding proteins in the assay. Because the structures of actin clouds created on the surface of the beads are similar to those in living cells, our protocol can be applied for comparing polymerisation kinetics in these two experimental systems and for analysing, how different actin-binding proteins regulate actin turnover in time and space.

Using our method, we analysed how the capping activity of gelsolin and the depolymerising activity of ADF/cofilin could support actin treadmilling in the assay. The simultaneous modulation of these two components has shown that their orchestrated work, rather than individual activities, should be considered to study rate limiting factors of actin turnover and its spatial regulation. Further experiments with simultaneous changes of capping, depolymerising and nucleating proteins are necessary for the comparison of experimental results with the detailed mathematical models describing actin regulation (see discussion in Chapter 6).

Chapter 5 Analysing the dynamics of the actin cytoskeleton at focal adhesions of living cells

5.1 Zyxin and Tes - focal adhesion proteins regulating actin dynamics (introduction)

Focal adhesions (FAs) link the actin cytoskeleton to the extracellular environment and play a key role in cell attachment and spreading. Perturbation of cell adherence changes motile properties of the cells and can lead to pathological situations such as migration of primary tumours. FAs also work as molecular sensors, responsible for transmitting extracellular signals to the cell interior. More than 100 FA proteins have been identified and characterised biochemically. Many of them were found to interact with multiple binding partners via their structural domains. However the roles of various FA proteins in the regulation of the actin cytoskeleton linked to FAs, are far from being understood (Lo, 2006; Wolfenson et al., 2009).

Among other proteins localised in FAs, LIM domain proteins (named after the first three identified proteins: Lin-11, Isl-1, Mec3) have captured the attention of researchers for more than a decade, because some of them were shown to have properties of tumour suppressors and to regulate actin-dependent motility (Kadmas and Beckerle, 2004). Zyxin is the founding member of LIM domain proteins that regulate the actin cytoskeleton (Amsellem et al., 2005). Zyxin can stimulate actin polymerisation independently of well characterised nucleators, such as Arp2/3 complex and formins (Fradelizi et al., 2001). Zyxin is unable to bind actin directly, but serves as a molecular scaffold to recruit actin-binding as well as other FA proteins. Among others, zyxin can recruit VASP to FAs and promote VASP-dependent actin filament elongation (Drees et al., 2000; Fradelizi et al., 2001). In FAs zyxin affects actin dynamics in a force-dependent manner (Hirata et al., 2008a; Hoffman et al., 2012), which suggests that changes of its function, and probably of its associated molecular partners, occur at different stages of FA cycle.

Tes is another FA protein of the same family possessing, like zyxin, three LIM domains in its C-terminal part (Fig. 5.1a). Initially, Tes was identified as a potential tumour suppressor (Tobias et al., 2001). Indeed, overexpression of Tes can suppress growth of cancer cell lines as well as induce senescence in some of these cells. Furthermore, overexpression of Tes can facilitate cell spreading, and affect the morphology of stress fibers (Coutts et al., 2003; Garvalov et al., 2003). Loss of Tes

gene expression significantly increases the chance of cancer development in mice (Drusco et al., 2005).

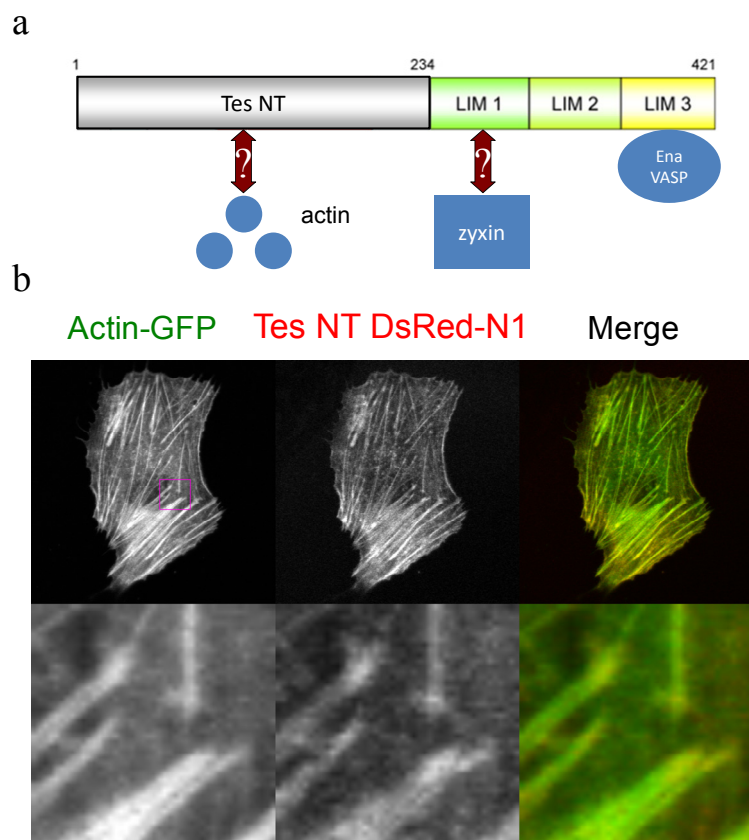


Figure 5.1: Tes is a focal adhesion protein that interacts with actin and other actin-binding proteins

a) Domain structure of Tes. The binding sites of actin, zyxin and Ena/VASP proteins are shown. Arrows with question-marks indicate interactions, the role of which in cytoskeleton dynamics at FAs was addressed in this work; b) GFP-actin and Tes NT DsRed-N1 in a Vero cell. The bottom panel shows an enlargement of the part of the cell surrounded by the rectangle. Tes NT colocalises with actin in FAs and to a lesser degree in stress fibers in agreement with Garvalov and coworkers (Garvalov et al., 2003).

In vitro and *in vivo* experiments have shown that Tes interacts with various actin-associated proteins. Previous studies carried out in our lab have shown that the N-terminal region of Tes (Tes NT) directly interacts with actin *in vitro* and can facilitate actin polymerisation. In addition, Tes NT associates with several FA proteins, such as α -actinin, paxillin and talin (Coutts et al., 2003; Garvalov et al., 2003). The C-terminal region of Tes, which consists of LIM domains (Tes LIM), is able to interact with Mena, VASP and zyxin (Boeda et al., 2007; Garvalov et al., 2003). Zyxin has been proposed to recruit Tes to FAs by binding its LIM1 domain (Garvalov et al., 2003). According to this hypothesis, in the cytoplasm Tes is present

in a closed conformation that cannot bind to zyxin. The mechanism which switches Tes from the closed to the open conformation, recruitable by zyxin, is not yet known.

We aimed at studying the role of the interactions between zyxin, Tes and actin in the regulation of cytoskeleton dynamics at FAs. To this end, we carried out several series of FRAP experiments with fluorescently labelled actin and zyxin in FAs of cells, where Tes, zyxin or their mutants were either overexpressed or silenced with siRNA. To account for the intercellular or intracellular variability of protein dynamics in different FAs, at least 15 recovery curves per condition were acquired and each curve was analysed individually to estimate appropriate turnover parameters. Three bleaching iterations resulted in complete bleach of FAs. On the images, acquired immediately after the bleach, the intensity inside the bleached spot was homogeneous, indicating the presence of only diffusing non-bleached molecules. Rapid fluorescence recovery during the first two seconds after the bleach due to the diffusion was followed by much slower recovery due to reaction kinetics (see Fig. 5.2a as an example). Therefore first two data points on each FRAP curve were excluded from the analysis.

Zyxin undergoes binding/unbinding kinetics at FAs, hence the corresponding recovery curves were fitted with Eq. (5.1), which reflects a one-binding state FRAP model in a reaction-dominant (diffusion-uncoupled) regime (Sprague et al., 2004):

$$FRAP(t) = F_{eq} \left(1 + \frac{k_{on}}{k_{off}} \left(1 - e^{-k_{off}t} \right) \right) \quad (5.1)$$

where F_{eq} – the fraction of unbound zyxin molecules; k_{on} – pseudo-binding rate constant; k_{off} – unbinding rate constant.

Because of the currently limited knowledge about mechanisms that control spatial organisation and dynamics of actin filaments in FAs, we estimated only the fractions of polymerised actin (c_{eq}) and turnover rates (k_t) from those FRAP curves by fitting them with Eq. (5.2):

$$FRAP(t) = (1 - r) \left(1 - c_{eq} e^{-k_t t} \right) \quad (5.2)$$

where factor r accounts for incomplete recoveries.

5.2 *Role of Tes in actin turnover at focal adhesions*

5.2.1. *Overexpression of Tes stimulates actin polymerisation at focal adhesions*

Experiments previously carried out in the host lab indicated that Tes NT, which stimulates actin polymerisation *in vitro*, is also able to affect actin dynamics in cells (Medves *et. al.*, submitted). To validate these findings and to explore the properties of actin turnover at individual FAs, we conducted a new series FRAP experiments with GFP-actin in presence or absence of Tes NT DsRed. Co-transfection of GFP-actin and Tes NT DsRed showed that these proteins co-localise predominantly in FAs and less in stress fibers (Fig. 5.1b). Using the developed computational tools we estimated parameters of actin turnover for each FRAP curve (Fig. 5.2). Higher fraction of polymerised actin and slower turnover were observed in cells expressing Tes NT DsRed in comparison with control cells expressing DsRed. Interestingly, FAs and stress fibers were thicker in Tes NT cells, leading to the hypothesis, that accumulation of actin in stress fibers induced by Tes is coupled to the inhibition of turnover via enhanced polymerisation or stabilization of actin filaments.

In spite of faster actin turnover in the control cells, the corresponding recovery curves did not reach prebleach levels during the observation time period. Rapid recovery at the tips of FAs and absence or very slow recovery in their parts situated closer to stress fibers was observed (Fig. 5.2c). Fluorescence in Tes NT transfected cells recovered almost completely. The recovery was also faster at the tips of FAs, however it propagated through the whole bleached spot. In future, the spatial analysis of actin exchange in FAs similar to those performed with the biomimetic assay will help to understand Tes-induced changes of the structural properties of actin filaments.

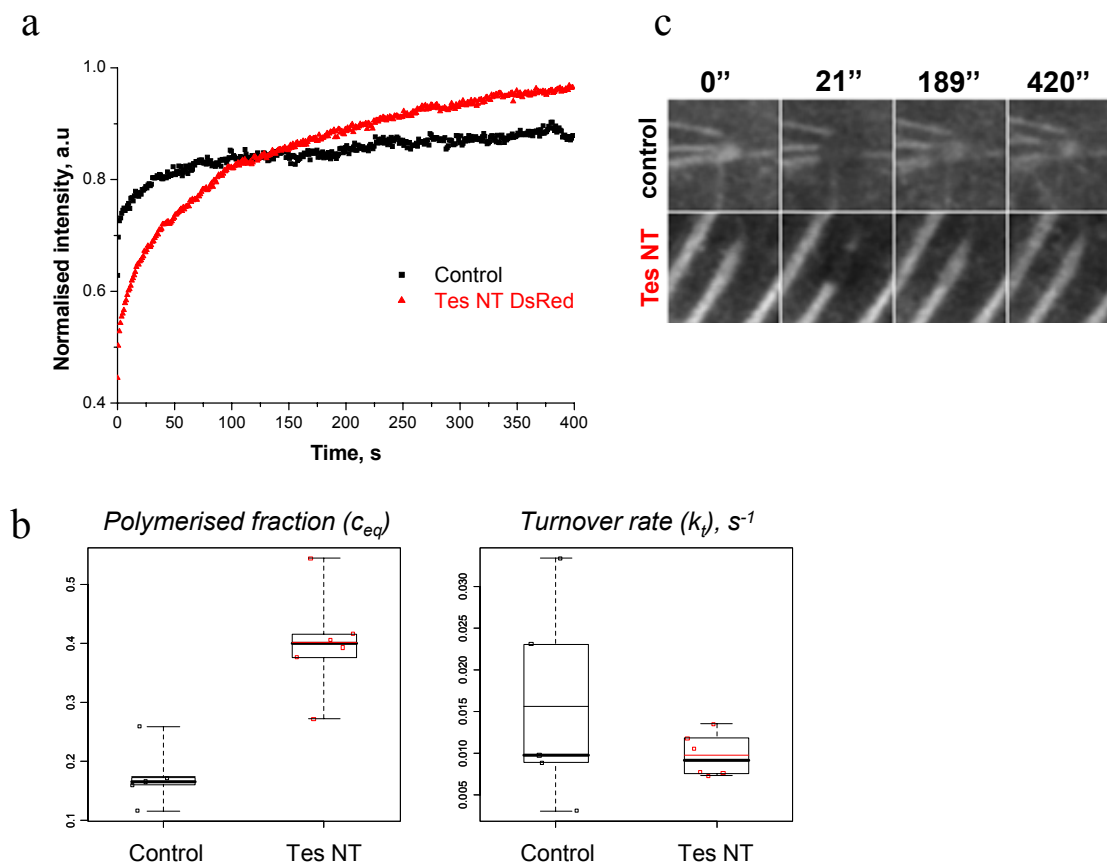


Figure 5.2: Results of FRAP experiments with GFP-actin at FAs in Vero cells expressing DsRed (control) or Tes NT DsRed.

a) Normalised and averaged recovery curves; b) Boxplots for the estimated parameters of actin turnover: polymerised fraction c_{eq} and turnover rate k_t . Points represent individual measurements; c) Time course of FRAP experiment with FAs in control cells (*upper panels*) and Tes NT transfected cells (*lower panels*).

5.2.2. Silencing of endogenous Tes slows down actin turnover

Furthermore, we wanted to investigate if the stimulation of actin polymerisation by Tes NT represents indeed a physiological function of Tes. Therefore we performed FRAP analysis in cells where endogenous Tes was silenced by siRNA (Fig. 5.3). The results revealed little difference when compared to control cells. This may be due to the heterogeneity of the analysed cells or the incomplete knock-down of endogenous Tes. Estimation of turnover parameters for each recovery independently resulted in slightly lower c_{eq} and k_t values for Tes siRNA cells in comparison with control cells. Silencing of mDia2 formin, a well characterised actin nucleator localised in FAs (Gupton et al., 2007), had a similar effect on actin dynamics (data not shown). Therefore, we assume that turnover is slowed down

because of a slower actin assembly rather than enhanced polymerisation/stabilisation of actin filaments as in the case of Tes NT overexpression.

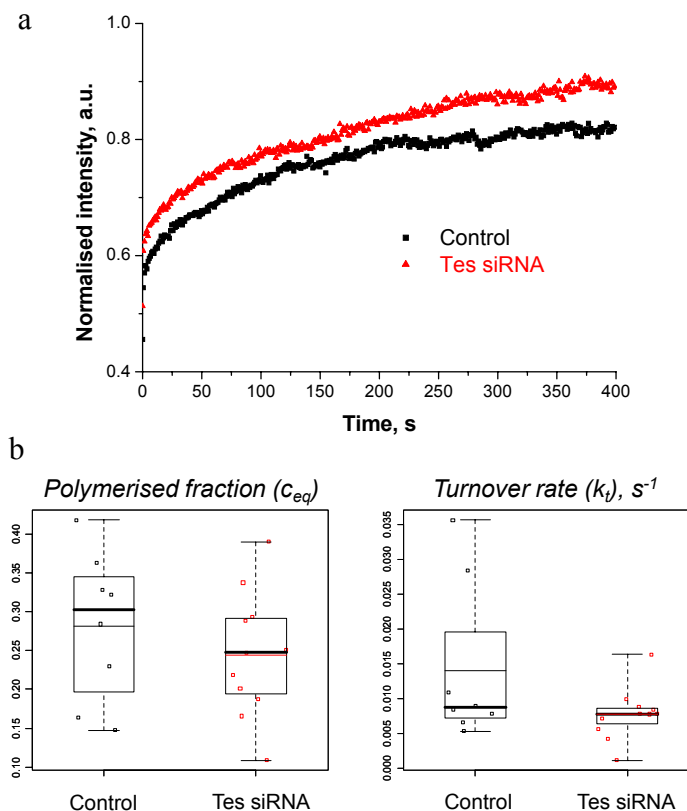


Figure 5.3: Results of FRAP experiments with GFP-actin at FAs in Vero cells expressing control siRNA (control) or Tes siRNA.

a) Normalised and averaged recovery curves; b) Boxplots for the estimated parameters of actin turnover: polymerised fraction c_{eq} and turnover rate k_t . Points represent individual measurements.

5.3 Role of zyxin-Tes interactions in the regulation of the cytoskeleton at focal adhesions

5.3.1. The binding kinetics of zyxin in focal adhesions accelerates upon loss of its interaction with Tes

As follows from the previous sections, Tes is one of the proteins that stimulate actin assembly at FAs. Since the interaction with zyxin influences the recruitment of Tes to FAs (Griffith et al., 2005), we decided to analyse if this interaction plays a role in regulating actin cytoskeleton dynamics. To this end, a cell line stably expressing zyxin silencing HairPin siRNA (HeLa B9) was generated in the lab. At the same time

plasmids for two zyxin variants that are not targeted by zyxin siRNA were constructed: i) zyxin wild type (WT) and ii) zyxin mutant (MT) with the invalidated Tes interaction motif (Fig. 5.4 and section 2.2).

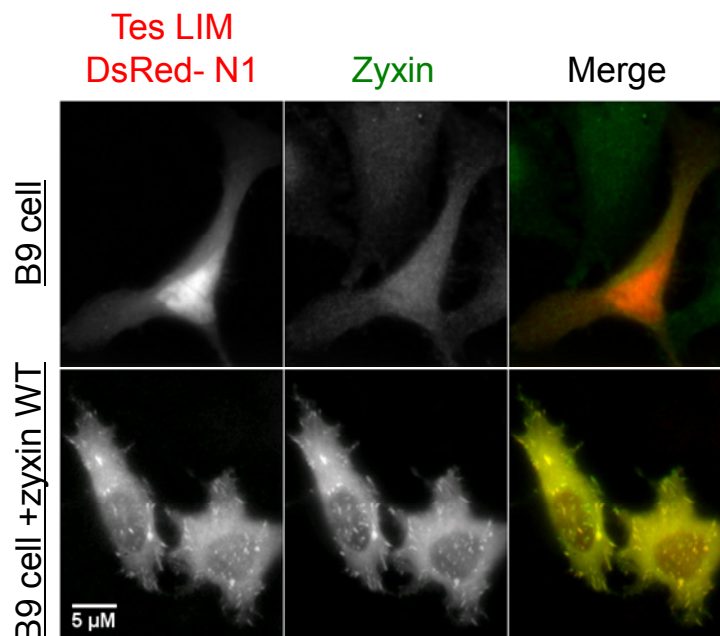


Figure 5.4: The recruitment of Tes LIM DsRed is restored in HeLa B9 cells following re-expression of zyxin (pictures provided by Ermin Hadzic).

HeLa B9 cells were transfected with Tes LIM DsRed with or without zyxin WT. Zyxin was detected with a monoclonal antibody (SLU10). In the absence of zyxin, Tes is not recruited into the FAs and consequently presents a diffuse localization in the cytoplasm (*upper panels*). A re-expression of zyxin WT restitutes the recruitment of Tes LIM DsRed into the FAs (*lower panels*).

First, we performed FRAP experiments to compare the kinetics of WT and MT zyxin at FAs (Fig. 5.5). When expressed in HeLa B9 cells, both zyxin variants were localised at FAs. The FAs on the cell periphery were significantly bigger than those localised closer to the cell center (Fig. 5.5a). Because the position of FAs in the cells correlates with their age and phase of their development (Berginski et al., 2011), we decided to measure and analyse separately the dynamics of zyxin variants at the cell border and closer to the cell center.

The turnover of zyxin at FAs was significantly faster than the turnover of actin with the recovery plateau reached between 30 and 90 s. In most cases fluorescence recovered to about 100% of the prebleach level indicating that all zyxin molecules in FAs undergo rapid exchange between bound and non-bound pools. The

fluorescence recoveries for zyxin WT were significantly slower than for zyxin mutant both at the border and in the cell center (Fig. 5.5b). Most of the recoveries were well fitted with the one-binding state model (Sprague et al., 2004). Pseudo-binding (k_{on}) and unbinding (k_{off}) rate constants were higher for zyxin mutant in comparison to zyxin wild type, although no significant deviations in the unbound protein fraction (F_{eq}) were observed. Parameters k_{on} and k_{off} were higher for the FAs localised closer to the cell center (Fig. 5.5c). We conclude that the loss of interaction with Tes facilitates zyxin kinetics at FAs and, hence, that this interaction might be required to stabilise zyxin-Tes complexes at FAs.

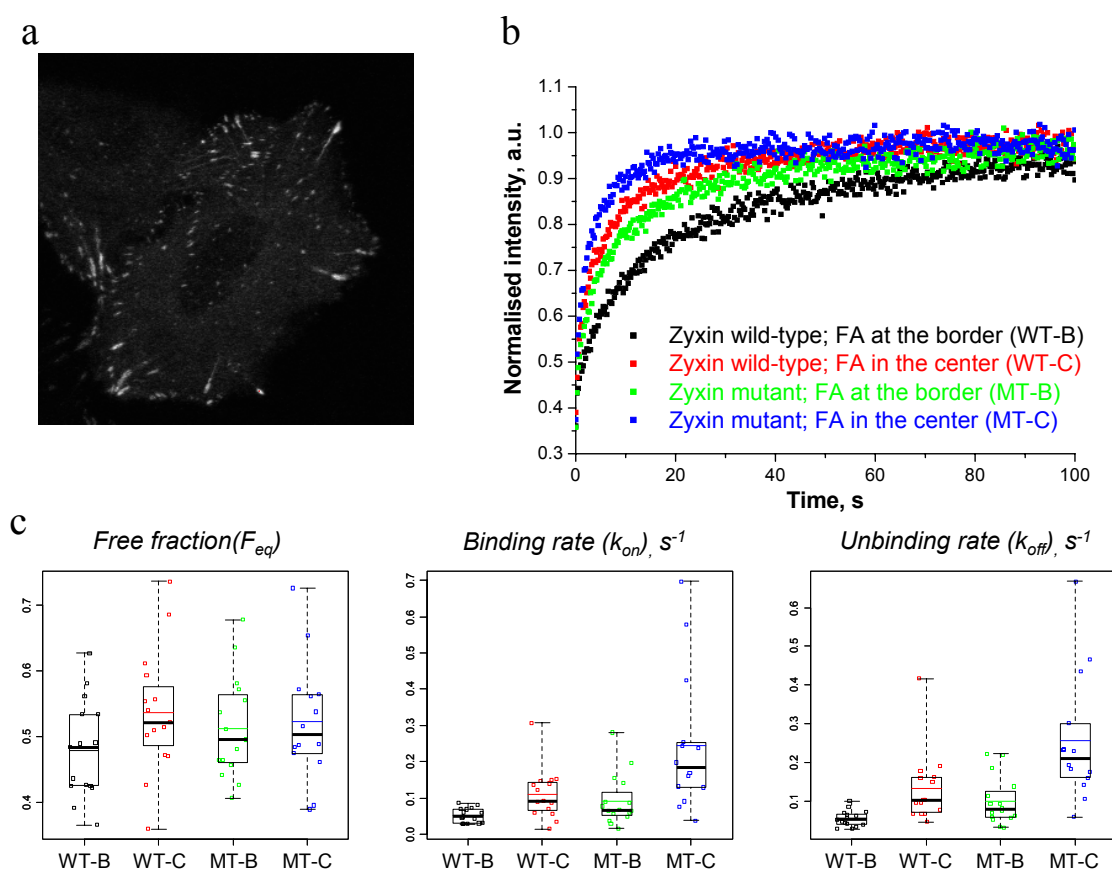


Figure 5.5: Results of FRAP experiments with GFP-zyxin at FAs in HeLa B9 cells silenced for endogenous zyxin. Kinetics of wild type zyxin WT is compared to kinetics of zyxin MT, lacking the Tes interaction domain.

a) GFP-zyxin WT in a HeLa B9 cell; b) Normalised and averaged FRAP recoveries for WT and MT in FAs. Bigger focal adhesions at the cell border (B) and smaller focal adhesions in the cell center (C) were assumed to have different kinetic parameters and were therefore analysed separately; c) Estimation of biochemical parameters from the collected recoveries: unbound protein fraction (F_{eq}), pseudo-binding rate constant (k_{on}), unbinding rate constant (k_{off}).

5.3.2. Loss of interaction between zyxin and Tes decreases the rate of actin turnover at focal adhesions

To investigate whether the interaction of Tes with zyxin affects actin turnover at FAs, we cotransfected HeLa B9 cells with GFP-actin and either zyxin WT DsRed or zyxin MT DsRed and conducted FRAP acquisitions to measure the parameters of actin dynamics (Fig. 5.6). Averaged recovery curves were almost identical in zyxin WT and zyxin MT transfected cells. However, fitting of individual measurements revealed that turnover was slower when the interaction between zyxin and Tes was inhibited by mutation. This result is in line with the slow-down of actin turnover upon Tes inhibition. This example also highlights that the explicit analysis of individual FRAP measurements is required to properly account for potential intercellular and intracellular variations.

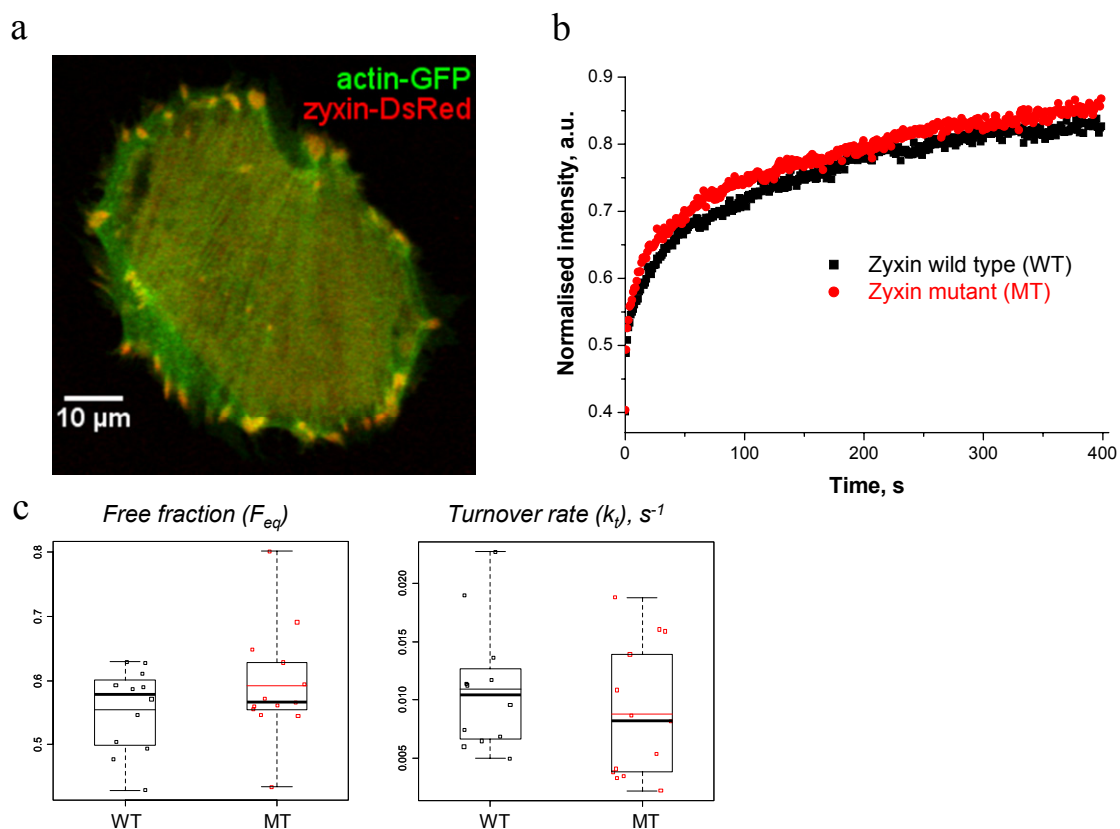


Figure 5.6: Results of FRAP experiments with GFP-actin at FAs in HeLa B9 cells expressing zyxin WT DsRed and zyxin MT DsRed.

a) Colocalisation of GFP-actin and zyxin DsRed at FAs in transfected HeLa B9 cells; b) Normalised and averaged recovery curves; c) Boxplots for the estimated parameters of actin turnover: non-polymerised fraction F_{eq} and turnover rate k_t . Points represent individual measurements.

5.4 *Conclusions*

Here we applied the FRAP methodology to study the regulation of actin cytoskeleton dynamics at FAs by zyxin and Tes, which are two LIM domain proteins that affect cell movement and adherence. All data were analysed with the computational tools that I have developed in this work and that allowed us to properly account for the variability of the measured turnover parameters. Our data indicate that: i) Tes is able to stimulate actin polymerisation at FAs and ii) loss of interaction between zyxin and Tes increases kinetics of binding/unbinding reactions of zyxin and slows down actin turnover. Taken together, these results lead to the hypothesis that zyxin-Tes interaction promotes actin turnover at FAs.

Despite the significant amount of quantitative data collected on the dynamics of the considered cytoskeleton components, additional experiments are required to formulate the mechanistic model describing the functions of zyxin and Tes in the actin turnover cycle. Zyxin binds Ena/VASP proteins which have a positive effect on actin assembly. The double knock-downs of Tes and Ena/VASP might therefore help to analyse if these two interactions are linked and/or play supplementary roles in regulating actin dynamics at FAs. The fact that Tes stimulates actin polymerisation suggests that its activity might be similar to that of proteins binding to the BEs that stabilise newly formed actin nuclei or stay progressively associated with the BEs during its growth and change locally critical actin concentration. The BEs of actin filaments associated with FAs are directed toward their tips. Thus, changes in the regulation of filament's BEs should affect spatial properties of actin turnover at FAs. In the previous chapter we have shown that the combination of FRAP with quantitative image analysis allows to address the spatial properties of actin turnover. Hence, the in-depth analysis of the actin cytoskeleton turnover and its regulation at FAs could be performed with this approach, if it is properly adapted for the spatial organisation of actin in SFs and its link to FA proteins.

Chapter 6 General discussion and perspectives

6.1 Linking experiments and mathematical models for the quantitative analysis of the actin polymerisation cycle

Despite a high degree of organisation in cells, the actin cytoskeleton is essentially a stochastic system. Different biochemical reactions, such as fragmentation and hydrolysis of F-actin-bound nucleotides, occur simultaneously and lead to significant structural variations of filaments (Fass et al., 2008; Stukalin and Kolomeisky, 2006). These sets of heterogeneous filaments, and not individual filaments, are involved in actin-associated biological functions. Many biochemical models of actin polymerisation accounting for this heterogeneity have been established (Bindschadler et al., 2004; Carlsson et al., 2004; Michelot et al., 2007; Vavylonis et al., 2006; Yarmola et al., 2008), but most of them have focused on the activities of only one or a few actin-binding proteins. The stochastic simulation algorithm (SSA), which was developed in this work (section 3.1), accounts for the filament structures and the properties of all their subunits. As a result, we were able to predict how the cooperative activity of several actin-binding proteins regulates the polymerisation kinetics and distribution of filament lengths.

In addition to predicting the complex behaviour of the actin system, the newly developed mathematical models aim at characterising new regulatory factors based on experimental data. The SSA can be used to analyse results of *in vitro* experiments as it has been done for the bulk pyrene-actin assay (Fig. 3.5; (Brooks and Carlsson, 2008; Matzavinos and Othmer, 2007) or for the measurements of the filament lengths using TIRF (Roland et al., 2008; Vavylonis et al., 2006). In contrast, the lack of knowledge about the intracellular regulation of actin dynamics limits the analysis of experiments in living cells to rather simple models, which ignore the relations between structural arrangement and biochemical kinetics of filaments (Campbell and Knight, 2007; McGrath et al., 2000). We developed a mathematical model based on stochastic differential equations, which predicts the relationship between the length of filaments, assembly/disassembly kinetics of their ends and the speed of FRAP recovery (Halavatyi et al., 2010). Validation with the SSA confirmed that this simplified FRAP model, which depends on only a few parameters, correctly predicts FRAP curves for the bleached actin networks. However, the orientation and the

spatial organisation of filaments in the analysed actin structures need to be incorporated into the model to estimate the unbiased kinetic parameters of actin turnover from the measured FRAP recoveries.

As an alternative to FRAP method, other techniques, in particular FCS and FSM, have been recently customised to measure intracellular dynamics of the actin cytoskeleton (Gowrishankar et al., 2012; Watanabe, 2012). The major reported disadvantage of the classical FRAP protocol, as compared to other methods, is the inability of FRAP to provide information about spatially inhomogeneous actin (de-)polymerisation and to distinguish between biochemical kinetics and the directed flux of polymerised networks. As discussed in the following sections, the combination of FRAP with image analysis procedures is suitable to analyse in details the kinetics of the different actin structures, including dendritic actin networks and dense actin bundles.

6.2 *Measurements of actin turnover with the actin-based biomimetic assay*

Because of its ability to mimic the motion of cells and intracellular pathogens, the actin-based biomimetic assay was widely used to investigate how the assembly of filament networks near the surfaces of functionalised particles generates and maintains their movement (Achard et al., 2010; Bernheim-Groswasser et al., 2005; Heuvingh et al., 2007). Various biophysical models have been developed to link the elastic properties of the formed actin clouds to the generated force and the speed of particle movement (Dayel et al., 2009; John et al., 2008; Kawska et al., 2012; van der Gucht et al., 2005). Many of these studies, however, considered the actin assembly near the bead surface stimulated by NPFs as the only factor determining the generated motility.

Here, we have used the biomimetic assay to address another important property of actin-based motile systems: the spatially-regulated filament turnover cycle, required for the protrusion of cellular membranes (Lai et al., 2008; Watanabe and Mitchison, 2002). To this end, we have established a new protocol based on FRAP methodology and we have applied it to directly measure the concentration-dependent effects of actin-binding proteins in the motility medium on the rate of actin turnover and to analyse spatial properties of actin exchange in the cloud. Importantly, our method allows to experimentally evaluate the role of filament treadmilling in the

dendritic nucleation network and could potentially be applied to quantitatively investigate the highly disputable actin turnover in lamellipodia (Iwasa and Mullins, 2007; Pantaloni et al., 2001; Watanabe and Mitchison, 2002).

Proteins of the ADF/cofilin family have been previously characterised as major promoters of filament disassembly and as suppliers of actin monomers for the elongation of uncapped filaments (Kiuchi et al., 2007). In the biomimetic assay, ADF/cofilin has been shown to sever filaments in an actin-nucleotide-dependent manner (Reymann et al., 2011). Here, we studied the functions of these proteins in the assay by changing their concentrations and by comparing two representatives of this family. Both human cofilin and *Arabidopsis* ADF1 facilitated actin exchange, but ADF1 stimulated actin depolymerisation much more efficiently than cofilin. Furthermore, capping did not have any significant effect on treadmilling in the presence of ADF1. Previously the effects of both proteins on actin treadmilling in similar biomimetic assays were determined by measuring the rates of protrusion of bacteria or functionalised beads (Loisel et al., 1999; Paluch et al., 2006; Wiesner et al., 2003). Maximal protrusion rates were reached for 2-6 μM of ADF (Loisel et al., 1999) or cofilin (Paluch et al., 2006). However the efficient disassembly of comet tails was observed in experiments with ADF, but not with cofilin. Furthermore, low quantities of gelsolin (50 nM) led to an optimal protrusion when ADF was used (Wiesner et al., 2003), whereas $\sim 0.8 \mu\text{M}$ of gelsolin were required in the presence of cofilin (Paluch et al., 2006).

Importantly, in these studies the effects of individual proteins were measured while keeping constant the quantities of other components of the motility medium. In contrast, our data indicate that the collective effects of all proteins in the motility medium have to be considered to understand filament turnover and associated biophysical processes. The cooperation between capping and nucleation by the Arp2/3 complex has been widely discussed, suggesting different effects of these components on the architecture of the filaments (Akin and Mullins, 2008; Wiesner et al., 2003). Simultaneous filament disassembly is essential for completing the actin turnover cycle and depends on the filament lengths and structures. We intend to further test the cooperation between the nucleation by the Arp2/3 complex and the disassembly by ADF/cofilin to understand the spatio-temporal regulation of the actin cycle in dendritic networks.

The experimental data qualitatively agree with our model for the analysis of FRAP experiments with actin filaments (section 3.2). According to the model predictions, the filament length L and the treadmilling rate v are two major parameters, which determine the rate of fluorescence recovery. Capping of the BEs limited the filament length and accelerated the recoveries, although the incorporation of actin monomers into the network was spatially restricted by capping to the bead vicinity (Fig. 4.6). ADF/cofilin is likely to affect both the distribution of filament length via severing and the treadmilling via accelerating the rates of ATP hydrolysis and of debranching. In particular, stochastic simulations revealed that efficient severing results in an exponential distribution of the filament lengths with a large fraction of rapidly depolymerising short filaments, whereas a bell-shaped distribution of filament lengths is expected without fragmentation (Appendix C and (Fass et al., 2008)).

The comparison of modelling and experimental results pointed out further ways for improving experimental protocols and theoretical methods needed for the accurate quantitative analysis of actin turnover with the assay. First, since actin-binding proteins interact with partially polymerised actin in the motility medium, changes in their concentrations ultimately affect G-actin concentration and the organisation of spontaneously polymerised filaments. The association of actin monomers to the ends of filaments is diffusion-limited (Drenckhahn and Pollard, 1986), and the elongation rate depends therefore on G-actin concentration and on the viscosity of the medium. The direct measurement of these parameters for all tested combinations of actin-binding proteins would decrease the model ambiguity.

Second, in our model for the analysis of FRAP data, the photobleached actin network is assumed to be composed of identical filaments, which treadmill by simultaneously elongating at the BE and shortening at the PE. This assumption would be highly relevant for biomimetic assay experiments in which formin (Romero et al., 2004) or VASP (Breitsprecher et al., 2008) is coupled to the bead surface. The application of our methodology to these assays would be useful to investigate the turnover of filaments structurally similar to those in filopodia and stress fibers (Lan and Papoian, 2008; Stachowiak and O'Shaughnessy, 2008). In contrast, the Arp2/3 complex stays associated with the PE after the nucleation event. Therefore, PEs start to depolymerise only after debranching, whilst actin exchange on BEs occurs from the nucleation event until capping (see Fig. 4.1b). Fragmentation creates new BEs

and PEs and therefore contributes to the heterogeneity of the filaments in the cloud. Our analysis confirms that the separation of the zones of assembly and disassembly primarily depends on the capping of BEs (Fig. 4.6). Hence, the overall actin treadmilling process is achieved by the growth of some filaments and the simultaneous disassembly of others (Lai et al., 2008; Pollard and Borisy, 2003; Svitkina and Borisy, 1999). The FRAP model that we developed, has therefore to be updated to account for critical events in the turnover of the dendritic network, such as capping, unbranching, severing, and, most importantly, to derive parameters characterising the orchestrated effects of these reactions.

6.3 *Cytoskeleton turnover at focal adhesions: functions of zyxin and Tes*

Rather than being only the attachment points connecting actin SFs to the extracellular environment, FAs function as active sensors of their microenvironment (Geiger et al., 2009). In response to biochemical stimuli, stiffness of the ECM and external mechanical stress, FAs mediate various intracellular processes including the remodelling of the cellular cytoskeleton and gene expression (Legate et al., 2009). The growth, disassembly and biological functions of FAs are controlled by both SF-generated internal contractile forces and external mechanical loads (Balaban et al., 2001; Riveline et al., 2001; Wolfenson et al., 2011). In turn, FAs regulate the growth of SFs and serve as sites of fast actin incorporation into the SFs (Endlich et al., 2007; Fradelizi et al., 2001; Turnacioglu et al., 1998).

Many studies have shown that the FA protein zyxin is involved in cell mechanosensing and the associated cytoskeleton remodelling (Hirata et al., 2008b; Hoffman et al., 2006). Zyxin binds to FAs when they mature from focal complexes and give rise to the associated SFs (Zaidel-Bar et al., 2003). The affinity of zyxin for FAs depends on external and internal mechanical forces and the release of these forces facilitates the disassembly of zyxin from FAs (Lele et al., 2006). In the mechanically stretched cells, zyxin translocates to SFs and stimulates their thickening, while zyxin knock-out cells do not exhibit such cytoskeleton reinforcement (Hoffman et al., 2012; Yoshigi et al., 2005). The recruitment of zyxin to FAs and its flux to SFs is coupled to the polymerisation and flux of actin, suggesting the existence of a molecular link between zyxin and actin filaments (Hirata et al., 2008a).

The role of zyxin in actin polymerisation at FAs and in the assembly of SFs was assumed to result from its ability to recruit Ena/VASP proteins (Drees et al., 2000; Hoffman et al., 2006), which stimulate the elongation of actin filaments at their BEs (Hansen and Mullins, 2010). Remarkably, the loss of interaction between zyxin and Ena/VASP only partially inhibits cytoskeleton reinforcement by zyxin upon mechanical stress (Hoffman et al., 2012). Because Tes is another molecular link between zyxin and actin at FAs (Garvalov et al., 2003) we addressed its role in actin turnover cycle. Tes affects the cell spreading and motility (Coutts et al., 2003; Griffith et al., 2004) and therefore it is likely to be involved in the regulation of the FA-associated actin cytoskeleton. We have found that Tes slows down actin turnover and increases actin recruitment at FAs suggesting that it contributes to actin assembly. Whether Tes affects properties of filament BEs to stimulate their growth or whether it stabilises filaments to prevent actin disassembly still needs to be clarified. Comparable to zyxin, Tes can also bind Ena/VASP family proteins (Boeda et al., 2007; Coutts et al., 2003). This raises the question of how these proteins work together to coordinate the actin cytoskeleton linked to FAs.

Therefore, more experimental data on the dynamics of zyxin, Tes and associated proteins at FAs are needed to understand the mechanistic details of Tes interactions with actin filaments and other FA proteins. The incorporation of actin into bleached FAs does not occur homogeneously, which is most likely due to the flux of polymerised actin in SFs (Hu et al., 2007). Tes affects the spatial inhomogeneity of fluorescent actin incorporation to the bleached FAs (Fig. 5.2c). The spatial analysis of actin exchange using two-colour FRAP experiments similar to those which we performed with the biomimetic motility assay, would provide information on the structures of filaments. Most filaments at FAs are parallel with their BEs directed towards the FA tip (Patla et al., 2010). Hence, simultaneous analysis of the rate of fluorescence recovery and of the movement of the bleached FA parts would separate the effects of filament turnover due to assembly/disassembly on the one hand and directed flow of polymerised actin on the other hand.

FRAP experiments using fluorescently-labelled zyxin revealed that large FAs were localised closer to the cell border and were characterised by slower zyxin turnover in comparison with more centrally located smaller FAs. In agreement with our findings, zyxin incorporation and actin polymerisation was previously found to be

more favourable at the peripheral FAs (Hirata et al., 2008a) presumably due to the higher mechanical load on them coming from the SFs. Disruption of the interaction between zyxin and Tes increased the rate of zyxin turnover at both peripheral and central FAs. This result suggests, that the interaction between these two proteins might be in a causal connection with the force-dependent recruitment and function of zyxin. The slowdown of actin assembly upon loss of zyxin-Tes binding indirectly supports this hypothesis. Whether Tes translocates together with zyxin to the SFs upon mechanical stress similarly to VASP (Hoffman et al., 2012) still needs to be investigated.

Zyxin-dependent actin polymerisation at FAs is also a potential reason for the high diversity of measured actin turnover rates. Alternatively, the stages of FA life cycle could account for the variability of the measured parameters. As previously reported, actin polymerisation at some FAs leads to the elongation of SFs, while other SFs do not grow whilst being still associated to FAs (Endlich et al., 2007). Tracking of FAs with well established markers, such as paxillin and Focal Adhesion Kinase (FAK), showed, that the phases of FA assembly, stability and disassembly lie within a range of a dozen of minutes (Berginski et al., 2011). The perturbation of FA dynamics changes the duration of these phases. The comparison of turnover rates between control and perturbed cells for different phases of FA cycle will allow identifying, which of these phases is regulated by zyxin and Tes. Tes facilitates cell spreading without affecting the surface occupied by fully spread cells (Coutts et al., 2003; Griffith et al., 2004), suggesting that Tes could be involved in the regulation of younger FAs.

In any of the cases discussed herein, simultaneous measurement of turnover and directional flux of actin and other FA proteins, including the currently studied proteins and other well-characterised FA markers, would be necessary to understand the spatio-temporal regulation of FAs. Previously, fluxes of actin and zyxin at FAs were found to be only partially correlated (Hu et al., 2007), although the precise link between the turnover parameters of these proteins remains to be elucidated.

6.4 *General conclusions*

Taken together, the results of this work provide a quantitative link between: i) the biochemical kinetics of actin assembly and its regulation by actin-binding proteins

working in concert, ii) the structural properties of filaments and iii) the kinetic parameters of actin cytoskeleton turnover measured using fluorescence photobleaching in physiological conditions. Stochastic simulations predict the time-course of actin turnover for any combination of involved actin-binding proteins. However, they have limited applicability for the processing of experimental data and for the estimation of representative non-correlated parameters of underlying molecular processes. The model dedicated to the analysis of actin kinetics with FRAP allowed exploring the relation between filament length, their assembly/disassembly reactions and parameters of fluorescence recovery. Now this model needs to be updated to account for the biochemical reactions that limit the recovery rate in particular experimental configurations.

Using FRAP to analyse actin turnover in two experimental systems, in actin-based biomimetic assay and in living cells, we characterised the influence of several actin-binding proteins and of their orchestrated activities on actin turnover. In both cases, actin exchange was spatially inhomogeneous and governed by superimposition of two processes: i) the turnover of actin filaments due to actin assembly and disassembly at their ends; and ii) the directed flow of polymerised actin and its spatial reorganisation because of the involved mechanical tensions. The analysis of spatial properties of actin turnover using the biomimetic assay helped to correlate the measured turnover parameters with the spatial organisation of filaments. Ultimately, studying actin turnover at FAs with similar analysis procedures will shed light on the biomolecular and biophysical effectors influencing the cytoskeleton dynamics at FAs and associated SFs.

References

- Achard, V., J.L. Martiel, A. Michelot, C. Guerin, A.C. Reymann, L. Blanchoin, and R. Boujemaa-Paterski. 2010. A "primer"-based mechanism underlies branched actin filament network formation and motility. *Curr Biol.* 20:423-428.
- Ahuja, R., R. Pinyol, N. Reichenbach, L. Custer, J. Klingensmith, M.M. Kessels, and B. Qualmann. 2007. Cordon-bleu is an actin nucleation factor and controls neuronal morphology. *Cell.* 131:337-350.
- Akin, O., and R.D. Mullins. 2008. Capping protein increases the rate of actin-based motility by promoting filament nucleation by the Arp2/3 complex. *Cell.* 133:841-851.
- Al Tanoury, Z., E. Schaffner-Reckinger, A. Halavatyi, C. Hoffmann, M. Moes, E. Hadzic, M. Catillon, M. Yatskou, and E. Friederich. 2010. Quantitative kinetic study of the actin-bundling protein L-plastin and of its impact on actin turn-over. *PLoS ONE.* 5:e9210.
- Alberts, J.B., and G.M. Odell. 2004. In silico reconstitution of Listeria propulsion exhibits nano-saltation. *PLoS Biol.* 2:e412.
- Amann, K.J., and T.D. Pollard. 2001. Direct real-time observation of actin filament branching mediated by Arp2/3 complex using total internal reflection fluorescence microscopy. *Proc Natl Acad Sci U S A.* 98:15009-15013.
- Amsellem, V., M.H. Kryszke, M. Hervy, F. Subra, R. Athman, H. Leh, C. Brachet-Ducos, and C. Auclair. 2005. The actin cytoskeleton-associated protein zyxin acts as a tumor suppressor in Ewing tumor cells. *Experimental cell research.* 304:443-456.
- Andrianantoandro, E., L. Blanchoin, D. Sept, J.A. McCammon, and T.D. Pollard. 2001. Kinetic mechanism of end-to-end annealing of actin filaments. *J Mol Biol.* 312:721-730.
- Andrianantoandro, E., and T.D. Pollard. 2006. Mechanism of actin filament turnover by severing and nucleation at different concentrations of ADF/cofilin. *Mol Cell.* 24:13-23.
- Atilgan, E., D. Wirtz, and S.X. Sun. 2006. Mechanics and dynamics of actin-driven thin membrane protrusions. *Biophys J.* 90:65-76.
- Axelrod, D., D.E. Koppel, J. Schlessinger, E. Elson, and W.W. Webb. 1976. Mobility measurement by analysis of fluorescence photobleaching recovery kinetics. *Biophys J.* 16:1055-1069.
- Balaban, N.Q., U.S. Schwarz, D. Riveline, P. Goichberg, G. Tzur, I. Sabanay, D. Mahalu, S. Safran, A. Bershadsky, L. Addadi, and B. Geiger. 2001. Force and focal adhesion assembly: a close relationship studied using elastic micropatterned substrates. *Nat Cell Biol.* 3:466-472.
- Bamburg, J.R., and B.W. Bernstein. 2010. Roles of ADF/cofilin in actin polymerization and beyond. *F1000 biology reports.* 2:62.
- Barzik, M., T.I. Kotova, H.N. Higgs, L. Hazelwood, D. Hanein, F.B. Gertler, and D.A. Schafer. 2005. Ena/VASP proteins enhance actin polymerization in the presence of barbed end capping proteins. *J Biol Chem.* 280:28653-28662.
- Beaudouin, J., F. Mora-Bermudez, T. Klee, N. Daigle, and J. Ellenberg. 2006. Dissecting the contribution of diffusion and interactions to the mobility of nuclear proteins. *Biophys J.* 90:1878-1894.
- Berginski, M.E., E.A. Vitriol, K.M. Hahn, and S.M. Gomez. 2011. High-resolution quantification of focal adhesion spatiotemporal dynamics in living cells. *PLoS ONE.* 6:e22025.
- Bernheim-Groswasser, A., J. Prost, and C. Sykes. 2005. Mechanism of actin-based motility: a dynamic state diagram. *Biophys J.* 89:1411-1419.

- Bernheim-Groswasser, A., S. Wiesner, R.M. Golsteyn, M.F. Carlier, and C. Sykes. 2002. The dynamics of actin-based motility depend on surface parameters. *Nature*. 417:308-311.
- Bernstein, B.W., and J.R. Bamburg. 2010. ADF/cofilin: a functional node in cell biology. *Trends Cell Biol.* 20:187-195.
- Bershadsky, A., M. Kozlov, and B. Geiger. 2006. Adhesion-mediated mechanosensitivity: a time to experiment, and a time to theorize. *Curr Opin Cell Biol.* 18:472-481.
- Binder, K., and D.W. Heermann. 2010. Monte Carlo methods in statistical physics. Springer-Verlag, Berlin.
- Bindschadler, M. 2010. Modeling actin dynamics. *Wiley interdisciplinary reviews. Systems biology and medicine*. 2:481-488.
- Bindschadler, M., E.A. Osborn, C.F. Dewey, Jr., and J.L. McGrath. 2004. A mechanistic model of the actin cycle. *Biophys J.* 86:2720-2739.
- Blanchoin, L., and T.D. Pollard. 2002. Hydrolysis of ATP by polymerized actin depends on the bound divalent cation but not profilin. *Biochemistry*. 41:597-602.
- Blanchoin, L., T.D. Pollard, and R.D. Mullins. 2000. Interactions of ADF/cofilin, Arp2/3 complex, capping protein and profilin in remodeling of branched actin filament networks. *Curr Biol.* 10:1273-1282.
- Boeda, B., D.C. Briggs, T. Higgins, B.K. Garvalov, A.J. Fadden, N.Q. McDonald, and M. Way. 2007. Tes, a specific Mena interacting partner, breaks the rules for EVH1 binding. *Mol Cell*. 28:1071-1082.
- Bosch, M., K.H. Le, B. Bugyi, J.J. Correia, L. Renault, and M.F. Carlier. 2007. Analysis of the function of Spire in actin assembly and its synergy with formin and profilin. *Mol Cell*. 28:555-568.
- Braeckmans, K., K. Remaut, R.E. Vandenbroucke, B. Lucas, S.C. De Smedt, and J. Demeester. 2007. Line FRAP with the confocal laser scanning microscope for diffusion measurements in small regions of 3-D samples. *Biophys J.* 92:2172-2183.
- Breitsprecher, D., A.K. Kieseewetter, J. Linkner, C. Urbanke, G.P. Resch, J.V. Small, and J. Faix. 2008. Clustering of VASP actively drives processive, WH2 domain-mediated actin filament elongation. *EMBO J.* 27:2943-2954.
- Breitsprecher, D., A.K. Kieseewetter, J. Linkner, M. Vinzenz, T.E. Stradal, J.V. Small, U. Curth, R.B. Dickinson, and J. Faix. 2011. Molecular mechanism of Ena/VASP-mediated actin-filament elongation. *EMBO J.* 30:456-467.
- Brieher, W.M., M. Coughlin, and T.J. Mitchison. 2004. Fascin-mediated propulsion of *Listeria monocytogenes* independent of frequent nucleation by the Arp2/3 complex. *J Cell Biol.* 165:233-242.
- Brieher, W.M., H.Y. Kueh, B.A. Ballif, and T.J. Mitchison. 2006. Rapid actin monomer-insensitive depolymerization of *Listeria* actin comet tails by cofilin, coronin, and Aip1. *J Cell Biol.* 175:315-324.
- Brooks, F.J., and A.E. Carlsson. 2008. Actin polymerization overshoots and ATP hydrolysis as assayed by pyrene fluorescence. *Biophys J.* 95:1050-1062.
- Bugyi, B., and M.F. Carlier. 2010. Control of actin filament treadmilling in cell motility. *Annu Rev Biophys.* 39:449-470.
- Bugyi, B., D. Didry, and M.F. Carlier. 2010. How tropomyosin regulates lamellipodial actin-based motility: a combined biochemical and reconstituted motility approach. *EMBO J.* 29:14-26.
- Bugyi, B., C. Le Clainche, G. Romet-Lemonne, and M.F. Carlier. 2008. How do in vitro reconstituted actin-based motility assays provide insight into in vivo behavior? *FEBS Lett.* 582:2086-2092.

- Campbell, J.J., and M.M. Knight. 2007. An improved confocal FRAP technique for the measurement of long-term actin dynamics in individual stress fibers. *Microsc Res Tech.* 70:1034-1040.
- Cao, Y., H. Li, and L. Petzold. 2004. Efficient formulation of the stochastic simulation algorithm for chemically reacting systems. *J Chem Phys.* 121:4059-4067.
- Capoulade, J., M. Wachsmuth, L. Hufnagel, and M. Knop. 2011. Quantitative fluorescence imaging of protein diffusion and interaction in living cells. *Nature biotechnology.* 29:835-839.
- Carlier, M.F., V. Laurent, J. Santolini, R. Melki, D. Didry, G.X. Xia, Y. Hong, N.H. Chua, and D. Pantaloni. 1997. Actin depolymerizing factor (ADF/cofilin) enhances the rate of filament turnover: implication in actin-based motility. *J Cell Biol.* 136:1307-1322.
- Carlier, M.F., and D. Pantaloni. 1986. Direct evidence for ADP-Pi-F-actin as the major intermediate in ATP-actin polymerization. Rate of dissociation of Pi from actin filaments. *Biochemistry.* 25:7789-7792.
- Carlier, M.F., and D. Pantaloni. 1997. Control of actin dynamics in cell motility. *J Mol Biol.* 269:459-467.
- Carlier, M.F., D. Pantaloni, and E.D. Korn. 1984. Evidence for an ATP cap at the ends of actin filaments and its regulation of the F-actin steady state. *J Biol Chem.* 259:9983-9986.
- Carlier, M.F., D. Pantaloni, S. Romero, and C. Le Clainche. 2007. How actin assembly is modulated at filament barbed ends in motile processes. In *Actin-monomer-binding proteins*. P. Lappalainen, editor. Springer Science+Business Media, New York, USA. 1-10.
- Carlier, M.F., S. Wiesner, C. Le Clainche, and D. Pantaloni. 2003. Actin-based motility as a self-organized system: mechanism and reconstitution in vitro. *Comptes rendus biologies.* 326:161-170.
- Carlsson, A.E. 2005. The effect of branching on the critical concentration and average filament length of actin. *Biophys J.* 89:130-140.
- Carlsson, A.E. 2006. Stimulation of actin polymerization by filament severing. *Biophys J.* 90:413-422.
- Carlsson, A.E., M.A. Wear, and J.A. Cooper. 2004. End versus side branching by Arp2/3 complex. *Biophys J.* 86:1074-1081.
- Carrero, G., E. Crawford, M.J. Hendzel, and G. de Vries. 2004. Characterizing fluorescence recovery curves for nuclear proteins undergoing binding events. *Bull Math Biol.* 66:1515-1545.
- Carrero, G., D. McDonald, E. Crawford, G. de Vries, and M.J. Hendzel. 2003. Using FRAP and mathematical modeling to determine the in vivo kinetics of nuclear proteins. *Methods.* 29:14-28.
- Chan, C., C.C. Beltzner, and T.D. Pollard. 2009. Cofilin dissociates Arp2/3 complex and branches from actin filaments. *Curr Biol.* 19:537-545.
- Chen, H., B.W. Bernstein, J.M. Sneider, J.A. Boyle, L.S. Minamide, and J.R. Bamberg. 2004. In vitro activity differences between proteins of the ADF/cofilin family define two distinct subgroups. *Biochemistry.* 43:7127-7142.
- Chesarone, M.A., and B.L. Goode. 2009. Actin nucleation and elongation factors: mechanisms and interplay. *Curr Opin Cell Biol.* 21:28-37.
- Chu, J.W., and G.A. Voth. 2006. Coarse-grained modeling of the actin filament derived from atomistic-scale simulations. *Biophys J.* 90:1572-1582.
- Cooper, J.A., and T.D. Pollard. 1985. Effect of capping protein on the kinetics of actin polymerization. *Biochemistry.* 24:793-799.
- Cooper, J.A., S.B. Walker, and T.D. Pollard. 1983. Pyrene actin: documentation of the validity of a sensitive assay for actin polymerization. *Journal of muscle research and cell motility.* 4:253-262.

- Coutts, A.S., E. MacKenzie, E. Griffith, and D.M. Black. 2003. TES is a novel focal adhesion protein with a role in cell spreading. *J Cell Sci.* 116:897-906.
- Dalhaimer, P., T.D. Pollard, and B.J. Nolen. 2008. Nucleotide-mediated conformational changes of monomeric actin and Arp3 studied by molecular dynamics simulations. *J Mol Biol.* 376:166-183.
- Danuser, G., and C.M. Waterman-Storer. 2006. Quantitative fluorescent speckle microscopy of cytoskeleton dynamics. *Annual review of biophysics and biomolecular structure.* 35:361-387.
- Dayel, M.J., O. Akin, M. Landeryou, V. Risca, A. Mogilner, and R.D. Mullins. 2009. In silico reconstitution of actin-based symmetry breaking and motility. *PLoS Biol.* 7:e1000201.
- De La Cruz, E.M., A. Mandinova, M.O. Steinmetz, D. Stoffler, U. Aebi, and T.D. Pollard. 2000. Polymerization and structure of nucleotide-free actin filaments. *J Mol Biol.* 295:517-526.
- Delatour, V., E. Helfer, D. Didry, K.H. Le, J.F. Gaucher, M.F. Carlier, and G. Romet-Lemonne. 2008. Arp2/3 controls the motile behavior of N-WASP-functionalized GUVs and modulates N-WASP surface distribution by mediating transient links with actin filaments. *Biophys J.* 94:4890-4905.
- DesMarais, V., M. Ghosh, R. Eddy, and J. Condeelis. 2005. Cofilin takes the lead. *J Cell Sci.* 118:19-26.
- Didry, D., M.F. Carlier, and D. Pantaloni. 1998. Synergy between actin depolymerizing factor/cofilin and profilin in increasing actin filament turnover. *J Biol Chem.* 273:25602-25611.
- Digman, M.A., C.M. Brown, A.R. Horwitz, W.W. Mantulin, and E. Gratton. 2008. Paxillin dynamics measured during adhesion assembly and disassembly by correlation spectroscopy. *Biophys J.* 94:2819-2831.
- Digman, M.A., P.W. Wiseman, C. Choi, A.R. Horwitz, and E. Gratton. 2009. Stoichiometry of molecular complexes at adhesions in living cells. *Proc Natl Acad Sci U S A.* 106:2170-2175.
- Ditlev, J.A., N.M. Vacanti, I.L. Novak, and L.M. Loew. 2009. An open model of actin dendritic nucleation. *Biophys J.* 96:3529-3542.
- Ditsch, A., and A. Wegner. 1994. Nucleation of actin polymerization by gelsolin. *European journal of biochemistry / FEBS.* 224:223-227.
- Dos Remedios, C.G., and D. Chhabra. 2008. Actin-binding proteins and disease. Springer, New York.
- dos Remedios, C.G., D. Chhabra, M. Kekic, I.V. Dedova, M. Tsubakihara, D.A. Berry, and N.J. Nosworthy. 2003. Actin binding proteins: regulation of cytoskeletal microfilaments. *Physiol Rev.* 83:433-473.
- Drees, B., E. Friederich, J. Fradelizi, D. Louvard, M.C. Beckerle, and R.M. Golsteyn. 2000. Characterization of the interaction between zyxin and members of the Ena/vasodilator-stimulated phosphoprotein family of proteins. *J Biol Chem.* 275:22503-22511.
- Drenckhahn, D., and T.D. Pollard. 1986. Elongation of actin filaments is a diffusion-limited reaction at the barbed end and is accelerated by inert macromolecules. *J Biol Chem.* 261:12754-12758.
- Drusco, A., N. Zanesi, C. Roldo, F. Trapasso, J.L. Farber, L.Y. Fong, and C.M. Croce. 2005. Knockout mice reveal a tumor suppressor function for Testin. *Proc Natl Acad Sci U S A.* 102:10947-10951.
- Dunn, G.A., I.M. Dobbie, J. Monypenny, M.R. Holt, and D. Zicha. 2002. Fluorescence localization after photobleaching (FLAP): a new method for studying protein dynamics in living cells. *J Microsc.* 205:109-112.

- E, W., D. Liu, and E. Vanden-Eijnden. 2005. Nested stochastic simulation algorithm for chemical kinetic systems with disparate rates. *J Chem Phys.* 123:194107.
- Edelstein-Keshet, L., and G.B. Ermentrout. 2001. A model for actin-filament length distribution in a lamellipod. *Journal of mathematical biology.* 43:325-355.
- Ellenberg, J., E.D. Siggia, J.E. Moreira, C.L. Smith, J.F. Presley, H.J. Worman, and J. Lippincott-Schwartz. 1997. Nuclear membrane dynamics and reassembly in living cells: targeting of an inner nuclear membrane protein in interphase and mitosis. *J Cell Biol.* 138:1193-1206.
- Endlich, N., C.A. Otey, W. Kriz, and K. Endlich. 2007. Movement of stress fibers away from focal adhesions identifies focal adhesions as sites of stress fiber assembly in stationary cells. *Cell Motil Cytoskeleton.* 64:966-976.
- Fass, J., C. Pak, J. Bamburg, and A. Mogilner. 2008. Stochastic simulation of actin dynamics reveals the role of annealing and fragmentation. *J Theor Biol.* 252:173-183.
- Forster, R., M. Weiss, T. Zimmermann, E.G. Reynaud, F. Verissimo, D.J. Stephens, and R. Pepperkok. 2006. Secretory cargo regulates the turnover of COPII subunits at single ER exit sites. *Curr Biol.* 16:173-179.
- Fradelizi, J., V. Noireaux, J. Plastino, B. Menichi, D. Louvard, C. Sykes, R.M. Golsteyn, and E. Friederich. 2001. ActA and human zyxin harbour Arp2/3-independent actin-polymerization activity. *Nat Cell Biol.* 3:699-707.
- Fujiwara, I., S. Takahashi, H. Tadakuma, T. Funatsu, and S. Ishiwata. 2002. Microscopic analysis of polymerization dynamics with individual actin filaments. *Nat Cell Biol.* 4:666-673.
- Gadgil, C., C.H. Lee, and H.G. Othmer. 2005. A stochastic analysis of first-order reaction networks. *Bull Math Biol.* 67:901-946.
- Garbett, D., and A. Bretscher. 2012. PDZ interactions regulate rapid turnover of the scaffolding protein EBP50 in microvilli. *J Cell Biol.* 198:195-203.
- Gardiner, C.W. 2004. Handbook of stochastic methods for physics, chemistry and natural sciences. Springer, Verlag Berlin Heidelberg New York. 415 pp.
- Garvalov, B.K., T.E. Higgins, J.D. Sutherland, M. Zettl, N. Scaplehorn, T. Kocher, E. Piddini, G. Griffiths, and M. Way. 2003. The conformational state of Tes regulates its zyxin-dependent recruitment to focal adhesions. *J Cell Biol.* 161:33-39.
- Geiger, B., J.P. Spatz, and A.D. Bershadsky. 2009. Environmental sensing through focal adhesions. *Nat Rev Mol Cell Biol.* 10:21-33.
- Gerbal, F., P. Chaikin, Y. Rabin, and J. Prost. 2000. An elastic analysis of Listeria monocytogenes propulsion. *Biophys J.* 79:2259-2275.
- Gerlich, D., J. Beaudouin, M. Gebhard, J. Ellenberg, and R. Eils. 2001. Four-dimensional imaging and quantitative reconstruction to analyse complex spatiotemporal processes in live cells. *Nat Cell Biol.* 3:852-855.
- Gibson, M.A., and J. Bruck. 2000. Efficient Exact Stochastic Simulation of Chemical Systems with Many Species and Many Channels. *J. Phys. Chem.* 104:1876-1889.
- Giganti, A., J. Plastino, B. Janji, M. Van Troys, D. Lentz, C. Ampe, C. Sykes, and E. Friederich. 2005. Actin-filament cross-linking protein T-plastin increases Arp2/3-mediated actin-based movement. *J Cell Sci.* 118:1255-1265.
- Gillespie, D.T. 1976. A general method for numerically simulating the stochastic time evolution of coupled chemical reactions. *J. Comput. Phys.* 22:403-434.
- Gillespie, D.T. 1977. Exact stochastic simulation of coupled chemical reactions. *J. Phys. Chem.* 81:2340-2361.
- Gillespie, D.T. 2001. Approximate accelerated stochastic simulation of chemically reacting systems. *J. Phys. Chem.* 115:1716-1733.

- Gillo, D., B. Gilboa, R. Gurka, and A. Bernheim-Groswasser. 2009. The fusion of actin bundles driven by interacting motor proteins. *Physical biology*. 6:036003.
- Golsteyn, R.M., D. Louvard, and E. Friederich. 1997. The role of actin binding proteins in epithelial morphogenesis: models based upon Listeria movement. *Biophys Chem*. 68:73-82.
- Goode, B.L., and M.J. Eck. 2007. Mechanism and function of formins in the control of actin assembly. *Annu Rev Biochem*. 76:593-627.
- Gould, C.J., S. Maiti, A. Michelot, B.R. Graziano, L. Blanchoin, and B.L. Goode. 2011. The formin DAD domain plays dual roles in autoinhibition and actin nucleation. *Curr Biol*. 21:384-390.
- Gowrishankar, K., S. Ghosh, S. Saha, R. C, S. Mayor, and M. Rao. 2012. Active remodeling of cortical actin regulates spatiotemporal organization of cell surface molecules. *Cell*. 149:1353-1367.
- Graham, F.L., and A.J. van der Eb. 1973. A new technique for the assay of infectivity of human adenovirus 5 DNA. *Virology*. 52:456-467.
- Grazi, E. 1985. Polymerization of N-(1-pyrenyl) iodoacetamide-labelled actin: the fluorescence signal is not directly proportional to the incorporation of the monomer into the polymer. *Biochem Biophys Res Commun*. 128:1058-1063.
- Griffith, E., A.S. Coutts, and D.M. Black. 2004. Characterisation of chicken TES and its role in cell spreading and motility. *Cell Motil Cytoskeleton*. 57:133-142.
- Griffith, E., A.S. Coutts, and D.M. Black. 2005. RNAi knockdown of the focal adhesion protein TES reveals its role in actin stress fibre organisation. *Cell Motil Cytoskeleton*. 60:140-152.
- Gupton, S.L., K.L. Anderson, T.P. Kole, R.S. Fischer, A. Ponti, S.E. Hitchcock-DeGregori, G. Danuser, V.M. Fowler, D. Wirtz, D. Hanein, and C.M. Waterman-Storer. 2005. Cell migration without a lamellipodium: translation of actin dynamics into cell movement mediated by tropomyosin. *J Cell Biol*. 168:619-631.
- Gupton, S.L., K. Eisenmann, A.S. Alberts, and C.M. Waterman-Storer. 2007. mDia2 regulates actin and focal adhesion dynamics and organization in the lamella for efficient epithelial cell migration. *J Cell Sci*. 120:3475-3487.
- Halavatyi, A.A., P.V. Nazarov, Z. Al Tanoury, V.V. Apanasovich, M. Yatskou, and E. Friederich. 2010. A mathematical model of actin filament turnover for fitting FRAP data. *Eur Biophys J*. 39:669-677.
- Halavatyi, A.A., P.V. Nazarov, S. Medves, M. van Troys, C. Ampe, M. Yatskou, and E. Friederich. 2009. An integrative simulation model linking major biochemical reactions of actin-polymerization to structural properties of actin filaments. *Biophys Chem*. 140:24-34.
- Hansen, S.D., and R.D. Mullins. 2010. VASP is a processive actin polymerase that requires monomeric actin for barbed end association. *J Cell Biol*. 191:571-584.
- Harris, E.S., I. Rouiller, D. Hanein, and H.N. Higgs. 2006. Mechanistic differences in actin bundling activity of two mammalian formins, FRL1 and mDia2. *J Biol Chem*. 281:14383-14392.
- Haviv, L., Y. Brill-Karniely, R. Mahaffy, F. Backouche, A. Ben-Shaul, T.D. Pollard, and A. Bernheim-Groswasser. 2006. Reconstitution of the transition from lamellipodium to filopodium in a membrane-free system. *Proc Natl Acad Sci U S A*. 103:4906-4911.
- Heuvingh, J., M. Franco, P. Chavrier, and C. Sykes. 2007. ARF1-mediated actin polymerization produces movement of artificial vesicles. *Proc Natl Acad Sci U S A*. 104:16928-16933.
- Higgs, H.N. 2005. Formin proteins: a domain-based approach. *Trends Biochem Sci*. 30:342-353.

- Hill, T.L. 1981. Microfilament or microtubule assembly or disassembly against a force. *Proc Natl Acad Sci U S A*. 78:5613-5617.
- Hirata, H., H. Tatsumi, and M. Sokabe. 2008a. Mechanical forces facilitate actin polymerization at focal adhesions in a zyxin-dependent manner. *J Cell Sci*. 121:2795-2804.
- Hirata, H., H. Tatsumi, and M. Sokabe. 2008b. Zyxin emerges as a key player in the mechanotransduction at cell adhesive structures. *Communicative & integrative biology*. 1:192-195.
- Hoffman, L.M., C.C. Jensen, A. Chaturvedi, M. Yoshigi, and M.C. Beckerle. 2012. Stretch-induced actin remodeling requires targeting of zyxin to stress fibers and recruitment of actin regulators. *Mol Biol Cell*. 23:1846-1859.
- Hoffman, L.M., C.C. Jensen, S. Kloeker, C.L. Wang, M. Yoshigi, and M.C. Beckerle. 2006. Genetic ablation of zyxin causes Mena/VASP mislocalization, increased motility, and deficits in actin remodeling. *J Cell Biol*. 172:771-782.
- Holmes, K.C., D. Popp, W. Gebhard, and W. Kabsch. 1990. Atomic model of the actin filament. *Nature*. 347:44-49.
- Hotulainen, P., and P. Lappalainen. 2006. Stress fibers are generated by two distinct actin assembly mechanisms in motile cells. *J Cell Biol*. 173:383-394.
- Hu, K., L. Ji, K.T. Applegate, G. Danuser, and C.M. Waterman-Storer. 2007. Differential transmission of actin motion within focal adhesions. *Science*. 315:111-115.
- Huber, F., and J. Kas. 2011. Self-regulative organization of the cytoskeleton. *Cytoskeleton (Hoboken)*. 68:259-265.
- Huber, F., J. Kas, and B. Stuhmann. 2008. Growing actin networks form lamellipodium and lamellum by self-assembly. *Biophys J*. 95:5508-5523.
- Husson, C., L. Renault, D. Didry, D. Pantaloni, and M.F. Carlier. 2011. Cordon-Bleu uses WH2 domains as multifunctional dynamizers of actin filament assembly. *Mol Cell*. 43:464-477.
- Iwasa, J.H., and R.D. Mullins. 2007. Spatial and temporal relationships between actin-filament nucleation, capping, and disassembly. *Curr Biol*. 17:395-406.
- Janji, B., L. Vallar, Z. Al Tanoury, F. Bernardin, G. Vetter, E. Schaffner-Reckinger, G. Berchem, E. Friederich, and S. Chouaib. 2010. The actin filament cross-linker L-plastin confers resistance to TNF-alpha in MCF-7 breast cancer cells in a phosphorylation-dependent manner. *J Cell Mol Med*. 14:1264-1275.
- Janmey, P.A., C. Chaponnier, S.E. Lind, K.S. Zaner, T.P. Stossel, and H.L. Yin. 1985. Interactions of gelsolin and gelsolin-actin complexes with actin. Effects of calcium on actin nucleation, filament severing, and end blocking. *Biochemistry*. 24:3714-3723.
- Janmey, P.A., and P.T. Matsudaira. 1988. Functional comparison of villin and gelsolin. Effects of Ca²⁺, KCl, and polyphosphoinositides. *J Biol Chem*. 263:16738-16743.
- Janmey, P.A., and T.P. Stossel. 1987. Modulation of gelsolin function by phosphatidylinositol 4,5-bisphosphate. *Nature*. 325:362-364.
- John, K., P. Peyla, K. Kassner, J. Prost, and C. Misbah. 2008. Nonlinear study of symmetry breaking in actin gels: implications for cellular motility. *Phys Rev Lett*. 100:068101.
- Jordan, M., A. Schallhorn, and F.M. Wurm. 1996. Transfecting mammalian cells: optimization of critical parameters affecting calcium-phosphate precipitate formation. *Nucleic acids research*. 24:596-601.
- Jung, G., K. Remmert, X. Wu, J.M. Volosky, and J.A. Hammer, 3rd. 2001. The Dictyostelium CARMIL protein links capping protein and the Arp2/3 complex to type I myosins through their SH3 domains. *J Cell Biol*. 153:1479-1497.
- Kadmas, J.L., and M.C. Beckerle. 2004. The LIM domain: from the cytoskeleton to the nucleus. *Nat Rev Mol Cell Biol*. 5:920-931.

- Kang, H., D.S. Perlmutter, V.B. Shenoy, and J.X. Tang. 2010. Observation and kinematic description of long actin tracks induced by spherical beads. *Biophys J.* 99:2793-2802.
- Kawska, A., K. Carvalho, J. Manzi, R. Boujemaa-Paterski, L. Blanchoin, J.L. Martiel, and C. Sykes. 2012. How actin network dynamics control the onset of actin-based motility. *Proc Natl Acad Sci U S A.* 109:14440-14445.
- Kim, T., G.E. Ravilious, D. Sept, and J.A. Cooper. 2012. Mechanism for CARMIL protein inhibition of heterodimeric actin-capping protein. *J Biol Chem.* 287:15251-15262.
- Kiuchi, T., K. Ohashi, S. Kurita, and K. Mizuno. 2007. Cofilin promotes stimulus-induced lamellipodium formation by generating an abundant supply of actin monomers. *J Cell Biol.* 177:465-476.
- Korn, E.D., M.F. Carrier, and D. Pantaloni. 1987. Actin polymerization and ATP hydrolysis. *Science.* 238:638-644.
- Kouyama, T., and K. Mihashi. 1981. Fluorimetry study of N-(1-pyrenyl)iodoacetamide-labelled F-actin. Local structural change of actin protomer both on polymerization and on binding of heavy meromyosin. *European journal of biochemistry / FEBS.* 114:33-38.
- Kovar, D.R. 2006. Molecular details of formin-mediated actin assembly. *Curr Opin Cell Biol.* 18:11-17.
- Kovar, D.R., E.S. Harris, R. Mahaffy, H.N. Higgs, and T.D. Pollard. 2006. Control of the assembly of ATP- and ADP-actin by formins and profilin. *Cell.* 124:423-435.
- Kueh, H.Y., W.M. Brieher, and T.J. Mitchison. 2008a. Dynamic stabilization of actin filaments. *Proc Natl Acad Sci U S A.* 105:16531-16536.
- Kueh, H.Y., W.M. Brieher, and T.J. Mitchison. 2010. Quantitative analysis of actin turnover in *Listeria* comet tails: evidence for catastrophic filament turnover. *Biophys J.* 99:2153-2162.
- Kueh, H.Y., G.T. Charras, T.J. Mitchison, and W.M. Brieher. 2008b. Actin disassembly by cofilin, coronin, and Aip1 occurs in bursts and is inhibited by barbed-end cappers. *J Cell Biol.* 182:341-353.
- Kuhn, J.R., and T.D. Pollard. 2005. Real-time measurements of actin filament polymerization by total internal reflection fluorescence microscopy. *Biophys J.* 88:1387-1402.
- Lai, F.P., M. Szczodrak, J. Block, J. Faix, D. Breitsprecher, H.G. Mannherz, T.E. Stradal, G.A. Dunn, J.V. Small, and K. Rottner. 2008. Arp2/3 complex interactions and actin network turnover in lamellipodia. *EMBO J.* 27:982-992.
- Lambrechts, A., M. Van Troys, and C. Ampe. 2004. The actin cytoskeleton in normal and pathological cell motility. *The international journal of biochemistry & cell biology.* 36:1890-1909.
- Lan, Y., and G.A. Papoian. 2008. The stochastic dynamics of filopodial growth. *Biophys J.* 94:3839-3852.
- Le Clainche, C., and M.F. Carrier. 2004. Actin-based motility assay. *Curr Protoc Cell Biol.* Chapter 12:Unit 12 17.
- Le Clainche, C., and M.F. Carrier. 2008. Regulation of actin assembly associated with protrusion and adhesion in cell migration. *Physiol Rev.* 88:489-513.
- Lee, K.C., and A.J. Liu. 2009. Force-velocity relation for actin-polymerization-driven motility from Brownian dynamics simulations. *Biophys J.* 97:1295-1304.
- Legate, K.R., S.A. Wickstrom, and R. Fassler. 2009. Genetic and cell biological analysis of integrin outside-in signaling. *Genes & development.* 23:397-418.
- Lele, T.P., J. Pendse, S. Kumar, M. Salanga, J. Karavitis, and D.E. Ingber. 2006. Mechanical forces alter zyxin unbinding kinetics within focal adhesions of living cells. *J Cell Physiol.* 207:187-194.

- Lele, T.P., C.K. Thodeti, J. Pendse, and D.E. Ingber. 2008. Investigating complexity of protein-protein interactions in focal adhesions. *Biochem Biophys Res Commun.* 369:929-934.
- Li, F., and H.N. Higgs. 2005. Dissecting requirements for auto-inhibition of actin nucleation by the formin, mDia1. *J Biol Chem.* 280:6986-6992.
- Lippincott-Schwartz, J., N. Altan-Bonnet, and G.H. Patterson. 2003. Photobleaching and photoactivation: following protein dynamics in living cells. *Nat Cell Biol.* Suppl:S7-14.
- Lippincott-Schwartz, J., and G.H. Patterson. 2008. Fluorescent proteins for photoactivation experiments. *Methods Cell Biol.* 85:45-61.
- Lippincott-Schwartz, J., E. Snapp, and A. Kenworthy. 2001. Studying protein dynamics in living cells. *Nat Rev Mol Cell Biol.* 2:444-456.
- Lo, S.H. 2006. Focal adhesions: what's new inside. *Developmental biology.* 294:280-291.
- Loisel, T.P., R. Boujemaa, D. Pantaloni, and M.F. Carlier. 1999. Reconstitution of actin-based motility of *Listeria* and *Shigella* using pure proteins. *Nature.* 401:613-616.
- Maciver, S.K., and A.G. Weeds. 1994. Actophorin preferentially binds monomeric ADP-actin over ATP-bound actin: consequences for cell locomotion. *FEBS Lett.* 347:251-256.
- Mahaffy, R.E., and T.D. Pollard. 2006. Kinetics of the formation and dissociation of actin filament branches mediated by Arp2/3 complex. *Biophys J.* 91:3519-3528.
- Marchand, J.B., D.A. Kaiser, T.D. Pollard, and H.N. Higgs. 2001. Interaction of WASP/Scar proteins with actin and vertebrate Arp2/3 complex. *Nat Cell Biol.* 3:76-82.
- Maree, A.F., A. Jilkin, A. Dawes, V.A. Grieneisen, and L. Edelstein-Keshet. 2006. Polarization and movement of keratocytes: a multiscale modelling approach. *Bull Math Biol.* 68:1169-1211.
- Marushchak, D., S. Grenklo, T. Johansson, R. Karlsson, and L.B. Johansson. 2007. Fluorescence depolarization studies of filamentous actin analyzed with a genetic algorithm. *Biophys J.* 93:3291-3299.
- Mattila, P.K., and P. Lappalainen. 2008. Filopodia: molecular architecture and cellular functions. *Nat Rev Mol Cell Biol.* 9:446-454.
- Matzavinos, A., and H.G. Othmer. 2007. A stochastic analysis of actin polymerization in the presence of twinfilin and gelsolin. *J Theor Biol.* 249:723-736.
- McDonald, D., G. Carrero, C. Andrin, G. de Vries, and M.J. Hendzel. 2006. Nucleoplasmic beta-actin exists in a dynamic equilibrium between low-mobility polymeric species and rapidly diffusing populations. *J Cell Biol.* 172:541-552.
- McGough, A., W. Chiu, and M. Way. 1998. Determination of the gelsolin binding site on F-actin: implications for severing and capping. *Biophys J.* 74:764-772.
- McGrath, J.L., N.J. Eungdamrong, C.I. Fisher, F. Peng, L. Mahadevan, T.J. Mitchison, and S.C. Kuo. 2003. The force-velocity relationship for the actin-based motility of *Listeria monocytogenes*. *Curr Biol.* 13:329-332.
- McGrath, J.L., E.A. Osborn, Y.S. Tardy, C.F. Dewey, Jr., and J.H. Hartwig. 2000. Regulation of the actin cycle in vivo by actin filament severing. *Proc Natl Acad Sci U S A.* 97:6532-6537.
- McGrath, J.L., Y. Tardy, C.F. Dewey, Jr., J.J. Meister, and J.H. Hartwig. 1998. Simultaneous measurements of actin filament turnover, filament fraction, and monomer diffusion in endothelial cells. *Biophys J.* 75:2070-2078.
- Michelot, A., J. Berro, C. Guerin, R. Boujemaa-Paterski, C.J. Staiger, J.L. Martiel, and L. Blanchoin. 2007. Actin-filament stochastic dynamics mediated by ADF/cofilin. *Curr Biol.* 17:825-833.

- Minehardt, T.J., P.A. Kollman, R. Cooke, and E. Pate. 2006. The open nucleotide pocket of the profilin/actin x-ray structure is unstable and closes in the absence of profilin. *Biophys J.* 90:2445-2449.
- Mogilner, A. 2009. Mathematics of cell motility: have we got its number? *Journal of mathematical biology.* 58:105-134.
- Mogilner, A., and L. Edelstein-Keshet. 2002. Regulation of actin dynamics in rapidly moving cells: a quantitative analysis. *Biophys J.* 83:1237-1258.
- Mogilner, A., and G. Oster. 1996. Cell motility driven by actin polymerization. *Biophys J.* 71:3030-3045.
- Mogilner, A., and G. Oster. 2003. Force generation by actin polymerization II: the elastic ratchet and tethered filaments. *Biophys J.* 84:1591-1605.
- Moseley, J.B., S. Maiti, and B.L. Goode. 2006. Formin proteins: purification and measurement of effects on actin assembly. *Methods Enzymol.* 406:215-234.
- Mueller, F., D. Mazza, T.J. Stasevich, and J.G. McNally. 2010. FRAP and kinetic modeling in the analysis of nuclear protein dynamics: what do we really know? *Curr Opin Cell Biol.*
- Mueller, F., P. Wach, and J.G. McNally. 2008. Evidence for a common mode of transcription factor interaction with chromatin as revealed by improved quantitative fluorescence recovery after photobleaching. *Biophys J.* 94:3323-3339.
- Mullins, R.D., J.A. Heuser, and T.D. Pollard. 1998. The interaction of Arp2/3 complex with actin: nucleation, high affinity pointed end capping, and formation of branching networks of filaments. *Proc Natl Acad Sci U S A.* 95:6181-6186.
- Nazarov, P.V., V.V. Apanasovich, V.M. Lutkovski, M.M. Yatskou, R.B. Koehorst, and M.A. Hemminga. 2004. Artificial neural network modification of simulation-based fitting: application to a protein-lipid system. *Journal of chemical information and computer sciences.* 44:568-574.
- Nazarov, P.V., R.B. Koehorst, W.L. Vos, V.V. Apanasovich, and M.A. Hemminga. 2006. FRET study of membrane proteins: simulation-based fitting for analysis of membrane protein embedment and association. *Biophys J.* 91:454-466.
- Neidl, C., and J. Engel. 1979. Exchange of ADP, ATP and 1: N6-ethenoadenosine 5'-triphosphate at G-actin. Equilibrium and kinetics. *European journal of biochemistry / FEBS.* 101:163-169.
- Neidt, E.M., B.J. Scott, and D.R. Kovar. 2009. Formin differentially utilizes profilin isoforms to rapidly assemble actin filaments. *J Biol Chem.* 284:673-684.
- Nelder, J.A., and R. Mead. 1965. A simplex method for function minimization. *Computer J.* 7:308-313.
- Ng, R., and J. Abelson. 1980. Isolation and sequence of the gene for actin in *Saccharomyces cerevisiae*. *Proc Natl Acad Sci U S A.* 77:3912-3916.
- Noireaux, V., R.M. Golsteyn, E. Friederich, J. Prost, C. Antony, D. Louvard, and C. Sykes. 2000. Growing an actin gel on spherical surfaces. *Biophys J.* 78:1643-1654.
- Oda, T., M. Iwasa, T. Aihara, Y. Maeda, and A. Narita. 2009. The nature of the globular- to fibrous-actin transition. *Nature.* 457:441-445.
- Orlova, A., A. Shvetsov, V.E. Galkin, D.S. Kudryashov, P.A. Rubenstein, E.H. Egelman, and E. Reisler. 2004. Actin-destabilizing factors disrupt filaments by means of a time reversal of polymerization. *Proc Natl Acad Sci U S A.* 101:17664-17668.
- Paavilainen, V.O., E. Bertling, S. Falck, and P. Lappalainen. 2004. Regulation of cytoskeletal dynamics by actin-monomer-binding proteins. *Trends Cell Biol.* 14:386-394.
- Paluch, E., and C.P. Heisenberg. 2009. Biology and physics of cell shape changes in development. *Curr Biol.* 19:R790-799.

- Paluch, E., J. van der Gucht, J.F. Joanny, and C. Sykes. 2006. Deformations in actin comets from rocketing beads. *Biophys J.* 91:3113-3122.
- Pantaloni, D., C. Le Clainche, and M.F. Carrier. 2001. Mechanism of actin-based motility. *Science.* 292:1502-1506.
- Patla, I., T. Volberg, N. Elad, V. Hirschfeld-Warneken, C. Grashoff, R. Fassler, J.P. Spatz, B. Geiger, and O. Medalia. 2010. Dissecting the molecular architecture of integrin adhesion sites by cryo-electron tomography. *Nat Cell Biol.* 12:909-915.
- Paul, A.S., and T.D. Pollard. 2008. The role of the FH1 domain and profilin in formin-mediated actin-filament elongation and nucleation. *Curr Biol.* 18:9-19.
- Paul, A.S., and T.D. Pollard. 2009. Review of the mechanism of processive actin filament elongation by formins. *Cell Motil Cytoskeleton.* 66:606-617.
- Peskin, C.S., G.M. Odell, and G.F. Oster. 1993. Cellular motions and thermal fluctuations: the Brownian ratchet. *Biophys J.* 65:316-324.
- Phair, R.D., S.A. Gorski, and T. Misteli. 2004. Measurement of dynamic protein binding to chromatin in vivo, using photobleaching microscopy. *Methods Enzymol.* 375:393-414.
- Phair, R.D., and T. Misteli. 2000. High mobility of proteins in the mammalian cell nucleus. *Nature.* 404:604-609.
- Plastino, J., S. Olivier, and C. Sykes. 2004. Actin filaments align into hollow comets for rapid VASP-mediated propulsion. *Curr Biol.* 14:1766-1771.
- Pollard, T.D. 1986. Rate constants for the reactions of ATP- and ADP-actin with the ends of actin filaments. *J Cell Biol.* 103:2747-2754.
- Pollard, T.D. 2007. Regulation of actin filament assembly by Arp2/3 complex and formins. *Annual review of biophysics and biomolecular structure.* 36:451-477.
- Pollard, T.D., and C.C. Beltzner. 2002. Structure and function of the Arp2/3 complex. *Current opinion in structural biology.* 12:768-774.
- Pollard, T.D., and G.G. Borisy. 2003. Cellular motility driven by assembly and disassembly of actin filaments. *Cell.* 112:453-465.
- Pollard, T.D., and J.A. Cooper. 2009. Actin, a central player in cell shape and movement. *Science.* 326:1208-1212.
- Ponti, A., P. Valtotton, W.C. Salmon, C.M. Waterman-Storer, and G. Danuser. 2003. Computational analysis of F-actin turnover in cortical actin meshworks using fluorescent speckle microscopy. *Biophys J.* 84:3336-3352.
- Poukkula, M., E. Kremneva, M. Serlachius, and P. Lappalainen. 2011. Actin-depolymerizing factor homology domain: a conserved fold performing diverse roles in cytoskeletal dynamics. *Cytoskeleton (Hoboken).* 68:471-490.
- Press, W.H., S.A. Teukolsky, W.T. Vetterling, and B.P. Flannery. 2007. Numerical recipes: The Art of scientific computing. Cambridge University Press, Cambridge. 1235 pp.
- Pring, M., M. Evangelista, C. Boone, C. Yang, and S.H. Zigmond. 2003. Mechanism of formin-induced nucleation of actin filaments. *Biochemistry.* 42:486-496.
- Quinlan, M.E., J.E. Heuser, E. Kerkhoff, and R.D. Mullins. 2005. Drosophila Spire is an actin nucleation factor. *Nature.* 433:382-388.
- Renault, L., B. Bugyi, and M.F. Carrier. 2008. Spire and Cordon-bleu: multifunctional regulators of actin dynamics. *Trends Cell Biol.* 18:494-504.
- Reymann, A.C., C. Suarez, C. Guerin, J.L. Martiel, C.J. Staiger, L. Blanchoin, and R. Boujemaa-Paterski. 2011. Turnover of branched actin filament networks by stochastic fragmentation with ADF/cofilin. *Mol Biol Cell.* 22:2541-2550.
- Riveline, D., E. Zamir, N.Q. Balaban, U.S. Schwarz, T. Ishizaki, S. Narumiya, Z. Kam, B. Geiger, and A.D. Bershadsky. 2001. Focal contacts as mechanosensors: externally

applied local mechanical force induces growth of focal contacts by an mDia1-dependent and ROCK-independent mechanism. *J Cell Biol.* 153:1175-1186.

Roland, J., J. Berro, A. Michelot, L. Blanchoin, and J.L. Martiel. 2008. Stochastic severing of actin filaments by actin depolymerizing factor/cofilin controls the emergence of a steady dynamical regime. *Biophys J.* 94:2082-2094.

Romero, S., C. Le Clainche, D. Didry, C. Egile, D. Pantaloni, and M.F. Carlier. 2004. Formin is a processive motor that requires profilin to accelerate actin assembly and associated ATP hydrolysis. *Cell.* 119:419-429.

Sabass, B., and U.S. Schwarz. 2010. Modeling cytoskeletal flow over adhesion sites: competition between stochastic bond dynamics and intracellular relaxation. *Journal of physics. Condensed matter : an Institute of Physics journal.* 22:194112.

Samarin, S., S. Romero, C. Kocks, D. Didry, D. Pantaloni, and M.F. Carlier. 2003. How VASP enhances actin-based motility. *J Cell Biol.* 163:131-142.

Schafer, D.A., P.B. Jennings, and J.A. Cooper. 1996. Dynamics of capping protein and actin assembly in vitro: uncapping barbed ends by polyphosphoinositides. *J Cell Biol.* 135:169-179.

Schaub, S., J.J. Meister, and A.B. Verkhovsky. 2007. Analysis of actin filament network organization in lamellipodia by comparing experimental and simulated images. *J Cell Sci.* 120:1491-1500.

Schreiber, C.H., M. Stewart, and T. Duke. 2010. Simulation of cell motility that reproduces the force-velocity relationship. *Proc Natl Acad Sci U S A.* 107:9141-9146.

Seiffert, S., and W. Oppermann. 2005. Systematic evaluation of FRAP experiments performed in a confocal laser scanning microscope. *J Microsc.* 220:20-30.

Sellers, J.R., and C. Veigel. 2006. Walking with myosin V. *Curr Opin Cell Biol.* 18:68-73.

Sept, D., and J.A. McCammon. 2001. Thermodynamics and kinetics of actin filament nucleation. *Biophys J.* 81:667-674.

Sept, D., J. Xu, T.D. Pollard, and J.A. McCammon. 1999. Annealing accounts for the length of actin filaments formed by spontaneous polymerization. *Biophys J.* 77:2911-2919.

Shaner, N.C., G.H. Patterson, and M.W. Davidson. 2007. Advances in fluorescent protein technology. *J Cell Sci.* 120:4247-4260.

Small, J.V. 1994. Lamellipodia architecture: actin filament turnover and the lateral flow of actin filaments during motility. *Semin Cell Biol.* 5:157-163.

Soumpasis, D.M. 1983. Theoretical analysis of fluorescence photobleaching recovery experiments. *Biophys J.* 41:95-97.

Splettstoesser, T., K.C. Holmes, F. Noe, and J.C. Smith. 2011. Structural modeling and molecular dynamics simulation of the actin filament. *Proteins.* 79:2033-2043.

Sprague, B.L., F. Muller, R.L. Pego, P.M. Bungay, D.A. Stavreva, and J.G. McNally. 2006. Analysis of binding at a single spatially localized cluster of binding sites by fluorescence recovery after photobleaching. *Biophys J.* 91:1169-1191.

Sprague, B.L., R.L. Pego, D.A. Stavreva, and J.G. McNally. 2004. Analysis of binding reactions by fluorescence recovery after photobleaching. *Biophys J.* 86:3473-3495.

Stachowiak, M.R., and B. O'Shaughnessy. 2008. Kinetics of stress fibers. *New Journal of Physics.* 10:025002.

Steffen, A., J. Faix, G.P. Resch, J. Linkner, J. Wehland, J.V. Small, K. Rottner, and T.E. Stradal. 2006. Filopodia formation in the absence of functional WAVE- and Arp2/3-complexes. *Mol Biol Cell.* 17:2581-2591.

Stossel, T.P. 1993. On the crawling of animal cells. *Science.* 260:1086-1094.

Stukalin, E.B., and A.B. Kolomeisky. 2006. ATP hydrolysis stimulates large length fluctuations in single actin filaments. *Biophys J.* 90:2673-2685.

- Svitkina, T.M., and G.G. Borisy. 1999. Arp2/3 complex and actin depolymerizing factor/cofilin in dendritic organization and treadmilling of actin filament array in lamellipodia. *J Cell Biol.* 145:1009-1026.
- Svitkina, T.M., E.A. Bulanova, O.Y. Chaga, D.M. Vignjevic, S. Kojima, J.M. Vasiliev, and G.G. Borisy. 2003. Mechanism of filopodia initiation by reorganization of a dendritic network. *J Cell Biol.* 160:409-421.
- Tardy, Y., J.L. McGrath, J.H. Hartwig, and C.F. Dewey. 1995. Interpreting photoactivated fluorescence microscopy measurements of steady-state actin dynamics. *Biophys J.* 69:1674-1682.
- Theriot, J.A. 1997. Accelerating on a treadmill: ADF/cofilin promotes rapid actin filament turnover in the dynamic cytoskeleton. *J Cell Biol.* 136:1165-1168.
- Theriot, J.A., T.J. Mitchison, L.G. Tilney, and D.A. Portnoy. 1992. The rate of actin-based motility of intracellular *Listeria monocytogenes* equals the rate of actin polymerization. *Nature.* 357:257-260.
- Tholl, S., F. Moreau, C. Hoffmann, K. Arumugam, M. Dieterle, D. Moes, K. Neumann, A. Steinmetz, and C. Thomas. 2011. Arabidopsis actin-depolymerizing factors (ADFs) 1 and 9 display antagonist activities. *FEBS Lett.* 585:1821-1827.
- Tobacman, L.S., and E.D. Korn. 1983. The kinetics of actin nucleation and polymerization. *J Biol Chem.* 258:3207-3214.
- Tobias, E.S., A.F. Hurlstone, E. MacKenzie, R. McFarlane, and D.M. Black. 2001. The TES gene at 7q31.1 is methylated in tumours and encodes a novel growth-suppressing LIM domain protein. *Oncogene.* 20:2844-2853.
- Toneguzzo, F., A.C. Hayday, and A. Keating. 1986. Electric field-mediated DNA transfer: transient and stable gene expression in human and mouse lymphoid cells. *Molecular and cellular biology.* 6:703-706.
- Tseng, Y., B.W. Schafer, S.C. Almo, and D. Wirtz. 2002. Functional synergy of actin filament cross-linking proteins. *J Biol Chem.* 277:25609-25616.
- Turnacioglu, K.K., J.W. Sanger, and J.M. Sanger. 1998. Sites of monomeric actin incorporation in living PtK2 and REF-52 cells. *Cell Motil Cytoskeleton.* 40:59-70.
- Upadhyaya, A., and A. van Oudenaarden. 2003. Biomimetic systems for studying actin-based motility. *Curr Biol.* 13:R734-744.
- Uruno, T., K. Remmert, and J.A. Hammer, 3rd. 2006. CARMIL is a potent capping protein antagonist: identification of a conserved CARMIL domain that inhibits the activity of capping protein and uncaps capped actin filaments. *J Biol Chem.* 281:10635-10650.
- Vallotton, P., S.L. Gupton, C.M. Waterman-Storer, and G. Danuser. 2004. Simultaneous mapping of filamentous actin flow and turnover in migrating cells by quantitative fluorescent speckle microscopy. *Proc Natl Acad Sci U S A.* 101:9660-9665.
- van der Gucht, J., E. Paluch, J. Plastino, and C. Sykes. 2005. Stress release drives symmetry breaking for actin-based movement. *Proc Natl Acad Sci U S A.* 102:7847-7852.
- van Kampen, N.G. 2007. Stochastic processes in physics and chemistry. Elsevier, Amsterdam. 464 pp.
- Van Troys, M., L. Huyck, S. Leyman, S. Dhaese, J. Vandekerckhove, and C. Ampe. 2008. Ins and outs of ADF/cofilin activity and regulation. *Eur J Cell Biol.* 87:649-667.
- Vandekerckhove, J., and K. Weber. 1978. Actin amino-acid sequences. Comparison of actins from calf thymus, bovine brain, and SV40-transformed mouse 3T3 cells with rabbit skeletal muscle actin. *European journal of biochemistry / FEBS.* 90:451-462.
- Vavylonis, D., D.R. Kovar, B. O'Shaughnessy, and T.D. Pollard. 2006. Model of formin-associated actin filament elongation. *Mol Cell.* 21:455-466.
- Vavylonis, D., Q. Yang, and B. O'Shaughnessy. 2005. Actin polymerization kinetics, cap structure, and fluctuations. *Proc Natl Acad Sci U S A.* 102:8543-8548.

- Vink, M., M. Simonetta, P. Transidico, K. Ferrari, M. Mapelli, A. De Antoni, L. Massimiliano, A. Ciliberto, M. Faretta, E.D. Salmon, and A. Musacchio. 2006. In vitro FRAP identifies the minimal requirements for Mad2 kinetochore dynamics. *Curr Biol.* 16:755-766.
- Wagner, A.E., P. Huebbe, T. Konishi, M.M. Rahman, M. Nakahara, S. Matsugo, and G. Rimbach. 2008. Free radical scavenging and antioxidant activity of ascorbigen versus ascorbic acid: studies in vitro and in cultured human keratinocytes. *Journal of agricultural and food chemistry.* 56:11694-11699.
- Wang, Y.L. 1984. Reorganization of actin filament bundles in living fibroblasts. *J Cell Biol.* 99:1478-1485.
- Watanabe, N. 2012. Fluorescence single-molecule imaging of actin turnover and regulatory mechanisms. *Methods Enzymol.* 505:219-232.
- Watanabe, N., and T.J. Mitchison. 2002. Single-molecule speckle analysis of actin filament turnover in lamellipodia. *Science.* 295:1083-1086.
- Webb, D.J., J.T. Parsons, and A.F. Horwitz. 2002. Adhesion assembly, disassembly and turnover in migrating cells -- over and over and over again. *Nat Cell Biol.* 4:E97-100.
- Wegner, A. 1976. Head to tail polymerization of actin. *J Mol Biol.* 108:139-150.
- Weisswange, I., T.P. Newsome, S. Schleich, and M. Way. 2009. The rate of N-WASP exchange limits the extent of ARP2/3-complex-dependent actin-based motility. *Nature.* 458:87-91.
- Wiesner, S., E. Helfer, D. Didry, G. Ducouret, F. Lafuma, M.F. Carlier, and D. Pantaloni. 2003. A biomimetic motility assay provides insight into the mechanism of actin-based motility. *J Cell Biol.* 160:387-398.
- Witke, W. 2004. The role of profilin complexes in cell motility and other cellular processes. *Trends Cell Biol.* 14:461-469.
- Wolfenson, H., A. Bershadsky, Y.I. Henis, and B. Geiger. 2011. Actomyosin-generated tension controls the molecular kinetics of focal adhesions. *J Cell Sci.* 124:1425-1432.
- Wolfenson, H., Y.I. Henis, B. Geiger, and A.D. Bershadsky. 2009. The heel and toe of the cell's foot: a multifaceted approach for understanding the structure and dynamics of focal adhesions. *Cell Motil Cytoskeleton.* 66:1017-1029.
- Yang, C., M. Pring, M.A. Wear, M. Huang, J.A. Cooper, T.M. Svitkina, and S.H. Zigmond. 2005. Mammalian CARMIL inhibits actin filament capping by capping protein. *Dev Cell.* 9:209-221.
- Yang, C., and T. Svitkina. 2011. Filopodia initiation: focus on the Arp2/3 complex and formins. *Cell adhesion & migration.* 5:402-408.
- Yarmola, E.G., D.A. Dranishnikov, and M.R. Bubb. 2008. Effect of profilin on actin critical concentration: a theoretical analysis. *Biophys J.* 95:5544-5573.
- Yatskou, M.M., H. Donker, E.G. Novikov, R.B.M. Koehorst, A. van Hoek, V.V. Apanasovich, and T.J. Schaafsma. 2001. Nonisotropic excitation energy transport in organized molecular systems: Monte Carlo simulation-based analysis of time-resolved fluorescence. *J Phys Chem A.* 105:9498-9508.
- Yatskou, M.M., M. Meyer, S. Huber, M. Pfenniger, and G. Calzaferri. 2003. Electronic excitation energy migration in a photonic dye--zeolite antenna. *Chemphyschem : a European journal of chemical physics and physical chemistry.* 4:567-587.
- Yeoh, S., B. Pope, H.G. Mannherz, and A. Weeds. 2002. Determining the differences in actin binding by human ADF and cofilin. *J Mol Biol.* 315:911-925.
- Yoshigi, M., L.M. Hoffman, C.C. Jensen, H.J. Yost, and M.C. Beckerle. 2005. Mechanical force mobilizes zyxin from focal adhesions to actin filaments and regulates cytoskeletal reinforcement. *J Cell Biol.* 171:209-215.

Zaidel-Bar, R., C. Ballestrem, Z. Kam, and B. Geiger. 2003. Early molecular events in the assembly of matrix adhesions at the leading edge of migrating cells. *J Cell Sci.* 116:4605-4613.

Zamir, E., M. Katz, Y. Posen, N. Erez, K.M. Yamada, B.Z. Katz, S. Lin, D.C. Lin, A. Bershadsky, Z. Kam, and B. Geiger. 2000. Dynamics and segregation of cell-matrix adhesions in cultured fibroblasts. *Nat Cell Biol.* 2:191-196.

Zheng, X., K. Diraviyam, and D. Sept. 2007. Nucleotide effects on the structure and dynamics of actin. *Biophys J.* 93:1277-1283.

Zigmond, S.H. 2004. Formin-induced nucleation of actin filaments. *Curr Opin Cell Biol.* 16:99-105.

Appendix

Appendix A. List of computational tools and other supplementary files available at the webpage <http://actinsim.uni.lu>

1. ActinSimChem executable – stand-alone software for simulating actin polymerisation cycle;
2. ActinSimChem manual – user manual for ActinSimChem program;
3. ActinFRAP – computational script for modelling FRAP experiments with actin filaments in Mathematica (Wolfram Research Inc.);
4. FRAPAnalyser – stand-alone software for the processing FRAP intensities;
5. FRAPAnalyser manual – user manual for FRAPAnalyser program;
6. frap_parameters_plots – R script for the statistical analysis and plotting model parameters estimated using FRAPAnalyser;
7. BiomimFRAPQuant – ImageJ macro for quantification of FRAP recoveries in experiments with the actin-based biomimetic assay;
8. BiomimFRAPKymo – ImageJ macro for the analysis of spatial effects of actin turnover with FRAP and the actin-based biomimetic assay.

Appendix B. Protocol for preparation of the actin-based motility assay

I. Coating beads with GST-VCA

Materials:

- Polystyrene beads (Polysciences), 3 μ m, 2.5% solids
- Borate buffer, 0.1M pH8
- Xb-buffer: HEPES pH7.8 – 10 mM; KCl – 100 mM; MgCl₂ – 1 mM; ATP – 1 mM; CaCl₂ – 0.1 mM
- Xb-buffer supplemented with 1% BSA

Procedure:

Preparation in 500 μ l tube

1. Washing of the beads – repeat twice
 - a. Mix 7.9 μ l of beads with 50 μ l of borate buffer
 - b. Centrifuge (1', 10000g, 4C), remove supernatant
2. Coating of the beads
 - a. Mix 7.9 μ l of the washed beads with 3.8 μ l of GST-VCA stock solution and 38.3 μ l of Xb-buffer. *Calculated for 66 μ M of GST-VCA stock concentration. Final mix volume is 50 μ l with 5 μ M of GST-VCA.*
 - b. Incubate 1 hour on the rotating wheel at 4C
 - c. Centrifuge (1', 10000g, 4C), remove supernatant
3. Washing after coating (to remove unbound protein) – repeat two times
 - a. Mix beads with 50 μ l of Xb-buffer
 - b. Centrifuge (1', 10000g, 4C), remove supernatant
4. Saturation of bead surface with BSA
 - a. Mix beads with 50 μ l of Xb-buffer+BSA1%
 - b. Incubate 15 min on ice
 - c. Centrifuge (1', 10000g, 4C), remove supernatant
5. Storage of the coated beads
 - a. Mix beads with 45 μ l of Xb-buffer and 5 μ l of Xb-buffer+BSA1%. *Bead are stored in Xb-buffer containing 0.1%BSA on ice and used during 4 days after coating.*

II. Preparation of F-actin

Materials:

- Skeletal muscle G-actin stock solution ($\approx 232 \mu\text{M}$) – stored at -80°C
- G-buffer: Tris pH7.8 – 5 mM; CaCl_2 – 0.1 mM; ATP – 0.2 mM; DTT – 1 mM;
- EGTA (10 mM)
- MgCl_2 (2 mM and 50mM)
- KCl (1M)

Procedure:

1. Mix the following:
9.1 μl of G-actin
+ 20.8 μl of G-buffer (completed)
+ 1.25 μl of MgCl_2 (2 mM)
+ 0.6 μl of EGTA (10mM)
2. Incubate 5 min on ice, vortex gently
3. Add:
+ 0.72 μl of MgCl_2 (50 mM)
+ 3.6 μl of KCl (1 M)
4. Vortex gently
5. Polymerise 1h on ice.
Polymerised actin stored on ice and used during 3 following days.

III. Motility sample preparation

Materials:

- Ascorbic acid (Vitamin C)
- Xb-buffer 5x: HEPES pH7.8 – 50 mM; KCl – 500 mM; MgCl_2 – 5 mM; ATP – 5 mM; CaCl_2 – 0.5 mM
- BSA 10% (100 mg/ml, filtered)
- ATP mix: ATP – 12 mM; MgCl_2 – 24 mM; DabCo – 0.88 mM; DTT – 40 mM
- Coated beads (see above)
- Polymerised actin (see above)
- Methylcellulose 1%
- Cofilin
- Profilin
- Gelsolin
- Arp2/3
- Alexa-488 labelled actin
- Rhodamine-labelled actin
- CaCl_2 (10 mM)

All proteins are supplied as a powder and stored at 4°C . When required, protein is reconstituted in Milli-Q water. This solution is aliquoted into experiment-sized amounts and stored at -80°C . Because actual concentration of stock solutions was found to vary from one delivery to another, actual stock concentrations of all proteins are determined by scanning Commasie Blue-stained SDS PAGE gels using BSA as a standard.

Procedure:

Mix in 500 µl tube, keep the order:

| | Stock conc-ion | Volume, µl | Final conc-ion | Remarks |
|----------------------------|-----------------------|-------------------|-----------------------|--|
| Ascorbic acid, mg/ml | 40 | 0.90 | 1.5 | Personal experience: not to affect polymerisation by observation with fluorescent light |
| Xb buffer5X | | 4.00 | | To have ~1X of Xb-buffer in the final mix |
| BSA(10% - filtered), mg/ml | 100 | 1.20 | 5.0 | |
| h Cofilin µM | 123 | 1.95 | 10.0 | 0-10 µM is normally used |
| Profilin µM | 31 | 0.78 | 1.0 | 1-3 µM is normally used |
| F-Actin µM | 58 | 2.48 | 6.0 | |
| Gelsolin µM | 2.6 | 0.46 | 0.05 | 0.05-0.25 µM is normally used |
| Arp2/3 µM | 3.0 | 0.80 | 0.10 | 0.05-0.20 µM is normally used |
| G-actin Alexa 488 µM | 20.0 | 0.90 | 0.75 | Total actin concentration is always 7.5 µM. For experiments with two fluorescent labels 10% of Alexa-labelled actin and 10% of rhodamine-labelled actin are used |
| Actin rhodamine µM | 23.2 | 0.78 | 0.75 | |
| CaCl ₂ , mM | 10 | 0.36 | 0.15 | Required for activation of gelsolin |
| ATP Mix | | 3.60 | | In the final mix - 1.8 mM of ATP; - 0.13 mM of DabCo; - 6 mM of DTT |
| Coated beads | | 1.00 | | |
| Methylcellulose % | 1 | 4.80 | 0.2 | |
| Total volume | | 24 | | |

Distribute 5 microliters of the final mix between a microscopy glass slide and a coverslip. Image immediately with epifluorescence or confocal microscope.

Appendix C. Supplementary data on stochastic simulation model

Evaluation of the biochemical parameters

To investigate further the consistency of systems behaviour, we tested the effects of variations of biochemical parameters on the simulation results.

Sensitivity to concentrations

We first evaluated the influence of concentration effects. The concentration of actin monomers affects two key steps of the polymerization kinetics (see Fig. 3.4a, main text): the rate of spontaneous nucleation, which is, at least in a cubic, proportional to actin monomer concentration (Table 3.1, main text) and the elongation rate. Capping proteins work as a filament nucleator and cap the corresponding ends of filaments, stopping both elongation and dissociation at that end. Both effects are depicted in Fig. S4a (barbed-end capping protein) and S4b (pointed end capping proteins). Obviously, increasing the concentration of these proteins leads to increase of the overall polymerization rate due to faster nucleation. Even for barbed-end capping proteins this holds true, however, the effect is less pronounced than in the case of pointed-end cappers, because the filaments exclusively elongate from their minus end. As a consequence, the critical concentration (steady-state concentration of actin monomers) is higher in the presence of barbed-end capping proteins.

If we exclude the nucleation activity of capping proteins, i.e. setting $k_{CBNU}=k_{CPNU}=0$, the concentration dependency significantly changes. As expected from experimental data, the increase of barbed-end capping protein concentration leads now to a decrease of the polymerization rate (Fig. S4c). A saturation effect can be observed in this plot since almost no difference in actin dynamics can be seen using a concentration of capping proteins of 0.1 to 1 μM . This corresponds to the situation when all barbed ends are capped.

Interestingly, pointed-end capping proteins had no significant effect on actin polymerization kinetics (Fig. S4d). Concentration variation of the pointed-end capping protein by a factor of 1000, ranging from 0.001 to 1 μM , did not affect actin polymerization kinetics under the assumption that the capping protein does not act as a nucleator.

Among the proteins we considered, formin had the most pronounced effect. It works both as a nucleator and an enhancer of the elongation (Romero et al., 2004) and this is evident from Figs. 3.4e and 3.5c of the main text. Due to its high nucleation ability, almost no *lag phase* is observed in the simulations and in the pyrene-actin experiments for formin-containing samples.

Sensitivity to the rate constants

We estimated the effects of various rate constants on actin polymerization. The association and dissociation rate constants of ATP-actin monomers to or from actin filaments were first investigated (Figs. S4e and S4f). Fig. S4e shows that already a moderate, two fold increase (top curve, squares) or decrease (bottom curve, triangles) in monomer association and dissociation rates at the barbed ends strongly affects actin polymerization kinetics. However, if the same numerical experiment is performed for the pointed ends, almost no effect can be seen (Fig. S4f). This is due to the fact that the actin exchange at the pointed ends is approximately 10 times slower than that at the barbed ends and thus elongation proceeds mainly via the barbed end. This underscores why in cells the actin system requires a more extensive array of barbed end regulators.

Fig. S4g shows the effect of the spontaneous nucleation (the rate k_{SNUC}) on actin polymerization. The change in k_{SNUC} from 10^{-9} to $5 \times 10^{-9} \mu\text{M}^{-2}\text{s}^{-1}$ leads to significant changes in the predicted concentration of F-actin protomers (diamonds and triangles in Fig. S4g). The simulation shows that increasing the

nucleation rate results in a considerable increase in polymerized actin due to the formation of oligomeric nuclei. It suggests that the spontaneous nucleation is an important effect that plays a key role in polymerization and thus cannot be neglected or shut off during analysis of experimental systems with computational models. However, our simulations do not provide the exact value of the elongation rate constant at which nuclei started to grow since the elongation process may generally be depended on other systems parameters, such as association/dissociation rates of monomers at plus ends, that often might hardly be distinguishable in experiments.

Fig. S4h demonstrates the effect of filament aging on the concentration of F-actin. Variation in the aging rate does not modify the actin polymerization kinetics until steady-state is reached. Moreover, changing of k_{TOD} from $7 \times 10^{-4} \text{ s}^{-1}$ to 0.7 s^{-1} has only a minor effect on the steady state level of protomer concentration. This is not surprising since polymerization of pure actin is uncoupled from ATP hydrolysis.

Validation of the source code

To ensure the quality of the simulation algorithm we performed several validation procedures. Our simulation algorithms were tested against reported analytical models covering some selected idealised actin systems of a relatively limited number of reagents and reactions. Any further update of the simulation model, by adding additional reagents or reactions, does/will not perturb the stochastic simulation scheme since the procedure of decision control at each simulation step is integrative and hierarchically built in terms of reagents and reactions. The extension of the model with new reagents and reactions consists in updating classes of individual filaments and properties of simulated volume. In order to control a balance between internal/external objects of the classes and limits for systems parameters we developed a dedicated debug system. The debug procedure summarizes any quantities of objects of check-in properties and compares the matching with numbers of currently simulated molecules for the considered reagents, e.g. – a number of filament branches with capped barbed ends or a number of the ATF protomers. For SRF model an additional validation step was implemented that verifies the nucleotide sequence of filament subunits.

In order to extensively validate the source code, the debug procedure was launched after simulation of each reaction shown in Fig. 3.1 of the main text. The code was verified for a wide range of reaction rate constants, typically covering ± 2 orders of magnitudes from the values presented in Table 3.2 of the main text, and validated for simulated volumes higher than $30 \mu\text{m}^3$.

Comparison of the simulation algorithms

We examined several formulations of the main stochastic simulation algorithm. In particular, the exact Gillespie's "direct" and "first reaction" and the "next reaction" algorithms (Gibson and Bruck, 2000). The inexact "τ-leap" algorithm has been tested as well.

The "next reaction" algorithm is the improvement of the "direct" and "first reaction" algorithms, where three specific features are implemented: i) in each modelling iteration just one random number is generated (*versus* two random numbers in the "direct" method and l random numbers in "first reaction" algorithm, where l is the number of reactions in a system); ii) an advanced search of a minimal value for the reaction time due to indexed priority queue; iii) re-calculation of reaction probabilities a_i , (*cf.* Eq. (3.1), (3.2), main text) for those reactions that were affected in the current simulation cycle; subsequently, the dependency graph is constructed. In this graph, nodes represent the reactions in the system, an edge from the i -th node to j -th node is drawn if the i -th reaction influences the probability a_j of j -th reaction. For our models the *a priori* prediction of this graph is not evident, because many reactions have multiple outcome and can potentially change different concentrations, e.g. the dissociation of an ATF monomer from a barbed end can result in changing either two concentrations, [ATF] and [ATM], or four concentrations, [ATF], [ATM], [FTB], [FDB], or even more concentrations in the case of complete filament dissociation. Therefore in our realization of the

Gibson-Bruck algorithm, we introduced only the repeatable usage of the random events times and advanced search of minimal time.

The comparison of the algorithms was performed for several compositions of the actin system: actin alone, actin with barbed-end capping protein, actin with pointed-end capping protein, actin with capping proteins of both types, actin with formin, and finally the mix of all mentioned reagents, except the Arp2/3 complex. The initial concentrations of reagents were: $[ATM]_{t=0} = 2 \mu\text{M}$, $[CBM]_{t=0} = [CPM]_{t=0} = 10^{-2} \mu\text{M}$, $[FOM]_{t=0} = 10^{-3} \mu\text{M}$. The maximal simulation time t_{max} was 8000 s. Computer simulations were performed for a volume V equal to $8000 \mu\text{m}^3$. The resulted times spent for the simulations by the "direct" and "first reaction", "next reaction" algorithms are plotted in Fig. S5a. The Gillespie's "direct" modelling technique has demonstrated the most efficient in time simulations.

The "first" reaction method was found as the slowest one among the modelling methods. It is due to enormous generation of random numbers in modelling of one reaction. The modelling by the "next reaction" algorithm was faster than "first reaction" method, but obviously slower than the Gillespie's direct algorithm. A similar observation for these three methods has been reported Cao and coworkers (Cao et al., 2004). According their conclusions, the "direct" algorithm works faster than the "next reaction" algorithm when the occurrence of a reaction influences probability values a_i for a small number of reactions, i.e. each node of the directed graph has a few incoming and outgoing edges. In our case, when the current reaction may have an influence on many reaction probabilities a_i , the realization of a dependency graph would not give any improvement for simulation speed, even if it was algorithmically realistic.

The inexact " τ -leap" algorithm was found unusable for the systems under consideration here. It simulates properly the molecular systems where the number of molecules in a molecular pool significantly exceeds the number of reacting molecules during each time step. This is not the case in our modelled systems where the filament binding sites are approaching the low concentration of 10^{-10} M .

Error analysis

The analysis of the approximation error of the simulation model is an important factor to take into account when evaluating results of computer simulations. One of the chief concerns is to be able to get as accurate an approximation as possible. Increasing the simulated volume V or/and averaging the results of n_A independent simulations may improve the approximation accuracy in simulations. We therefore discuss here the associated error statistics and computational efficiency of the developed models.

As an approximation error we chose the sum of squared residuals E of the simulated data S and the precise or reference data F . Such reference data are expected to be either an exact solution or a stochastic approximation at $n_A \rightarrow \infty$ and $V \rightarrow \infty$. Then, the equation for E is

$$E = \sum_{i=1}^{N_t} (S_i(n_A, V) - F_i)^2 \quad (\text{S1})$$

where N_t is the number of data points, $S_i(n, V)$ and F_i are the simulated and reference concentrations, for example of F-actin at the time t_i (i -th data point).

As the values of n_A and V are finite, any estimation of the sum of squared residuals E is a random variable. We estimate the expected value of E using Eq. S2.

$$\langle E \rangle_{M \rightarrow \infty} = \frac{1}{M} \sum_{m=1}^M E_m = \frac{1}{M} \sum_{m=1}^M \sum_{i=1}^{N_t} (S_{im}(n_A, V) - F_{im})^2 \quad (S2)$$

where M is the number of independent statistical experiments, E_m is the sum of squared residuals in the m -th statistical experiment. Manipulating with the summation order in Eq. S2 yields

$$\langle E \rangle_{M \rightarrow \infty} = \sum_{i=1}^{N_t} \left[\frac{1}{M} \sum_{m=1}^M (S_{im}(n_A, V) - F_{im})^2 \right] \quad (S3)$$

Noticing that the expression in the square brackets is the variation σ_i^2 of a residual at the i -th time point Eq. (S2) transforms into Eq. (S4). The expected value for the sum of squared residuals $\langle E \rangle_{M \rightarrow \infty}$ equals to the sum of variations in the time points N_t :

$$\langle E \rangle_{M \rightarrow \infty} = \sum_{i=1}^{N_t} \sigma_i^2 \quad (S4)$$

The problem of calculation of an approximation error is therefore converted to calculating the variations of the residuals at the selected time points. The simulated concentration $S_i(n, V)$, is a result of n_A simulations in the volume V , that is

$$S_i(n_A, V) = \frac{1}{n_A} \sum_{j=1}^{n_A} S_{ij}(V) \quad (S5)$$

Assume that the simulated volume V can be approximated by the k small independent minimal (critical) volumes V_{min} , $V = k * V_{min}$, the size of which is calculated from the estimation of a certain amount of protomers required to simulate a representative filament structure. Then, the simulated concentration $S_{ij}(V)$ is

$$S_{ij}(V) = \frac{N_{ij}}{V} = \frac{\sum_{l=1}^k N_{ijl}}{k V_{min}} = \frac{1}{k} \sum_{l=1}^k S_{ijl} \quad (S6)$$

Where N_{ij} and N_{ijl} are the number of molecules in the volumes V and V_{min} respectively, $s_{ijl} = \frac{N_{ijl}}{V_{min}}$

is the simulated concentration of the F-actin in the l -th minimal volume V_{min} . Putting Eq. S6 into Eq. S5 gives

$$S_i(n_A, V) = \frac{1}{n_A} \sum_{j=1}^{n_A} \left(\frac{1}{k} \sum_{l=1}^k s_{ijl} \right) = \frac{1}{n_A k} \sum_{j=1}^{n_A} \sum_{l=1}^k s_{ijl} \quad (S7)$$

Recounting for the index $q = k(j-1) + l$ simplifies Eq. (S7) to

$$S_i(n_A, V) = \frac{1}{n_A k} \sum_{q=1}^{n_A k} s_{iq} \quad (S8)$$

Suppose that the simulated concentration s_{iq} for the minimal volume at the i -th time point is a normally distributed random variable, with mean F_i and variance $\hat{\sigma}_i^2$. Then, the estimation of the variance of the concentration in the volume V after n_A averaging at the i -th time point is

$$\sigma_i^2 = \frac{\hat{\sigma}_i^2}{n_A k} = \frac{\hat{\sigma}_i^2 V_{\min}}{n_A V} \quad (\text{S9})$$

Combining Eq. (S4) and Eq. (S9) yields

$$\langle E \rangle_{M \rightarrow \infty} = \frac{V_{\min}}{n_A V} \sum_{i=1}^{N_i} \hat{\sigma}_i^2. \quad (\text{S10})$$

For the given system V_{\min} is constant, and, therefore, the expected value of the sum of squared residuals E is inversely proportional to n_A and V .

To control the computational efficiency of the developed models, we take the simulation time T , that is the time spent by a PC to compute a model in the “virtual” time range $[t_0, t_{\max}]$. Evidently, on the one hand, the simulation time T is a linear function of the number of simulations $T = \alpha \cdot n_A$, where α is a constant coefficient of proportionality. On the other hand, the simulation time T should be a function of the simulated volume V . We checked the dependence between V and T on two representative examples of actin polymerization systems: i) the actin polymerization and ii) full-reactant assay, except the Arp2/3 complex, in terms of the nSRF model. The corresponding results are shown in Fig. S5b. We observed a nonlinear dependence between the simulation time T and the simulated volume V that can be well fitted using Eq. (S11).

$$T = \gamma \cdot V^2 + \beta \cdot V \quad (\text{S11})$$

where γ, β are constants, coefficients of proportionality. It is well known (Gillespie, 1976) that the computational cost of the Gillespie’s direct method depends linearly on the number of reactions present in the system, that, in turn, are proportional to the simulated volume V , as is evident from the Eqs. (3.1) and (3.2) of the main text. We justify the nonlinear computational cost as the consequence of the filament structure simulation. It algorithmically resulted from the procedure of searching a specific filament, for example, the filaments with ATP actin on the barbed end for the simulation of the reaction DITB (Table 3.2). We estimated the computational time of latter search that is proportional to the total number of filaments, i.e. to the volume V , and a sum of other minor calculations independent on the volume. Therefore, the total simulation time is the product of the computational costs required for simulating the bulk of reaction events and specific filament structures and searches.

Eqs. (S10) and (S11) indicate that an increase in n_A is computationally more efficient than expanding the V to minimize the computational time for the desired approximation error E .

Analytical models for actin polymerization systems

Actin polymerization system. An analytical model of a pure actin system can mathematically be described by a balanced set of ordinary differential equations for changes in concentrations of reagents. This model can be used to interpret a simple system and to validate a simulation model (which can be used further for more complex systems). A similar analytical approach for the evaluation of filamentous actin kinetics was reported in (Carlsson et al., 2004). In several reports (Bindschadler et al., 2004; Stukalin and Kolomeisky, 2006) equations were derived to study the nucleotide profile in the steady-state actin cycle (changes in concentrations were equated to zero).

The aging (ATP-hydrolysis) is not considered in this analytical model. To include it, the nucleotide profile of filaments, dynamically changed with time, must be developed.

The analytical model integrates as reagents: actin monomers (ATM), actin protomers (ATF), barbed ends (FTB) and pointed ends (FDB). Taking in account that $[ATF] + [ATM] = A = \text{const}$ and $[FTB] = [FDB]$, there are two linearly independent variables in this system, for example, $[ATF]$ and $[FTB]$. The reagents participate in five biochemical reactions: spontaneous nucleation, associations at barbed and pointed ends and dissociations at barbed and pointed ends (*cf.* Table 3.2 of the main text). The resulting set of differential equations is:

$$\begin{cases} \frac{d[ATF]}{dt} = 3k_{\text{SNUC}} \left(A - [ATF] - \frac{k_{\text{DITB}}}{k_{\text{ASTB}}} \right)^3 + k_{\text{ASTB}}[FTB] \left(A - [ATF] - \frac{k_{\text{DITB}}}{k_{\text{ASTB}}} \right) + \\ \quad + k_{\text{ASTP}}[FTB] \left(A - [ATF] - \frac{k_{\text{DITP}}}{k_{\text{ASTP}}} \right) \\ \frac{d[FTB]}{dt} = k_{\text{SNUC}} \left(A - [ATF] - \frac{k_{\text{DITB}}}{k_{\text{ASTB}}} \right)^3 \end{cases}, \quad (\text{S12})$$

where $A = [ATF] + [ATM]$ is the total concentration of actin monomers and protomers. The ratios $k_{\text{DITB}}/k_{\text{ASTB}}$ and $k_{\text{DITP}}/k_{\text{ASTP}}$ are the critical concentrations of actin monomers for barbed and pointed ends respectively. The critical concentration of barbed ends can be used in the nucleation part of the equations to approximate an effect of short filaments dissociations (Carlsson et al., 2004).

Actin and capping protein. The second analytical model considers the same reagents as in a pure actin system plus free and bound barbed-end capping proteins ((CBM) and (CBF)). Three additional reactions are included: nucleation by barbed end capping protein, capping of barbed end and uncapping of barbed end. The number of active pointed and barbed ends differs in this situation. This system, combining six reagents and eight reactions, is described by a set of three linearly independent differential equations S13, if: i) the total actin concentration is constant, $[ATF] + [ATM] = A = \text{const}$; ii) the total concentration of barbed end capping protein is constant, $[CBF] + [CBM] = C = \text{const}$; iii) the equality for total concentrations of barbed and pointed ends is $[FTP] = [FTB] + [CBF]$.

$$\begin{cases} \frac{d[ATF]}{dt} = 3k_{\text{SNUC}} \left(A - [ATF] - \frac{k_{\text{DITB}}}{k_{\text{ASTB}}} \right)^3 + 3k_{\text{CBNU}} \left(A - [ATF] - \frac{k_{\text{DITB}} + k_{\text{DITP}}}{k_{\text{ASTB}} + k_{\text{ASTP}}} \right)^3 (C - [CBF]) + \\ \quad + k_{\text{ASTB}}[FTB] \cdot \left(A - [ATF] - \frac{k_{\text{DITB}}}{k_{\text{ASTB}}} \right) + k_{\text{ASTP}}([FTB] + [CBF]) \left(A - [ATF] - \frac{k_{\text{DITP}}}{k_{\text{ASTP}}} \right) \\ \frac{d[FTB]}{dt} = k_{\text{SNUC}} \left(A - [ATF] - \frac{k_{\text{DITB}}}{k_{\text{ASTB}}} \right)^3 - k_{\text{ASCB}}[FTB](C - [CBF]) + k_{\text{DICB}}[CBF] \\ \frac{d[CBF]}{dt} = k_{\text{CBNU}} \left(A - [ATF] - \frac{k_{\text{DITB}} + k_{\text{DITP}}}{k_{\text{ASTB}} + k_{\text{ASTP}}} \right)^3 (C - [CBF]) + k_{\text{ASCB}}[FTB](C - [CBF]) - k_{\text{DICB}}[CBF] \end{cases} \quad (\text{S13})$$

The ratios $k_{\text{DITB}}/k_{\text{ASTB}}$ and $k_{\text{DITP}}/k_{\text{ASTP}}$ are the critical concentrations of actins for barbed and pointed ends respectively. The critical concentration of barbed ends can be used in the actin nucleation part of the equations to approximate an effect of short filaments dissociations (Carlsson et al., 2004).

The ratio $(k_{DITB} + k_{DITP})/(k_{ASTB} + k_{ASTP})$ can be used in the barbed end capping protein nucleation part of the equations to approximate an effect of short capped filaments dissociations.

The differential equations S12 and S13 were solved numerically using Mathematica 6.

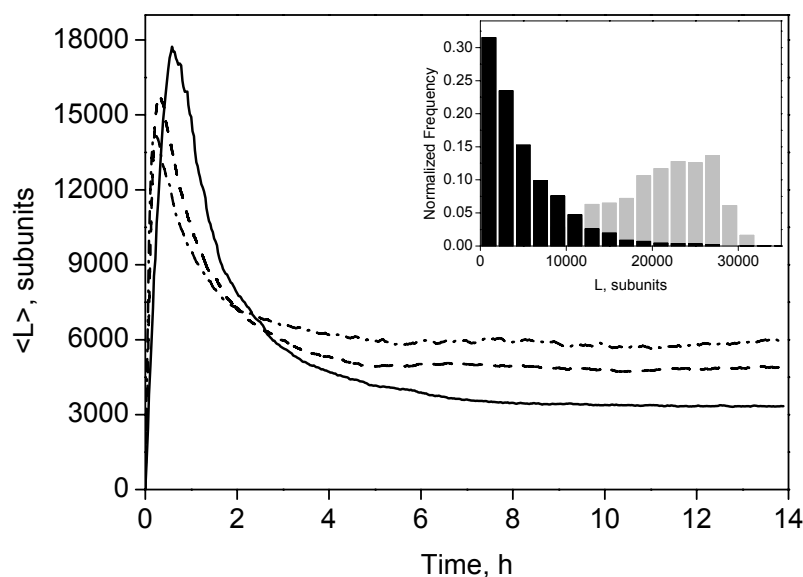
Software package ActinSimChem

ActinSimChem is the stand-alone software package for the Monte Carlo simulation of actin polymerization processes. *ActinSimChem* integrates the nSRF and SRF models (switching between two models is optional). *ActinSimChem* provides the possibility for: i) input/variation of the model parameters; ii) simulation of actin polymerization; iii) graphical representation of simulation results; iv) storage of the results. The program and its manual can be obtained on request or can be downloaded from the website <http://actinsim.uni.lu>.

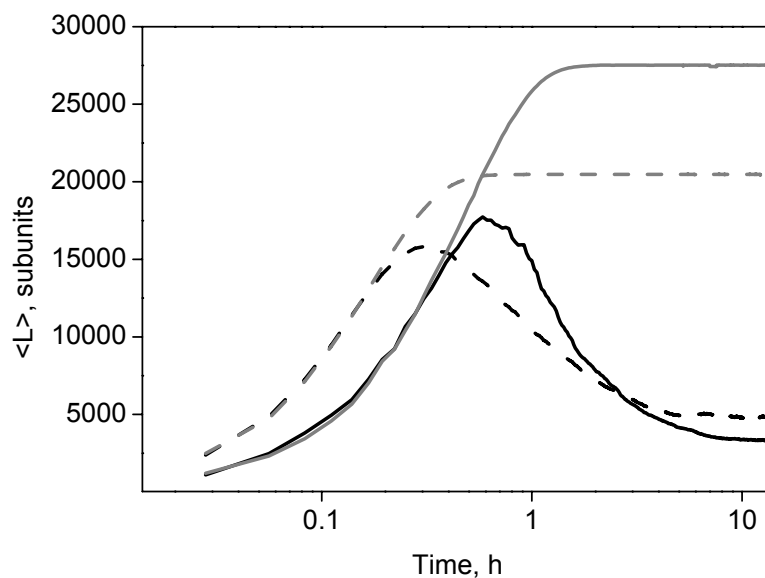
The *ActinSimChem* is designed as a simple network of bound object-oriented classes (*cf.* Fig. S6):

- class *CSimpleCell* is an abstract parent class, in which the numbers of molecules for reagents are stored and the methods of stochastic chemical reactions simulations are implemented (the “direct” method, the “first reaction” method (Gillespie, 1976), the “next reaction” method (Gibson and Bruck, 2000)). The functions of the class operate by a list of 21 reagents in the same way for both nSRF and SRF models. Procedures, which perform changes in the simulated system, are abstract in this class and are realized further in the child classes.
- Class *CCell* is the child class to the *CSimpleCell* class that implements the nSRF model. The corresponding procedures control filaments, filament branches, and the numbers of molecules for reagents according the nSRF model. Classes *CFilament* and *CFilBranch* are used to describe filaments and filament branches correspondingly.
- Class *CCellStruct* is the child of the class *CSimpleCell* that employs the SRF model. The corresponding procedures perform modifications of filaments, filament branches, and the number of molecules for reagents according the SRF model. Classes *CFilamentStruct* and the *CFilBranchStruct* are used to define filaments and filament branches correspondingly.
- Class *CFilament* is required for definition of a filament in the nSRF model. The filament is represented by the number of proteins, branch units, and by a pointer to the first branch unit.
- Class *CFilamentStruct* is used for description of a filament in the SRF model. The filament is represented by the number of proteins, branch units, and by a pointer to the first branch unit.
- Class *CBranch* is utilised for description of a ‘daughter’ filament or a branch in the nSRF model. A branch is represented by the number of proteins, types of barbed and pointed ends. The class *CFilBranch* is a child class to the *CBranch* that defines a pointer to the filament unit, a pointer to the ‘mother’ branch unit, pointers to the ‘daughter’ branch units, and that manages branch structures in the nSRF model.
- Class *CFilBranchStruct* is used for definition of a ‘daughter’ filament or a branch in the SRF model. Type and positions of proteins in filament branch are stored as a sequence of elements. The class *CElement* defines subunit. The class *CFilBranchStruct* is a child class to the *CBranchStruct* that contains a list of pointers to the ‘daughter’ branch units, a pointer to the ‘mother’ branch unit, a pointer to the filament unit, a position of the branch unit relative to pointed end of the ‘mother’ branch.
- Class *CElement* is needed to manage filament subunits in the SRF model. In particular, type of protein (ATF, APF, ADF, CBF, CPF, FOF, ARF) and the links to the next and previous elements in the filament branch are stored.

ActinSimChem was developed using the C++ Builder 2007.



a



b

Fig. S1. Testing the model for annealing and fragmentation of actin filaments.

a) Examples of predicted average lengths of actin filaments for total actin concentrations $[ATM]_{t=0} = 2.0 \mu\text{M}$ (*solid*), $4.0 \mu\text{M}$ (*dashed*), and $6.0 \mu\text{M}$ (*dash-dot*) including normal fragmentation and annealing events. The *Inset* represents the steady state length distributions for simulations with $4.0 \mu\text{M}$ total actin both with and without normal fragmentation and annealing (*black bars* and *grey bars*, respectively). b) Predicted average lengths of actin filaments for actin concentrations $[ATM]_{t=0} = 2.0 \mu\text{M}$ (*solid*) and $4.0 \mu\text{M}$ (*dashed*) with (*black color*) and without (*grey color*) normal fragmentation and annealing. $k_{FRGM} = 1.8 \times 10^{-8} \text{ s}^{-1}$, $k_{ANNL} = 0.10 \mu\text{M}^{-1} \text{ s}^{-1}$. Other reaction rates are the same as listed in Table 1, Manuscript.

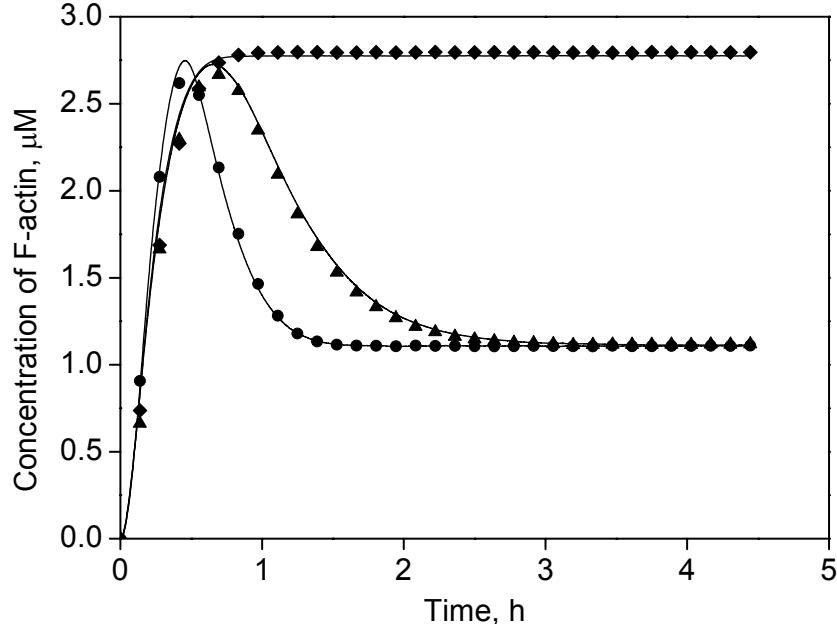


Fig. S2. Testing the model for the occurrence of overshoots in the concentration of polymerized actin.

Examples of time series for predicted actin polymerization kinetics for three systems of initial actin concentration $[ATM]_{t=0} = 3.0 \mu\text{M}$: (i) actin $\{k_{DTOT} = 20 \text{ s}^{-1}\}$ (\blacklozenge), (ii) actin in the absence of excess ATP $\{k_{DTOT} = 0 \text{ s}^{-1}\}$ (\blacktriangle), and (iii) actin in the absence of excess ATP with Arp2/3 complex-induced branching included $\{k_{DTOT} = 0 \text{ s}^{-1}, [ARM]_{t=0} = 0.01 \mu\text{M}, k_{ASRT} = 10^{-5} \mu\text{M}^{-1}\text{s}^{-1}, k_{DIRP} = 10^{-3} \text{ s}^{-1}\}$ (\bullet). Other reaction rates are the same as listed in Table 1, Manuscript.

As is reported previously, several mechanisms of actin polymerization may yield overshoots, for example, the absence of excess ATP, Arp2/3 complex-induced branching, severing, etc. (Brooks and Carlsson, 2008). We reproduced some of these overshoots. The maximum overshoot was observed for the actin system with an absence of excess ATP, resulting in the overshoot magnitude of $\Delta = F_{max} - F_{min} = ([ATM]_{t=0} - C_c^{B,T}) - ([ATM]_{t=0} - C_c^{B,D}) \approx 1.7 \mu\text{M}$, where F_{max} and F_{min} are maximum and minimum steady state limits at the actin polymerization curve, $C_c^{B,T}$ and $C_c^{B,D}$ are the ATP- and ADP-actin critical concentrations at the barbed end. Polymerization overshoot became faster ($k_{DTOT} = 0 \text{ s}^{-1}$) or enhanced ($k_{DTOT} = 0.01 \text{ s}^{-1}$, data not shown) as high concentration of Arp2/3 complexes ($> 0.1 \mu\text{M}$) were included in simulation. No overshoot was observed for a high nucleotide exchange rate ($k_{DTOT} = 20 \text{ s}^{-1}$) as is in presence of profilin.

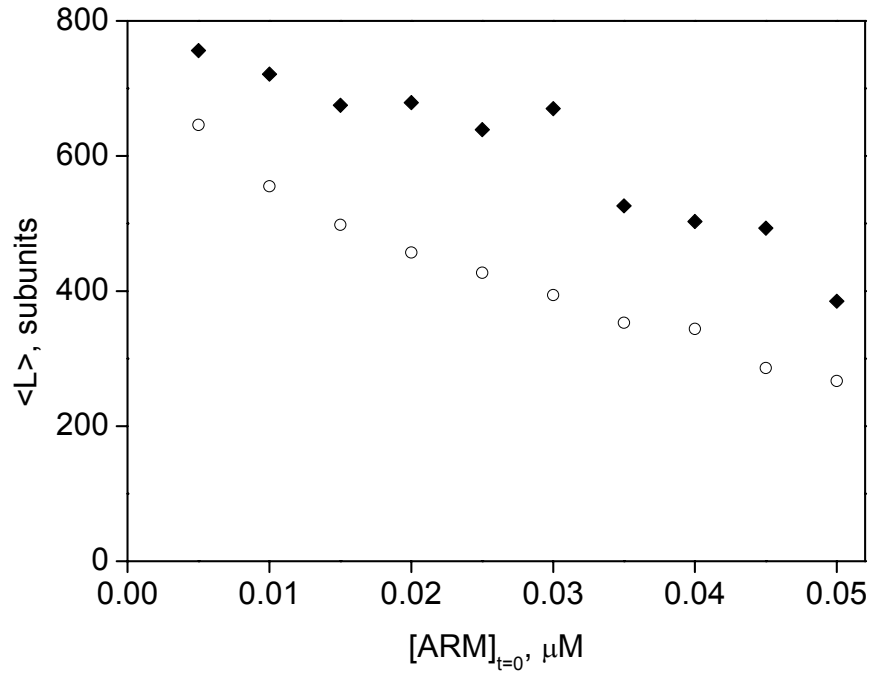
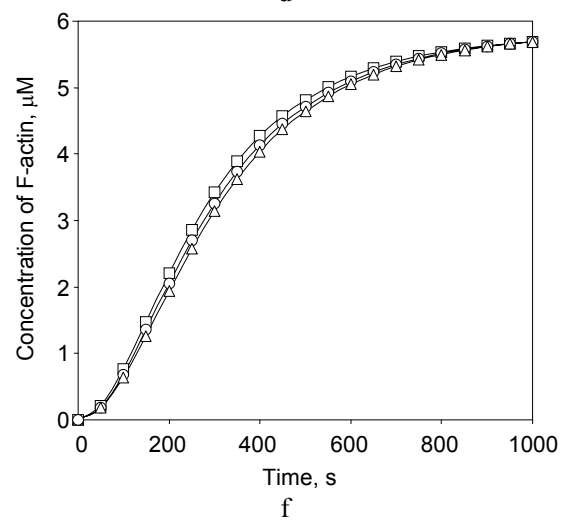
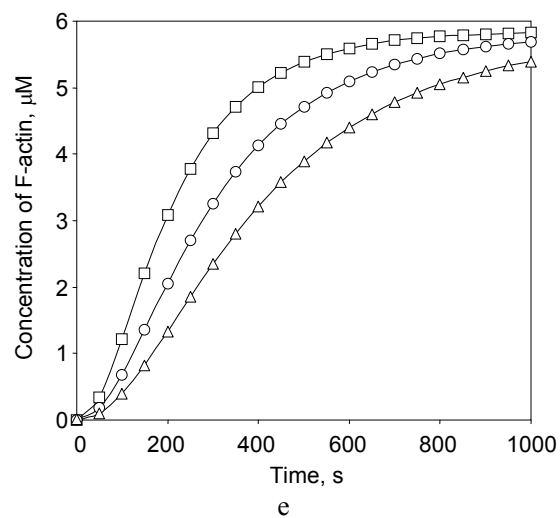
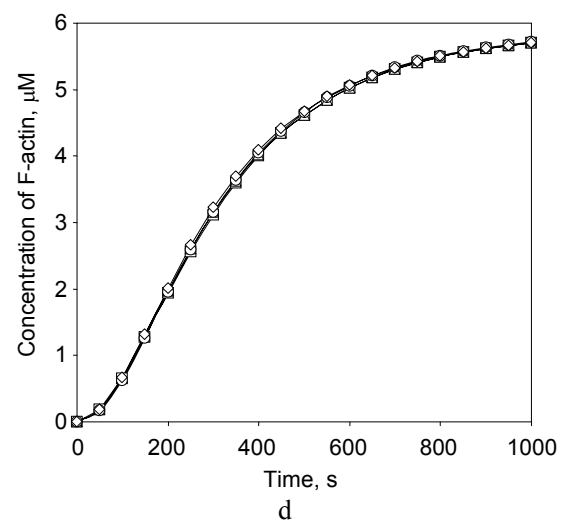
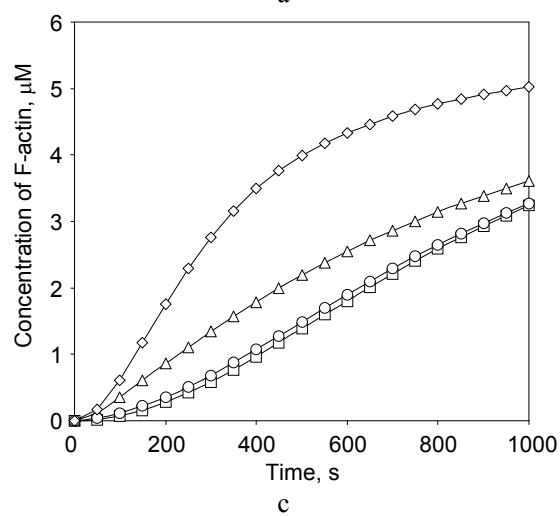
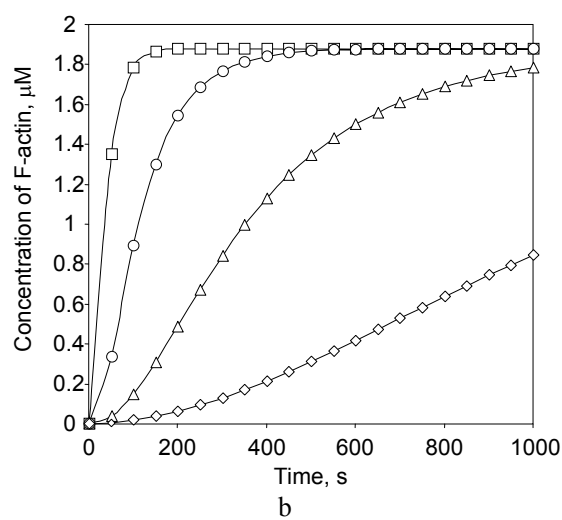
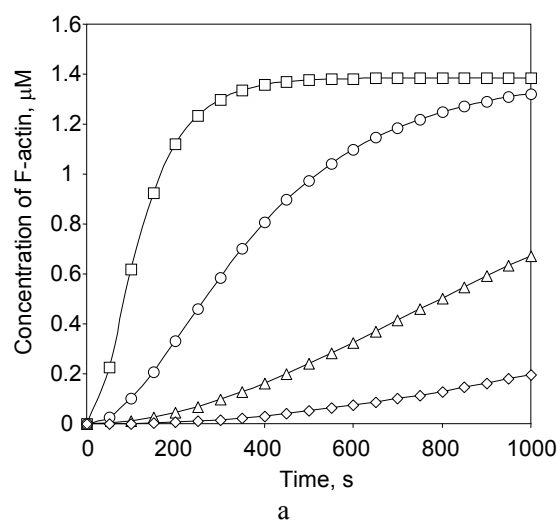


Fig. S3. nSRF (○) and SRF (◆) models differ when considering Arp2/3-complex dependent actin filament branching.

Decrease of the average filament length $\langle L \rangle$ in the steady-state phase with increasing concentration of the Arp2/3 complex and its nucleation activity at ATF-protomers in a ‘mother’ filament. $[\text{ATM}]_{t=0} = 3.0 \mu\text{M}$, $[\text{CBM}]_{t=0} = [\text{CPM}]_{t=0} = 0.01 \mu\text{M}$, $k_{\text{SNUC}} = 10^{-8} \mu\text{M}^{-2}\text{s}^{-1}$, $k_{\text{CBNU}} = k_{\text{CPNU}} = 10^{-5} \mu\text{M}^{-3}\text{s}^{-1}$, $k_{\text{ASRT}} = 10^{-2} \mu\text{M}^{-1}\text{s}^{-1}$, $k_{\text{DIRP}} = 10^{-3} \text{s}^{-1}$, $k_{\text{FRGM}} = 1.8 \times 10^{-8} \text{s}^{-1}$, $k_{\text{ANNL}} = 10^{-8} \mu\text{M}^{-1}\text{s}^{-1}$. If a parameter is not mentioned specifically, the value from Table 1 is used.



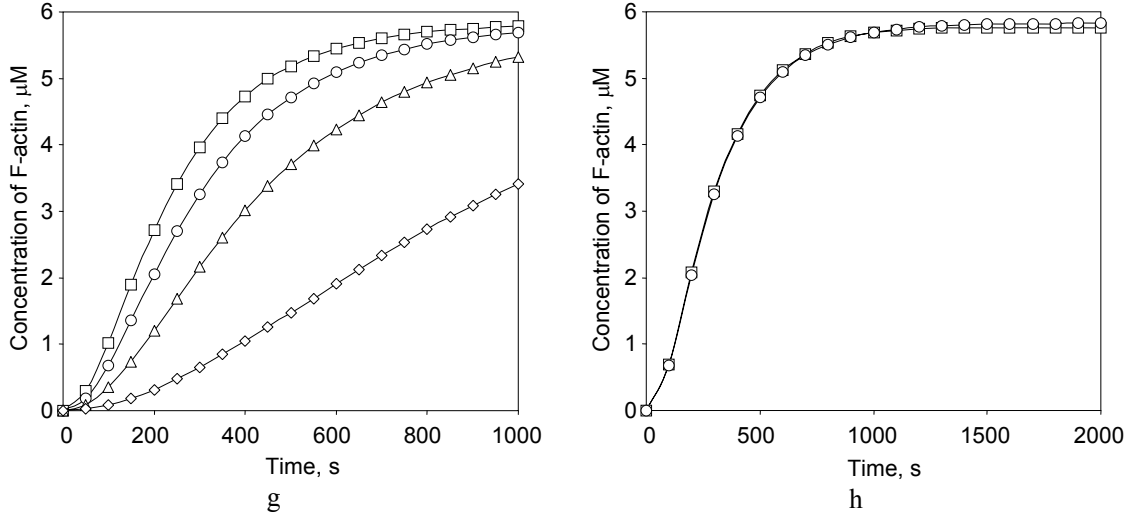


Fig. S4. Sensitivity of actin systems to the concentrations of capping proteins and various rate constants.

Plots (a-d) show the sensitivity of the system to barbed-end (a, c) and pointed-end (b, d) capping proteins. Spontaneous nucleation: $k_{SNUC} = 10^{-9} \mu\text{M}^{-2}\text{s}^{-1}$, squares, circles, triangles and diamonds correspond to capping protein concentrations of 1, 0.1, 0.01, and 0.001 μM respectively.

a) Sensitivity to [CBM] working as a nucleator ($k_{CBNU} = 2 \times 10^{-5} \mu\text{M}^{-3}\text{s}^{-1}$), $[\text{ATM}]_{t=0} = 2 \mu\text{M}$.

b) Sensitivity to [CPM] working as a nucleator ($k_{CPNU} = 2 \times 10^{-5} \mu\text{M}^{-3}\text{s}^{-1}$), $[\text{ATM}]_{t=0} = 2 \mu\text{M}$.

c) Sensitivity to [CBM], when it does not work as a nucleator ($k_{CBNU} = 0$), $[\text{ATM}]_{t=0} = 6 \mu\text{M}$.

d) Sensitivity to [CPM], when it does not work as a nucleator ($k_{CBNU} = 0$), $[\text{ATM}]_{t=0} = 6 \mu\text{M}$.

Plots (e-h) show the sensitivity of the system to the rates. In all plots the pure actin system was considered, with the same actin concentration $[\text{ATM}]_{t=0} = 6 \mu\text{M}$.

e) and f) represents the effect of actin exchange at barbed and pointed ends respectively. Circles correspond to the experimentally determined exchange rates (see Table 1, reactions of elongation and dissociations). Lines with squares have been obtained for the case, when these rates are multiplied by 2, and triangles when they are divided by 2.

g) Sensitivity of the actin system to the spontaneous nucleation rate. Squares, circles, triangles and diamonds corresponds to k_{SNUC} of 15×10^{-9} , 10×10^{-9} , 5×10^{-9} , $10^{-9} \mu\text{M}^{-2}\text{s}^{-1}$.

h) Sensitivity of the actin system to effect of the actin aging in filaments. Circles correspond to $k_{TTOD} = 7 \times 10^{-4} \text{s}^{-1}$, squares to $k_{TTOD} = 0.7 \text{s}^{-1}$.

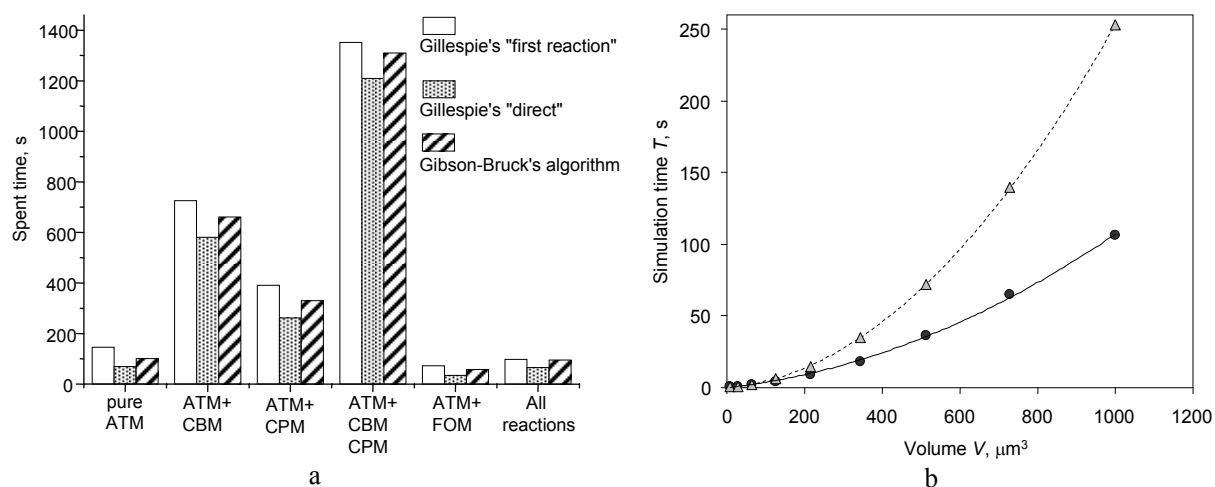


Fig. S5. Comparison of different stochastic simulation schemes and computational efficiency.

a) Comparison of the times spent for simulations by three stochastic simulation algorithms. White bars correspond to the Gillespie's "first reaction" algorithm, gray bars to "direct" Gillespie's algorithm and striped bars to a partially realized Gibson-Bruck's algorithm.

b) Simulation time increase in relation to the volume V of simulated systems (i.e. number of simulated events). Circles represent timing obtained for simulation of the actin polymerization system whereas triangles represent a simulation with the complete reaction and reagent set (excluding the Arp2/3 complex and its reactions). Solid and dashed curves resulted from the fits by an approximating regression $T = \alpha \cdot V^2 + \beta \cdot V$, where α and β are the fitted constants.

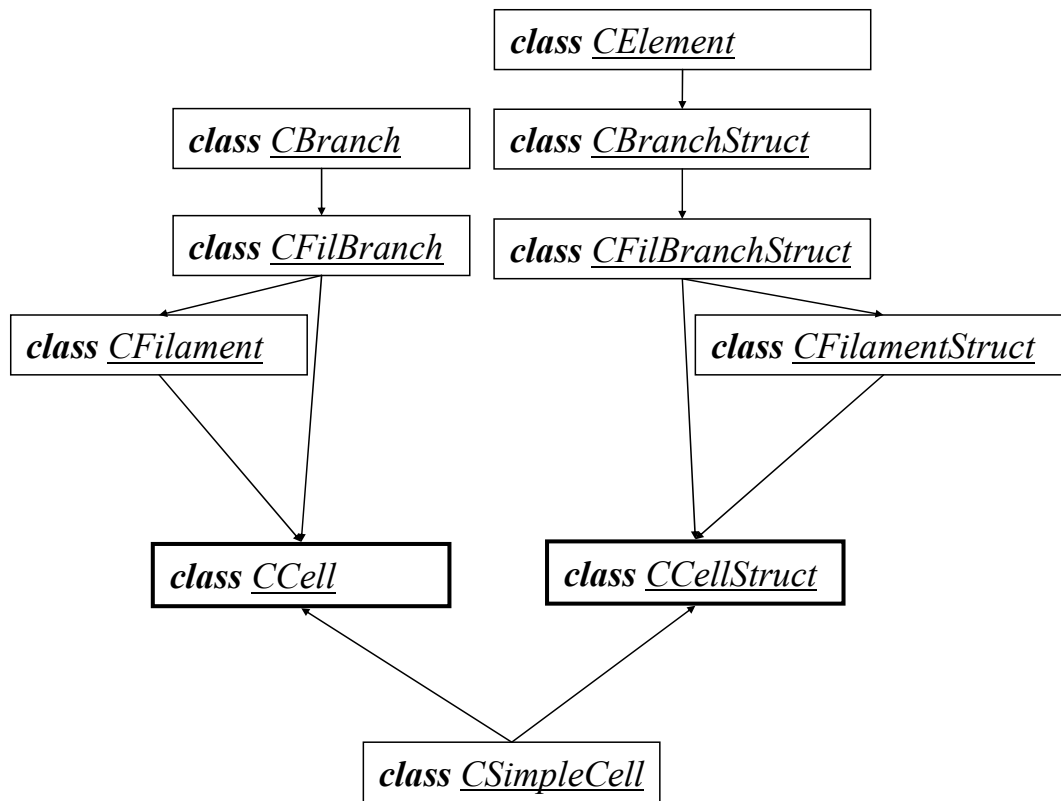


Fig. S6. The network of the object-oriented classes in the program *ActinSimChem*. Class *CSimpleCell* is the abstract class that contains a stochastic simulation algorithm. Class *CElement* holds filament subunits in the SRF model. Classes *CFilament* and *CFilamentStruct* realize a model component of a filament in the nSRF and SRF models correspondingly. Classes *CFilBranch* and *CFilBranchStruct* are used to describe a filament branch in the nSRF/SRF models. Classes *CCell* and *CCellStruct* perform simulations according to the nSRF and SRF models.

Appendix D. Additional co-authored publications

1. Al Tanoury, Z., et al., *Quantitative kinetic study of the actin-bundling protein L-plastin and of its impact on actin turn-over*. PLoS ONE, 2010. **5**(2): p. e9210.
2. Moes, M., et al., *A Novel Network Integrating a miRNA-203/SNAI1 Feedback Loop which Regulates Epithelial to Mesenchymal Transition*. PLoS One, 2012. **7**(4): p. e35440.

Quantitative Kinetic Study of the Actin-Bundling Protein L-Plastin and of Its Impact on Actin Turn-Over

Ziad Al Tanoury¹, Elisabeth Schaffner-Reckinger¹, Aliaksandr Halavatyi¹, Céline Hoffmann², Michèle Moes¹, Ermin Hadzic¹, Marie Catillon¹, Mikalai Yatskou¹, Evelyne Friederich^{1*}

¹ Laboratory of Cytoskeleton and Cell Plasticity, Life Sciences Research Unit, University of Luxembourg, Luxembourg City, Luxembourg, ² Laboratory of Plant Molecular Biology, Public Research Center for Health (CRP-Santé), Strassen, Luxembourg

Abstract

Background: Initially detected in leukocytes and cancer cells derived from solid tissues, L-plastin/fimbrin belongs to a large family of actin crosslinkers and is considered as a marker for many cancers. Phosphorylation of L-plastin on residue Ser5 increases its F-actin binding activity and is required for L-plastin-mediated cell invasion.

Methodology/Principal Findings: To study the kinetics of L-plastin and the impact of L-plastin Ser5 phosphorylation on L-plastin dynamics and actin turn-over in live cells, simian Vero cells were transfected with GFP-coupled WT-L-plastin, Ser5 substitution variants (S5/A, S5/E) or actin and analyzed by fluorescence recovery after photobleaching (FRAP). FRAP data were explored by mathematical modeling to estimate steady-state reaction parameters. We demonstrate that in Vero cell focal adhesions L-plastin undergoes rapid cycles of association/dissociation following a two-binding-state model. Phosphorylation of L-plastin increased its association rates by two-fold, whereas dissociation rates were unaffected. Importantly, L-plastin affected actin turn-over by decreasing the actin dissociation rate by four-fold, increasing thereby the amount of F-actin in the focal adhesions, all these effects being promoted by Ser5 phosphorylation. In MCF-7 breast carcinoma cells, phorbol 12-myristate 13-acetate (PMA) treatment induced L-plastin translocation to *de novo* actin polymerization sites in ruffling membranes and spike-like structures and highly increased its Ser5 phosphorylation. Both inhibition studies and siRNA knock-down of PKC isozymes pointed to the involvement of the novel PKC- δ isozyme in the PMA-elicited signaling pathway leading to L-plastin Ser5 phosphorylation. Furthermore, the L-plastin contribution to actin dynamics regulation was substantiated by its association with a protein complex comprising cortactin, which is known to be involved in this process.

Conclusions/Significance: Altogether these findings quantitatively demonstrate for the first time that L-plastin contributes to the fine-tuning of actin turn-over, an activity which is regulated by Ser5 phosphorylation promoting its high affinity binding to the cytoskeleton. In carcinoma cells, PKC- δ signaling pathways appear to link L-plastin phosphorylation to actin polymerization and invasion.

Citation: Al Tanoury Z, Schaffner-Reckinger E, Halavatyi A, Hoffmann C, Moes M, et al. (2010) Quantitative Kinetic Study of the Actin-Bundling Protein L-Plastin and of Its Impact on Actin Turn-Over. PLoS ONE 5(2): e9210. doi:10.1371/journal.pone.0009210

Editor: Neil A. Hotchin, University of Birmingham, United Kingdom

Received: August 24, 2009; **Accepted:** January 26, 2010; **Published:** February 15, 2010

Copyright: © 2010 Al Tanoury et al. This is an open-access article distributed under the terms of the Creative Commons Attribution License, which permits unrestricted use, distribution, and reproduction in any medium, provided the original author and source are credited.

Funding: Ziad Al Tanoury, Aliaksandr Halavatyi and Ermin Hadzic were supported by fellowships from the Ministère de la Culture, de l'Enseignement Supérieur et de la Recherche, Luxembourg, and from the Fonds National de la Recherche, Luxembourg. This work was supported by a grant of the Human Frontier Science Program (RGP0058/2005). The funders had no role in study design, data collection and analysis, decision to publish, or preparation of the manuscript.

Competing Interests: The authors have declared that no competing interests exist.

* E-mail: Evelyne.Friederich@uni.lu

Introduction

Cell motility is driven by remodeling of the actin cytoskeleton and cell contacts with the extracellular matrix (ECM) [1], a process which is under the control of a plethora of actin-binding proteins. In particular, actin filament crosslinkers have been proposed to play a critical role in the organization and dynamics of the actin cytoskeleton and its cellular functions.

L-plastin (also termed L-fimbrin), the hematopoietic plastin isoform, was initially detected in leukocytes [2]. Aberrantly expressed in cancer cells derived from solid tissues [3–7], L-plastin promotes invasion of cultured epithelial cells supporting its role in cancer progression [8,9]. L-plastin is a representative member of a large family of actin-crosslinking or -bundling proteins, including α -actinin and filamin [10]. Members of this

family share a conserved ~250 amino acid F-actin binding domain (ABD) [11] which is composed of two tandemly arranged calponin-homology (CH) domains [12]. Plastins contain two ABDs which are packed into a compact fold [13,14] enabling them to organize actin filaments into tight bundles [15], as well as an amino-terminal calmodulin-like headpiece that comprises two Ca²⁺-binding EF-hand modules [16]. In cells, L-plastin localizes to various actin-rich membrane structures involved in locomotion, adhesion, signaling and immune defense, including focal adhesions, podosomes, filopodia and the phagocytic cup, thus supporting a role for L-plastin in the organization of the actin cytoskeleton and in signal transduction [9,17–19]. Biochemical *in vitro* data have shown that L-plastin not only organizes filaments into arrays but also prevents them from depolymerization suggesting that it may regulate their turn-over [20]. Further

evidence for a role in the control of actin turn-over is provided by the observation that L-plastin could substitute for yeast plastin in a *Sac6* null mutant which exhibited defects in actin polymerization [21].

Among the three human plastin isoforms which also include T- and I-plastin, only L-plastin has been reported to be regulated through phosphorylation [22] in response to signals triggering the activation of the immune response, cell migration and proliferation. Phosphorylation on residue serine-5 (Ser5), the major L-plastin phosphorylation site [22–24], has been shown to increase its F-actin-binding and -bundling activities *in vitro* and to be required for efficient targeting of L-plastin to focal adhesion sites as well as for cancer cell invasion [8,9]. However, the impact of L-plastin Ser5 phosphorylation on L-plastin binding-unbinding kinetics and on actin turn-over in live cells remains to be investigated.

Distinct protein kinases appear to be responsible for L-plastin phosphorylation depending on the cell type and environment. In hematopoietic cells and in various other non-transformed cell types, it is well-established that L-plastin can be phosphorylated on residue Ser5 by the cAMP-dependent Protein Kinase A (PKA) which has also been shown to directly phosphorylate L-plastin *in vitro* [9,24]. However, in addition to PKA, other kinases such as PKC have been suggested to contribute to L-plastin phosphorylation in leukocytes, fibroblasts and neutrophils [22,25].

Here we studied L-plastin/actin kinetics in live cells and L-plastin phosphorylation in response to signals triggering cytoskeletal rearrangements. Quantitative fluorescence recovery after photobleaching (FRAP) assays revealed that L-plastin associated with focal adhesions following a two-binding-state model and that L-plastin phosphorylation increased its association rates and, hence, its capacity to stably dock to specific cytoskeleton structures. Importantly, L-plastin induced an increase of the F-actin content at focal adhesion sites by decreasing the actin dissociation rate. These effects on actin turn-over were considerably enhanced by L-plastin phosphorylation on residue Ser5. Furthermore, treatment of MCF-7 breast cancer cells with the cell invasion promoting agent phorbol 12-myristate 13-acetate (PMA), triggered the translocation of endogenous L-plastin to ruffling membranes and spike-like structures as well as L-plastin Ser5 phosphorylation, through activation of PKC- δ signaling pathways.

Results

Binding Kinetics of L-Plastin Follow a Two-Binding-State Model and Are Modulated by Ser5 Phosphorylation in Live Vero Cells

To investigate the steady-state dynamics of L-plastin and actin in living cells and the role of L-plastin phosphorylation on Ser5 herein (Fig. 1A), we performed confocal microscopy-based fluorescence recovery after photobleaching (FRAP) experiments using previously characterized L-plastin variants in fibroblast-like Vero cells which do not express endogenous L-plastin [9]. FRAP, which is a powerful approach for studying molecular mobility in live cells [26,27] was combined with mathematical modeling to estimate the steady-state kinetics of L-plastin variants and actin turn-over which reflects actin polymerization and depolymerization reactions [28,29]. Similar to epitope-tagged wild type L-plastin [9], wild type (WT-) L-plastin fused to GFP colocalized with actin in focal adhesions, membrane protrusions and along stress fibers, as visualised by epifluorescence microscopy (Fig. 1B, upper panels). To study the kinetics of the phosphorylated pool of L-plastin in Vero cells, we took advantage of the fact that transfected WT-L-plastin is phosphorylated on Ser5 and targeted to focal adhesions in these cells [9]. The bleach was

therefore performed in a small region of interest (ROI) in focal adhesions (Fig. 1C). For each ROI, the experimental intensity recoveries were normalized and averaged. The obtained curves exhibited a fast and a slow phase of recovery (Fig. 1D). Twenty seconds after photobleaching, 89% of recovery was reached for WT GFP-L-plastin suggesting that the protein is highly mobile, undergoing rapid cycles of association and dissociation, as reported for other crosslinking proteins [26,30]. Quantitatively, the best fits of the FRAP curves were obtained with a “two-binding-state” model [31]. This model may be applied to a system in which a molecule exhibits two distinct binding states involved in the interaction with the free binding sites of a partner molecule to form a complex. Analysis with the two-binding-state model allowed the separation of FRAP recovery curves into two largely independent phases, a first relatively quick phase from zero to ten seconds ($k_{1off} = 0.616 \text{ s}^{-1}$ for WT) and a second much slower phase that represented the plateau ($k_{2off} = 0.03 \text{ s}^{-1}$ for WT), such that $k_{1off} \gg k_{2off}$. Based on this model, we estimated the equilibrium normalized concentration of free WT-L-plastin molecules F_{eq} ($F_{eq(WT)} = 0.513 \pm 0.01$) and the association rates k^*_{1on} ($k^*_{1on(WT)} = 0.338 \pm 0.032 \text{ s}^{-1}$) and k^*_{2on} ($k^*_{2on(WT)} = 0.01 \pm 0.001 \text{ s}^{-1}$) by fitting the normalized experimental FRAP curves with equation (5) (Fig. 1E, see Materials and Methods).

To estimate how phosphorylation of L-plastin affects these parameters, we used two previously characterized phosphorylation variants of L-plastin in which residue Ser5 of L-plastin was replaced with an alanine (L-plastin Ser5/Ala) or a glutamate residue (L-plastin Ser5/Glu), to inactivate or to mimic phosphorylation respectively [9]. In agreement with previous results obtained with epitope-tagged variants, a comparable yet more pronounced localization to F-actin structures was observed with Ser5/Glu (S5/E) GFP-L-plastin as compared to WT GFP-L-plastin. In contrast, Ser5/Ala (S5/A) GFP-L-plastin exhibited a diffuse cytoplasmic staining with merely a weak localization in focal adhesions and membrane protrusions (Fig. 1B).

The recovery curve of GFP-coupled S5/A-L-plastin varied from that of WT- and S5/E-L-plastin. Indeed the S5/A variant exhibited a faster recovery curve as compared to WT and S5/E variants suggesting a higher mobility of this variant (96% of recovery twenty seconds after photobleaching) (Fig. 1D). This difference was unlikely to be merely due to fast molecule diffusion, as an additional set of FRAP experiments, in which the size of the bleached region was increased at least three-fold, yielded similar recoveries (data not shown). Calculation of F_{eq} confirmed that, for the GFP-coupled S5/A-L-plastin variant, more unbound molecules were observed at the equilibrium than for the WT or S5/E GFP-L-plastin variants (Fig. 1E). The rate of association at the first ‘quick’ binding state k^*_{1on} was two-fold lower for S5/A- as compared to WT-L-plastin ($k^*_{1on(WT)} = 0.338 \pm 0.032 \text{ s}^{-1}$; $k^*_{1on(SA)} = 0.173 \pm 0.012 \text{ s}^{-1}$), reflecting a lower association rate of the phosphorylation-defective S5/A variant. Conversely, the phosphomimetic S5/E-L-plastin variant exhibited a k^*_{1on} which was even higher than that of the WT ($k^*_{1on(SE)} = 0.42 \pm 0.04 \text{ s}^{-1}$). Accordingly, the association rate at the second so-called ‘slow’ binding state k^*_{2on} was also two-fold lower for S5/A-L-plastin as compared with WT- and S5/E-L-plastin variants which exhibited similar k^*_{2on} association rates. Interestingly, WT-L-plastin and Ser5 substitution variants exhibited very similar dissociation rates at the quick-binding state k_{1off} ($k_{1off(WT)} = 0.616 \pm 0.041 \text{ s}^{-1}$; $k_{1off(SA)} = 0.073 \pm 0.041 \text{ s}^{-1}$; $k_{1off(SE)} = 0.612 \pm 0.042 \text{ s}^{-1}$; see Fig. 1E) and at the slow-binding state k_{2off} (data not shown).

Altogether, these findings suggest that the interaction of L-plastin with specific F-actin structures follows a “two-binding-state” model and that the association rates are up-regulated by L-plastin phosphorylation on residue Ser5.

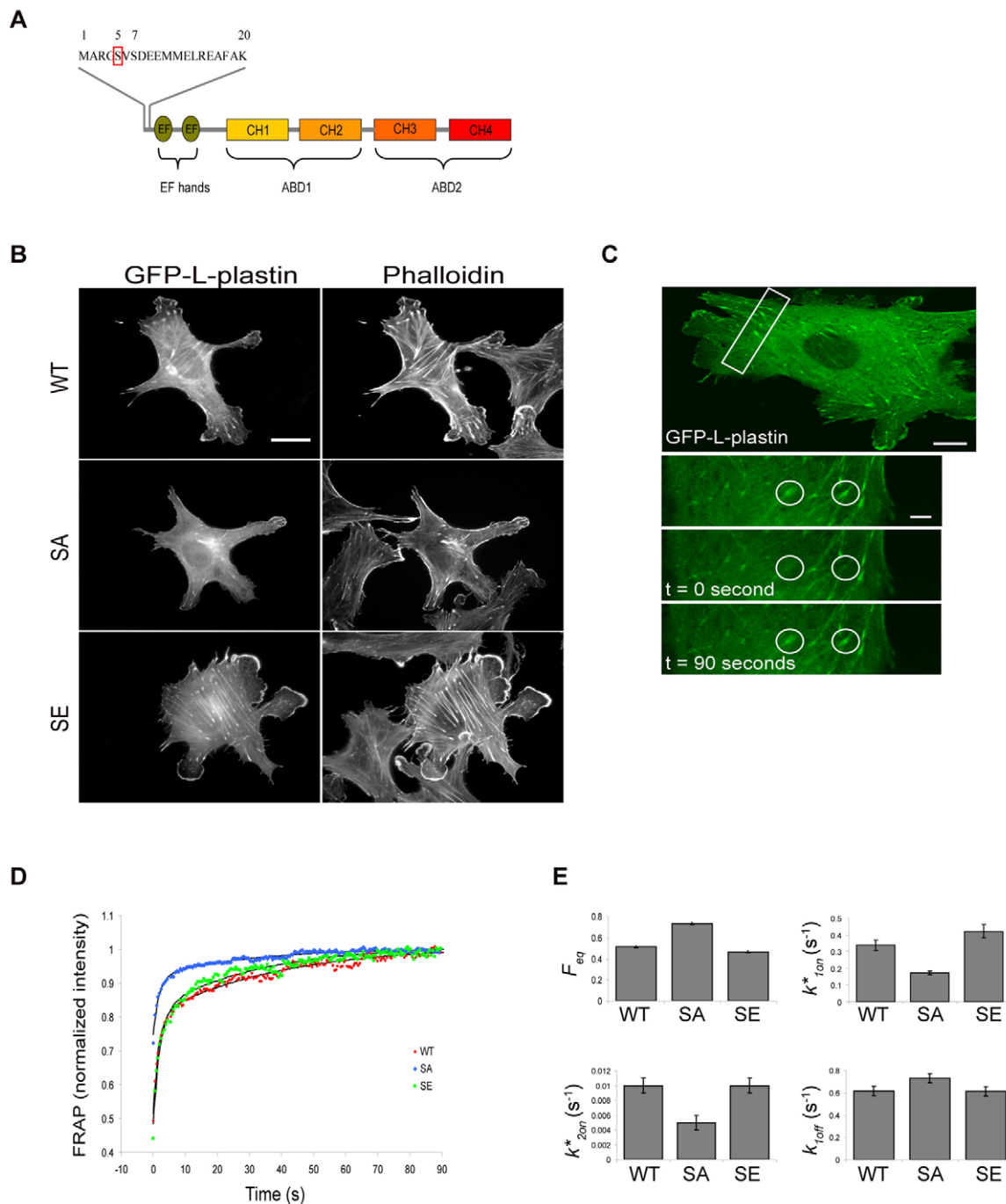


Figure 1. L-plastin phosphorylation modulates its mobility in focal adhesions. (A). Schematic representation of wild-type (WT) L-plastin showing the headpiece domain followed by two independent actin binding domains (ABDs). Residue serine-5 (Ser5) of the headpiece was mutated to alanine (SA) to generate unphosphorylatable L-plastin or to glutamic acid (SE) to generate an L-plastin variant mimicking constitutive phosphorylation. (B). Expression and localization of GFP-coupled L-plastin phosphorylation variants in Vero cells. Vero cells were transfected with cDNA encoding GFP-L-plastin phosphorylation variants. After 48 hours, cells were fixed and processed for immunofluorescence. The localization of L-plastin and F-actin was analyzed with an epifluorescence microscope (Leica DMRX microscope) after staining with Rhodamine-conjugated phalloidin to visualize polymerized actin. Scale bar, 20 μ m. (C). A typical FRAP experiment carried out on a Vero cell transfected with WT GFP-L-plastin. The boxed region in the upper panel (scale bar, 10 μ m) is shown enlarged in the bottom panels (scale bar, 4 μ m). Circular spots, surrounded by a white line, are regions of interest (ROI) that are submitted to photobleaching and that have a diameter of 5 μ m. Such spot size was selected to smooth local area effects and visually well-represents the focal adhesion region. Pictures were recorded before bleaching, immediately after bleaching and 90 seconds after bleaching. (D). Normalized FRAP recovery curves of wild type (WT, red), Ser5/Ala (SA, blue) and Ser5/Glu (SE, green) GFP-L-plastin fusions are compared to the curves predicted by the two-binding-state model (black curves). Data were obtained from three independent experiments representing 10 FRAP recordings for each condition. (E). Charts representing biochemical parameters obtained from fitting data with a two-binding-state model. Bars represent the mean \pm s.d. *P*-values were calculated using standard Student's *t*-test. A *p*-value < 0.05, considered as statistically significant, was obtained for F_{eq} , k_{1on}^* and k_{2on}^* but not for k_{1off}^* . doi:10.1371/journal.pone.0009210.g001

L-Plastin Modulates Actin Dynamics in a Phosphorylation-Dependent Manner in Vero Cells

L-plastin appears to affect actin dynamics by binding along actin filaments, as supported by previous biochemical data [9,20]. To address this issue, FRAP experiments were performed on GFP-actin in Vero cell focal adhesions, co-transfected with GFP-actin and L-plastin variants fused to monomeric DsRed (Fig. 2A). In agreement with previous kinetic studies of GFP-actin in cells [32], the fast recovery phase of GFP-actin involved rapid diffusion of the large free pool of actin monomers into the bleached area. Indeed, diffusion of the free monomers led to recovery in less than one second, which was below the characteristic time of the association/dissociation kinetics and time resolution of our experiments. The measured postbleach fluorescence intensity of GFP-actin was strongly reduced in WT-L-plastin expressing cells as compared to control cells (Fig. 2B), suggesting a decrease of the fraction of free diffusible actin monomers in response to L-plastin expression.

We applied a one-binding-state model in a reaction dominant regime to analyze our FRAP data [31]. This equation is applicable to various FRAP behaviours for a single binding reaction in the presence of fast monomer diffusion at steady-state. We estimated the equilibrium concentration of free actin monomers F_{eq} , the dissociation rate k_{off} and the association rate k_{on}^* by fitting the normalized experimental FRAP curves with equation (3) (see Materials and Methods). We also calculated the ratio of bound to free G-actin molecules K_{eq} , defined by $K_{eq} = k_{on}^*/k_{off}$ [31]. These parameters provide information on how L-plastin variants influence the fraction of polymerized actin and the turn-over of actin filaments in focal adhesions. The estimated values for F_{eq} revealed that the concentration of free actin monomers was clearly decreased in cells expressing WT-, S5/A- or S5/E-L-plastin-DsRed fusions when compared with control cells (Ctrl) expressing DsRed alone ($F_{eq(Ctrl)} = 0.787 \pm 0.002$; $F_{eq(WT)} = 0.588 \pm 0.002$; $F_{eq(SA)} = 0.662 \pm 0.001$; $F_{eq(SE)} = 0.531 \pm 0.002$) (Fig. 2C). Similarly, more F-actin was present at focal adhesion sites as illustrated by the K_{eq} values ($K_{eq(Ctrl)} = 0.112 \pm 0.009$; $K_{eq(WT)} = 0.563 \pm 0.064$; $K_{eq(SA)} = 0.23 \pm 0.021$; $K_{eq(SE)} = 0.694 \pm 0.098$). This effect was more pronounced for the S5/E-L-plastin and less strong for the S5/A-L-plastin variants than for WT-L-plastin. Moreover the actin dissociation rate k_{off} was affected in a comparable way by the three L-plastin variants, with a k_{off} decrease of two-fold observed with the S5/A-L-plastin variant and a four-fold k_{off} decrease obtained with WT- or S5/E-L-plastin (Fig. 2C). No significant changes in k_{on}^* could be detected between S5/A-L-plastin- or WT-L-plastin-expressing cells and control cells, whereas the expression of the S5/E-L-plastin variant in cells led to a notable increase of the actin association rate k_{on}^* . Based on previous results, it can be excluded that the observed differences described above are due to dissimilar expression levels or stability of the phosphorylation variants [9].

Altogether, these data demonstrate that L-plastin affects actin dynamics and turn-over in focal adhesions by lowering the dissociation rate of actin, an effect which appears to be considerably enhanced by L-plastin Ser5 phosphorylation.

PMA Induces Translocation of L-Plastin to *De Novo* Assembled Actin Structures and Enhances Its Ser5 Phosphorylation in MCF-7 Cells

Our results point to an important role for L-plastin in regulating actin dynamics, an activity which is promoted by Ser5 phosphorylation. In addition, it has been shown previously that Ser5 phosphorylation is required for L-plastin-mediated cell invasion [8,9]. L-plastin phosphorylation in macrophages and leukocytes

has been shown to be increased upon treatment with the phorbol ester PMA [24,33], which is an invasion inducing agent that is generally used as a potent activator of classical (α , β , and γ) and novel (δ , ϵ , and η) PKC family members [34–36]. Here, we wanted to investigate the effects of PMA treatment in a cancer cell model, the MCF-7 breast carcinoma cell line. MCF-7 cells have been shown to express endogenous L-plastin although the expression level has been described as being heterogeneous [37]. Indeed, a fraction of MCF-7 cells highly expresses L-plastin, whereas other cells express L-plastin at a level close to or below immunofluorescence detection limits. Without PMA treatment, MCF-7 cells exhibited few prominent actin structures, as visualized by phalloidin staining, and L-plastin displayed a diffuse cytoplasmic distribution with a very weak localization to the cortical cytoskeleton (Fig. 3A, upper panels). PMA treatment of MCF-7 cells led to an important modification of the actin cytoskeleton organization and, in consequence, of the cell morphology. Interestingly, the phenotype of MCF-7 cells following PMA treatment was heterogeneous, with some cells exhibiting more or less pronounced ruffling membranes (Fig. 3A, second and third row panels) and others displaying protruding spike-like structures (Fig. 3A, fourth row panels). Surprisingly, L-plastin translocated to these newly assembled actin-rich structures in response to PMA treatment. Notably, L-plastin was mainly targeted to the proximal, membrane-embedded part of the protruding spike-like structures, whereas actin could be visualized throughout the entire length of the spikes. To discriminate between *de novo* actin polymerization and reorganization of existing actin filaments, cells were treated with the actin polymerization inhibitor cytochalasin D (CytoD), prior to the incubation with PMA. CytoD inhibited the PMA-induced actin reorganization and translocation of L-plastin, suggesting that PMA treatment induced *de novo* actin assembly rather than the reorganization of existing actin filaments (Fig. 3A, lower panels).

Next, a highly specific anti-serine-5 phosphorylated L-plastin (anti-Ser5-P) antibody, that had been characterized before [9], was used to determine L-plastin phosphorylation in immunoblotting experiments. Treatment of MCF-7 cells with PMA highly increased L-plastin phosphorylation (Fig. 3B), suggesting that PKC-elicited signaling upregulates L-plastin phosphorylation in these cells. Notably, the treatment of MCF-7 cells with a lower PMA concentration (0.1 μ M) led to similar L-plastin translocation and phosphorylation events (data not shown).

Finally, we investigated the intracellular localization of Ser5 phosphorylated L-plastin in PMA-treated MCF-7 cells (Fig. 3C). Immunofluorescence analysis using the anti-Ser5-P antibody and Rhodamine-phalloidin revealed that L-plastin translocated to F-actin rich structures following PMA treatment was essentially the phosphorylated form. Indeed both ruffling membranes (upper and middle panels) and protruding spike-like structures formed at the cell periphery (lower panels) were stained with the anti-Ser5-P antibody. It is noteworthy that transfected S5/A-L-plastin also translocated to F-actin structures although to a lesser degree than WT- or S5/E-L-plastin, suggesting that phosphorylation is not strictly required for its translocation (data not shown). Altogether, these data support a PKC-dependent mechanism for L-plastin phosphorylation and its concomitant translocation to *de novo* assembled actin-rich structures in epithelial cancer cells, linking the regulation of L-plastin phosphorylation to that of actin dynamics.

L-Plastin Associates with a Protein Complex Containing Cortactin, a Regulator of Actin Dynamics

To biochemically corroborate these observations, we investigated whether L-plastin associates with protein complexes

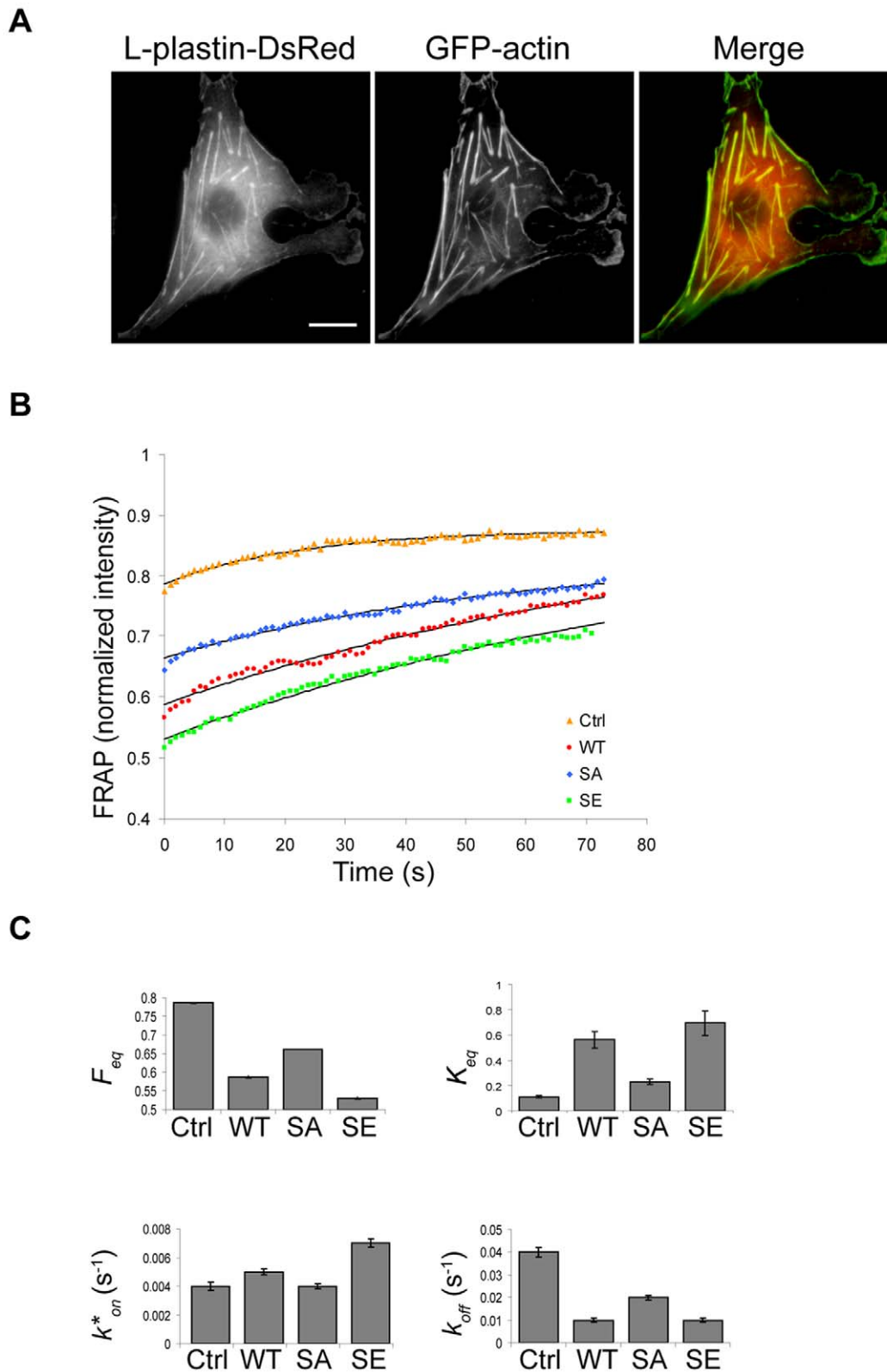


Figure 2. L-plastin phosphorylation modulates actin dynamics in focal adhesions. (A). Expression of L-plastin and actin in live Vero cells. Vero cells were cotransfected with monomeric L-plastin-DsRed-N1 fusion variants and GFP-actin. Wild type L-plastin-DsRed is shown here. Scale bar, 20 μm . (B). Normalized FRAP recovery curves obtained for actin in presence of wild type (WT, red), Ser5/Ala (SA, blue) and Ser5/Glu (SE, green) L-plastin-DsRed fusions or DsRed alone (control, orange) are compared to the curves predicted by the one-binding-state model (black curves). Data were obtained from three independent experiments representing 10 FRAP recordings for each condition. (C). Charts representing biochemical parameters obtained from data fitted with a one-binding-state model. Bars represent the mean \pm s.d. doi:10.1371/journal.pone.0009210.g002

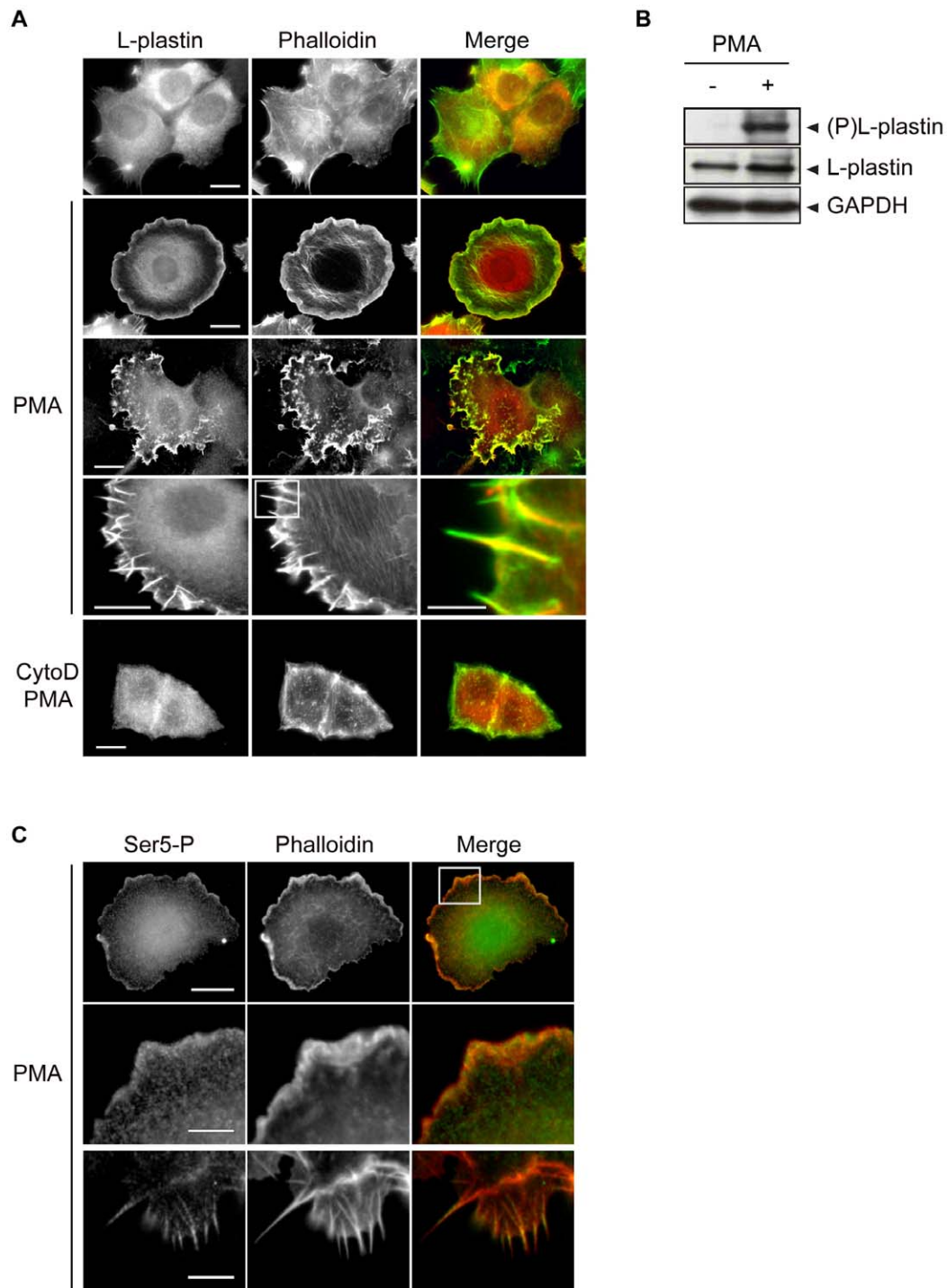


Figure 3. PMA induces the translocation of L-plastin to *de novo* assembled actin structures and triggers L-plastin phosphorylation. (A). PMA induces actin reorganization with concurrent local accumulation of L-plastin in actin-rich structures. MCF-7 cells were pretreated with or without 0.5 μ M cytochalasin D (CytoD) and then treated with 1 μ M PMA as indicated. The localization of L-plastin and F-actin was analyzed by epifluorescence microscopy after staining with an anti-L-plastin antibody and Alexa 488-conjugated phalloidin. The merged image of the boxed region indicated in the fourth row middle panel is shown enlarged on the right; scale bar, 2.5 μ m. Other scale bars, 10 μ m. (B). PMA induces phosphorylation of L-plastin on residue Ser5. MCF-7 cells were treated for 1 hour with or without 1 μ M PMA at 37°C. Total cell extracts (50 μ g) were analyzed by immunoblotting using antibodies specific for Ser5 phosphorylated L-plastin (anti-Ser5-P, upper panel), L-plastin (middle panel) or GAPDH (lower panel) to monitor equal protein loading. (C). Intracellular localization of Ser5 phosphorylated L-plastin in PMA-treated MCF-7 cells. MCF-7 cells treated for 1 h with 1 μ M PMA were analyzed by epifluorescence microscopy after staining with an anti-Ser5-P antibody and Rhodamine-conjugated phalloidin. Upper panels illustrate the colocalization of Ser5 phosphorylated L-plastin with F-actin in ruffling membranes. Middle panels represent an enlarged detail of the cell shown in the upper panels (squared area). Lower panels represent a magnified detail of another cell showing the colocalization of Ser5 phosphorylated L-plastin with F-actin in spike-like structures. Scale bars, 10 μ m (upper panels) and 2.5 μ m (middle and lower panels). doi:10.1371/journal.pone.0009210.g003

involved in the regulation of actin polymerization. We decided to use cortactin as a marker for sites of active actin polymerization. Cortactin, a Src-kinase protein substrate, which localizes to dynamic actin assembly sites such as lamellipodia, endosomes, podosomes and invadopodia [38], translocates to ruffling membranes upon PMA treatment [39]. As shown in figure 4A, a fraction of L-plastin colocalized with cortactin in PMA-treated MCF-7 cells, mainly in ruffling membranes (Fig. 4A, upper and middle panels) and, at a lower extent, in the membranous area where the spike-like structures protrude but not along the spikes themselves (Fig. 4A lower panels). Immunofluorescence analysis of PMA-treated cells using the anti-Ser5-P antibody provided evidence for the colocalization of phosphorylated L-plastin with cortactin in ruffling membranes (Fig. 4B).

Furthermore, we performed coimmunoprecipitation experiments with PMA-treated MCF-7 cells, using GFP-nanotrap [40]. This assay makes use of bead-linked monovalent llama antibodies directed against GFP and allows fast and efficient purification of GFP fusion proteins and their associated complexes formed in the cell. Importantly, immunoblot analysis revealed that cortactin efficiently coprecipitated with WT GFP-L-plastin extracted from PMA-treated cells (Fig. 4C). It is noteworthy that phosphorylation-defective S5/A GFP-L-plastin as well as WT GFP-L-plastin in PMA non-treated cells were both able to coimmunoprecipitate cortactin in some experiments (data not shown). These observations suggest that Ser5 phosphorylation is not an absolute requirement for binding, without excluding that it may modulate/promote L-plastin association with cytoskeletal protein complexes, as suggested by the FRAP data. Accordingly, pull-down assays with MCF-7 cell extracts using recombinant unphosphorylated GST-L-plastin also revealed cortactin in a complex with L-plastin (Fig. 4D). Altogether, our results identify L-plastin as a component of a protein complex comprising cortactin and provide further evidence for its recruitment to sites of active actin polymerization in cells.

Novel PKC Isozymes Are Required for PMA-Induced Actin Cytoskeleton Rearrangements and L-Plastin Ser5 Phosphorylation

We have shown very recently that, in the highly invasive 1001 cells, PKC- δ is the major PKC isozyme responsible for endogenous L-plastin phosphorylation [37]. To identify the PKC isozymes involved in L-plastin phosphorylation in non-invasive epithelial carcinoma MCF-7 cells treated with PMA, we used two different PKC inhibitors GF109203X (specific for α , β 1, δ , ϵ , ζ isozyme inhibition) or Gö6976 (inhibiting α and β 1 isozymes) [41]. Interestingly, treatment with GF109203X but not with Gö6976 prevented PMA-induced L-plastin phosphorylation (Fig. 5A).

Accordingly, GF109203X, but not Gö6976, strongly inhibited the formation of ruffling structures and spikes and consequently, the PMA-induced translocation of L-plastin to these structures (Fig. 5B). A role for the atypical PKC- ζ could be excluded at the outset, since unlike classical and novel PKC isozymes, atypical PKC isozymes do not respond to phorbol esters [42]. These results argue in favor of an involvement of novel PKC isozymes (δ and/or ϵ) in L-plastin phosphorylation and actin cytoskeleton reorganization in response to PMA.

PKC- δ Is the Major Kinase Involved in PMA-Enhanced L-Plastin Ser5 Phosphorylation

Although the majority of the non-conventional PKC isozymes are expressed in MCF-7 cells [43], it is the novel PKC- δ isozyme

that has been extensively described as a regulator of the actin cytoskeleton in epithelial cells [44,45]. To further dissect the contribution of novel PKC isozymes in PMA-triggered L-plastin phosphorylation, we performed knock-down experiments using siRNA technology resulting in 85% of PKC- δ or 71% of PKC- ϵ knock-down. The knock-down of PKC- δ significantly inhibited PMA-dependent L-plastin phosphorylation in MCF-7 cells (63% decrease of the amount of phosphorylated L-plastin), whereas PKC- ϵ knock-down had no significant effect (Fig. 5C). Accordingly, knock-down of PKC- δ , but not of PKC- ϵ considerably impaired the formation of ruffling membranes and spike-like structures (data not shown). These findings suggest that PKC- δ is the major PKC isozyme involved in PMA-triggered signaling pathways leading to L-plastin phosphorylation. Altogether our results point to a role for PKC- δ signaling in the regulation of L-plastin activity in MCF-7 carcinoma cells.

Discussion

L-plastin is an actin filament bundling protein which contributes to cancer cell invasion in a phosphorylation-dependent manner. In the present study, we have shown that L-plastin associates with the cytoskeleton following a two-binding-state model, in support of biochemical and structural models. Phosphorylation on Ser5 increased its association rate and, hence, appears to promote the L-plastin capacity to dock efficiently to the actin cytoskeleton and regulate actin turn-over. In support of this hypothesis, we have provided evidence for the first time that L-plastin modulates actin dynamics in focal adhesions and increases their F-actin content by decreasing the actin dissociation rate at actin filament ends, this effect being also promoted by L-plastin Ser5 phosphorylation. In carcinoma cells, consistent with the role of L-plastin in controlling actin dynamics, the PKC activator PMA induced the translocation of L-plastin to *de novo* actin polymerization sites in ruffling membranes and protruding spike-like structures, and significantly enhanced its phosphorylation on Ser5 via PKC- δ signaling pathways. In agreement with these findings, we identified L-plastin as a component of a protein complex comprising cortactin, a major regulator of actin dynamics. Altogether, our data support a role for L-plastin in the control of actin turn-over which is modulated by its phosphorylation on residue Ser5. In MCF-7 carcinoma cells, invasion-promoting pathways appear to upregulate L-plastin phosphorylation in parallel to actin cytoskeleton reorganization.

In our FRAP assays, the recovery of GFP-L-plastin fluorescence fitted a two-binding-state model [31], comprising a first quick and a second slow binding phase. Such a mechanism would be in good agreement with previous data suggesting that the two ABDs of L-plastin have non-identical interactions with F-actin [20] and that ABD2 binds actin first, enabling the subsequent binding of ABD1 to a second filament [14]. Phosphorylation on residue Ser5 was proposed to regulate the targeting of L-plastin to the actin cytoskeleton [9,33]. Here we found that the non-phosphorylatable S5/A-L-plastin variant exhibited a lower association rate with focal adhesions in Vero cells than WT-L-plastin, in line with its weak colocalization with actin-rich structures, as reflected by the large pool of unbound S5/A-L-plastin in the cytosol. Phosphorylation of L-plastin mainly increased the association rates k_{on}^* and k_{2on}^* and decreased the concentration of free unbound L-plastin molecules F_{eq} . Although our experimental set-up does not allow to determine the order of binding of the two ABDs, our FRAP data favor a mechanism in which phosphorylation regulates the docking of the protein to the cytoskeleton rather than its dissociation. Interestingly, the two ABDs have been described as

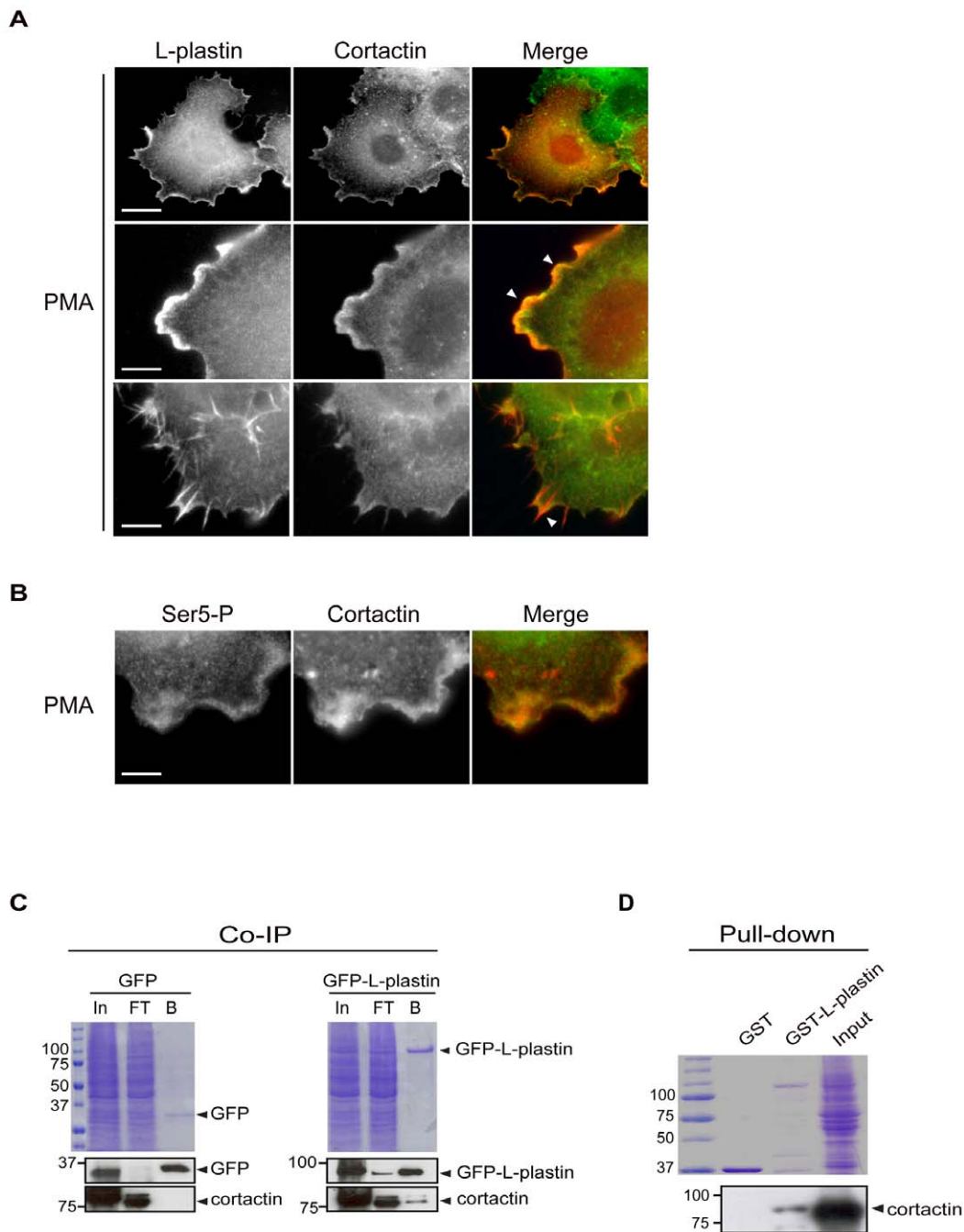


Figure 4. L-plastin associates with cortactin in protein complexes. (A). Colocalization of L-plastin with cortactin in MCF-7 cells. MCF-7 cells were treated with 1 μ M PMA as described and analyzed by epifluorescence microscopy after staining with antibodies specific for L-plastin and cortactin. Immunofluorescence images illustrate the colocalization of L-plastin (red) and cortactin (green) in ruffling membranes (upper and middle panels) and at a lower extent in the membrane-embedded portion of spikes (lower panel). Arrows point to regions of colocalization. Scale bars, 10 μ m (upper panels) and 3 μ m (middle and lower panels). (B). Colocalization of serine-5 phosphorylated L-plastin with cortactin in MCF-7 cells. PMA-treated MCF-7 cells were stained with anti-Ser5-P and anti-cortactin antibodies and analyzed by epifluorescence microscopy. Serine-5 phosphorylated L-plastin (green) and cortactin (red) are colocalized in ruffling membranes. Scale bar, 3 μ m. (C). Coimmunoprecipitation of cortactin with GFP-L-plastin in MCF-7 cells. GFP- or GFP-L-plastin-expressing MCF-7 cells were treated with PMA as described. Following cell lysis, protein extracts were subjected to immunoprecipitation with GFP-nanotrap. Aliquots of input [In], flow-through [FT], and bound fraction [B] were separated by SDS-PAGE and visualized either by Coomassie Blue staining (upper panels) or by immunoblot analysis using antibodies specific for GFP (middle panels) or cortactin (bottom panels). (D). Pull-down assay with cell extracts. GST and GST-L-plastin (20 μ g) immobilized on glutathione-sepharose beads were incubated with untreated MCF-7 cell extracts (200 μ g). The resulting complex was precipitated by centrifugation, separated by SDS-PAGE and visualized by Coomassie Blue staining (upper panel) or by immunoblotting using a cortactin-specific antibody (lower panel). doi:10.1371/journal.pone.0009210.g004

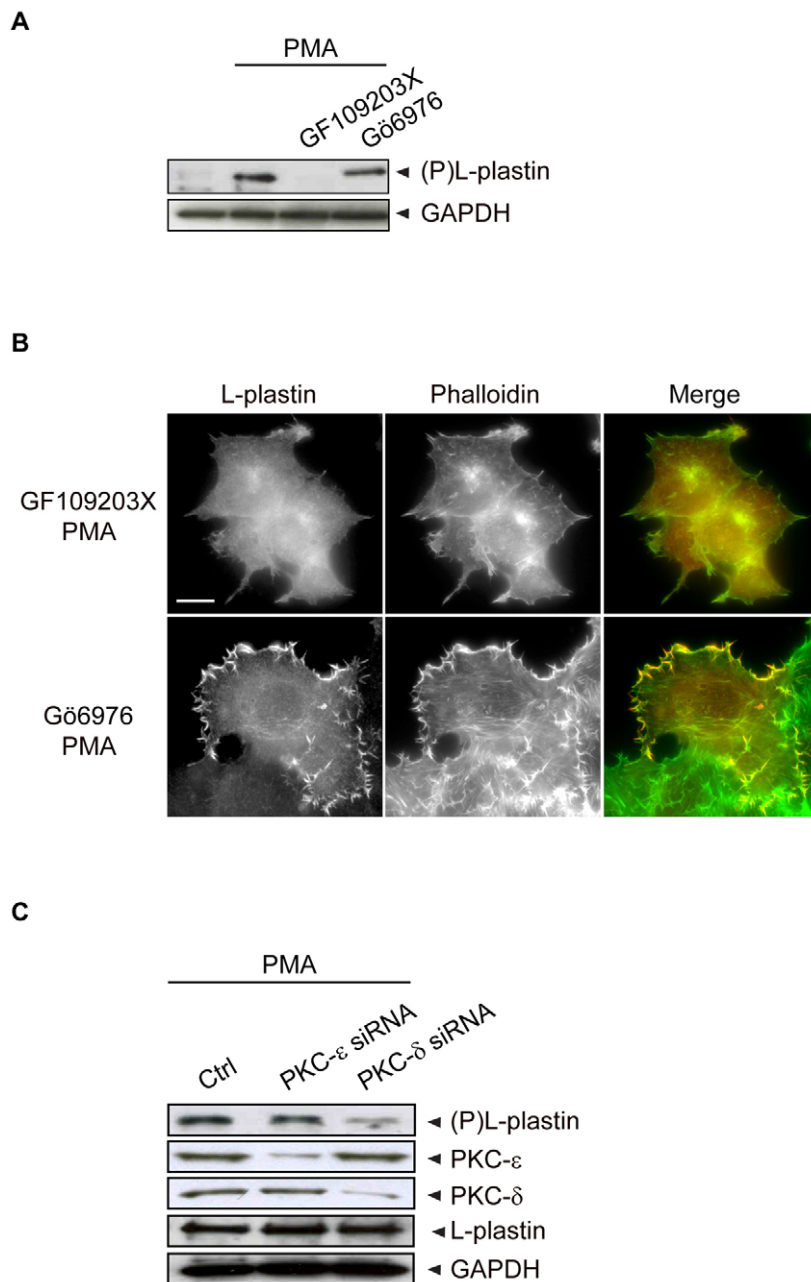


Figure 5. The novel PKC- δ isozyme is necessary for PMA-induced cytoskeleton reorganization and L-plastin Ser5 phosphorylation.

(A). Novel PKC isozymes regulate PMA-induced L-plastin phosphorylation in MCF-7 cells. MCF-7 cells were pretreated for 3 hours with 5 μ M of GF109203X (specific for α , β 1, δ , ϵ , and ζ) or 0.5 μ M of Gö6976 (specific for α and β 1) and then treated for 1 hour with or without 1 μ M PMA at 37°C. Total cell extracts (50 μ g) were analyzed by immunoblotting using anti-Ser5-P L-plastin (upper panel) or anti-GAPDH (lower panel) antibodies. (B). PMA-induced actin cytoskeleton remodeling and L-plastin translocation involves novel PKC isozymes. MCF-7 cells were pretreated for 3 hours with 5 μ M GF109203X or 0.5 μ M Gö6976, then treated for 1 hour with 1 μ M PMA at 37°C. Cells were then fixed and processed for immunofluorescence. Labeled cells were analyzed with an epifluorescence microscope after staining with an anti-L-plastin antibody and Alexa 488-conjugated phalloidin. Scale bar, 10 μ m. (C). SiRNA knock-down of PKC- δ decreased PMA-induced L-plastin phosphorylation in MCF-7. MCF-7 cells were transfected with either PKC- δ or PKC- ϵ siRNAs as well as with negative control siRNA (Ctrl) for 48 hours and then treated with PMA as indicated. Total cell extracts (50 μ g) were analyzed by immunoblotting using antibodies specific for Ser5 phosphorylated L-plastin, PKC- ϵ , PKC- δ and total L-plastin. GAPDH was used to monitor equal protein loading. doi:10.1371/journal.pone.0009210.g005

being packed tightly together in an approximately antiparallel arrangement. Since a subset of the presumed actin-binding sequences within the ABDs face toward the ABD1-ABD2 interface, a conformational rearrangement appears to be required for their participation to F-actin binding [13]. Whether L-plastin

phosphorylation contributes to such a conformational change enabling efficient F-actin binding remains to be investigated.

Importantly, our data support a role for L-plastin in the control of actin dynamics and turn-over which is modulated by L-plastin phosphorylation. Indeed, all L-plastin variants decreased the pool

of free actin monomers F_{eq} and the actin dissociation rate k_{off} in focal adhesions when compared with those of control cells, indicating the presence of more F-actin. Several mechanisms may account for the decrease in actin filament turn-over. L-plastin may, by binding along actin filaments, protect them against depolymerization as supported by previous *in vitro* data [20]. This effect might not necessarily rely on actin bundling since binding of the single ABDs of L-plastin and its closely related T-plastin isoform, were sufficient for decreasing actin depolymerization *in vitro* [20,46]. Alternatively, L-plastin may protect actin filaments against disassembly by cofilin, as previously proposed for T-plastin [46]. The observed effect on actin turn-over was clearly more pronounced for the phosphorylatable WT- or the phosphomimetic S5/E-L-plastin variants than for the unphosphorylatable S5/A-L-plastin. L-plastin phosphorylation may have a direct effect on actin filament stabilization by enhancing L-plastin binding along their side and/or L-plastin-mediated bundling, a mechanism which is supported by previous biochemical data [9]. Such a mechanism of regulation has also been reported for ABP-280, an actin-binding protein that binds and crosslinks actin filaments more readily when tyrosine phosphorylated [47]. Most interestingly, the S5/E-L-plastin variant induced even more strikingly varying K_{eq} , k_{on}^* and F_{eq} values for actin than WT-L-plastin as compared to non-transfected control cells. These observations suggest that the negatively charged glutamate residue, mimicking Ser5 phosphorylation and escaping inactivation through dephosphorylation, might keep the S5/E variant locked in a high affinity state. Thus phosphorylation-dephosphorylation cycles of L-plastin might be coupled to actin dynamics, as also supported by our results obtained in MCF-7 cells. A similar, yet opposite phosphorylation-dependent fascin activity has been proposed to regulate filopodial dynamics, since an unphosphorylatable fascin mutant was constitutively active and enhanced filopodia formation and length, whereas a phosphomimetic variant acted as a dominant negative mutant [26]. Compared to the actin-bundling protein fascin, L-plastin may have a more pleiotropic function since it associates with various actin-rich structures, including ruffling membranes, in cells.

As L-plastin Ser5 phosphorylation has been correlated with the progression to an invasive cell phenotype [8], there is growing interest in studying the effect of L-plastin phosphorylation in epithelial cancer cells. PMA, a potent PKC activator, is known to have profound effects on MCF-7 breast carcinoma cell morphology and motility [48], and to contribute to the invasive behaviour of MCF-7 cells [49]. Here, we have shown that PMA treatment of MCF-7 cells leads to L-plastin phosphorylation and cytoskeletal rearrangements with concurrent L-plastin translocation to newly formed spikes and ruffling membranes in these cells. Inhibition assays using PKC isozyme-specific inhibitors have highlighted a role for novel PKC isozymes in PMA-triggered L-plastin phosphorylation and actin cytoskeleton remodeling, although the contribution of other kinases is not necessarily excluded. More precisely, our siRNA knock-down studies have revealed that PKC- δ signaling pathways are necessary for PMA-induced L-plastin phosphorylation. Notably, constitutive L-plastin phosphorylation in the highly invasive MCF-7-derived 1001 cells has also been shown to depend predominantly on the novel PKC- δ isozyme [37]. In hematopoietic cells, the role of PKCs remains highly controversial [22,24,50]. Whereas recent work has shown the involvement of a distinct subset of PKC isozymes in L-plastin phosphorylation in neutrophils upon N-formyl-L-methionyl-L-leucyl-L-phenylalanine stimulation [25], most of the past studies made no distinction between the different PKC isozymes. Altogether our results suggest that, in carcinoma cells, PKC- δ

signaling is involved in L-plastin phosphorylation, an event that appears to link signal transduction pathways and cytoskeletal dynamics. However, it is important to note that a direct L-plastin phosphorylation by PKC- δ or by any other PKC isoform could not be demonstrated *in vitro* [51].

PMA treatment of MCF-7 cells induced a profound change in cell morphology with concomitant L-plastin translocation to *de novo* assembled actin-rich structures. Based on its actin filament bundling activity, we had expected L-plastin to be recruited to F-actin structures containing tightly bundled actin filaments such as stress fibers. However, L-plastin associated barely with these structures and mainly targeted to sites of active actin polymerization such as the proximal part of protruding spikes or ruffling membranes. While microspikes and filopodia contain aligned actin filaments, ruffling membranes harbour a dendritic network of actin (reviewed in [52]). Thus, unlike other bundling proteins such as fascin [26], L-plastin appears to be able to associate with both types of actin organization, dendritic networks and aligned filaments. Notably, recent results using L-plastin nanobodies have demonstrated that L-plastin bundling activity is necessary to maintain filopodial integrity [53]. An implication of L-plastin in controlling actin dynamics is supported by our observation that cortactin, an Arp2/3 complex-binding protein [54–56], was found in a complex with phosphorylated L-plastin in PMA-treated MCF-7 cells. It is noteworthy that cortactin could also be associated with protein complexes containing unphosphorylated L-plastin depending on the experiment. Thus, phosphorylation of L-plastin does not appear to be strictly required for protein complex formation, although it might stabilize such complexes. Localization of L-plastin to ruffling membranes and its presence in a complex comprising cortactin links this protein to the active remodeling of actin filaments where it may contribute to stabilize the filaments. In support of this mechanism, the T-plastin isoform has also been reported to stabilize actin filaments and modulate Arp2/3-mediated actin assembly in an *in vitro* reconstitution assay [46].

Taken together, our results quantitatively demonstrate for the first time that L-plastin affects actin dynamics and turn-over in live cells, an effect which is modulated by its phosphorylation on Ser5. Although phosphorylation of L-plastin does not appear to be absolutely required for its recruitment to actin polymerization sites, it might, by increasing the pool of high affinity L-plastin, contribute to the fine-tuning of actin turn-over. Our study paves the way for future investigations of the role of L-plastin in carcinoma cell invasion as a modulator of actin turn-over.

Materials and Methods

Ethics

An ethics statement is not required for this work.

Cell Culture

Monkey kidney Vero cells were grown in DMEM (Dulbecco's modified Eagle's medium). The human breast carcinoma MCF-7 cell line was grown in RPMI (Roswell Park Memorial Institute) medium. Media were supplemented with 10% fetal bovine serum. Cells were grown at 37°C, under 5% CO₂ atmosphere.

Antibodies and Reagents

Polyclonal rabbit IgGs against L-plastin and serine-5 phosphorylated L-plastin (anti-Ser5-P) have been characterized before [3,9]. Mouse monoclonal anti-GFP and anti-cortactin antibodies were obtained from Sigma (Bornem, Belgium) and from Millipore (Billerica, MA), respectively. Rabbit polyclonal anti-PKC- δ and

rabbit monoclonal anti-PKC- ϵ were from Cell Signaling Technology, Inc. (Danvers, MA). Mouse anti-glyceraldehyde-3-phosphate dehydrogenase (GAPDH), Rhodamine-conjugated phalloidin and Alexa 488-conjugated phalloidin were purchased from Molecular Probes (Invitrogen, Merelbeke, Belgium). Texas red- and Cy2 green-conjugated secondary antibodies were from Jackson ImmunoResearch Laboratories (De Pinte, Belgium). The anti-rabbit and anti-mouse IgG antibodies coupled to horseradish peroxidase were purchased from Amersham, GE Healthcare (Diegem, Belgium). Phorbol 12-myristate 13-acetate (PMA) and cytochalasin D (CytoD) were obtained from Sigma, the PKC inhibitors GF109203X and Gö6976 from Calbiochem (Leuven, Belgium) and lipofectamine 2000 from Invitrogen.

Construction of DNA Constructs

pDsRed-Monomer-N1 vectors (Takara Bio-Europe/Clontech, Saint-Germain-en-Laye, France) containing wild-type- (WT), unphosphorylatable Ser5/Ala (S5/A) or phosphomimetic Ser5/Glu (S5/E)-L-plastin were generated from previously described pGEX-2T-WT-L-plastin, pGEX-2T-S5/A-L-plastin and pGEX-2T-S5/E-L-plastin vectors, respectively [9]. Briefly, WT-, S5/A-, or S5/E-L-plastin 1880-bp *EcoRI*-restricted cDNA fragments were inserted into DsRedN1 *EcoRI*-cut vectors. The correct orientation of inserts was verified by sequencing. pEGFP-C vectors (Clontech) containing WT-, S5/A-, or S5/E-L-plastin were generated from pDsRedN1-WT-L-plastin, pDsRedN1-S5/A-L-plastin, or pDsRedN1-S5/E-L-plastin vectors, respectively. Briefly, the pEGFP2-S5/A-L-plastin was cloned by *EcoRI/BamHI* restriction of the pDsRedN1-S5/A-L-plastin vector. The resulting fragment was inserted into the *EcoRI/BamHI*-restricted pEGFP2 vector. The pEGFP2-WT- or -S5/E-L-plastin vectors were constructed by substitution of the 5'-end of the pEGFP2-S5/A-L-plastin vector by the 5'-end of WT- or S5/E-L-plastin, obtained by *EcoRI/ScaI* restriction of pDsRedN1-WT- or -S5/E-L-plastin vectors, respectively. All constructs were verified by sequencing.

Recombinant Proteins

GST and GST-fusion proteins were produced in *E. coli* from the pGEX-2T expression vector and purified as described previously [17]. The concentration of thrombin-cleaved proteins was determined using the Bradford assay (Bio-Rad, Nazareth, Belgium) and by SDS-polyacrylamide gel electrophoresis (PAGE) using a BSA protein standard curve.

Transient Transfection of Cells

5–10 μ g of cDNA encoding L-plastin phosphorylation variants or β -actin were transfected into 5×10^6 Vero cells by electroporation at 240 V and 950 μ F [57]. MCF-7 cells were transfected using lipofectamine 2000. For knock-down experiments, cells were seeded at a density of 5×10^4 cells per well in a 6-well plate 24 hours prior to transfection. siRNA transfection was performed using lipofectamine 2000 according to the manufacturer's protocol. Double stranded 21-mers validated siRNA for PKC- δ , - ϵ and negative control were purchased from Qiagen (Venlo, The Netherlands). The mRNA and protein levels of siRNA targeted genes were analyzed 48 hours after transfection by RT-qPCR and immunoblotting, respectively. Quantification of siRNA-mediated knock-down of PKC- δ and PKC- ϵ was performed by densitometric scanning of the autoradiograms (hp scanjet 5470c and ImageJ software). The percentage of PKC- δ or PKC- ϵ expression was calculated as the ratio between PKC- δ or PKC- ϵ expression after PKC- δ or PKC- ϵ siRNA transfection respectively versus their expression after control siRNA transfection (100%).

Treatment of Cells with Pharmacological Agents

MCF-7 cells were pretreated for 3 hours in the presence or absence of PKC inhibitors and incubated for 1 hour with or without 1 μ M PMA. In some experiments, MCF-7 cells were pretreated for 1 hour with 0.5 μ M cytochalasin D and then incubated 1 hour with or without 1 μ M PMA. Cells were then processed either for indirect immunofluorescence or for cell lysis.

Indirect Immunofluorescence

Cells were washed with PBS supplemented with 0.1 mM CaCl_2 and 0.1 mM MgCl_2 , fixed with 3% paraformaldehyde and processed for immunofluorescence labeling as described previously [58]. Labeled cells were analyzed by epifluorescence microscopy (Leica DMRX microscope) or a Zeiss laser scanning confocal microscope (LSM-510 Meta, Carl Zeiss, Jena, Germany). Images were acquired with a linear CCD camera (Micromax, Princeton Instruments, Trenton, NJ) and analyzed with Metaview software (Universal Imaging Corporation Ltd., Buckinghamshire, UK).

Immunoblotting

Cells were lysed for 30 minutes in ice-cold RIPA buffer (10 mM Tris-HCl pH 7.4, 150 mM NaCl, 0.1% SDS, 1% Triton X-100, and 1% Na-deoxycholate) containing a cocktail of protease inhibitors (Roche Diagnostics GmbH, Mannheim, Germany). Lysates were cleared by centrifugation at $20000 \times g$ for 10 minutes at 4°C. The total protein concentration was determined using the Bradford assay. Total cell lysates (50 μ g of proteins) were separated by SDS-PAGE and transferred onto nitrocellulose membrane (Amersham, GE Healthcare) using a semi-dry transblot apparatus. Primary antibodies were revealed using secondary antibodies coupled to horseradish peroxidase and enhanced chemiluminescence (ECL) detection method. Quantification of L-plastin phosphorylation was performed by densitometric scanning of the autoradiograms obtained using the anti-Ser5-P antibody (hp scanjet 5470c and ImageJ software). The percentage of L-plastin phosphorylation was expressed as the ratio of phosphorylated L-plastin after PKC isozyme-specific siRNA transfection versus phosphorylated L-plastin after control siRNA transfection (100%).

Pull-Down and Immunoprecipitation

GST or GST-fusion proteins (20 μ g), immobilized on glutathione-sepharoseTM 4B beads (Amersham, GE Healthcare), were incubated overnight with cell extracts (200 μ g) on an end-over-end rotor at 4°C. The bead pellet was rinsed three times with cold PBS, then resuspended in 2 x SDS-containing sample buffer and boiled for 5 minutes at 95°C.

For immunoprecipitation, 10^6 cells transiently transfected with expression vectors encoding GFP or WT GFP-L-plastin were homogenized in 500 μ l lysis buffer (10 mM Tris-HCl, pH 7.5, 100 mM NaCl, 0.5 mM EDTA, 1 mM PMSF, 0.5% Nonidet P-40). After a centrifugation step of 10 minutes at $20000 \times g$ at 4°C, the supernatant was adjusted to 1 ml with dilution buffer (10 mM Tris-HCl, pH 7.5, 150 mM NaCl, 0.5 mM EDTA, 2 mM PMSF). 20 μ l (2%) were added to SDS-containing sample buffer and used for SDS-PAGE (referred to as input). 30 μ l of GFP-nanotrap beads [40] were added and incubated for 30 minutes on an end-over-end rotor at 4°C. After a centrifugation step of 2 minutes at $2700 \times g$ at 4°C, the supernatant was removed, and 20 μ l (2%) of the supernatant were used for SDS-PAGE (referred to as flow-through). The bead pellet was washed three times with 500 μ l dilution buffer. After the last washing step, the beads were

resuspended in 2 x SDS-containing sample buffer and boiled for 10 minutes at 95°C.

The obtained samples were analyzed by SDS-PAGE with subsequent Coomassie Blue staining or immunoblotting.

FRAP Experiments

FRAP experiments were performed with a Zeiss LSM510 Meta laser scanning confocal microscope. Transfected Vero cells were kept at 37°C using an air-stream incubator-XL and a heating frame (Carl Zeiss). The excitation wavelength and emission filters were 488 nm/band-pass 505 to 530 nm and 543 nm/long-pass 560 nm for GFP and DsRed respectively. Image processing was performed using Zeiss LSM510 Image Browser version 4.0.

For FRAP experiments, a 63x/1.4 NA oil-immersion objective was used, and the confocal pinhole was set to 2.5 µm. Prebleach and recovery images were acquired at a rate of 1 image/second. We intentionally used the rather long time step (1 s) in order to acquire fluorescence recovery over the optimal time range (90 s) for investigation of L-plastin binding and actin polymerization properties. For photobleaching, all argon laser lines (458, 477, 488, and 514 nm) were used simultaneously at 100% transmittance for 3 iterations to bleach a circular area of 5 µm diameter, the region of interest (ROI). Normalized FRAP curves were generated from raw data as described [59]. Briefly, intensity in the bleached region ($I_{frap}(t)$) and in the whole cell ($I_{whole}(t)$) at each time point are initially subtracted by the corresponding background intensity ($I_{base}(t)$). These intensities are then rescaled to the average prebleach intensities in the corresponding regions ($I_{frap-pre}$ and $I_{whole-pre}$). The normalized FRAP curve ($I_{frap-norm}(t)$) is the ratio of FRAP and whole cell rescaled intensities. The resulting equation is

$$I_{frap-norm}(t) = \frac{I_{whole-pre}}{I_{whole}(t) - I_{base}(t)} \cdot \frac{I_{frap}(t) - I_{base}(t)}{I_{frap-pre}} \quad (1)$$

To fit the normalized recoveries, we applied the models of binding reactions in a reaction dominant regime; a one-binding-state or a two-binding-state [31]. The general chemical rate equation for a single binding reaction is



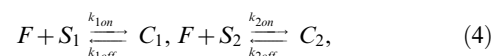
where F represents a free protein, S is a vacant binding site, C denotes bound $[FS]$ complexes, and k_{on} and k_{off} are the association

and dissociation rates respectively. Assuming that the biological system is in equilibrium and the number of binding sites is constant, then the fluorescence intensity within the bleached spot is

$$FRAP(t) = F_{eq} \left(1 + \frac{k_{on}^*}{k_{off}} (1 - e^{-k_{off}t}) \right), \quad (3)$$

where F_{eq} is the equilibrium normalized concentration of free monomers, the pseudo-association rate k_{on}^* is the product of the association rate, k_{on} and the steady-state concentration of vacant binding sites, S_{eq} ($k_{on}^* = k_{on} \cdot S_{eq}$) [59]. From the values of model parameters, the ratio of bound to free molecule concentrations (K_{eq}) is calculated as $K_{eq} = k_{on}^* / k_{off}$.

In a two-binding-state model, the chemical rate equations are



where subscripts 1 and 2 refer to the different binding states. Using similar assumptions as for the one-binding-state model the total fluorescence intensity is

$$FRAP(t) = F_{eq} \left(1 + \frac{k_{1on}^*}{k_{1off}} (1 - e^{-k_{1off}t}) + \frac{k_{2on}^*}{k_{2off}} (1 - e^{-k_{2off}t}) \right), \quad (5)$$

where k_{1on}^* , k_{2on}^* , k_{1off} , k_{2off} are the pseudo-association and -dissociation rate constants at the first and second binding states, respectively [31].

FRAP curves were fitted with equations (3) or (5), yielding the parameters F_{eq} , k_{on}^* and k_{off} , k_{1on}^* and k_{1off} , k_{2on}^* and k_{2off} . All fitting procedures were performed with *Nonlinear Regress* function in Mathematica 6 (Wolfram Research).

Acknowledgments

GFP-actin was a kind gift from Christoph Ballestrem (University of Manchester, UK). The authors thank Guillaume Vetter for providing useful discussion.

Author Contributions

Conceived and designed the experiments: ZAT ESR MY EF. Performed the experiments: ZAT ESR MM EH. Analyzed the data: ZAT ESR AH CH MC MY. Contributed reagents/materials/analysis tools: EF. Wrote the paper: ZAT ESR EF.

References

- Fidler IJ (1999) Critical determinants of cancer metastasis: rationale for therapy. *Cancer Chemother Pharmacol* 43 Suppl: S3–10.
- Matsushima K, Shiroo M, Kung HF, Copeland TD (1988) Purification and characterization of a cytosolic 65-kilodalton phosphoprotein in human leukocytes whose phosphorylation is augmented by stimulation with interleukin 1. *Biochemistry* 27: 3765–3770.
- Lapillonne A, Coue O, Friederich E, Nicolas A, Del Maestro L, et al. (2000) Expression patterns of L-plastin isoform in normal and carcinomatous breast tissues. *Anticancer Res* 20: 3177–3182.
- Park T, Chen ZP, Leavitt J (1994) Activation of the leukocyte plastin gene occurs in most human cancer cells. *Cancer Res* 54: 1775–1781.
- Lin CS, Park T, Chen ZP, Leavitt J (1993) Human plastin genes. Comparative gene structure, chromosome location, and differential expression in normal and neoplastic cells. *J Biol Chem* 268: 2781–2792.
- Goldstein D, Djeu J, Latter G, Burbeck S, Leavitt J (1985) Abundant synthesis of the transformation-induced protein of neoplastic human fibroblasts, plastin, in normal lymphocytes. *Cancer Res* 45: 5643–5647.
- Lin CS, Chen ZP, Park T, Ghosh K, Leavitt J (1993) Characterization of the human L-plastin gene promoter in normal and neoplastic cells. *J Biol Chem* 268: 2793–2801.
- Klemke M, Rafael MT, Wabnitz GH, Weschenfelder T, Konstantin MH, et al. (2007) Phosphorylation of ectopically expressed L-plastin enhances invasiveness of human melanoma cells. *Int J Cancer* 120: 2590–2599.
- Janji B, Giganti A, De Corte V, Catillon M, Bruyneel E, et al. (2006) Phosphorylation on Ser5 increases the F-actin-binding activity of L-plastin and promotes its targeting to sites of actin assembly in cells. *J Cell Sci* 119: 1947–1960.
- Stossel TP, Condeelis JS, Cooley L, Hartwig JH, Noegel A, et al. (2001) Filamins as integrators of cell mechanics and signalling. *Nat Rev Mol Cell Biol* 2: 138–145.
- Matsudaira P (1991) Modular organization of actin crosslinking proteins. *Trends Biochem Sci* 16: 87–92.
- Gimona M, Djinnovic-Carugo K, Kranewitter WJ, Winder SJ (2002) Functional plasticity of CH domains. *FEBS Lett* 513: 98–106.
- Klein MG, Shi W, Ramagopal U, Tseng Y, Wirtz D, et al. (2004) Structure of the actin crosslinking core of fimbrin. *Structure* 12: 999–1013.
- Galkin VE, Orlova A, Cherepanova O, Lebart MC, Egelman EH (2008) High-resolution cryo-EM structure of the F-actin-fimbrin/plastin ABD2 complex. *Proc Natl Acad Sci U S A* 105: 1494–1498.
- Bretscher A (1981) Fimbrin is a cytoskeletal protein that crosslinks F-actin in vitro. *Proc Natl Acad Sci U S A* 78: 6849–6853.

16. de Arruda MV, Watson S, Lin CS, Leavitt J, Matsudaira P (1990) Fimbrin is a homologue of the cytoplasmic phosphoprotein plastin and has domains homologous with calmodulin and actin gelation proteins. *J Cell Biol* 111: 1069–1079.
17. Arpin M, Friederich E, Algrain M, Vernel F, Louvard D (1994) Functional differences between L- and T-plastin isoforms. *J Cell Biol* 127: 1995–2008.
18. Jones SL, Brown EJ (1996) FcγRII-mediated adhesion and phagocytosis induce L-plastin phosphorylation in human neutrophils. *J Biol Chem* 271: 14623–14630.
19. Babb SG, Matsudaira P, Sato M, Correia I, Lim SS (1997) Fimbrin in podosomes of monocyte-derived osteoclasts. *Cell Motil Cytoskeleton* 37: 308–325.
20. Lebart MC, Hubert F, Boiteau C, Venteo S, Roustan C, et al. (2004) Biochemical characterization of the L-plastin-actin interaction shows a resemblance with that of alpha-actinin and allows a distinction to be made between the two actin-binding domains of the molecule. *Biochemistry* 43: 2428–2437.
21. Adams AE, Shen W, Lin CS, Leavitt J, Matsudaira P (1995) Isoform-specific complementation of the yeast sac6 null mutation by human fimbrin. *Mol Cell Biol* 15: 69–75.
22. Lin CS, Lau A, Lue TF (1998) Analysis and mapping of plastin phosphorylation. *DNA Cell Biol* 17: 1041–1046.
23. Shinomiya H, Hagi A, Fukuzumi M, Mizobuchi M, Hirata H, et al. (1995) Complete primary structure and phosphorylation site of the 65-kDa macrophage protein phosphorylated by stimulation with bacterial lipopolysaccharide. *J Immunol* 154: 3471–3478.
24. Wang J, Brown EJ (1999) Immune complex-induced integrin activation and L-plastin phosphorylation require protein kinase A. *J Biol Chem* 274: 24349–24356.
25. Paclet MH, Davis C, Kotsonis P, Godovac-Zimmermann J, Segal AW, et al. (2004) N-Formyl peptide receptor subtypes in human neutrophils activate L-plastin phosphorylation through different signal transduction intermediates. *Biochem J* 377: 469–477.
26. Vignjevic D, Kojima S, Aratyn Y, Danciu O, Svitkina T, et al. (2006) Role of fascin in filopodial protrusion. *J Cell Biol* 174: 863–875.
27. Weisswange I, Newsome TP, Schleich S, Way M (2009) The rate of N-WASP exchange limits the extent of ARP2/3-complex-dependent actin-based motility. *Nature* 458: 87–91.
28. Lippincott-Schwartz J, Patterson GH (2003) Development and use of fluorescent protein markers in living cells. *Science* 300: 87–91.
29. Sprague BL, McNally JG (2005) FRAP analysis of binding: proper and fitting. *Trends Cell Biol* 15: 84–91.
30. Hotulainen P, Lappalainen P (2006) Stress fibers are generated by two distinct actin assembly mechanisms in motile cells. *J Cell Biol* 173: 383–394.
31. Sprague BL, Pego RL, Stavreva DA, McNally JG (2004) Analysis of binding reactions by fluorescence recovery after photobleaching. *Biophys J* 86: 3473–3495.
32. Hofmann WA, de Lanerolle P (2006) Nuclear actin: to polymerize or not to polymerize. *J Cell Biol* 172: 495–496.
33. Messier JM, Shaw LM, Chafel M, Matsudaira P, Mercurio AM (1993) Fimbrin localized to an insoluble cytoskeletal fraction is constitutively phosphorylated on its headpiece domain in adherent macrophages. *Cell Motil Cytoskeleton* 25: 223–233.
34. Woodsome TP, Eto M, Everett A, Brautigan DL, Kitazawa T (2001) Expression of CPI-17 and myosin phosphatase correlates with Ca(2+) sensitivity of protein kinase C-induced contraction in rabbit smooth muscle. *J Physiol* 535: 553–564.
35. Zhou LY, Disatnik M, Herron GS, Mochly-Rosen D, Karasek MA (1996) Differential activation of protein kinase C isozymes by phorbol ester and collagen in human skin microvascular endothelial cells. *J Invest Dermatol* 107: 248–252.
36. Hai CM, Hahne P, Harrington EO, Gimona M (2002) Conventional protein kinase C mediates phorbol-dibutyrate-induced cytoskeletal remodeling in a7r5 smooth muscle cells. *Exp Cell Res* 280: 64–74.
37. Janji B, Vallar L, Al-Tanoury Z, Bernardin F, Vetter G, et al. (2009) The actin filament cross-linker L-plastin confers resistance to TNF-α in MCF-7 breast cancer cells in a phosphorylation-dependent manner. *J Cell Mol Med*.
38. Daly RJ (2004) Cortactin signalling and dynamic actin networks. *Biochem J* 382: 13–25.
39. Hiroyama M, Exton JH (2005) Studies of the roles of ADP-ribosylation factors and phospholipase D in phorbol ester-induced membrane ruffling. *J Cell Physiol* 202: 608–622.
40. Rothbauer U, Zolghadr K, Muyldermans S, Schepers A, Cardoso MC, et al. (2008) A versatile nanotrap for biochemical and functional studies with fluorescent fusion proteins. *Mol Cell Proteomics* 7: 282–289.
41. Martiny-Baron G, Kazanietz MG, Mischak H, Blumberg PM, Kochs G, et al. (1993) Selective inhibition of protein kinase C isozymes by the indolocarbazole Go 6976. *J Biol Chem* 268: 9194–9197.
42. Ono Y, Fujii T, Ogita K, Kikkawa U, Igarashi K, et al. (1989) Protein kinase C zeta subspecies from rat brain: its structure, expression, and properties. *Proc Natl Acad Sci U S A* 86: 3099–3103.
43. Basu A, Mohanty S, Sun B (2001) Differential sensitivity of breast cancer cells to tumor necrosis factor-α: involvement of protein kinase C. *Biochem Biophys Res Commun* 280: 883–891.
44. Liedtke CM, Hubbard M, Wang X (2003) Stability of actin cytoskeleton and PKC-δ binding to actin regulate NKCC1 function in airway epithelial cells. *Am J Physiol Cell Physiol* 284: C487–496.
45. Chen CL, Hsieh YT, Chen HC (2007) Phosphorylation of adducin by protein kinase Cδ promotes cell motility. *J Cell Sci* 120: 1157–1167.
46. Giganti A, Plastino J, Janji B, Van Troys M, Lentz D, et al. (2005) Actin-filament cross-linking protein T-plastin increases Arp2/3-mediated actin-based movement. *J Cell Sci* 118: 1255–1265.
47. Pal Sharma C, Goldmann WH (2004) Phosphorylation of actin-binding protein (ABP-280; filamin) by tyrosine kinase p56lck modulates actin filament cross-linking. *Cell Biol Int* 28: 935–941.
48. Lacroix M, Haibe-Kains B, Hennuy B, Laes JF, Lallemand F, et al. (2004) Gene regulation by phorbol 12-myristate 13-acetate in MCF-7 and MDA-MB-231, two breast cancer cell lines exhibiting highly different phenotypes. *Oncol Rep* 12: 701–707.
49. Lee SO, Jeong YJ, Kim M, Kim CH, Lee IS (2008) Suppression of PMA-induced tumor cell invasion by capillarisin via the inhibition of NF-κB-dependent MMP-9 expression. *Biochem Biophys Res Commun* 366: 1019–1024.
50. Shiroo M, Matsushima K (1990) Enhanced phosphorylation of 65 and 74 kDa proteins by tumor necrosis factor and interleukin-1 in human peripheral blood mononuclear cells. *Cytokine* 2: 13–20.
51. Jones SL, Wang J, Turck CW, Brown EJ (1998) A role for the actin-bundling protein L-plastin in the regulation of leukocyte integrin function. *Proc Natl Acad Sci U S A* 95: 9331–9336.
52. Le Clainche C, Carlier MF (2008) Regulation of actin assembly associated with protrusion and adhesion in cell migration. *Physiol Rev* 88: 489–513.
53. Delanote V, Vanloo B, Catillon M, Friederich E, Vandekerckhove J, et al. (2009) An alpaca single-domain antibody blocks filopodia formation by obstructing L-plastin-mediated F-actin bundling. *Faseb J*.
54. Lai FP, Szczodrak M, Oelkers JM, Ladwein M, Acconcia F, et al. (2009) Cortactin promotes migration and platelet-derived growth factor-induced actin reorganization by signaling to Rho-GTPases. *Mol Biol Cell* 20: 3209–3223.
55. Weed SA, Parsons JT (2001) Cortactin: coupling membrane dynamics to cortical actin assembly. *Oncogene* 20: 6418–6434.
56. Weed SA, Karginov AV, Schafer DA, Weaver AM, Kinley AW, et al. (2000) Cortactin localization to sites of actin assembly in lamellipodia requires interactions with F-actin and the Arp2/3 complex. *J Cell Biol* 151: 29–40.
57. Toneguzzo F, Hayday AC, Keating A (1986) Electric field-mediated DNA transfer: transient and stable gene expression in human and mouse lymphoid cells. *Mol Cell Biol* 6: 703–706.
58. Friederich E, Vancompernelle K, Louvard D, Vandekerckhove J (1999) Villin function in the organization of the actin cytoskeleton. Correlation of in vivo effects to its biochemical activities in vitro. *J Biol Chem* 274: 26751–26760.
59. Phair RD, Gorski SA, Misteli T (2004) Measurement of dynamic protein binding to chromatin in vivo, using photobleaching microscopy. *Methods Enzymol* 375: 393–414.

A Novel Network Integrating a miRNA-203/SNAI1 Feedback Loop which Regulates Epithelial to Mesenchymal Transition

Michèle Moes^{1*}, Antony Le Béhec¹, Isaac Crespo², Christina Laurini¹, Aliaksandr Halavatyi¹, Guillaume Vetter¹, Antonio del Sol², Evelyne Friederich^{1*}

¹ Cytoskeleton and Cell Plasticity Lab, Life Sciences Research Unit-FSCT, University of Luxembourg, Luxembourg, Luxembourg, ² Luxembourg Centre for Systems Biomedicine, University of Luxembourg, Esch-sur-Alzette, Luxembourg

Abstract

Background: The majority of human cancer deaths are caused by metastasis. The metastatic dissemination is initiated by the breakdown of epithelial cell homeostasis. During this phenomenon, referred to as epithelial to mesenchymal transition (EMT), cells change their genetic and transcriptomic program leading to phenotypic and functional alterations. The challenge of understanding this dynamic process resides in unraveling regulatory networks involving master transcription factors (e.g. SNAI1/2, ZEB1/2 and TWIST1) and microRNAs. Here we investigated microRNAs regulated by SNAI1 and their potential role in the regulatory networks underlying epithelial plasticity.

Results: By a large-scale analysis on epithelial plasticity, we highlighted miR-203 and its molecular link with SNAI1 and the miR-200 family, key regulators of epithelial homeostasis. During SNAI1-induced EMT in MCF7 breast cancer cells, miR-203 and miR-200 family members were repressed in a timely correlated manner. Importantly, miR-203 repressed endogenous SNAI1, forming a double negative miR203/SNAI1 feedback loop. We integrated this novel miR203/SNAI1 with the known miR200/ZEB feedback loops to construct an *a priori* EMT core network. Dynamic simulations revealed stable epithelial and mesenchymal states, and underscored the crucial role of the miR203/SNAI1 feedback loop in state transitions underlying epithelial plasticity.

Conclusion: By combining computational biology and experimental approaches, we propose a novel EMT core network integrating two fundamental negative feedback loops, miR203/SNAI1 and miR200/ZEB. Altogether our analysis implies that this novel EMT core network could function as a switch controlling epithelial cell plasticity during differentiation and cancer progression.

Citation: Moes M, Le Béhec A, Crespo I, Laurini C, Halavatyi A, et al. (2012) A Novel Network Integrating a miRNA-203/SNAI1 Feedback Loop which Regulates Epithelial to Mesenchymal Transition. PLoS ONE 7(4): e35440. doi:10.1371/journal.pone.0035440

Editor: Michael Klymkowsky, University of Colorado, Boulder, United States of America

Received: September 9, 2011; **Accepted:** March 16, 2012; **Published:** April 13, 2012

Copyright: © 2012 Moes et al. This is an open-access article distributed under the terms of the Creative Commons Attribution License, which permits unrestricted use, distribution, and reproduction in any medium, provided the original author and source are credited.

Funding: This work has been supported by the National Research Fund, Luxembourg (FNR/BIOSAN/07/12, ALB: AFR fellowship TR-PDR BFR08-084; AH: AFR PhD Fellowship TR-PHD BFR08-112), the "Fondation Cancer" and the University of Luxembourg. The funders had no role in study design, data collection and analysis, decision to publish, or preparation of the manuscript.

Competing Interests: The authors have declared that no competing interests exist.

* E-mail: evelyne.friederich@uni.lu (EF); moesmichele@gmail.com (MM)

Introduction

Carcinomas arise in epithelial tissues and the metastatic cascade is initiated by the breakdown of epithelial cell homeostasis. During this transient phenomenon, referred to as epithelial to mesenchymal transition (EMT) which also occurs during embryonic development, cells lose their epithelial features, including cell-cell adhesions and cell polarity, and gain cell motility, mesenchymal and stem cell-like properties. EMT can be initiated by multiple pathways converging in the activation of EMT inducers, such as SNAI1/2, ZEB1/2 and TWIST1, transcription factors which repress epithelial-specific genes [1,2].

MicroRNAs (miRNAs) are short noncoding RNAs that post-transcriptionally control gene expression through imperfect base-pairing to the 3' untranslated region (3'UTR) of target messenger RNAs. MiRNAs recently emerged as important regulators in EMT, the most prominent being the two clusters of the miR-200

epithelial marker family: miR-200b/200a/429 (miR-200b) and miR-200c/141 (miR-200c) [3,4]. The miR-200s regulate EMT through a double negative feedback loop with the ZEB factors, which, depending on the relative levels of miR-200 and ZEB, can direct the switch from epithelial- to mesenchymal-like states and back [5–8]. In addition, the transcription factor SNAI1, which plays a key role during the early steps of EMT, activates the expression of ZEB factors in a context-dependent manner [1,9–12]. An integrated view, on how these transcription factors and miRNAs contribute together to regulatory networks acting as switches between epithelial and mesenchymal states, is however lacking. The dynamic properties of such networks [13,14] are affected notably through feedback loops involving miRNAs and transcription factors acting as toggle switches [15,16].

Here, we performed a large-scale analysis highlighting miR-203 as consistently associated with epithelial plasticity and correlated to

the miR-200 family which plays a key role in epithelial homeostasis. Furthermore, our experimental data connected miR-203 and the transcription factor SNAI1 in a double negative feedback loop. Based on our present and published data, we integrated this novel miR203/SNAI1 and the well-characterized miR200/ZEB feedback loops into a SNAI1-orchestrated EMT core network. Dynamic simulation revealed the existence of two stable states for this network and showed that the miR203/SNAI1 loop plays a crucial role in the switch from an epithelial to a mesenchymal state and in the stabilization of the core network in these two states. These findings support previous studies [13,17] showing the key role of feedback loops in network stability and determination of cell fate and plasticity.

Results and Discussion

MiR-203 is associated with SNAI1 and the miR-200s

To identify miRNAs participating in SNAI1-orchestrated regulatory networks, we analysed our time-resolved microarray data (GEO accession: GSE35074) of EMT, triggered by conditional expression of SNAI1 in “Tet-Off” MCF7-SNAI1 breast carcinoma cells [18,19]. At an established EMT state, 61 miRNAs were differentially expressed (Table S1). Among those, 29 miRNAs were repressed and potentially regulated by the transcriptional repressor SNAI1. We combined these experimental results with miRNA expression signature analyses of four published datasets of epithelial and mesenchymal NCI60 cancer cell lines (Fig. 1A, Table S2) [20–23], and calculated expression correlations with the miR-200 epithelial marker family (Table S3). Interestingly, these analyses highlighted miR-203, whose expression was downregulated in our EMT model and mesenchymal cancer cell lines, as well as highly correlated to the expression of the miR-200s. Co-regulated overexpression of miR-203 and miR-200 family members has been reported during early stages of human stem cell differentiation into epidermal cells suggesting their participation to this process [24]. Conversely, miRNA expression analysis in endometrial carcinosarcomas, a *bona fide* example of EMT *in vivo*, revealed a marked downregulation of miR-203 and miR-200 family members in the mesenchymal areas, concomitant to the upregulation of EMT inducers, including SNAI1 [25]. Further expression profiling in human primary and metastatic cancers showed that miR-203 and miR-200 family members were significantly suppressed in the latter, suggesting a direct involvement in cancer metastasis [26]. These large-scale analyses indicated that these molecular actors may work together, as positive or negative regulators. Therefore, we decided exploring the regulation of miR-203 and miR-200 family members through SNAI1, and their integration into regulatory networks governing epithelial cell plasticity.

SNAI1 represses miR-203 and miR-200b expression

First, we assayed miR-203 expression during SNAI1 induction in our EMT model by qRT-PCR analyses. MiR-203 was continuously repressed upon SNAI1 induction, similarly to the miR-200b cluster (Fig. 1B; Fig. S1). We further showed that miR-203 and miR-200b promoter activity significantly decreased upon 12 h of SNAI1 induction (Fig. 1C). In line with our findings, overexpressed SNAI1 reduced promoter activity of miR-203 [27], and of the miR-200c cluster [7,27], in a HEK293T and HCT116 cell system, respectively. Also, SNAI1 has been shown to repress miR-200 family members during murine embryonic stem cell differentiation [28]. In addition, in line with previous results [9,10], overexpression of SNAI1 in our MCF7-SNAI1 cell model induced an upregulation of ZEB1 (our unpublished observation)

which targets miR-203 and the miR-200s [6,7,27]. Altogether these data suggest that SNAI1 regulates expression of miR-203 and both miR-200 clusters in a coordinated manner, and that these miRNAs co-act in SNAI1-regulated programs.

MiR-203 downregulates endogenous SNAI1 and promotes epithelial-like properties in breast cancer cells

Next, we investigated the role of miR-203 in relationship with SNAI1 expression in breast carcinoma cells. In MCF7-SNAI1 cells, ectopically expressed SNAI1 lacks its natural 3'UTR [18] and therefore, these cells are not suitable to study whether miR-203 regulates SNAI1 messenger RNA (mRNA). The mesenchymal breast cancer cell line HTB129 presents high levels of endogenous SNAI1 and low levels of miR-203 as compared to epithelial MCF7 cells [21,29]. HTB129 cells stably transfected with miR-203 (HTB129-miR203) exhibited a significant decrease in SNAI1 mRNA (Fig. 2A, Fig. S2). HTB129-miR203 cells lost their typical fibroblastic, dispersed phenotype and acquired a more compact and cohesive appearance (Fig. 2B). HTB129-miR203 cells further lost about 25% of their migratory and 15% of their invasive capacity (Fig. 2C, D). By performing MTT proliferation and AnnexinV apoptosis assays we excluded that observed inhibitions were due to decreased cell proliferation and/or programmed cell death (Fig. S3). Interestingly, previous studies in prostate cancer progression and metastasis showed that miR-203 expression not only controlled cell migration and invasion of prostate cancer cell lines, but also suppressed prostate cancer metastasis *in vivo* via repression of prometastatic targets such as ZEB2 [30,31]. HTB129 cells expressed high levels of ZEB1/2 factors, but in the present cellular context, miR-203 expression did not lead to significant decrease of ZEB2 mRNA. This may be due, in part, to incomplete miR-203-mediated repression of SNAI1 which has been shown previously to promote upregulation of ZEB factors [32]. In addition, HTB129 cells co-expressed high levels of SNAI2 and TWIST1 (our unpublished data), two EMT inducers. Collectively, these factors may attenuate the effects of miR-203-mediated repression of SNAI1 in HTB129-miR203 cells. Accordingly, we did not detect a significant increase in expression of classical epithelial markers such as E-cadherin and keratin 18 in these cells (our unpublished observations). Altogether these results show that miR-203 significantly reduces SNAI1 expression and promotes epithelial-like features such as a more cohesive phenotype and reduced motility, motivating us to investigate whether miR-203 could directly target SNAI1.

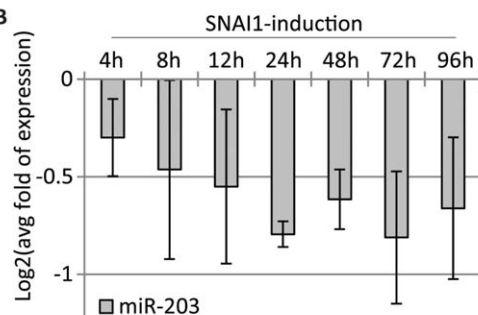
MiR-203, but not the miR-200s, directly represses SNAI1

In silico analysis predicted two binding sites for miR-203, but none for miR-200 family members, within the 3'UTR of the SNAI1 mRNA (Fig. 2E) (microRNA.org, August 2010 Release) [33]. The ability of miR-203 to directly target SNAI1 was evaluated by luciferase reporter assays in MDA231 cells, using SNAI1-3'UTR reporter constructs - wild type or lacking the predicted miR-203 target sites. Overexpression of miR-203 in MDA231 cells reduced the activity of the wild type SNAI1-3'UTR, but not the mutant construct (Fig. 2F). Further, in agreement with *in silico* predictions, miR-200a and miR-200c (miR-200a/c), representing both seed sequences found within the miR-200 family, did not repress wild type SNAI1-3'UTR reporter activity (Fig. 2G). A similar result was obtained in the unrelated HeLa cell line (data not shown). These results indicate that miR-203, but not the miR-200s, directly regulates SNAI1 expression, thus linking miR-203 and SNAI1 in a double negative feedback loop and suggesting convergent yet not identical roles for these miRNAs in the regulation of SNAI1-orchestrated processes.

A

| miRNA_id | MCF7-SNAI1 | NCI60 Cell line panel | | | |
|--------------|------------|-----------------------|------------|---------------|----------------|
| | EMT model | Park et al. | Liu et al. | Blower et al. | Sokilde et al. |
| hsa-miR-203 | DOWN | DOWN | DOWN | DOWN | DOWN |
| hsa-miR-200c | DOWN | DOWN | DOWN | DOWN | DOWN |
| hsa-miR-200b | DOWN | DOWN | DOWN | DOWN | DOWN |
| hsa-miR-200a | DOWN | DOWN | DOWN | | DOWN |
| hsa-miR-141 | | DOWN | DOWN | DOWN | DOWN |
| hsa-miR-375 | | DOWN | DOWN | DOWN | |
| hsa-miR-7 | | | DOWN | DOWN | DOWN |
| hsa-miR-429 | DOWN | | DOWN | | DOWN |
| hsa-miR-215 | | | DOWN | DOWN | DOWN |
| hsa-miR-205 | | | DOWN | DOWN | DOWN |
| hsa-miR-194 | | | DOWN | DOWN | DOWN |
| hsa-miR-192 | | | DOWN | DOWN | DOWN |

B



C

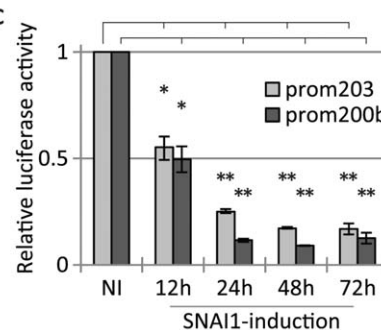


Figure 1. Large-scale analysis of miRNA expression signatures, and miR-203 expression during SNAI1 induction in MCF7-SNAI1 cells. A) List of miRNAs found downregulated, in at least three studies, in the large-scale analysis. B) qRT-PCR analyses of miR-203 expression levels normalized to U44 expression and expression levels in non-induced cells. C) Relative luciferase activity of miR-203 and miR-200b promoter constructs in non-induced (NI) and SNAI1-induced cells. Data are normalized to "NI" (*, $p < 0.05$; **, $p < 0.01$). doi:10.1371/journal.pone.0035440.g001

Integration of miR203/SNAI1 in an EMT core network

We integrated the novel miR203/SNAI1 feedback loop together with the known miR200/ZEB feedback loops [5] into an *a priori* SNAI1-centered EMT core network (Fig. 3A), based on our present and published data. SNAI1 represses the transcription of both miR-200 clusters (our data) [7,27,28] and indirectly activates expression of the ZEB factors (our unpublished observation) [9–11]. Further, ZEB1/2 inhibit miR-203 promoter activity [27] and in turn miR-203 targets and represses ZEB2 [30]. E-cadherin which is directly repressed by the SNAI1 and ZEB factors [1], was added to the network as an epithelial target gene.

Dynamic simulation of our core network revealed two stable states which we associated with an epithelial "E" and mesenchymal "M" phenotype as described in literature (Fig. 3A, Data S1) [1]. Transition probability further attributed a high robustness to both states (Data S1), implicating that the core network is unlikely to switch between states without external stimulus. Importantly, the simulation of an upregulation of SNAI1 triggered the transition from state "E" to "M" (Fig. 3A, B). Next, to show the importance of the miR203/SNAI1 feedback loop on the network dynamics, we performed an 'edgetic' (edge-specific genetic) perturbation, by removing the "miR-203 on SNAI1" interaction [34]. Interestingly, the dynamic simulation of the edge-altered core network revealed a single stable state "E_{ca}" (edge-altered state "E") (Data S1). Thus, the feedback regulation "miR-203 on SNAI1" is crucial for switching from an epithelial to a mesenchymal state and in stabilising the core network in both states.

Conclusion

Co-expression of EMT master regulators in cancer cells makes it difficult to understand the molecular hierarchy and cooperation between them. Our dynamic MCF7-SNAI1 cell model allowed evaluating the link between SNAI1 expression and other molecular actors involved in EMT, which we further analysed in HTB129 and MDA231 cells. Collectively, our integrative study implies that this core network (Fig. 3) could function as a robust switch controlling early steps of EMT and epithelial homeostasis, further emphasizing the importance of bistable feedback loops in determining cell plasticity [13,17]. Obviously, the present core network is embedded into a larger network with multiple molecular actors such as SNAI2 and TWIST1 (our observations) the expression of which is interconnected in a context-dependent manner and regulated by various pathways [1,32,35]. This core network will provide a good starting point to further study key regulatory circuits underlying EMT, such as TGF β signalling which plays an important role in transient cancer cell invasion. Indeed, TGF β induces EMT via upregulation of SNAI1 at early states of the transition while subsequent expression of ZEB1/2, SNAI2 and TWIST1 may maintain the mesenchymal, migratory phenotype [35,36]. Interestingly, in addition to ZEB1 also SNAI2 and TWIST1 increased during SNAI1-induction in MCF7-SNAI1 cells (our unpublished observations). Based on previous findings, it is likely that in our cell model, the transcriptional repressors SNAI1 and SNAI2 may work in concert and target common genes via binding to E-boxes of their promoters [1]. In future, further dissection of the molecular links between EMT master regulators

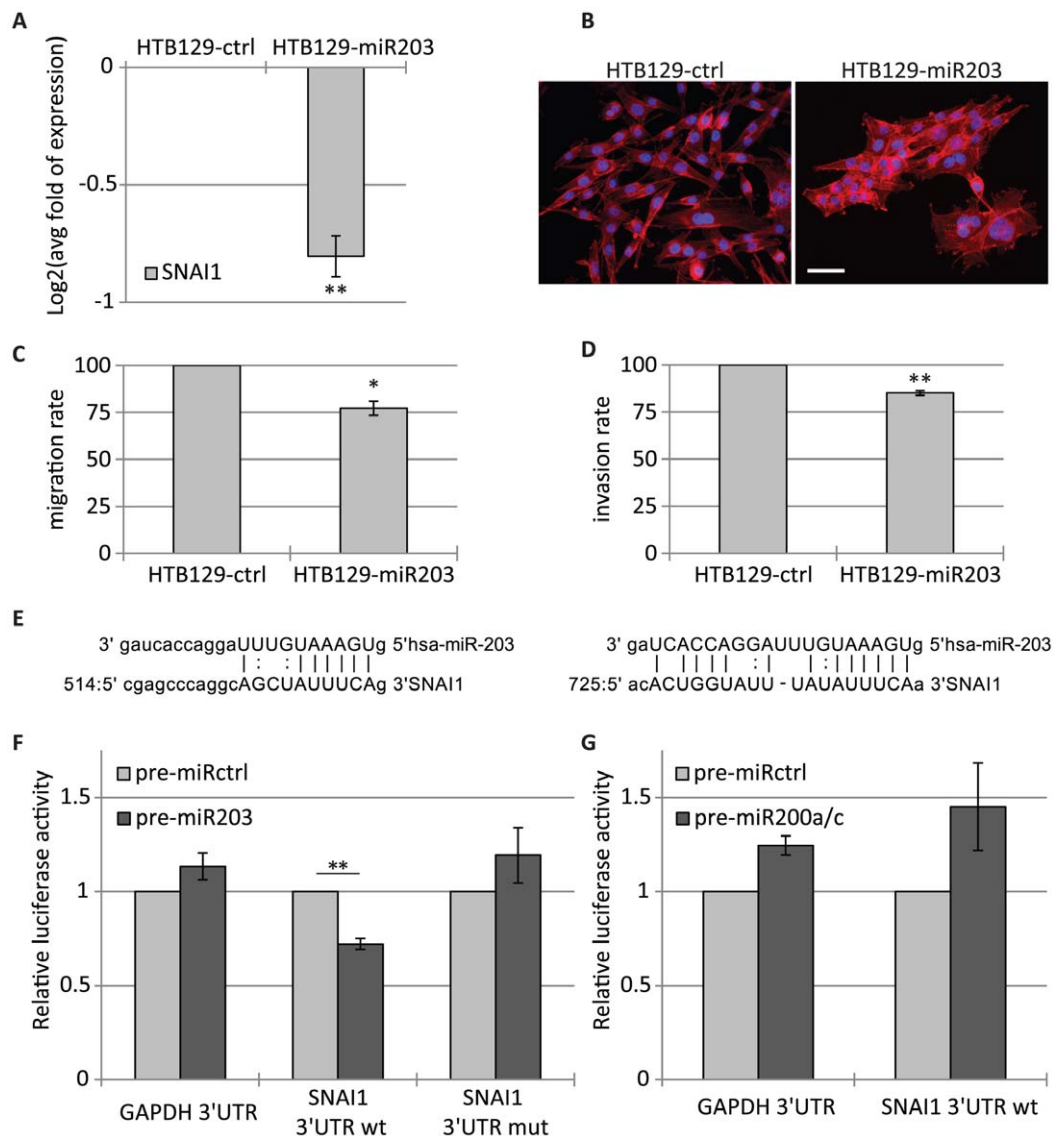


Figure 2. MiR-203 promotes epithelial-like features and represses endogenous SNAI1. HTB129-ctrl and HTB129-miR203 cells were subjected to A) qRT-PCR analyses of SNAI1 mRNA expression in HTB129-ctrl and HTB129-miR203 cells, B) fluorescent staining with DAPI (blue) and phalloidin (red) (scale bar, 20 μm), C) migration and D) invasion assays. E) Predicted miR-203 target sites within SNAI1 3'UTR. F, G) Relative luciferase activity of SNAI1-3'UTR wild type (wt) or mutant (mut) in MDA231 cells transfected with control (F, G), miR-203 (F) or miR-200a/c (G) precursors. Co-transfection with GAPDH 3'UTR vector served as additional negative control (*, $p < 0.05$; **, $p < 0.01$). doi:10.1371/journal.pone.0035440.g002

and miR-200s/miR-203, together with the consideration of quantitative binding parameters, will allow completing our core network and will contribute to the better understanding of key regulatory circuits underlying EMT.

Materials and Methods

Epithelial/mesenchymal miRNA expression signature study

Data from the NCI60 panel were analyzed using the same statistical analysis (t-test) and classification as described in Park et al [21]. Differentially expressed miRNAs were filtered using a p-value threshold of 0.01. Expression levels (UP or DOWN) correspond to the sign of the difference between the average of log-intensity values of mesenchymal cells and the average of log-intensity values of epithelial cells: $sign(\log(I_M) - \log(I_E))$.

MiRNA microarray analysis

MiRNA microarray design, protocols and data have been deposited in NCBI's Gene Expression Omnibus and are accessible through GEO Series accession number GSE35074. The established state of EMT is considered reached after 72 h to 96 h of SNAI1 induction and refers to the "late EMT stage" we previously defined by analyzing transcriptional events as well as phenotypic changes occurring upon SNAI1 induction in our MCF7-SNAI1 EMT model [18]. Averaged expression values for each time point (72 h and 96 h) were calculated taking into account only replicates which have moduli of log-ratios ≥ 0.5 and t-test p-values ≤ 0.01 (according to LCSciences data processing).

Vector constructs

For exogenous miR-203 expression, hsa-miR-203 stem-loop sequence (MI0000283) -200/+192 relative to the first and last

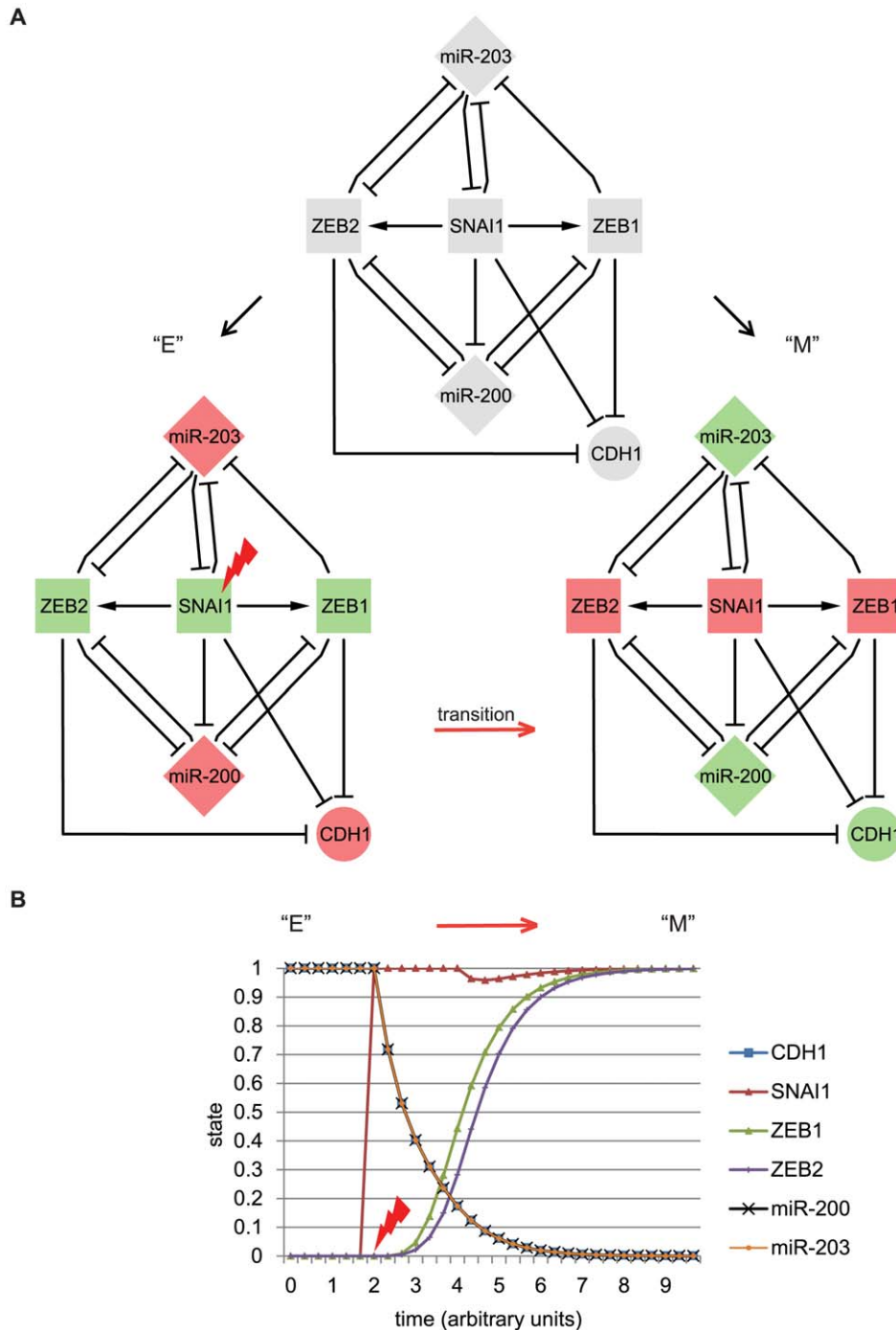


Figure 3. EMT core network integrating the miR203/SNAI1 and miR200/ZEB double negative feedback loops. A) The top panel corresponds to the core network integrating described interactions between miR-203, miR-200s (miR-200), SNAI1, ZEB1, ZEB2 and E-cadherin (CDH1). The bottom panels show the stable states “E” and “M” obtained after dynamic analyses. B) *In silico* upregulation of SNAI1 in a continuous dynamic system of the EMT core network. The state of SNAI1 is changed from “0” to “1” at time point 2 (arbitrary units of time), during two units of time. Diamonds represent miRNAs, squares transcription factors, and circles coding-genes other than transcription factors. Red and green colours stand for upregulated and downregulated expression levels, respectively. Edges represent an interaction between two actors, either activation (arrow) or inhibition (blunt arrow). The “lightning” indicates a SNAI1 upregulation triggering the transition from state “E” to “M” (red arrow).
doi:10.1371/journal.pone.0035440.g003

nucleotide of the stem-loop, was synthesized and cloned into *Bgl*II/*Hind*III sites of the pSUPER.retro.puro vector (pSUPER-miR-203) (OligoEngine) (DNA2.0). Hsa-miR-203 promoter region [27] was synthesized and cloned into pGL3-basic reporter using *Kpn*I/*Hind*III sites (DNA2.0). Wild type human GAPDH- and

SNAI1-3'UTR, and mutant SNAI1-3'UTR lacking the predicted miR-203 binding sites, were synthesized and cloned into the psiCHECKTM-2 (Promega) vector at *Xho*I/*Not*I sites (DNA2.0). Mir-200b promoter construct, pGL3miR200b/200a/429 (−321/+120) has been previously described [6].

Cell lines

“Tet-Off” MCF7-SNAI1 cells expressing human SNAI1 upon removal of tetracycline from the culture medium have been previously described [18,19]. The human breast cancer cell lines HTB129 and MDA231 (also named MDA-MB-231 or HTB-26), purchased from the ATCC, were maintained in RPMI1640 and Leibovitz culture media (Lonza), respectively, supplemented with 10% fetal bovine serum, 2 mM L-glutamine, 100 U/ml penicillin and 100 µg/ml streptomycin. HTB129 cells stably expressing miR-203 were generated by pSUPER-miR203 vector transfection and puromycin selection. Cells stably transfected with the empty pSUPER.retro.puro vector served as control.

Epifluorescence staining of cells

To reveal and illustrate the cell phenotype, DNA and F-actin were stained with DAPI (MPBiochemicals) and Phallo504 (Invitrogen), respectively. Cells were analyzed by epifluorescence microscopy (Leica DMRX microscope). Images were acquired with a linear CCD camera (Micromax) and analyzed with Metaview software (Universal Imaging Corporation Ltd).

RNA extraction and real-time quantitative PCR (qRT-PCR)

Total RNA was extracted using Trizol as recommended by the manufacturer (Invitrogen). RNA quality and concentration were evaluated spectroscopically using a NanoDrop 2000c instrument (ThermoScientific). Reverse transcription and qRT-PCR quantification of miRNA and mRNA were carried out as described previously [18,37]. U44 and GAPDH served as internal references, respectively. Oligonucleotides used in this study are listed in Table S4.

Luciferase reporter assays

Indicated cell lines were plated in 6-well plates and transfection was carried out using Lipofectamine 2000 (Invitrogen). For promoter reporter assays, cells were cotransfected with a pGL3-promoter construct (600 ng) and a pRL-TK reference plasmid (5 ng) (Promega). For 3'UTR reporter assays, cotransfection was realized with 90 ng 3'UTR-psiCHECKTM-2 constructs and a total of 75 pmol Pre-miRTM miRNA Precursor Molecules (Ambion). After 24 h of incubation cells were lysed, and firefly and *Renilla* luciferase activities were measured with a FluoStar Optima instrument (BMG LABTECH) using the Dual-Luciferase Reporter Assay System (Promega). All reporter assays are shown as relative luciferase activities, normalized to controls.

Cell migration assay

Cell migration was evaluated using Ibidi culture inserts according to the manufacturer's protocol (Ibidi). Cells were seeded into the Culture-Inserts and grown overnight to confluency. After removal of the insert a 500 µm cell-free gap was created. Phase contrast images of the same gap fields were captured at 0 h and 24 h of incubation using an inverted light microscope (Leica DMIL) with camera (Leica DFC360 FX). Gap closure was quantified using ImageJ software (NIH).

Cell invasion assay

5×10⁴ cells were seeded in 2% FBS medium, onto Transwell plates coated with 50 µg of extracellular matrix proteins (ECM gel E1270, Sigma). 10% FBS medium was added to the lower chamber as chemoattractant. After 24 h, cell invasion was quantified using the MTT assay (Sigma).

Statistical analysis

Assays were performed in technical triplicates and repeated in at least three biological replicates. Presented data are mean ± SEM of three biological replicates. Paired t-test was used to estimate p values. For the 3'UTR reporter assays one-tailed paired t-test was used to check for a potential decrease in relative luciferase activity. p<0.05 was considered to be statistically significant. For qRT-PCR assays, Log2-transformed mean fold changes (averaged over three biological replicates) are presented. Error bars are the SEM recalculated using the standard method for error propagation.

Supporting Information

Data S1 Continuous dynamic model generation and perturbation.

(DOC)

Figure S1 Expression profiles of miR-200b cluster members upon SNAI1-induction in the MCF7-SNAI1 EMT cell model. MiR-200b (A), miR-200a (B), miR-429 (C) expression levels were determined by qRT-PCR and normalized to U44 expression and expression levels in non-induced MCF7-SNAI1 cells.

(TIF)

Figure S2 Ectopic miR-203 expression levels in stably transfected HTB129 cells. Mir-203 expression levels were determined by qRT-PCR and normalized to U44 expression and expression levels in HTB129-ctrl cells.

(TIF)

Figure S3 Proliferation curves of and percentage of early apoptotic events in HTB129-ctrl and HTB129-miR203 cells. A) Representative proliferation curves of HTB129-ctrl and HTB129-miR203 cells. Cell proliferation was assayed over 96 h and quantified using the MTT assay. B)

Percentage of early apoptotic HTB129-ctrl and HTB129-miR203 cells, as determined by flow cytometry using AnnexinV/Propidium iodide staining (BD Pharmingen).

(TIF)

Table S1 Expression data of miRNAs differentially expressed at an established EMT state. Microarrays were performed at 72 h and 96 h of SNAI1 induction in our EMT cell model. Averaged expression values for each time point were calculated taking into account only replicates which have moduli of log-ratios≥0.5 and t-test p-values≤0.01.

(XLS)

Table S2 Large-scale analysis of miRNA expressions combining our SNAI1-induced EMT study with epithelial/mesenchymal signatures. The large-scale analysis combines our microarray analysis results and signatures from four published miRNA microarray analyses of the NCI60 cancer cell line panel.

For each analysis, a table provides a list of miRNAs with corresponding expression levels (UP or DOWN), selected with a p-value threshold of 0.01 (from a t-test using the Park et al. classification). This file includes a Venn diagram of the different analyses.

(XLS)

Table S3 Correlation analysis of miRNA expression levels. Expression matrices of four published NCI60 studies were processed with the M@IA environment [38], by merging replicates with the average method on the miRNA_id provided in each study (miRBase). Correlation matrices were calculated with the R environment (<http://www.r-project.org>), with the

Pearson method. For each miRNA, the average correlation was calculated, considering correlation with all members of the miR-200 family and allowed to establish a rank correlation (the higher the average correlation, the lower the rank). (XLS)

Table S4 Primers used for detection of miRNAs and mRNAs (primer sequences (5' – 3')) (Genecust). (TIF)

References

- Thiery JP, Acloque H, Huang RY, Nieto MA (2009) Epithelial-mesenchymal transitions in development and disease. *Cell* 139: 871–890.
- Chaffer CL, Weinberg RA (2011) A perspective on cancer cell metastasis. *Science* 331: 1559–1564.
- Bracken CP, Gregory PA, Khew-Goodall Y, Goodall GJ (2009) The role of microRNAs in metastasis and epithelial-mesenchymal transition. *Cell Mol Life Sci* 66: 1682–1699.
- Nicoloso MS, Spizzo R, Shimizu M, Rossi S, Calin GA (2009) MicroRNAs—the micro steering wheel of tumour metastases. *Nat Rev Cancer* 9: 293–302.
- Brabletz S, Brabletz T (2010) The ZEB/miR-200 feedback loop—a motor of cellular plasticity in development and cancer? *EMBO Rep* 11: 670–677.
- Bracken CP, Gregory PA, Kolesnikoff N, Bert AG, Wang J, et al. (2008) A double-negative feedback loop between ZEB1-SIP1 and the microRNA-200 family regulates epithelial-mesenchymal transition. *Cancer Res* 68: 7846–7854.
- Burk U, Schubert J, Wellner U, Schmalhofer O, Vincan E, et al. (2008) A reciprocal repression between ZEB1 and members of the miR-200 family promotes EMT and invasion in cancer cells. *EMBO Rep* 9: 582–589.
- Gregory PA, Bracken CP, Bert AG, Goodall GJ (2008) MicroRNAs as regulators of epithelial-mesenchymal transition. *Cell Cycle* 7: 3112–3118.
- Dave N, Guaita-Estrella S, Gutarra S, Frias A, Beltran M, et al. (2011) Functional cooperation between Snail1 and twist in the regulation of ZEB1 expression during epithelial to mesenchymal transition. *J Biol Chem* 286: 12024–12032.
- Guaita S, Puig I, Franci C, Garrido M, Dominguez D, et al. (2002) Snail induction of epithelial to mesenchymal transition in tumor cells is accompanied by MUC1 repression and ZEB1 expression. *J Biol Chem* 277: 39209–39216.
- Beltran M, Puig I, Pena C, Garcia JM, Alvarez AB, et al. (2008) A natural antisense transcript regulates Zeb2/Sip1 gene expression during Snail1-induced epithelial-mesenchymal transition. *Genes Dev* 22: 756–769.
- Peinado H, Olmeda D, Cano A (2007) Snail, Zeb and bHLH factors in tumour progression: an alliance against the epithelial phenotype? *Nat Rev Cancer* 7: 415–428.
- Huang S, Eichler G, Bar-Yam Y, Ingber DE (2005) Cell fates as high-dimensional attractor states of a complex gene regulatory network. *Phys Rev Lett* 94: 128701.
- Tasseff R, Nayak S, Salim S, Kaushik P, Rizvi N, et al. (2010) Analysis of the molecular networks in androgen dependent and independent prostate cancer revealed fragile and robust subsystems. *PLoS One* 5: e8864.
- Shiraishi T, Matsuyama S, Kitano H (2010) Large-scale analysis of network bistability for human cancers. *PLoS Comput Biol* 6: e1000851.
- Le Becqec A, Portales-Casamar E, Vetter G, Moes M, Zindy PJ, et al. (2011) MIR@NT@N: a framework integrating transcription factors, microRNAs and their targets to identify sub-network motifs in a meta-regulation network model. *BMC Bioinformatics* 12: 67.
- Gordon AJ, Halliday JA, Blankschien MD, Burns PA, Yatagai F, et al. (2009) Transcriptional infidelity promotes heritable phenotypic change in a bistable gene network. *PLoS Biol* 7: e44.
- Vetter G, Le Becqec A, Muller J, Muller A, Moes M, et al. (2009) Time-resolved analysis of transcriptional events during SNAIL-triggered epithelial to mesenchymal transition. *Biochem Biophys Res Commun* 385: 485–491.
- Yatskou M, Novikov E, Vetter G, Muller A, Barillot E, et al. (2008) Advanced spot quality analysis in two-colour microarray experiments. *BMC Res Notes* 1: 80.
- Blower PE, Verducci JS, Lin S, Zhou J, Chung JH, et al. (2007) MicroRNA expression profiles for the NCI-60 cancer cell panel. *Mol Cancer Ther* 6: 1483–1491.
- Park SM, Gaur AB, Lengyel E, Peter ME (2008) The miR-200 family determines the epithelial phenotype of cancer cells by targeting the E-cadherin repressors ZEB1 and ZEB2. *Genes Dev* 22: 894–907.
- Liu H, D'Andrade P, Fulmer-Smentek S, Lorenzi P, Kohn KW, et al. (2010) mRNA and microRNA expression profiles of the NCI-60 integrated with drug activities. *Mol Cancer Ther* 9: 1080–1091.
- Sokilde R, Kaczowski B, Podolska A, Cirera S, Gorodkin J, et al. (2011) Global microRNA analysis of the NCI-60 cancer cell panel. *Mol Cancer Ther* 10: 375–384.
- Nissan X, Denis JA, Saidani M, Lemaire G, Peschanski M, et al. (2011) miR-203 modulates epithelial differentiation of human embryonic stem cells towards epidermal stratification. *Dev Biol* 356: 506–515.
- Castilla MA, Moreno-Bueno G, Romero-Perez L, Van De Vijver K, Biscuola M, et al. (2010) Micro-RNA signature of the epithelial-mesenchymal transition in endometrial carcinosarcoma. *J Pathol* 223: 72–80.
- Baffa R, Fassan M, Volinia S, O'Hara B, Liu CG, et al. (2009) MicroRNA expression profiling of human metastatic cancers identifies cancer gene targets. *J Pathol* 219: 214–221.
- Wellner U, Schubert J, Burk UC, Schmalhofer O, Zhu F, et al. (2009) The EMT-activator ZEB1 promotes tumorigenicity by repressing stemness-inhibiting microRNAs. *Nat Cell Biol* 11: 1487–1495.
- Gill JG, Langer EM, Lindsley RC, Cai M, Murphy TL, et al. (2011) Snail and the microRNA-200 family act in opposition to regulate epithelial-to-mesenchymal transition and germ layer fate restriction in differentiating ESCs. *Stem Cells* 29: 764–776.
- Battle E, Sancho E, Franci C, Dominguez D, Monfar M, et al. (2000) The transcription factor snail is a repressor of E-cadherin gene expression in epithelial tumour cells. *Nat Cell Biol* 2: 84–89.
- Saini S, Majid S, Yamamura S, Tabatabai ZL, Suh SO, et al. (2011) Regulatory role of miR-203 in prostate cancer progression and metastasis. *Clin Cancer Res* 17: 5287–98.
- Vitchie G, Lena AM, Latina A, Formosa A, Gregersen LH, et al. (2011) MiR-203 controls proliferation, migration and invasive potential of prostate cancer cell lines. *Cell Cycle* 10: 1121–1131.
- Taube JH, Herschkowitz JI, Komurov K, Zhou AY, Gupta S, et al. (2010) Core epithelial-to-mesenchymal transition interactome gene-expression signature is associated with claudin-low and metaplastic breast cancer subtypes. *Proc Natl Acad Sci U S A* 107: 15449–15454.
- Betel D, Wilson M, Gabow A, Marks DS, Sander C (2008) The microRNA.org resource: targets and expression. *Nucleic Acids Res* 36: D149–153.
- Zhong Q, Simonis N, Li QR, Charlotiaux B, Heuze F, et al. (2009) Edgetic perturbation models of human inherited disorders. *Mol Syst Biol* 5: 321.
- Thiault S, Tan EJ, Peinado H, Cano A, Heldin CH, et al. (2008) HMGA2 and Smads co-regulate SNAIL1 expression during induction of epithelial-to-mesenchymal transition. *J Biol Chem* 283: 33437–33446.
- Tran DD, Corsa CA, Biswas H, Aft RL, Longmore GD (2011) Temporal and spatial cooperation of Snail1 and Twist1 during epithelial-mesenchymal transition predicts for human breast cancer recurrence. *Mol Cancer Res* 9: 1644–1657.
- Saumet A, Vetter G, Bouttier M, Portales-Casamar E, Wasserman WW, et al. (2009) Transcriptional repression of microRNA genes by PML-RARA increases expression of key cancer proteins in acute promyelocytic leukemia. *Blood* 113: 412–421.
- Le Becqec A, Zindy P, Sierocinski T, Petritis D, Bihouee A, et al. (2008) M@IA: a modular open-source application for microarray workflow and integrative datamining. *In Silico Biol* 8: 63–69.

Acknowledgments

We thank Goodall Gregory for providing the miR-200b promoter construct. We are grateful to Elisabeth Schaffner-Reckinger for reading the manuscript and for her comments and helpful suggestions. We thank Sébastien Plançon for his help with flow cytometric assays.

Author Contributions

Conceived and designed the experiments: MM EF. Performed the experiments: MM CL. Analyzed the data: MM ALB IC CL AH GV ADS EF. Contributed reagents/materials/analysis tools: ALB IC ADS. Wrote the paper: MM ALB EF. Initiated the project: GV EF.